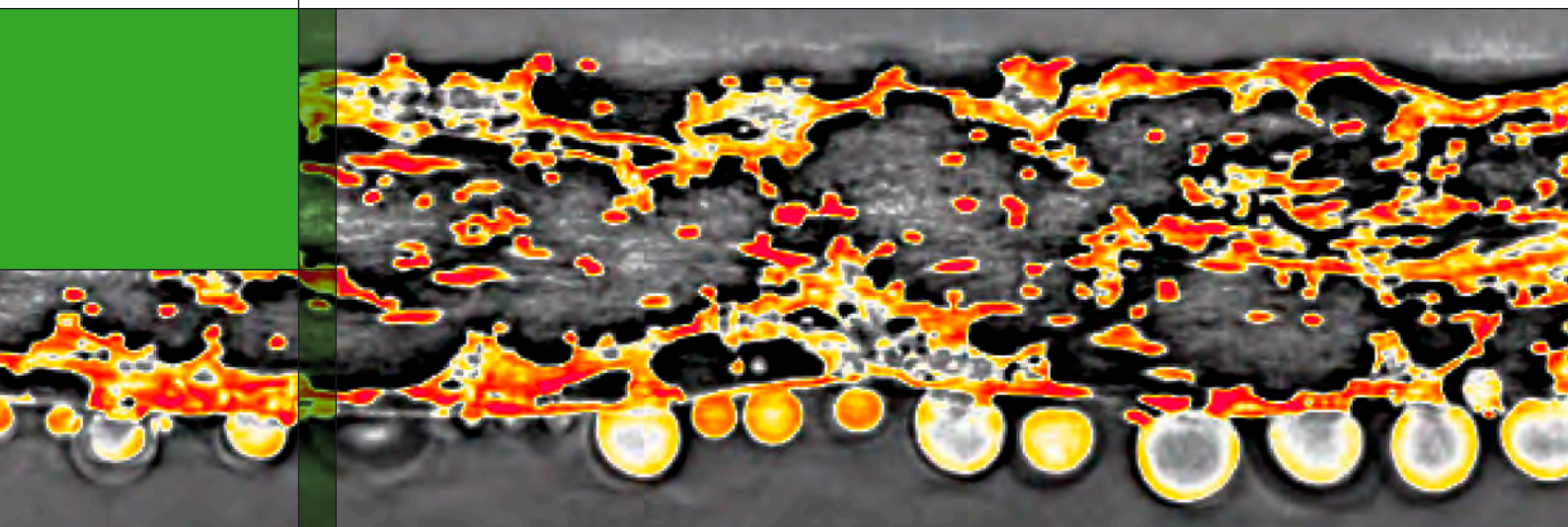


PAUL SCHERRER INSTITUT



Annual Report 2009

Electrochemistry Laboratory

<http://ecl.web.psi.ch>

COVER PHOTO:

Vertical cut through the gas diffusion layer (GDL) of a polymer electrolyte fuel cell recorded by X-ray tomography at the TOMCAT- Beamline of the SLS. The formation of water droplets can be observed *in situ*.

© Paul Scherrer Institut

PAUL SCHERRER INSTITUT



Electrochemistry Laboratory

Annual Report 2009

Hardcopies of this report are available from:
Isabella Kalt (isabella.kalt@psi.ch)
Paul Scherrer Institut
5232 Villigen PSI
Switzerland

A full version of this report is also available on the web:
<http://ecl.web.psi.ch>

Paul Scherrer Institut
Electrochemistry Laboratory
5232 Villigen PSI
Switzerland

Secretary
Phone +41 (0)56 310 29 19
Fax +41 (0)56 310 44 15

Publisher
Electrochemistry Laboratory
Paul Scherrer Institut
5232 Villigen PSI

Editorial Team
Isabella Kalt
Rüdiger Kötz
Günther G. Scherer

Printing
Paul Scherrer Institut

ISSN 1661-5379
PSI Electrochemistry Laboratory – Annual Report 2009

© Paul Scherrer Institut

CONTENTS

1 EDITORIAL

G.G. Scherer

3 SCIENTIFIC CONTRIBUTIONS 2009

FUEL CELLS - MATERIALS

5 Lifetime estimation of reactive oxygen species (ROS) in the polymer electrolyte fuel cell (PEFC)

7 Radical induced polymer electrolyte fuel cell membrane damage

9 Grafting kinetics of styrene-co-MAN onto ETFE

11 Effect of the styrene-MAN composition on the *ex situ* properties of grafted membranes based on ETFE

12 Diisopropenylbenzene as new crosslinker in radiation grafted ETFE based membranes for fuel cells: A kinetic study

13 Diisopropenylbenzene as new crosslinker in radiation grafted ETFE based membranes for fuel cells: *ex situ* and *in situ* characterization

15 *Ex situ* mechanical properties of PEFC membranes at 80 °C and 80 % relative humidity

17 FUEL CELLS - DIAGNOSTICS

19 Deuterium labeling of water combined with neutron radiography to study mass transport in the polymer electrolyte fuel cell (PEFC) membrane

21 Measurement of molecular diffusion limitations and their relation to liquid water in PEFC using helox mixture

23 3D imaging of PEFC electrodes

25 Investigation of transport mechanisms on Pt surfaces during hydrogen under potential deposition on micro-patterned electrodes

26 Negative resistance values in locally resolved impedance spectra of polymer electrolyte fuel cells

28 Modeling the effect of the air flow rate on locally resolved impedance spectra of polymer electrolyte fuel cells

30 A segmented microstructured flow field approach for sub-millimeter resolved local current measurement in channel and land areas of PEFCs

32 Simultaneous measurement of local flooding and current transients in channel and land areas of a polymer electrolyte fuel cell

34 In-plane current transients in channel and lands areas of a polymer electrolyte fuel cell during start-up

35 Dynamic measurement and modeling of the water vapor concentration during ac impedance measurements in PEFCs

37 Application of the Kramers Kronig relations on locally resolved impedance spectra of PEFCs

39 Investigations of local hysteresis effects in a PEFC

40 Locally resolved cyclic voltammetry in channel and land areas of a PEFC

41 Detectability of membrane defects by local online gas analysis

43 1+1-D dynamic full physics polymer electrolyte fuel cell model

44 Sub-millimeter current density distribution in PEFC at sub-zero temperatures

46 *In-situ* X-ray tomography and radiography of PEFCs

49 BATTERIES & SUPERCAPACITORS - MATERIALS

51 Preparation of an artificial SEI by surface modification of carbon electrodes

52 Influence of concentration of ions on the exfoliation of graphite at very positive potentials

53 *In situ* Raman monitoring of a microwave-assisted synthesis of LiFePO₄ nanoparticles for lithium-ion batteries

- 55 Layer formation on $\text{Li}_{1+x}\text{Mn}_2\text{O}_{4-\delta}$ films after electrochemical characterisation
- 57 Dialkoxyaryl-polymers as cathode materials for lithium batteries
- 58 X-ray photoelectron spectroscopy study of imidazolium based ionic liquids
- 59 Supercapacitor aging in laboratory cells at constant voltage
- 61 **BATTERIES & SUPERCAPACITORS - DIAGNOSTICS**
- 63 *In situ* synchrotron diffraction studies of NMC
- 65 *In situ* neutron diffraction study of Li insertion in $\text{Li}_4\text{Ti}_5\text{O}_{12}$
- 67 Investigation of the lithium-sulfur battery system
- 69 Investigations on the SEI formation kinetics on graphite surfaces with *post mortem* SEM and *in situ* DEMS
- 71 Characterization of bi - material electrode for electrochemical double layer capacitor / lithium ion battery hybrids
- 73 **CATALYSIS & INTERFACES**
- 75 Longevity studies of ultra low Pt anodes for PEFCs
- 76 Carbon corrosion in polymer electrolyte fuel cells
- 77 Influence of modified glassy carbon substrate on electrochemical platinum deposition
- 79 **THE ELECTROCHEMISTRY LABORATORY**
- 83 Structure
- 85 ECL-personnel
- 86 These PhD students from ECL graduated in 2009
- 88 Exchange students, diploma theses
- 89 Seminar, invited speakers
- 90 Awards
- 91 Conferences – Symposia
- 92 Review activities of the laboratory
- 93 Industrial partners
- 95 Documentation

EDITORIAL

“Learning from the past to master the future” was the topic of our 25th One-Day-Symposium on Electrochemistry, which took place on May 7, 2009. More than 100 participants from different countries expressed their interest in electrochemical research, attending the lectures delivered by Profs. Dieter Kolb, Ulm University, *The metal-electrolyte interface: What do we know?*, Nenad Markovic, Argonne National Laboratory, *Electrochemical interfaces: Structural and catalytic properties*, Joachim Maier, MPI Stuttgart, *Ionic charge carriers at solid-solid interfaces*, Jean-Marie Tarascon, CNRS Amiens, *Recent advances, new trends and future challenges within the Li-ion battery energy storage system*, Andreas Züttel, EMPA Dübendorf, *Aspects of energy storage, past and future*, and Manfred Waidhas, Siemens Erlangen *Electrochemical technologies for future industrial applications*. Over the past more than 20 years, this symposium has established itself as an international meeting, attracting speakers from around the world. Further, it demonstrates the continuity of electrochemical research, particularly addressed to energy conversion and storage, at the Paul Scherrer Institut.

Our laboratory’s effort is demonstrated in the wide scope of topics documented in this Annual Report 2009 with 39 contributions from our research groups. Again, we are happy to show considerable progress achieved in our main research areas fuel cells, batteries, and supercapacitors. This is further documented in the many peer reviewed publications, invited talks, and other contributions to disseminate our achievements to the scientific community, as mentioned in the Appendix of this report.

Education is another continuous task in our portfolio. During the past year, with success six of our young colleagues graduated with a PhD from the Swiss Federal Institute of Technology, Zürich. Additionally, several diploma students, summer students, and scientific guests experienced our hospitality.

Our collaboration with Belenos Clean Power Holding, Biel, to develop a “Swiss Fuel Cell Hybrid Power Train” is continuously progressing and we will report on this project in our next Annual Report.

We will be delighted to welcome many of you on the occasion of our 26th One-Day-Symposium on May 5, 2010. On this day, various speakers from our Swiss electrochemistry community will present an overview on the many facets of Swiss electrochemistry, ranging from fundamental aspects of electrochemical interfaces to technological applications in energy conversion and storage, surface processes, and sensor devices.

Please enjoy reading our Annual Report 2009.

Günther G. Scherer

SCIENTIFIC CONTRIBUTIONS 2009

FUEL CELLS

MATERIALS

Lifetime estimation of reactive oxygen species (ROS) in the polymer electrolyte fuel cell (PEFC)

L. Gubler, S.M. Dockheer¹, M.M. Menampambath, A. Wokaun, G.G. Scherer

phone: +41 56 310 2673, e-mail: lorenz.gubler@psi.ch

One of the factors limiting polymer electrolyte fuel cell (PEFC) durability is the susceptibility of the proton exchange membrane (PEM) towards oxidative degradation under the conditions prevailing in the PEFC. Oxidative stress is caused by the presence of reactive oxygen species (ROS), which are formed in the fuel cell as intermediates. Prime culprits are hydrogen peroxide (H₂O₂), the hydroxyl radical (HO[•]) and hydroperoxyl radical (HOO[•]). Due to the high oxidative strength of those ROS (Table 1), they can theoretically attack chemical bonds in the polymer constituting the fuel cell membrane.

Reactive oxygen species (ROS)	Standard electrode potential E° [V] vs NHE (at pH 0)
H ₂ O ₂	1.74
HO [•]	2.72
HOO [•]	1.46

Table 1. Oxidative strength of reactive oxygen species relevant to fuel cell operation, expressed as reduction potentials [1].

In particular HO[•] is a very powerful oxidizing agent and reacts non-specifically in a diffusion-controlled manner with almost any organic molecule. In general, however, although all three ROS can participate in polymer degradation reactions, the respective chemistries and the roles played by each are fundamentally different.

Origin of ROS

There has been a great deal of controversy regarding the origin of ROS in fuel cells. The detection of H₂O₂ in the fuel cell product water has been reported in 1990 [2]. Recently, the presence of H₂O₂ in the membrane has been confirmed electrochemically [3], by iodometric titration [4] and anode / cathode effluent analysis [5]. The formation of radical oxygen species has been confirmed by spin-trapping in combination with electron paramagnetic resonance (EPR) analysis and use of a fluorescent probe. The degradation of the ionomer, in particular perfluorosulfonic acid (PFSA) type materials (e.g. Nafion®), caused by HOO[•]/HO[•] radicals has been studied mechanistically within a thermochemical framework [1]. For the understanding of the chemical aging mechanisms in the membrane electrode assembly (MEA), it is important to establish an inventory of

ROS	Quasi steady-state concentration (μM)	Formation rate (μM/s)
H ₂ O ₂	60 – 680 [3] max. 300, typ. 180 [4] 200 (cath.) - 1800 (an.)* [6]	an.: 0.5..1, ca.: 0.1[4] an.: 0.14, ca.: 0.28 [5]
HO [•]	max. 30, avg. 10* [6]	max. 100, avg. 50* [6] an.: 5.8·10 ⁻⁵ , ca.: 2.8·10 ⁻⁵ [7]
HOO [•]	to be estimated	to be estimated

*modelling results, base case (5 ppm Fe²⁺ in ionomer)

Table 2. Kinetic data of ROS collated from literature.

possible reaction pathways for the formation of ROS as well as identify reaction pathways involving the polymer. The reaction mechanisms in PFSA membranes has been studied to some detail, yet little is known about the reactions of ROS in partially fluorinated or hydrocarbon membranes.

Concentration and formation rate of ROS

A first approach in the understanding of the kinetics of polymer deterioration is the estimation of the concentration of ROS and their rate of formation in the environment of the fuel cell. Based on available literature data, the relevant figures have been compiled (Table 2).

The concentration of H₂O₂ in a PEFC has been determined experimentally in two studies [3-4] with fairly good agreement, yielding values on the order of 0.5 mM. These are quasi-steady state values, i.e. the rate of formation is equal to the rate of consumption of H₂O₂. In the modelling study of Shah et al., large differences in local H₂O₂ concentration are found [6], yet the average agrees fairly well with the experimental data. The formation rate of H₂O₂ has been measured by effluent water analysis by two groups [4-5], yielding similar values around 0.5 μM/s.

The measurement of the concentration of HO[•] is less straightforward because its concentration and lifetime is expected to be very low. The calculation of HO[•] concentration through the detection of HO[•] via spin-trapping or fluorescence probe technique is misleading because of the much longer lifetime of the spin-adducts. Estimated values of HO[•] concentration (~10 μM) and formation rate (~50 μM/s) under OCV conditions are obtained from the modelling study by Shah et al. [6]. Measurement of the formation rate of HO[•] has been attempted using a fluorescent probe technique, yet the rates obtained were very low (~50 pM/s). The low values might be a consequence of the low collection yield of HO[•], as it may react very rapidly within the catalyst layer and not diffuse far enough to react with the fluorescent dye.

Lifetime Estimation of ROS

The lifetime of H₂O₂, HO[•] and HOO[•] in the MEA is estimated based on the consideration of several possible reactions pathways, whereby the likelihood of each is discussed and assessed, taking into account the chemical environment, reaction kinetics and the assumptions made.

Based on the premise of a quasi-steady state, we stipulate that the ROS consumption rate equals its formation rate. The pseudo-first order reaction rate k_{eff} for the consumption of ROS is then obtained according to

$$\frac{dc_{\text{ROS}}}{dt} = r_f - k_{\text{eff}} \cdot c_{\text{ROS}} \approx 0 \rightarrow k_{\text{eff}} = \frac{r_f}{c_{\text{ROS}}} \quad (1)$$

¹ Laboratory of Inorganic Chemistry, ETH Zürich

where r_f is the formation rate and c_{ROS} the quasi-steady state concentration (**Table 2**). The ROS lifetime is taken to be its half-life $\tau_{1/2}$, and the diffusion length L_D is calculated using the diffusion coefficient D of water in a fully swollen Nafion® membrane ($3 \cdot 10^{-6} \text{ cm}^2/\text{s}$):

$$\text{lifetime: } \tau_{1/2} = \frac{\ln 2}{k_{\text{eff}}} \quad , \text{ diffusion length: } L_D \approx \sqrt{4D\tau_{1/2}}$$

Using average values for the concentration and formation rate, a lifetime of 12 min and 0.14 s is obtained for H_2O_2 and HO^\bullet , respectively. These are upper limit values, since the formation rates are likely to be underestimated, because only the ROS leaving the MEA are accounted for. Yet, a fraction of the ROS, in particular HO^\bullet , may react before escaping the MEA.

We assume an ionomer based on poly(styrene sulfonic acid) (PSSA), such as the PSI membrane [8]. The hydroxyl radical reacts with poly(sodium styrene sulfonate) (PSSS) at a rate of $k = 5 \cdot 10^7 \text{ M}^{-1}\text{s}^{-1}$. Assuming an ion exchange capacity of 1.3 mmol/cm^3 , this would yield a very short HO^\bullet lifetime of 11 ns.

An important reaction to consider is the reaction of H_2O_2 with HO^\bullet :



having a rate constant of $2.7 \cdot 10^7 \text{ M}^{-1}\text{s}^{-1}$. Using typical values for the concentrations of the two reactants, this reaction would yield a lifetime of 3 ms for H_2O_2 and $50 \mu\text{s}$ for HO^\bullet . The reaction of HO^\bullet with the polymer substrate, however, is much faster, therefore reaction (2) can be safely neglected.

It is likely that the membrane contains metal ion impurities at the ppm level. Despite the low concentration, some of these may undergo reaction with the ROS. In particular, the Fenton reaction can be harmful because hydroxyl radicals are created:



with a rate constant of $56 \text{ M}^{-1}\text{s}^{-1}$ (25°C, pH 0.9). Using a typical impurity level of 5 ppm Fe^{2+} , an H_2O_2 lifetime of 140 s is obtained, which is also in the minute order, as the value estimated based on H_2O_2 formation rate (<12 min). Alternatively, we can assume that the only source of HO^\bullet is the Fenton reaction (3). The formation rate of HO^\bullet is then equal to the consumption rate of H_2O_2 , and with the quasi-steady state H_2O_2 concentration of $500 \mu\text{M}$ we obtain a lifetime for H_2O_2 of 7 s. This represents a lower limit of the estimate, because HO^\bullet can also be created via other pathways. The consumption rate of H_2O_2 is therefore likely to be smaller and, consequently, its lifetime longer.

Finally, we wish to estimate the lifetime of the hydroperoxyl radical (HOO^\bullet). A source of HOO^\bullet is reaction (2). As a sink, we assume the reaction of HOO^\bullet with iron impurities ($k \approx 1.2 \cdot 10^6 \text{ M}^{-1}\text{s}^{-1}$ at low pH). As a result, we obtain a quasi-steady state concentration of HOO^\bullet of 1.5 mM and a lifetime of 6 ms, assuming an iron impurity level of 5 ppm. It has to be pointed out that these values are associated with high uncertainty, because i) HOO^\bullet is also likely to react with the ionomer, with currently unknown reaction rates, and ii) HOO^\bullet can also be produced in a follow-up reaction of the attack of HO^\bullet on PSSA.

In summary, the lifetime estimates and their corresponding diffusion length (**Table 3**) suggest that the different ROS have profoundly different characteristics. The reactions they can undergo also strongly depend on the chemical environment of the ionomer. The dissimilar lifetimes also lead to vastly different diffusion lengths. HO^\bullet reacts very near to the location where it is formed, whereas H_2O_2 can diffuse over the entire MEA thickness before undergoing reaction. The results shown here are a mere estimate, yet the study may contribute to the fundamental understanding of ionomer degradation reactions and thereby help in the development of a fuel cell membrane aging model.

ROS	Life time $\tau_{1/2}$	Diffusion length L_D
H_2O_2	> 7 s (Fenton, $r_{\text{H}_2\text{O}_2} = r_{\text{HO}^\bullet}$) 140 s (Fenton reaction) < 11 min (from formation rate)	> 100 μm (~membrane thickness) 0.4 mm (>membrane thickness) < 0.9 mm (flow field scale)
HO^\bullet	11 ns (reaction with PSSA) < 50 μs (reaction with H_2O_2)	4 nm (cluster size in PEM) < 200 nm (catalyst agglomerate size)
HOO^\bullet	< 6 ms ?	< 3 μm ? (~catalyst layer)

Table 3. Estimated kinetic properties of reactive oxygen species (ROS).

Conclusion

The understanding of chemical fuel cell membrane degradation is intertwined with the understanding of ROS chemistry and reactivity. We have to distinguish between different species causing oxidative stress: HO^\bullet is a very strong oxidizing agent and reacts very rapidly (~10 ns) with the PSSA based ionomer. HOO^\bullet is less reactive, the reactions it undergoes strongly depend on the presence of the other ROS and the chemical nature of the ionomer. Its lifetime is probably on the order of micro- to milliseconds. The reactivity of H_2O_2 is relatively low and is strongly influenced by the presence of metal ion impurities. It may diffuse over hundreds of microns before reacting. H_2O_2 can be regarded as a “dormant” aggressive species that can unleash HO^\bullet upon decomposition. Strategies for chemically stabilizing the ionomer may include the addition of regenerative radical scavengers.

References

- [1] F.D. Coms, ECS Transactions **16**, 235-255 (2008).
- [2] G.G. Scherer, Ber. Bunsenges. Phys. Chem. **94**, 145 (1990).
- [3] W. Liu, D. Zuckerbrod, J. Electrochem. Soc. **152**, A1165-A1170 (2005).
- [4] C. Chen, T.F. Fuller, ECS Transactions **11**, 1127-1137 (2007).
- [5] V.O. Mittal, H.R. Kunz, J.M. Fenton, Electrochem. Solid-State Lett. **9**, A299-A302 (2006).
- [6] A.A. Shah, T.R. Ralph, F.C. Walsh, J. Electrochem. Soc. **156**, B465-B484 (2009).
- [7] N. Ohguri, A.Y. Nosaka, Y. Nosaka, Electrochem. Solid-State Lett. **12**, B94-B96 (2009).
- [8] L. Gubler, H. Kuhn, T.J. Schmidt, G.G. Scherer, H.P. Brack, K. Simbeck, Fuel Cells **4**, 196-207 (2004).

Radical induced polymer electrolyte fuel cell membrane damage

S.M. Dockheer¹, L. Gubler, G.G. Scherer, W.H. Koppenol¹

phone: +41 44 633 44 82, e-mail: sindy.dockheer@psi.ch

The reaction of hydroxyl (HO[•]) radicals with sulfonated aromatics is of interest because of their presumed involvement in the degradation of fuel cell membranes [1]. Based on electron paramagnetic resonance (EPR) spectroscopy and fluorescence measurements, hydroxyl radicals are postulated to be formed *in situ* in a fuel cell [2, 3]. Experimental investigation of the reaction of hydroxyl radicals with model compounds has been carried out by means of EPR spectroscopy in the absence of dioxygen [4, 5]. Here, we present the kinetics of formation of intermediate species in model compounds of the polymer backbone (water soluble short oligomer) in oxygenated solutions and at low pH, which, ultimately, result in chain-scission.

Experimental

Samples of solutions that contained 0.1 - 1.5 mM poly(sodium styrene sulfonate) with MW 1100, average molecular weight 1100 g / mol (PSSS MW 1100), were irradiated (doses of 10 - 40 Gy) with < 50 ns pulses of 2 MeV electrons from a Febetron 705 (manufactured by Titan Systems Corp., presently L-3 Communications, San Leandro, CA) at ETH Zürich. Details of the pulse radiolysis setup have been published [6].

Results and Discussion

From the absorption spectrum observed 5 μ s after pulse irradiation (8 Gy) of a 120 μ M PSSS MW 1100 N₂O-saturated solutions near neutral pH, we derive that 90 % of hydroxyl radicals react with the oligomer according to reaction 1, Scheme 1. The corresponding rate constants for the addition and hydrogen-abstraction reaction are $k_1 = (8.3 \pm 2) \times 10^9 \text{ M}^{-1} \text{ s}^{-1}$ and $k_2 = (1 \pm 0.2) \times 10^9 \text{ M}^{-1} \text{ s}^{-1}$, respectively [7]. The reaction of HO-adduct **1**, Scheme 1, with dioxygen proceeds with a forward rate constant k_3 of $(3 \pm 0.5) \times 10^7 \text{ M}^{-1} \text{ s}^{-1}$. The dioxygen adduct **2**, Scheme 1, thus formed, can release dioxygen with a rate constant $k_{-3} < (4.5 \pm 1.5) \times 10^3 \text{ s}^{-1}$ or eliminate HO₂[•] according to equation 4, with $k_4 < 950 \text{ s}^{-1}$ [7]. At higher dioxygen concentration, reaction 5 Scheme 1, becomes possible [8].

Low pH values are a relevant condition in a proton-exchange membrane fuel cell. We derived an overall first-order rate constant k of $(6 \pm 1) \times 10^3 \text{ s}^{-1}$ for the decay of the HO-adduct **1** at pH 1 - 3 [7]. Protonation of the HO-adduct **1**, reaction 6 Scheme 1, proceeds with $k_6 = 1.9 \times 10^9 \text{ M}^{-1} \text{ s}^{-1}$ [9], which results in a pseudo-first order rate constant k_{obs6} of $1.9 \times 10^6 \text{ s}^{-1}$ and $1.9 \times 10^8 \text{ s}^{-1}$ at pH 3 and pH 1, respectively.

Water elimination from the protonated HO-adduct of aromatic compounds with electron-donating substituents results in formation of a radical cation [9, 10]. In order to elucidate the reaction mechanism at low pH, we used SO₄^{•-}, which reacts with aromatic compounds via electron-transfer to yield an intermediate radical cation, reaction 7, Scheme 1. Figure 1 shows the formation and decay of SO₄^{•-},

followed at 450 nm, in the presence of 0.5 mM - 1.5 mM PSSS MW 1100. SO₄^{•-} reacts with PSSS MW 1100 with $k_7 = (5.5 \pm 1) \times 10^8 \text{ M}^{-1} \text{ s}^{-1}$. Figure 1 illustrates the simultaneous formation of a transient species that absorbs strongly at 280 nm. A spectrum recorded 6 μ s after pulse irradiation of an aqueous solution that contained 1 mM PSSS MW 1100, 0.1 M *tert*-butanol and 0.02 M K₂S₂O₈ at pH 3 is shown in Figure 2 and is characteristic of the benzyl radical **3**. We observed complete conversion of SO₄^{•-} to benzyl radicals. Benzyl radicals react with dioxygen with a second-order rate constant k_8 of $(2 - 5) \times 10^8 \text{ M}^{-1} \text{ s}^{-1}$ [7].

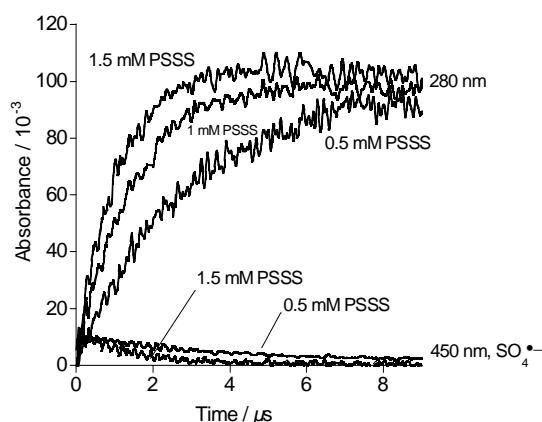


Figure 1. Absorbance changes at 280 nm and 450 nm, observed for irradiated argon-saturated solutions of 0.5 - 1.5 mM PSSS MW 1100, 0.02 - 0.05 M K₂S₂O₈, 0.05 - 0.1 M *tert*-butanol at pH 3 - 3.5, dose of ca. 30 Gy. The absorbance changes at 450 nm and 280 nm result from the formation and decay of SO₄^{•-} and benzyl radicals, respectively.

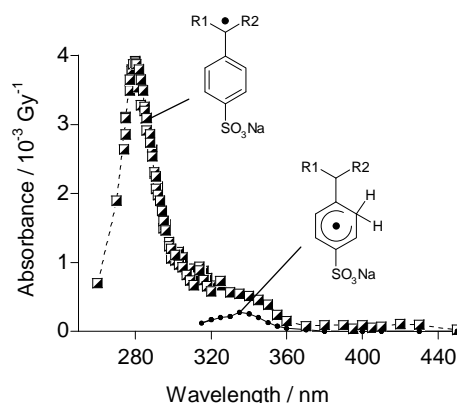


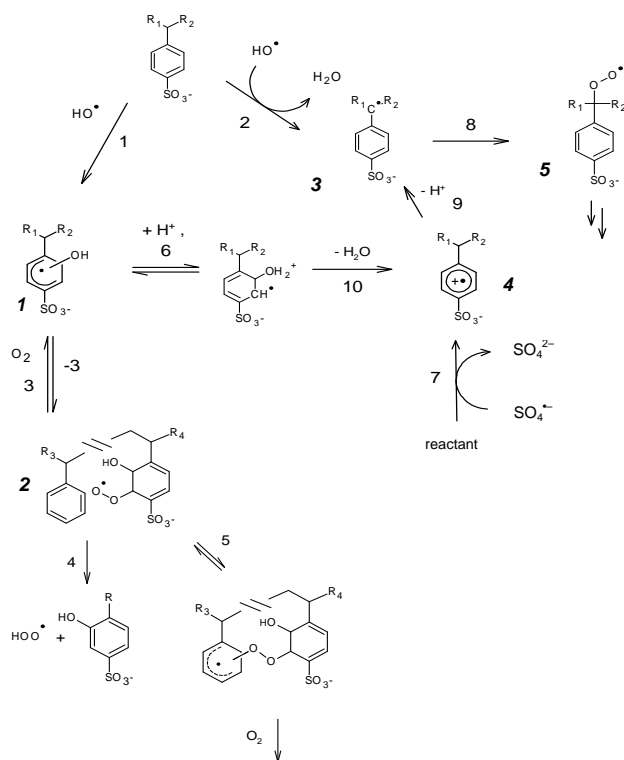
Figure 2. Normalized absorption spectrum recorded 6 μ s after pulse irradiation (8 Gy) of a 1 mM PSSS MW 1100, 0.1 M *tert*-butanol, 0.05 M K₂S₂O₈ argon-saturated solution, pH 3. The normalized spectrum of the H-adduct, which is formed in low yield ($G=0.57$) due to the reaction of hydrogen radicals with the oligomer is also shown.

The kinetics data described here are put into context in Scheme 1. The time dependence of formation of the benzyl radicals corresponds to the one of the decay of SO₄^{•-}. This observation can be rationalized with

¹ Laboratory of Inorganic Chemistry, ETH Zürich

formation of the radical cation **4**, which, in the presence of an electron-deactivating sulfonate group, is too short lived to be observed. It deprotonates with a rate constant $k_9 > 8 \times 10^5 \text{ s}^{-1}$. Thus, the rate limiting step in this reaction sequence is reaction 7.

In the reaction sequence from the HO-adduct to the protonated form, followed by water elimination and subsequent formation of the benzyl radical, our derived rate constant k of $(6 \pm 1) \times 10^3 \text{ s}^{-1}$ at pH 1 - 3, is 2 - 3 orders of magnitude lower than all other rate constants in this sequence. Therefore, the water elimination step proceeds with a first-order rate constant k_{10} of $(6 \pm 1) \times 10^3 \text{ s}^{-1}$.



Scheme 1

Reaction i	Rate constant, k_i
1	$(8.3 \pm 2) \times 10^9 \text{ M}^{-1} \text{ s}^{-1}$ [7]
2	$(1 \pm 0.2) \times 10^9 \text{ M}^{-1} \text{ s}^{-1}$ [7]
3	$(3 \pm 0.5) \times 10^7 \text{ M}^{-1} \text{ s}^{-1}$ [7]
-3	$< 4.5 \times 10^3 \text{ s}^{-1}$ [7]
4	$< 950 \text{ s}^{-1}$ [7]
6	$1.9 \times 10^9 \text{ M}^{-1} \text{ s}^{-1}$ [9]
7	$(5.5 \pm 1) \times 10^9 \text{ M}^{-1} \text{ s}^{-1}$ [11]
8	$(2 - 5) \times 10^8 \text{ M}^{-1} \text{ s}^{-1}$ [7]
9	$> 8 \times 10^5 \text{ s}^{-1}$ [11]
10	$(6 \pm 1) \times 10^3 \text{ s}^{-1}$ [7]

Table 1. Kinetics data for Scheme 1.

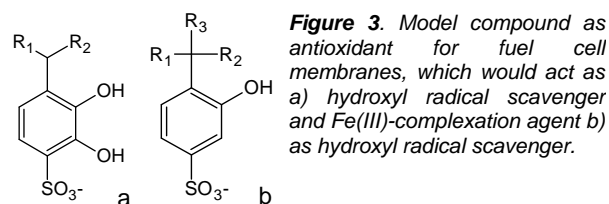


Figure 3. Model compound as antioxidant for fuel cell membranes, which would act as a) hydroxyl radical scavenger and Fe(III)-complexation agent b) as hydroxyl radical scavenger.

Conclusions

From Scheme 1, we conclude that the absence of the weak C α -H prevents formation of dioxyl radical **5** and, therefore, chain scission via subsequent reaction steps [7]. Higher stability of membranes based on alpha-methylstyrene has been demonstrated. On the other hand, if formation of HO-adduct **1** would be prevented, neither the acid-catalyzed water elimination that starts with reaction 6, nor formation of the dioxxygen adduct **2** would take place. Therefore, we propose here that introduction of a catechol-like group, see Figure 3, could be beneficial for membrane stability: Firstly, this antioxidant scavenges hydroxyl radicals, which results in formation of an intermediate oxyl radical that is inert to peroxidation. Secondly, it forms a stable complex with Fe(III), which does not redox-cycle according to Fenton's reaction. Therefore, we expect less formation of hydroxyl radicals. The simpler model compound b in Figure 3 would act as hydroxyl radical scavenger as well.

References

- [1] Y. Nosaka, K. Ohtaka, M. Kitazawa, S. Kishioka, A.Y. Nosaka, *Electrochem. Solid-State Lett.* **12**, B14-B17 (2009).
- [2] A. Panchenko, H. Dilger, J. Kerres, M. Hein, A. Ullrich, T. Kaz, E. Roduner, *Phys. Chem. Chem. Phys.* **6**, 2891 -2894 (2004).
- [3] K. Ohgushi, A.Y. Nosaka, Y. Nosaka, *Electrochem. Solid-State Lett.* **12**, B94-B96 (2009).
- [4] G. Hübner, E. Roduner, *J. Mater. Chem.* **9**, 409-418 (1999).
- [5] F. Schönberger, J. Kerres, H. Dilger, E. Roduner, *Phys. Chem. Chem. Phys.* **11**, 5782-5795 (2009).
- [6] A.S. Domazou, W.H. Koppenol, J.M. Gebicki, *Free Radical Biol. Med.* **46**, 1049-1057 (2009).
- [7] S.M. Dockheer, L. Gubler, A.S. Domazou, G.G. Scherer, A. Wokaun, W.H. Koppenol, in preparation.
- [8] M.I. Al-Sheikhly, D.L. Poster, J.-C. An, P. Neta, J. Silverman, R.E. Huie, *Environ. Sci. Technol.* **40**, 3082-3088 (2006).
- [9] P. O'Neill, S. Steenken, D. Schulte-Frohlinde, *J. Phys. Chem.* **79**, 2773-2779 (1975).
- [10] K. Sehested, J. Holcman, E.J. Hart, *J. Phys. Chem.* **81**, 1363-1367 (1975).

Grafting kinetics of styrene-co-MAN onto ETFE

K. Jetsrisuparb, H. Ben Youcef, G.G. Scherer, A. Wokaun, L. Gubler

phone: +41 56 310 2162, e-mail: kaewta.jetsrisuparb@psi.ch

ETFE is a partially fluorinated polymer, which, owing to its mechanical toughness, chemical stability and corrosion resistance, is used in chemical industry for protective coating and in architecture e.g. the Beijing National Aquatics Centre. In fuel cell applications, ETFE can be used as a base material for fuel cell membranes. The membranes are prepared by (co-) grafting monomer(s) onto the ETFE films, followed by sulfonation. The properties of the membranes can be controlled by the grafted monomers. The concept of graft co-polymerization has been applied to styrene-methacrylonitrile (MAN) on ETFE base film since styrene is readily grafted and the incorporation of MAN leads to an improvement of the oxidative stability under fuel cell operation [1]. In this study, we investigate the co-grafting kinetics of the styrene-MAN system.

Experimental

Electron irradiated ETFE films (25 μm) were introduced to the grafting solution, which consisted of different concentrations of styrene and MAN in isopropanol and water [1]. The content of styrene and MAN in the grafted films with approximately 40% graft level was determined by FTIR analysis.

Results and discussion

The amount of grafted components with respect to the base film is expressed by the graft level (GL):

$$GL = \frac{W_G - W_0}{W_0} \cdot 100\%$$

In which W_G indicates the mass of the grafted film and W_0 is the initial mass of the ETFE base film.

A large excess of monomers is provided in the reaction mixtures and no significant monomer depletion takes place throughout the experiment. The film can obtain a high graft level by providing a grafting solution consisting of monomers that can be easily grafted. The influence of initial monomer content in the reaction mixture on the graft level is shown in Figure 1, along with the fit corresponding to the kinetic model described in [2]. X symbolizes the molar fraction of styrene in the reaction mixture (styrene and MAN). There appears to be a significant difference in the weight based graft levels obtained from pure styrene and pure MAN grafting solutions. It is observed that the more styrene is provided in the grafting solution, the higher the graft level, except for $X=0$ which shows slightly higher graft levels than $X=0.2$.

Possibly, styrene is favored by grafting because its polarity is comparable to that of ETFE. This makes ETFE more accessible to styrene than MAN. However, at low styrene content ($X=0.2$), MAN is abundant, and as a large proportion of MAN is grafted in the film, the strong polarity of the $C\equiv N$ group in MAN might increase the polarity of the grafted film and disfavor the diffusion of styrene into the film.

Although the difference of the graft levels corresponding to pure styrene ($X=1$) and pure MAN

($X=0$) grafted films are significant, one should keep in mind that the molar mass of styrene is almost double that of MAN. Consequently, the variation of grafted monomers based on mole is less pronounced.

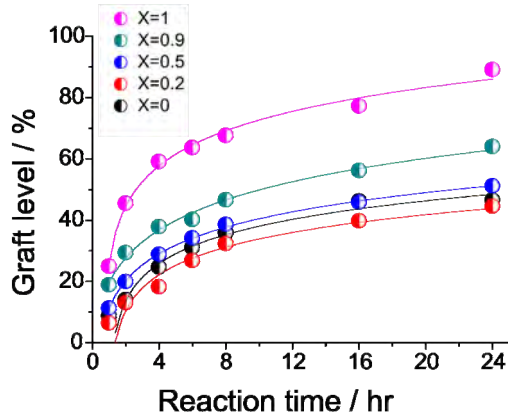


Figure 1. Effect of reaction time on graft level of styrene-co-MAN with different mixtures of styrene and MAN. X is the molar fraction of styrene with respect to the total monomer content.

Upon grafting, the graft level increases strongly in the beginning and subsequently levels off because the radicals decay as a function of time [3]. As the grafting proceeds, chain recombination and the decay of active species under the reaction conditions occur, resulting in a lower grafting rate. The kinetics model fitted most of the data reasonably well except for low styrene content in the reaction mixture ($X < 0.2$) during the first 4 hours where an induction period has been observed. The induction period could be assigned to the time required for monomers to diffuse into the film [4].

FTIR spectra of the grafted films showed pertinent vibrational bands for styrene ($C=C$) at 1493 cm^{-1} and MAN ($C\equiv N$) at 2231 cm^{-1} respectively (Figure 2 and 3). The intensity of the bands evidently indicates the amount of associated monomer in the grafted film.

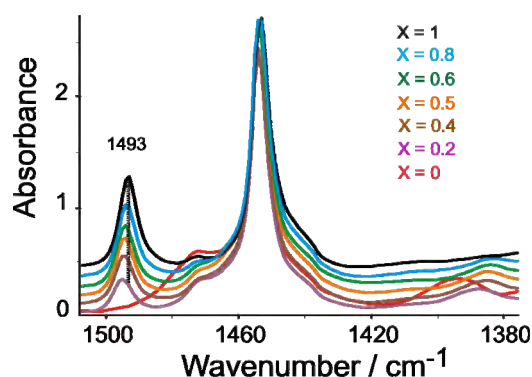


Figure 2. FTIR spectroscopic analysis of styrene characteristic band (1493 cm^{-1}). The films were prepared by different compositional feed to a fixed Graft level of 40%. X = molar fraction of styrene in the feed.

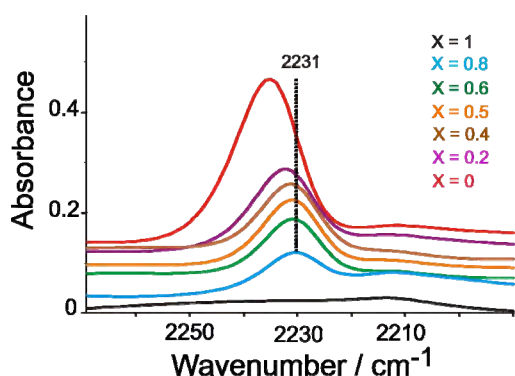


Figure 3. FTIR spectroscopic analysis of the MAN characteristic band (2231 cm^{-1}). The films were prepared by different compositional feed to a fixed graft level of 40%. X = molar fraction of styrene in the feed.

The FTIR spectra show that copolymerization of styrene and MAN is obtained. The composition of grafted monomers depends on the monomer content in the reaction mixture. At the same graft level, the intensity of styrene relevant vibrational band increases with increasing styrene content in the reaction mixture while the intensity of MAN relevant vibrational band decreases. A shift in the vibrational bands is observed with different reaction mixtures. In abundance of MAN in the reaction mixture, dimers or trimers of MAN might form and cause a change in the intra- and intermolecular forces due to the strong polarity of the $\text{C}\equiv\text{N}$ group [5].

The system of the grafted styrene-co-MAN onto ETFE can be described by the Mayo-Lewis model (Figure 4). The styrene content in the film ($\text{GL}=40\%$) is compared to that of the reaction mixture. The feature of Figure 4 represents a system where the reactivity ratios of both styrene and MAN (r_{styrene} , r_{MAN}) are lower than unity. This highlights that styrene and MAN have a slight tendency to form an alternating copolymer chain. The maximum degree of alternation (73% of diads) is obtained at $X=0.35$, based on a calculation described elsewhere [6].

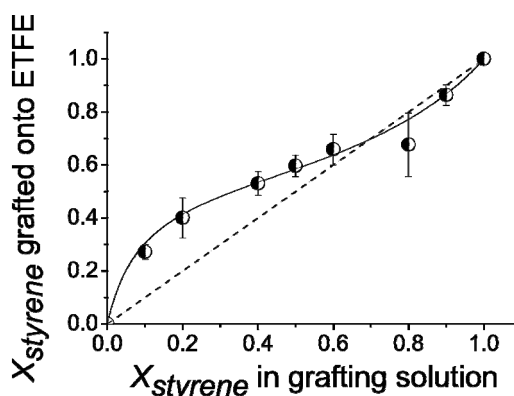


Figure 4. Mole fraction of styrene in the grafted film versus the mole fraction of styrene in the grafting solution. Selected films have a fixed graft level of approximately 40%. The curve is fitted by the weighted least squares method.

The reactivity ratios have been determined by the weighted non-linear least squares method and are compared with the reactivity ratios of bulk copolymerization (Table 1). The fairly large deviation of the reactivity ratios of the grafting experiment from those in bulk may be a result of the differences in the experimental conditions. Nevertheless, the

copolymerization kinetics of (co)grafting onto a polymer substrate and copolymerization in bulk do not need to be the same, since during grafting not only reaction takes place but also diffusion [7]. The diffusion rate of monomers into the base film might depend on the composition of the reaction mixture as well as the film.

System	Reactivity ratios	
	r_{styrene}	r_{MAN}
Experimental grafting (GL=40%)	0.67 ± 0.16	0.20 ± 0.04
Bulk copolymerization	0.25 ± 0.02 [8]	0.25 ± 0.02 [8]
	0.39 ± 0.07 [9]	0.32 ± 0.05 [9]

Table 1. Comparison of reactivity ratios of styrene and MAN copolymerization under different conditions

Conclusions

Grafted films were prepared by graft copolymerization of styrene and MAN onto $25\text{ }\mu\text{m}$ ETFE base film. Through the addition of styrene to the reaction mixture, higher graft levels have been obtained. Comparable polarity of styrene and ETFE could allow easier monomer transport into the film and yield a higher graft level. Selected films with a similar graft level of 40% were analyzed with FTIR spectroscopy and the reactivity ratios were determined. The FTIR spectra confirm that the content of grafted monomers depends on the composition of monomers in the reaction mixture. The reactivity ratios of styrene and MAN obtained from the Mayo-Lewis equation are 0.67 ± 0.16 and 0.20 ± 0.04 , respectively, indicating that cross-propagation is favored. The reactivity ratios obtained from graft copolymerization differ from those of bulk copolymerization. This emphasizes that the grafting process is rather complex; feed composition, monomer reactivity and diffusivity may play a role in the overall kinetics. The transport of monomer and solvent into the film during grafting is not well understood at this point and is subject of an ongoing study.

References

- [1] H. Ben youcef, PhD Thesis No. 18215, ETH Zürich (2009).
- [2] T. Rager, *Helv. Chim. Acta* **87**, 400-407 (2004).
- [3] S. Mitov, G. Hübner, H.P. Brack, G.G. Scherer, E. Roduner, *J. Polym. Sci. Part B: Polym. Phys.* **44**, 3324-3336 (1971).
- [4] L. Gubler, F. Wallasch, A. Wokaun, G.G. Scherer, *PSI Electrochemistry - Annual Report 2008*, 6, ISSN 1661-5379 (2008).
- [5] L. Dong, D. J. T. Hill, *Polymer Bulletin*. **34**, 323 (1995).
- [6] J.F. Kenney, *J. Polym. Sci.: Polym. Chem. Ed.* **14**, 113-121 (1976).
- [7] L. Gubler, M. Slaski, F. Wallasch, A. Wokaun, G.G. Scherer, *J. Membr. Sci.* **339**, 68-77 (2009).
- [8] R.G. Fordyce, E.C. Chapin, G.E. Ham, *J. Am. Chem. Soc.* **70**, 2490 (1948).
- [9] A. Rudin, R.G. Yule, *J. Polym. Sci. Part A-1: Polym. Chem.* **9**, 3009-3025 (1971).

Effect of the styrene-MAN composition on the *ex situ* properties of grafted membranes based on ETFE

K. Jetsrisuparb, H. Ben youcef, G.G. Scherer, A. Wokaun, L. Gubler

phone: +41 56 310 2162, e-mail: kaewta.jetsrisuparb@psi.ch

The synthesis of proton conducting membranes by irradiation induced graft copolymerization is known for its merits and potential in modifying the polymer properties [1]. The dependence of membrane performance on the grafted component is of particular interest. An acid side group is incorporated in co-grafted styrene and methacrylonitrile (MAN) onto ETFE base films to produce a proton conducting fuel cell membrane (page 9). The aim of this work is to investigate the influence of the composition of the grafted components on ion exchange capacity (IEC) and conductivity of the membrane.

Experimental

Styrene-co-MAN grafted ETFE films (with $41 \pm 4\%$ graft level) were sulfonated under the same conditions as reported previously [2]. The ion exchange capacity (IEC) was measured by titration. The molar ratio of styrene to MAN in the graft component was determined by FTIR spectroscopy. The theoretical IEC can be determined based on the graft level and the content of styrene and MAN in the grafted film [3]. The conductivity of the water swollen membranes was measured by AC impedance spectroscopy at room temperature.

Results and Discussion

The IEC is quantified by the amount of acid, sulfonic acid in this case, per unit mass of polymer. Assuming that each styrene group carries one sulfonic acid unit, the theoretical IEC can be determined from the graft level. We targeted a graft level of 40%, yet the obtained experimental graft levels lie between 37-45%. The minimum and maximum bounds for the theoretical IEC were determined, based on these lower and upper limits for the graft level. A good agreement has been found between experimental and theoretical IEC values (Figure 1). Evidently, the IEC increases with the molar fraction of styrene in the grafted components (X_{styrene}).

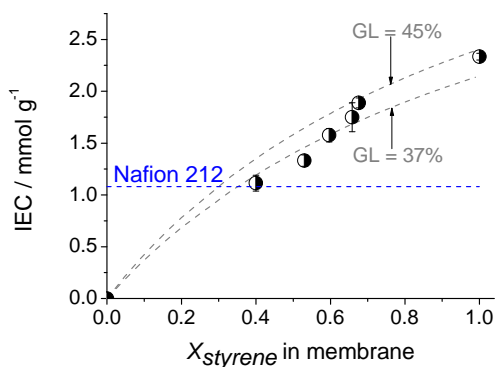


Figure 1. Ion exchange capacity of sulfonated membranes determined experimentally as a function of the grafted styrene content. X_{styrene} represents the mole fraction of styrene in the graft component ($X_{\text{MAN}} = 1 - X_{\text{styrene}}$) film. The theoretical IEC (assuming 100% sulfonation of styrene units) over a range of representative graft levels is plotted for comparison.

The radiation grafted membranes show comparable IEC values to Nafion 212. Analogous to the IEC, the conductivity is also enhanced with increasing styrene content (Figure 2), owing to the increasing proton concentration (IEC). Possibly, the degree of hydration and polymer chain mobility, due to the incorporation of the acid group, also affect the proton mobility. In the next step of this study, fuel cell tests will be carried out. Further, the influence of the MAN content on the chemical stability of the membrane will be investigated systematically.

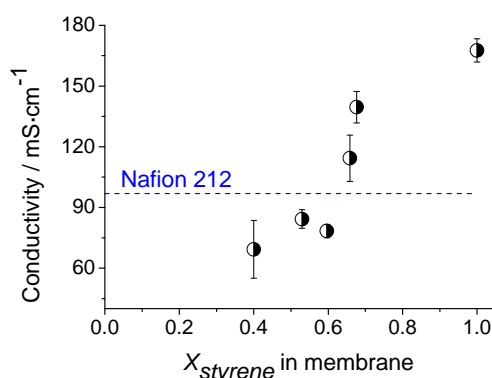


Figure 2. Conductivity for styrene-co-MAN grafted ETFE membranes as a function of the styrene content. The conductivity of Nafion 212 is shown as a dashed line for comparison.

Conclusions

Measurements of the IEC and conductivity of radiation grafted styrene-co-MAN membranes show that the composition of the grafted components plays an important role in affecting these fuel cell relevant properties. The IEC and conductivity rely on the content of grafted styrene in the membrane, since the grafted styrene determines the ionic content. Sulfonated polymers exhibit an increased hydrophilicity and water uptake, which favour IEC and conductivity, respectively. Both IEC and conductivity of styrene and MAN co-grafted membranes with approximately 40% graft level are comparable to Nafion 212, as demonstrated in the results. In the next step, water uptake characteristics, mechanical stability and fuel cell tests will be investigated to better understand the ETFE-g-styrene:MAN combination.

References

- [1] M.M. Nasef, E.-S.A. Hegazy, Prog. Polym. Sci. **29**, 499-561 (2004).
- [2] H. Ben youcef, L. Gubler, S. Alkan-Gürsel, D. Henkensmeier, A. Wokaun, G.G. Scherer, Electrochem. Commun. **11**, 941-944 (2009).
- [3] H. Ben youcef, PhD Thesis No. 18215, ETH Zürich (2009).

Diisopropenylbenzene as new crosslinker in radiation grafted ETFE based membranes for fuel cells: A kinetic study

H. Ben youcef, R. Gyr¹, L. Gubler, A. Wokaun, G.G. Scherer

phone: +41 56 310 4188, e-mail: hicham.ben-youcef@psi.ch

Crosslinking is a key method to increase the lifetime of radiation grafted membranes for fuel cells. The optimization of the crosslinker concentration in combination with the graft level is crucial to ensure higher stability without loss in performance and mechanical properties. The use of divinylbenzene (DVB) (mixture of four isomers) as crosslinking agent was previously investigated in detail [1]. Inhomogeneous distribution of the crosslinker concentration through the thickness of the grafted films was observed. In this study, a 1,3-diisopropenylbenzene (DIPB) was selected as crosslinker. The objective of this first investigation was to prove the incorporation of DIPB and its effectiveness as a crosslinker for the styrene grafted ETFE based membranes.

Experimental

ETFE (25 μm , Dupont) based grafted films were prepared in the presence of styrene/DIPB mixture with varying DIPB concentration in the initial grafting solution (0%, 5%, 8%, 10%, 15%, and 20%), using the grafting solution mixture as described elsewhere [1]. Selected grafted films with a graft level of 25 % and different crosslinking extent were characterized by means of FTIR and DSC techniques.

Results

The kinetics of grafting is governed mainly by monomer reactivity and its diffusion into the irradiated film.

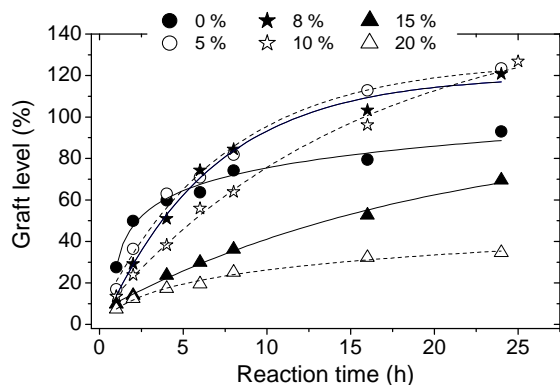


Figure 1. Grafting kinetics of styrene/DIPB into ETFE based films for different DIPB concentrations.

At an early phase of grafting ($< 4\text{h}$), the graft level (GL) decreases gradually with the DIPB concentration (Figure 1). However, for longer reaction times ($> 8\text{h}$) the grafted films with DIPB concentration of 5%, 8% and 10% yield higher GL than the uncrosslinked films. Initially, the grafting takes place in the surface of irradiated films, thereafter the reaction becomes diffusion controlled. The same observation was made for the DVB/styrene monomer combination, but for initial concentrations up to 5% DVB [1]. The extracted kinetic parameters (initial polymerization rate (R_{p0}) and radical recombination rate (γ)) from the fitted kinetic curves (Figure 1) were affected by the introduction of DIPB. Both parameters decrease with an increase in DIPB concentration, while γ does not

show any significant change for concentrations higher than 8% DIPB (Figure 2). For concentrations lower than 8% DIPB, the monomer diffusion is not significantly affected, while above this concentration the creation of a three-dimensional network slows down the polymerization reaction (radical lifetime increases).

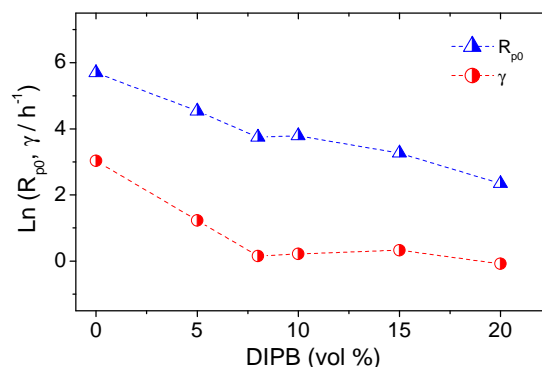


Figure 2. Kinetic parameters as function of DIPB concentration.

FTIR investigation (spectra not shown) of the grafted films showed the effective incorporation of DIPB into the ETFE grafted films, whereby the C-H deformation vibration of the DIPB methyl group was observed (the unreacted DIPB double bond was not observed).

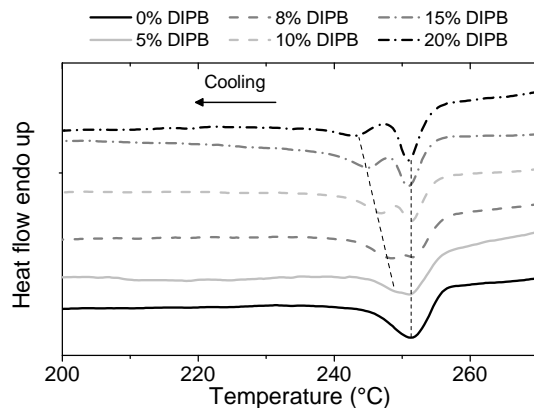


Figure 3. Recrystallization thermograms of styrene/DIPB grafted ETFE based films.

Recrystallization experiments were performed for the crosslinked grafted films with fixed GL of 25 % (Figure 3). Above 5% DIPB concentration, the exothermic peak shows two peaks with distinct maxima. It is suggested that the observed multiplicity is related to the morphological change occurring upon crosslinking (co-existence of two crystallite domains, near-surface crystallites (affected by crosslinking) and bulk crystallites (chain flexibility is not affected)).

References

[1] H. Ben youcef, Ph.D. thesis, No. 18215, ETH, Zürich (2009).

¹ Department of Materials, ETH Zürich

Diisopropenylbenzene as new crosslinker in radiation grafted ETFE based membranes for fuel cells: *ex situ* and *in situ* characterization

H. Ben youcef, R. Gyr¹, L. Gubler, A. Wokaun, G.G. Scherer

phone: +41 56 310 4188, e-mail: hicham.ben-youcef@psi.ch

The degree of crosslinking is a crucial parameter to improve the chemical, mechanical and dimensional stability of radiation grafted membranes in fuel cells [1]. Divinylbenzene (DVB), a technical mixture of different isomers, was extensively used as crosslinking agent for styrene grafted poly(ethylene-*alt*-tetrafluoroethylene) (ETFE) based membranes. The high reactivity of active DVB isomers as compared to the one of styrene induces a concentration gradient of the crosslinker through the thickness of the grafted films. In this study, the use of a new crosslinker, 1,3-diisopropenylbenzene (DIPB) (isomer pure monomer), and its effect on *ex situ* and *in situ* fuel cell relevant properties of styrene grafted ETFE based membranes are presented.

Experimental

ETFE (25 μm , Dupont) based grafted films were prepared in the presence of styrene/DIPB mixture with varying DIPB concentration in the initial grafting solution (0%, 5%, 10%, 15% and 20%), as described previously [2]. Selected grafted films with a fixed graft level of 25 % were sulfonated and the resulting membranes were characterized for their fuel cell relevant properties.

The radiation grafted membranes were assembled with JM electrodes (Johnson Matthey) with a noble metal loading of 0.4 mg Pt cm^{-2} , then hotpressed at 110 $^{\circ}\text{C}$ / 5 MPa / 180 s to form a membrane electrode assembly (MEA). The *ex situ* (ion exchange capacity (IEC), water uptake, dimensional stability, contact angle and conductivity) and *in situ* (impedance spectroscopy, polarization curves and H_2 crossover) characterizations of the membranes were performed, as described elsewhere [1, 3].

Results

To begin with, FTIR investigation and recrystallization experiments (DSC measurement) were performed (cf page xx), showing clearly the successful incorporation of DIPB in the grafted films. Moreover, the extent of crosslinker through the thickness was quantified based on peak fitting of the obtained FTIR-spectra.

By increasing the crosslinker (DIPB) concentration from 0% to 20% in the initial grafting solution, the conductivity decreases from a value of 104 $\text{mS}\cdot\text{cm}^{-1}$ to 20 $\text{mS}\cdot\text{cm}^{-1}$, while the ion exchange capacity does not show any significant change (Figure 1a and 1b). On the other hand, the water uptake is reduced upon crosslinking, which can be attributed to the enhancement of the compact three-dimensional network structure of the grafted chains and the decrease in the free volume available in the membrane (Figure 1c). The observed decrease in conductivity is due to the decrease in swelling and, as a consequence, to a reduced mobility of protons. Moreover, an approximately linear correlation between conductivity and hydration level is observed (not shown). Similar to the water uptake, the area and volume shrinking (wet \rightarrow dry) are decreasing with crosslinking, i.e. the dimensional stability of the crosslinked membranes is improved and the stress generated by swelling is

reduced (Figure 1d). The same observations were made for the styrene/divinylbenzene grafted ETFE based membranes, showing the effectiveness of the crosslinking using the DIPB. However, the gradient of crosslinker concentration through the thickness could not be measured, owing to only a weak signal of the DIPB in FTIR-ATR (attenuated total reflectance) mode [1].

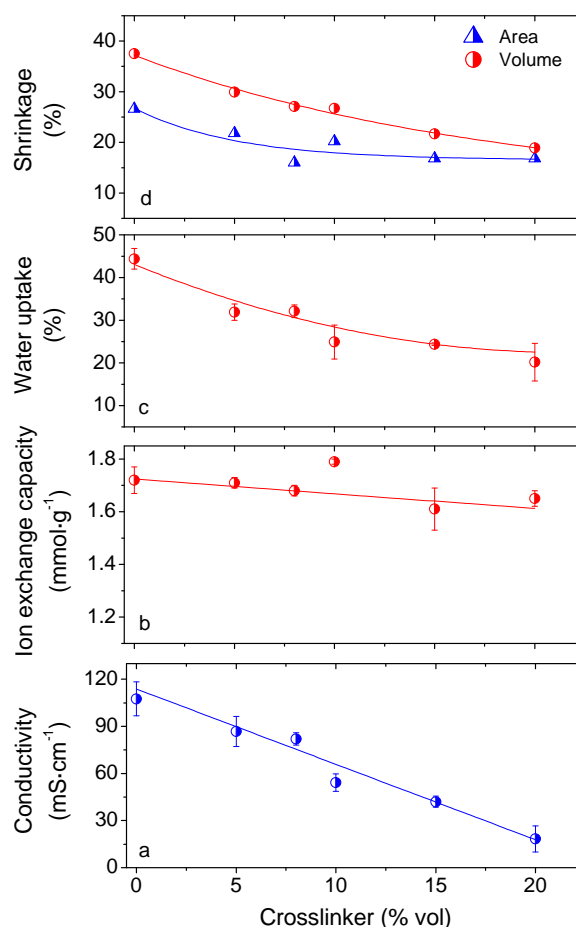


Figure 1. Effect of crosslinker (DIPB) concentration in the initial grafting solution on *ex situ* fuel cell relevant properties of the ETFE grafted membrane a) conductivity b) ion exchange capacity c) Water uptake d) area and volume shrinkage (wet \rightarrow dry). Measurements of a) and b) were performed in fully swollen state at room temperature.

The contact angle measurement performed on dried membranes showed no significant changes up to 10% DIPB concentration, while contact angle values increase, starting from 15% DIPB (Figure 2). This observed increase in surface hydrophobicity is not fully understood yet. However, it is suggested that the creation of a three-dimensional network induces a restriction on the grafted chain's mobility, thus reducing the re-orientation of the sulfonic groups towards the surface. In analogy to the contact angle measurement results, XPS investigation on uncrosslinked (0% DIPB) and crosslinked (20 % DIPB) grafted films shows that

¹ Department of Materials, ETH Zürich

the surface composition is completely different in both samples. In fact, the surface concentration of the grafted component is high in the uncrosslinked film, as similarly observed for poly(tetrafluoroethylene-co-hexafluoroprop-ylene) (FEP) grafted films and membranes using styrene/DVB as graft component [5]. We note here that the observed change in the surface composition might be very different when the grafted films and membranes are subjected to ultra high vacuum conditions.

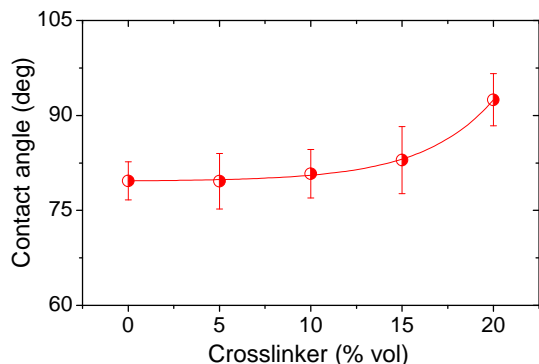


Figure 2. Contact angle measurement of dry ETFE-g-styrene/DIPB membranes.

To correlate the measured *ex situ* surface and bulk properties of the crosslinked grafted membranes to the *in situ* fuel cell relevant properties, MEAs were assembled and tested under constant current density of $500 \text{ mA}\cdot\text{cm}^{-2}$. Measurement of the ac impedance and H_2 crossover were taken after 90 h of operation. The derived ohmic resistance and polarization resistance values from the ac impedance spectra, recorded at a current density of $500 \text{ mA}\cdot\text{cm}^{-2}$, are presented in Figure 3.

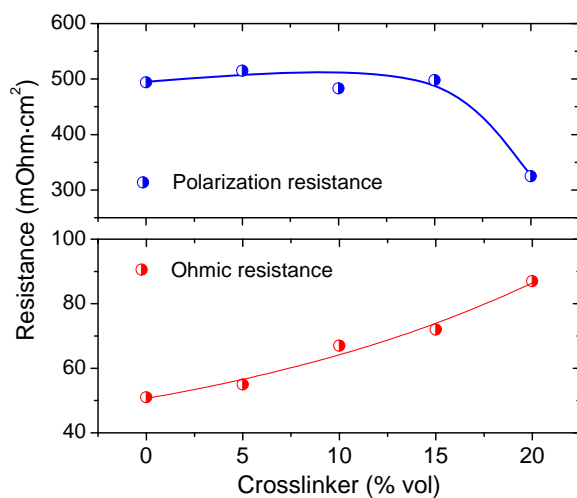


Figure 3. Ohmic resistance and polarization resistance of MEAs based on ETFE-g-styrene/DIPB membranes. Ac impedance spectra recorded at a dc current density of $500 \text{ mA}\cdot\text{cm}^{-2}$ (frequency range: 0.1 Hz – 50 kHz).

The initially measured ohmic resistance value of $50 \text{ mOhm}\cdot\text{cm}^{-2}$ for the uncrosslinked membrane increases with increasing extent of crosslinking, reaching a value of $87 \text{ mOhm}\cdot\text{cm}^{-2}$ for the highly crosslinked membrane (20 % DIPB). However, the polarization resistance does not show any significant change with the increase of crosslinking up to 15% DIPB, a marked decrease is only observed for the highly crosslinked membrane (20 % DIPB) (Figure 3). The observed trend for the extracted ohmic resistance correlates well with the

ohmic resistance measured via the online high frequency resistance technique (HFR) at 1 kHz, and is obviously associated with the decrease of membrane conductivity with increasing DIPB concentration (Figure 1a). Whereas the polarization resistance, which is assumed to be a measure of the properties of the membrane-electrode interface, shows a clear correlation with the contact angle measurement. So far, the observed trend is different from the one observed for the styrene/DVB based ETFE membranes, however assembled with a different electrode material (ETEK-electrode).

In order to evaluate the integrity of the membrane after 90 h of fuel cell operation, the *in situ* H_2 crossover was measured by operating the cell in H_2/N_2 mode and applying a cell voltage of 0.5 V (Figure 4).

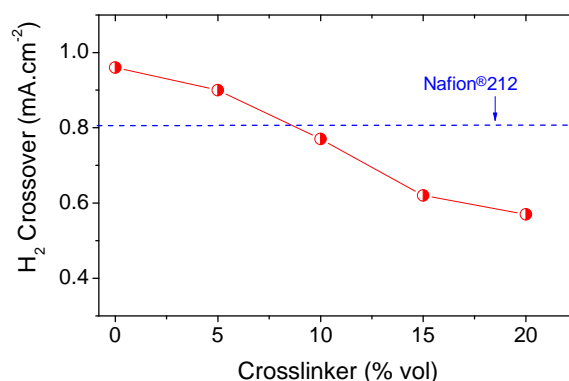


Figure 4. Hydrogen crossover of ETFE-g-styrene/DIPB based MEAs for different DIPB concentrations. Hydrogen crossover measured in H_2/N_2 mode at 80°C .

The H_2 -crossover gradually decreases with the extent of crosslinking, in particular the crosslinked membranes with a DIPB concentration of more than 10 % in the initial grafting solution showed a lower H_2 permeability in comparison to a Nafion®212 membrane. A correlation between the *ex situ* dimensional stability (wet→dry) and the membrane mechanical integrity measured *in situ* via H_2 crossover was already established [4]. It was stated that the changes in membrane hydration may cause a build-up of internal stress, leading to mechanical deterioration during fuel cell operation. Furthermore, crosslinking with DVB was found to improve the *ex situ* chemical stability of the grafted membranes. So far, no correlation between the *in situ* chemical stability, *ex situ* chemical stability and H_2 crossover was investigated. In the next step, *ex situ* chemical stability (treatment in a 3% H_2O_2 solution at 60°C) of ETFE-g-styrene/DIPB membranes will be investigated.

References

- [1] H. Ben youcef, Ph.D. thesis No. 18215, ETH, Zürich (2009).
- [2] H. Ben youcef, S. Alkan-Gürsel, A. Wokaun, G.G. Scherer, J. Membr. Sci. **311**, 208-215 (2008).
- [3] L. Gubler, H. Ben youcef, S. Alkan-Gürsel, A. Wokaun, G.G. Scherer, J. Electrochem. Soc. **155**, B921-B928 (2008).
- [4] L. Gubler, M. Schisslbauer, PSI Electrochemistry Laboratory – Annual Report 2007, 16, ISSN 1661-5379 (2008).
- [5] B. Schnyder, T. Rager, J. Appl. Polym. Sci. **104**, 1973-1978 (2007).

Ex situ mechanical properties of PEFC membranes at 80 °C and 80 % relative humidity

F. Wallasch, S. Bähler¹, L. Gubler, G.G. Scherer, A. Wokaun

phone: +41 56 310 2132, e-mail: frank.wallasch@psi.ch

The favoured technique to convert the chemical energy of hydrogen into electrical energy is the polymer electrolyte fuel cell (PEFC). The solid polymer electrolyte in its centre has to ensure gas separation, electrical insulation and proton conduction.

During fuel cell operation, the membrane is exposed to chemical and mechanical stress. Variation in the membrane humidification shrinks or swells the membrane and causes mechanical stress [1], which may lead to crack formation and result in failure of the fuel cell.

Fuel cell testing of membranes often induces a multitude of failure modes, wherefore *ex situ* methods to induce a single degradation mode are needed. *Ex situ* mechanical properties of fuel cell membranes are accessible in tensile tests and their investigation at 80 °C / 80 % relative humidity (r.h.) is described in the present article.

Experimental

Grafted films were prepared by graft copolymerization of AMS and MAN onto pre-irradiated ETFE base films (DuPont Tefzel[®] LZ100, 25 µm thick), as described elsewhere [2, 3]. The grafted films were sulfonated and subsequently hydrolysed to prepare membranes in acidic form. The mechanical properties of films and membranes were investigated in machining direction (MD), using the universal testing machine Zwick Roell 1-FR005TH (Zwick GmbH & Co. KG, Ulm, Germany) with a maximum load of 5 kN (Figure 1 left). The tensile testing machine was equipped with a climatic chamber, which was used to control the temperature (80 °C) and the humidity (80 % r.h.) during the experiment. The samples were cut with a scalpel into 10 cm long (MD) and 1 cm wide (transverse direction) rectangular specimens, mounted to the testing machine by fixing the upper and lower end between two Vulkollan[®] (Bayer AG) coated aluminium clamps (Figure 1 right).



Figure 1. Zwick Roell tensile testing machine and attached climatic chamber (left) and Vulkollan coated sample holder (right).

The tests were performed at a constant cross head velocity of 100 mm·min⁻¹ until the specimens ruptured. The stress-strain curves obtained in these tests were used to determine the mechanical properties, more precisely the Young's modulus E , tensile strength σ_{\max}

and elongation at break A (cf. Figure 2). Equal initial conditions for all tests were ensured by applying a preload of 0.3 N before the measurement was started. The Young's modulus was determined as slope $m = \Delta\sigma/\Delta\varepsilon$ of the initial stress-strain curve between 0.5 and 1 % strain.

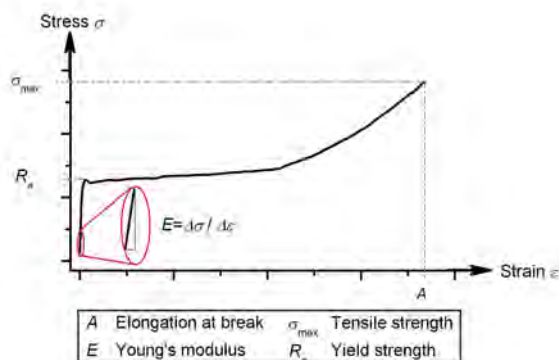


Figure 2. Stress σ as a function of strain ε for a FEP base film (DuPont Teflon[®] 100A) investigated in MD to show the elongation at break A , tensile strength σ_{\max} and Young's modulus E .

Results

The Nafion[®] 212CS membrane (DuPont) was investigated to evaluate the tensile testing procedure (Fig. 3).

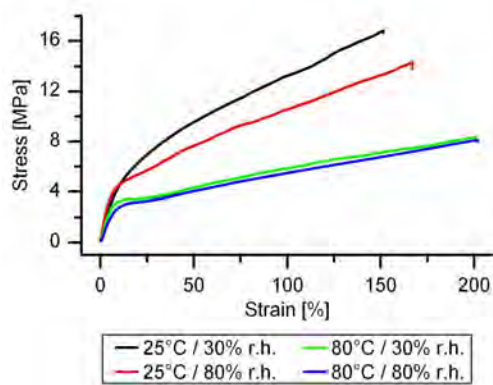


Figure 3. Stress-strain curves for Nafion[®] 212CS in MD recorded at different temperature (25 and 80 °C) and r.h. (30 and 80 %), recorded at 100 ml·min⁻¹ cross head velocity ($F_0 = 0.1$ N).

The Young's modulus was found to be the most reliable mechanical property, due to its higher independence on the specimen preparation, and determined to be (62±5) MPa in the present work (cf. (60±15) MPa reported in [4]).

Seven ETFE based samples, the pristine base film, an AMS/MAN co-grafted film with 34 % degree of grafting (DoG), three uncrosslinked membranes with various DoG in the range from 20 to 40 % and a DVB (1.3 mol% in solution) and a DIPB (0.7 mol% in solution) crosslinked membrane with 39 % DoG, were investigated in MD at 80 °C and 80 % r.h. The elongation at break, tensile strength and Young's modulus for each sample were calculated as average from six individual measured specimens (Figure 4).

¹ Department of Information Technology and Electrical Engineering, ETH Zürich

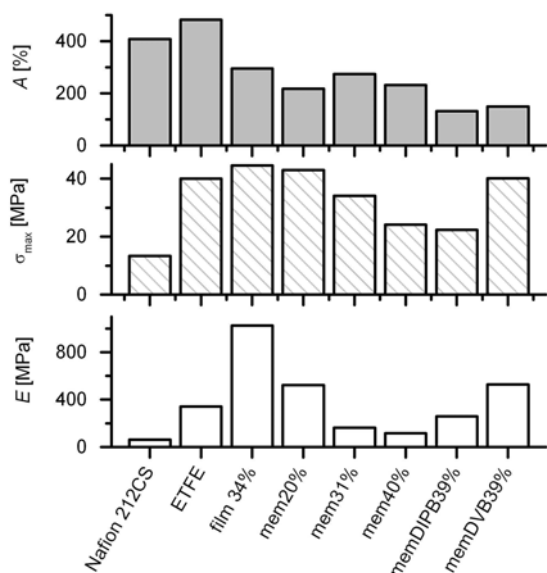


Figure 4. Elongation at break A (top), tensile strength σ_{max} (center) and Young's modulus E (bottom) in MD of Nafion[®] 212CS compared to ETFE base film, ETFE-g-[AMS-co-MAN] and ETFE-g-[AMSSA-co-MAN] membranes with various DoG, uncrosslinked and crosslinked with DIPB or DVB.

The behaviour of the poorly swellable samples, the ETFE base film and AMS/MAN co-grafted film with 34 % DoG, is comparable to results obtained at r.t. and ambient humidity. At both conditions, the Young's modulus increases, the tensile strength is not influenced and the elongation at break decreases by the grafting of the AMS/MAN copolymer onto the FEP base film. The swellability of samples, introduced by sulfonation and hydrolysis, reduces significantly all measured mechanical properties, obvious in the comparison of the grafted film with 34 % DoG with its corresponding membrane (31 % DoG). By contrast, the Young's modulus increased slightly, the tensile strength significantly and the elongation at break was not influenced by comparison of grafted films and the corresponding membranes in potassium form at ambient conditions, characterized in previous investigations [5]. Testing of the mechanical properties of membranes in the presence of water, which acts as plasticizer, leads to completely different results. For uncrosslinked membranes, the Young's modulus and tensile strength decrease and the elongation at break is not influenced by an increasing DoG. The swelling and therefore the water uptake scales with the DoG, which decreases the stiffness of the membrane. The water may form a hydration layer around the grafted chains and weaken the chain-chain interaction and therefore reduce the tensile strength. Hence, the picture of stiff and sterically hindered grafted copolymer chains, used so far to explain the DoG dependent behaviour of grafted films in tensile tests at r.t. and ambient humidity, becomes reversed for membranes investigated in water swollen state. The effect of crosslinking in membranes observed in the experiments at 80 °C and 80 % r.h. was the same as obvious with grafted films at r.t. and ambient humidity. The Young's modulus and tensile strength increase and the elongation at break decreases at both conditions due to a stiffer three-dimensional copolymer network.

Conclusion

The investigation of dry, potassium exchanged fuel cell membranes at r.t. and ambient humidity lead to misleading results, concerning the influence of the

degree of grafting on the mechanical properties. The mechanical properties at r.t. and ambient humidity became worse for the various materials along the preparation path, starting with a mechanically stable base film via a brittle grafted film to a more brittle K⁺-membrane. The investigation at 80 °C and 80 % r.h. clearly indicated the grafted film as intermediate with poor mechanical properties, while water acts as plasticizer in the swollen membrane and reduces the brittleness significantly, compared to the grafted film.

The comparison of the mechanical properties of grafted membranes with Nafion[®] 212CS membranes is difficult, because of the strong inherent differences between both systems. A comparison is possible, e.g. on the mass (IEC_m) or volume based ion exchange capacity (IEC_v), proton conductivity or hydration. The grafted membrane with 21 % DoG [(1.02±0.10) mEq•g⁻¹] has a comparable IEC to Nafion[®] 212CS [(1.07±0.05) mEq•g⁻¹], while the IEC_v was higher and the *ex situ* proton conductivity lower for all investigated ETFE based membranes up to 50 % DoG, compared to (1.23±0.06) mEq•ml⁻¹ and (88±10) mS•cm⁻¹ for Nafion[®] 212CS, respectively. The hydration of Nafion[®] 212CS was comparable within the experimental error to grafted membranes with DoG between 20 and 40 %. The ETFE based membrane with 21 % DoG was stiffer than Nafion[®] 212CS, apparent in the higher Young's modulus of [(520±20) MPa], and the maximum applicable force was higher [(43±5) MPa] compared to Nafion[®] 212CS [(13±2) MPa]. However, Nafion[®] 212CS is more ductile compared to the grafted film with 21 % DoG, shown in the elongation at break of (408±10) % and (220±20) %, respectively.

Further investigations at 80 °C and elevated humidity have to be carried out and correlated with *in situ* membrane stability. The creep behavior of membranes may also become important in an operating fuel cell under compressive force. Preliminarily, this was investigated by measuring the time dependent elongation of membranes at a constant load of 3 N. Nafion[®] 212CS shows a higher creep than ETFE- or FEP-based, uncrosslinked and crosslinked membranes with DoG up to 40 %.

References

- [1] F. Wallasch, S. Rudin, L. Gubler, G.G. Scherer, A. Wokaun, PSI Electrochemistry Laboratory – Annual Report 2007, ISSN 1661-5379, 13 (2008).
- [2] L. Gubler, M. Slaski, F. Wallasch, A. Wokaun, G.G. Scherer, J. Membr. Sci. **339**, 68-77 (2009).
- [3] F. Wallasch, L. Gubler, G.G. Scherer, A. Wokaun, PSI Electrochemistry Laboratory – Annual Report 2007, ISSN 1661-5379, 7 (2007).
- [4] Y. Tang, A.M. Karlsson, M.H. Santare, M. Gilbert, S. Cleghorn, W.B. Johnson, Mater. Sci. Eng., A **425**, 297-304 (2006).
- [5] H. Ben youcef, PhD thesis, No. 18215, ETH Zürich (2009).

FUEL CELLS

DIAGNOSTICS

Deuterium labeling of water combined with neutron radiography to study mass transport in the polymer electrolyte fuel cell (PEFC) membrane

P. Oberholzer, P. Boillat, R. Siegrist, R. Perego, A. Kästner, E.H. Lehmann, G.G. Scherer, A. Wokaun

phone: +41 56 310 5637, e-mail: pierre.oberholzer@psi.ch

The polymer electrolyte fuel cell (PEFC) is considered as a promising candidate for future mobile power supplies. The comprehension underlying the technological improvements includes as an essential part the understanding of the transport and exchange phenomena inside the bulk and at the interfaces of the proton exchange membrane (PEM). Experimental data are required beside the modelling works for this purpose.

Neutron imaging offers the ability of viewing liquid "normal" water $^1\text{H}_2\text{O}$ (see notation in next chapter) inside the fuel cell with high contrast, compared to its constitutive materials. On the contrary, liquid heavy water $^2\text{H}_2\text{O}$ is almost transparent to neutrons, due to the lower cross section of neutron interaction with deuterium. This property pointed out in [1] can be used in *in situ* configuration for visualizing the contributions of the three sources of H atoms in an operating cell (Figure 1), but the exchange processes complicate the interpretation.

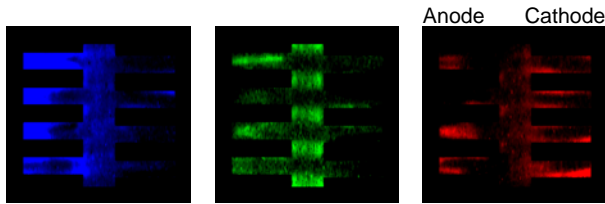


Figure 1. Difference images between normal state (Anode: $^1\text{H}_2 + ^1\text{H}_2\text{O}$, Cathode: $\text{O}_2 + ^1\text{H}_2\text{O}$) and: $^1\text{H}_2 + ^2\text{H}_2\text{O}$ on anode (left), $^2\text{H}_2 + ^1\text{H}_2\text{O}$ on anode (middle) and $\text{O}_2 + ^2\text{H}_2\text{O}$ on cathode (right).

Considering the need of simplification, the present work aims to quantify the transport and exchange processes in the bulk and at the interfaces of a membrane without catalyst in *ex situ* configuration.

Definition

The ^1H and ^2H symbols refer hereunder to the protium (most abundant) and deuterium isotopes of hydrogen respectively, while the H symbol is used when considering an arbitrary mixture of them. The local ^1H isotope fraction is defined as:

$$^1F = \frac{c_{^1\text{H}}}{c_{^1\text{H}} + c_{^2\text{H}}}$$

whereby c represents the concentration of the indexed substance. For simplification, we call it isotope fraction and symbolize it by F , with the equality $F = ^1F$.

Experimental procedure

The strategy used for the quantification is to apply isotope changes in the fed gas, for example by changing the gas humidification from $^1\text{H}_2\text{O}$ to $^2\text{H}_2\text{O}$, and to estimate, based on the image sequence, the transient distribution of F in the membrane. A simple model fitted (see next chapter) on the experimental results leads to quantify the bulk transport and interface exchange parameters.

A system as simple as possible was dedicated to this investigation (Figure 2). A membrane without catalyst layer (CL) was used, in order to suppress the exchange current density of the electrochemical reaction and to study exclusively, at first, the exchange occurring between the membrane and the water vapour in the gas phase. The thickness of the membrane was chosen to be 200 μm , to reach a reasonable precision by evaluating $F(x)$ with the resolution of the imaging setup used here ($r_{FWMH} = 20 \mu\text{m}$, as defined in [2]). To avoid as much as possible mass transport limitations in the gas diffusion layer (GDL), a flow field made of micro-interdigitated channels [3] was employed to enforce the gas flows in the GDL by convection. Finally, the gases were fed on one face only to suppress exchanges on the other face.

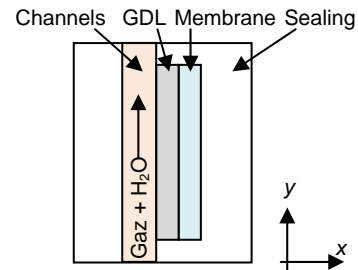


Figure 2. Experimental system.

For accessing the temporal evolution of F , a change in gas humidification was applied, namely between $\text{N}_2 + ^2\text{H}_2\text{O}$ and $\text{N}_2 + ^1\text{H}_2\text{O}$, followed by a 5 min observation time before changing back from $\text{N}_2 + ^1\text{H}_2\text{O}$ to $\text{N}_2 + ^2\text{H}_2\text{O}$. The sequence was repeated 5 times and the corresponding images were averaged in order to obtain a sufficient signal-to-noise ratio with the required temporal resolution. A specific image processing (Figure 4) leads finally to the estimation of the isotope fraction F under the assumption of a constant amount of water in the membrane during the experiment.

Model

By applying the species conservation law, the second Fick's law as expression of the fluxes, and by assuming a homogeneous distribution in the y direction, the local isotope conservation equation in the bulk of the membrane can be described by:

$$D \frac{\partial^2 (cF)}{\partial x^2} = \frac{\partial (cF)}{\partial t} \quad (1)$$

where D is the self-diffusion of H and c the concentration of H atoms (Figure 3). The latter is supposed to be constant in this model. As an approximation, all parameters are assumed to be independent on the isotope fraction F .

By fixing a known isotope fraction in the gas phase outside the membrane for both hydrogen and water vapor, called F_H and F_W here, the transfer at the interface of the membrane can be modelled as:

$$-\left(Dc \frac{\partial F}{\partial x}\right)_{x=0} = k_H(F_H - F(x=0)) + k_W(F_W - F(x=0)) \quad (2)$$

The dependency of F on time is not explicitly shown in equation (2) for simplification. At the other interface, there is no flux, due to the presence of sealing:

$$-\left(Dc \frac{\partial F}{\partial x}\right)_{x=L} = 0 \quad (3)$$

The temporal condition is an initial isotope fraction of zero in the whole membrane:

$$F(x, t = 0) = 0 \quad (4)$$

GDL Membrane

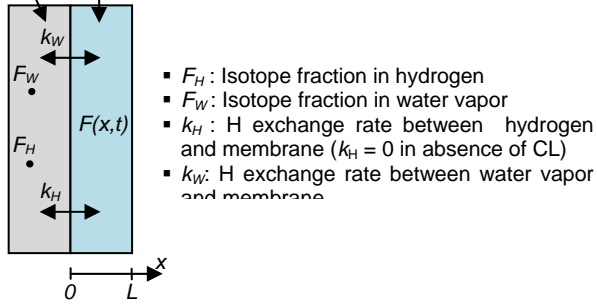


Figure 3. Model.

Although this equation set allows an analytical solution, a numerical discretization was preferred for potential modifications and extensions. This approach results in a linear system easy to solve, in case of this work in the *Matlab* environment.

Results and Analysis

The radiograms corresponding to the measured spatial distribution of isotope fraction F are presented hereunder (Figure 4). The isotope fraction F equals the pixel intensity, theoretically in the range [0,1].

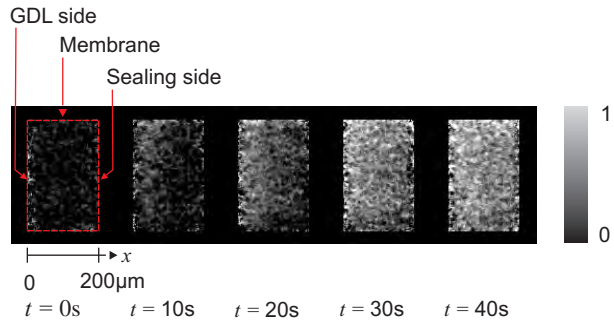


Figure 4. Processed sequence of images after changing from $N_2 + {}^2H_2O$ to $N_2 + {}^1H_2O$ at $t = 0s$. Pixel intensity = F .

Based on the experimental distribution, a least square method is applied to fit the parameters k_W and D of the model. The computed and fitted distribution of the model is compared with the experimental results below (Figure 5). A good agreement is observed between the modelled and the experimental data, which tends to indicate that the way the transports are modelled is reasonable. Each curve of the experimental results represents an average over 5 seconds, which explains the deviation of the curve at $t = 0$ from its theoretical value of 0.

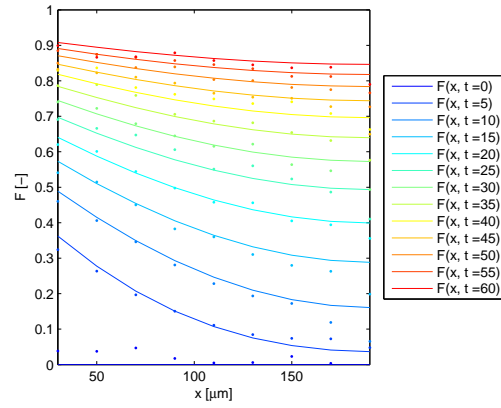


Figure 5. Temporal evolution of the spatial profile of the isotope fraction F in the membrane: comparison of the modeled and the experimental data.

For given operating conditions ($T = 70$ [°C], $RH = 80$ [%], $c = 0,027$ [mol/cm³]), the estimation of the parameters leads to the following values (Table 1).

Parameter	Type of isotope change
$D = 1,03 \cdot 10^{-5}$ [cm ² /s]	No dependence
$k_{W,1} = 3,19 \cdot 10^{-5}$ [mol/cm ² s]	$N_2 + {}^2H_2O$ to $N_2 + {}^1H_2$ $He + {}^2H_2O$ to $He + {}^1H_2$
$k_{W,2} = 1,93 \cdot 10^{-5}$ [mol/cm ² s]	$N_2 + {}^1H_2O$ to $N_2 + {}^2H_2$ $He + {}^1H_2O$ to $He + {}^2H_2$

Table 1. Estimated value of transport parameters

The value for D was averaged from 4 different experiments with a maximal error of 9%. It is in the same order of magnitude, but 50% higher, as the values found in the literature [4,5] and measured using NMR in similar conditions. The difference obtained here between $k_{W,1}$ and $k_{W,2}$ comes probably from isotope effects. Having the same value for both N_2 and He , this parameter can be considered as independent on diffusion effects. Further investigations must be made to refine the estimation of this parameter and its dependence on other parameters (T , RH , ...).

Conclusion

A method for investigating transport parameters at the surface and in the bulk of polymer electrolyte membranes was presented, which takes benefit of the isotope sensitivity of neutron imaging. As a first experiment, a simplified system was studied, namely a membrane without catalyst layer placed in *ex situ* configuration, with gas fed on one face only. Future experiments will be conducted step-by-step, complicating the system with the ambition of understanding better mass transports aspects in/on the membrane in *in situ* configuration.

References

- [1] P. Boillat, G.G. Scherer, A. Wokaun, G. Frei, E.H. Lehmann, *Electrochem. Commun.* **10**, 1311-1314 (2008).
- [2] P. Boillat, G. Frei, E.H. Lehmann, G.G. Scherer, A. Wokaun, *Electrochem. Solid St.* **13**, B25-B27 (2010).
- [3] P. Boillat, Ph.D. thesis No. 18397, ETH Zürich (2009).
- [4] K.-D. Kreuer, T. Dippel, W. Meyer, J. Maier, *Mat. Res. Soc. Symp. Proc. Vol.* **293**, 273-282 (1993).
- [5] S. Ochi, O. Kamishima, J. Mizusaki, J. Kawamura, *Solid State Ionics* **180**, 580-584 (2009).

Measurement of molecular diffusion limitations and their relation to liquid water in PEFC using helox mixture

P. Boillat, P. Oberholzer, R. Perego, E.H. Lehmann, A. Kästner, G.G. Scherer, A. Wokaun

phone: +41 56 310 2743, e-mail: pierre.boillat@psi.ch

Operating a cell using helox (mixture of 79% He and 21% O₂) at the cathode allows to reduce dramatically the losses related to the diffusive transport of oxygen, because oxygen diffuses approximately 8 times faster in helium than in nitrogen. In principle, the comparison of air and helox operation thus permits to quantify the diffusive losses. However, the liquid water distribution may as well be affected, which can in turn have some impact on the cell performance. Reasons for this are different physical properties of helium and nitrogen, which can be relevant for water transport (diffusivity of water vapor, viscosity). In this context, it is of high interest to study the transient behavior of water distribution after a switch from air operation to helox operation.

Experimental

A single polymer electrolyte fuel cell (PEFC), equivalent to that described in [1] was used. The cell was operated at a temperature of 70 °C and a pressure of 2 bar (abs). Gas flows of 1.0 nL/min were used, both on the anode and on the cathode side. All experiments were realized with a constant current density of 1.0 A/cm². Three different conditions of relative humidity were studied, as described in Table 1.

Condition	RH anode	RH cathode
A	60 %	0%
B	100 %	0%
C	100%	100%

Table 1. Different conditions of relative humidity

At time $t = 0$, the cathode gas was switched from air to helox. The gas mixtures were realized using one mass flow controller (MFC) for pure oxygen and another MFC for nitrogen or helium. A flow correction factor for the latter MFC was needed for helium operation, this MFC being primarily calibrated for nitrogen. The recorded parameters included the cell voltage as well as the cell AC resistance at 1 kHz (AC mOhm tester model 3566, Tsuruga Electric Corp., Japan).

Advantage was taken of the latest developments in neutron imaging realized at the ICON beam line of the SINQ spallation neutron source [1-3] to analyze the transient water distribution in the gas diffusion layers (GDL) following a change of inert gas. The same anisotropic imaging setup as described in [1] was used, resulting in a pixel size of 2.35 μm and an effective spatial resolution (FWHM) of approximately 20 μm in the direction across the membrane. Exposure times of 10 s were used, resulting in an acquisition rate of 4-5 images per minute, once taken into account the readout time of the camera. All neutron radiograms were referenced to radiograms of the dry cell, in order to measure the attenuation due to liquid water only.

Results

The neutron radiograms corresponding to air and helox operation are presented in Figure 1.

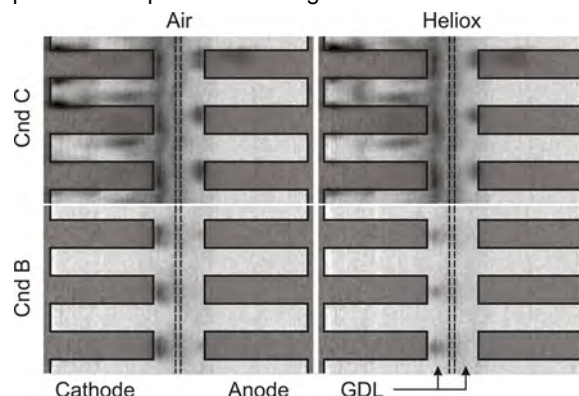


Figure 1. Images of water distribution for air and helox operation (conditions B and C)

When using dry gas at the cathode, liquid water is present only under the ribs of the cathode side. Operating the cell with helox significantly reduces the quantity of liquid water, which can clearly be attributed to the higher diffusivity of water vapor in helium. When using fully humidified gases, the water distribution on the cathode side does not seem to be affected at all, while a slight reduction of liquid water quantity is seen on the anode side. The latter can hardly be explained by a change of diffusivity under full humidified conditions. A probable explanation is an increased electro-osmotic drag in the rib region, due to a redistribution of the current density.

The evolution of the electrochemical parameters as well as the quantified water content in the cathode GDL are presented in Figure 2. A perturbation in the cell voltage appears, just after the change from air to helox, which is induced by a perturbation of the MFC when changing the gas. For this reason, the correct voltage can be measured at earliest 20 seconds after the switch.

In not fully humidified conditions (A and B), the reduction of water content happens during the 2 minutes following the change of gas. A slight change of the cell resistivity is observed as well, which happens on a quicker time scale (30 seconds – 1 minute after the change). At the measurement point at $t = 20$ s, the water distribution has only slightly evolved, but the major part of the resistivity change has already happened. In principle, this change is corrected for when we compute the so called *IR free voltage* (the actual cell voltage, to which the resistive losses are added). However, the measurement of the resistivity at high frequency might not catch all effects of a cell dry out (e.g. dry out of the cathode electrode). For this reason, a quicker and cleaner switch of air to helox would help getting more precise measurements. Under fully humidified condition, the resistivity, similarly to the water content in the cathode GDL, remains unchanged in helox operation.

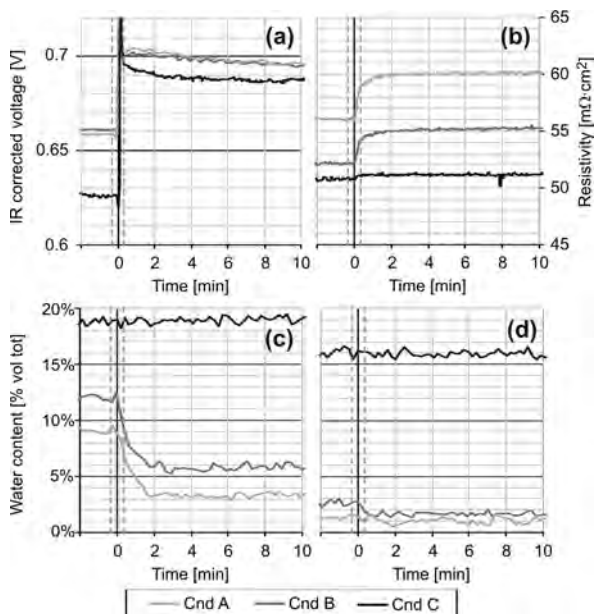


Figure 2. Evolution of electrochemical parameters after a change from air to helox operation. (a) IR free voltage (b) AC resistivity. (c,d) Measured water content in cathode GDL under ribs (c) and channels (d). The dashed lines indicate the time points used for the measurements in Figure 3.

It is worth noting that a slight reduction of the cell voltage (5-10 mV) occurs over approximately 4 minutes for condition C and 10 minutes for conditions A and B. This effect can neither be related to a change of AC resistivity, nor to an observable change of water content. As a hypothesis, we can advance a change of the catalyst surface (presence of adsorbed species and/or PtO) following the change of cell potential. A repetition of this experiment in potentiostatic mode instead of galvanostatic mode might help confirming this hypothesis.

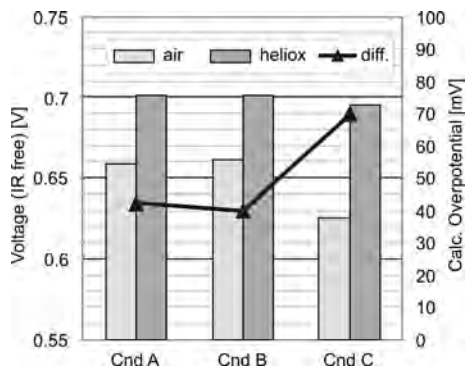


Figure 3. Voltage (IR free) measured before and after the change from air to helox.

The overpotential due to diffusive losses is calculated as the difference of IR free voltage before and after the change from air to helox, as illustrated in Figure 3. The values displayed correspond to measurements 20 seconds before, respectively 20 seconds after the change of gas. The voltage measured in heliox operation is virtually the same for all three conditions, with differences of approximately 5 mV. In air operation, larger differences are observed. The calculated diffusion overpotential is of approximately 40 mV for both conditions, with a dry cathode (A and B), and of 70 mV for the condition with fully humidified gases (condition C).

The fact that the differences of voltage observed with air operation are strongly reduced when using helox

indicates that, in the presented situation, the increased losses under condition C are effectively related to molecular diffusion limitations. In theory, this is not necessarily the case, as Knudsen diffusion might play a role in the transport of oxygen in the very small pores of the *micro-porous layer* (MPL) or of the electrode. Knudsen diffusion is dominated by the collisions of the molecules with the pore walls, and the change of inert gas is expected to exert no effect on it.

The calculated diffusion overpotential of 40 mV for conditions A and B cannot reasonably be attributed to the presence of liquid water, because no difference in voltage is observed between conditions A and B. The voltage loss is more likely partly caused by diffusion limitations, already present in the absence of liquid water. On the contrary, we can attribute with little doubt the additional 30 mV losses measured in conditions C to the increase of liquid water, and particularly to the apparition of liquid water in the GDL under the channels.

Conclusions and outlook

The evolution of water content and cell performance was studied, following a change of cathode gas from air to helox under different conditions of gas relative humidity, with the intention of distinguishing the losses related to molecular diffusion. Under certain conditions, the water distribution was observed to be affected by the change of inert gas from nitrogen to helium, though this happens slowly enough to allow a measurement of the voltage before any change. The resistivity, related to the hydration state of the membrane, is affected as well under conditions, where the diffusion of water vapor plays an important role. In order to avoid the issues in accuracy related to internal resistance correction, a neat transition between air and helox, allowing the measurement of voltage before any change of resistivity, is desirable. The repetition of short helox pulses (e.g. 1 second of duration) is expected to provide a time resolved measurement of diffusion related losses, which offer the chance to study correlations with time resolved liquid water saturation.

References

- [1] P. Boillat, G. Frei, E.H. Lehmann, G.G. Scherer, A. Wokaun, *Electrochem. Solid-State Lett.* **13**, B25-B27 (2010).
- [2] E.H. Lehmann, G. Frei, G. Kühne, P. Boillat, *Nucl. Instrum. Methods Phys. Res., Sect. A* **605**, 111-114 (2007).
- [3] P. Boillat, D. Kramer, B.C. Seyfang, G. Frei, E.H. Lehmann, G.G. Scherer, A. Wokaun, Y. Ichikawa, Y. Tasaki, K. Shinohara, *Electrochem. Commun.* **10**, 546-550 (2008).

3D imaging of PEFC electrodes

H. Schulenburg, B. Schwanitz, J. Krbanjevic¹, R. Mokso, A. Wokaun, G.G. Scherer

phone: +41 56 310 2125, e-mail: hendrik.schulenburg@psi.ch

Mass production of polymer electrolyte fuel cell (PEFC)-powered-cars require two achievements: significant cost reduction and improved stability of PEFC components [1]. In this regard, the cathode is playing a key role, due to the high Pt content (ca. $0.4\text{mg}_{\text{Pt}}/\text{cm}^2$). It is the most expensive component and is subject to complex degradation phenomena during fuel cell operation. These degradation processes may include (i) carbon support corrosion, (ii) Pt dissolution (iii) particle sintering and (iv) Ostwald ripening [2-4]. These processes lead to morphological changes of the catalyst layer. Quantification and separation of these effects is difficult or impossible, using conventional electrochemical and analytical techniques [2-4].

Our mid-term goal is to develop an analytical procedure to quantify the morphological changes of electrochemical degradation and to apply these methods to in-house developed catalysts layers. This quantification includes parameters like porosity, surface volume, layer thickness distribution, Pt volume density and surface area. These sought-after values may be accessible using new 3D microscopic techniques.

As a first step, we are investigating a commercial membrane electrode assembly (MEA) using 3D microscopic methods, i.e. X-Ray tomography and FIB/SEM serial sectioning, as well as TEM.

Experimental

We investigated a catalyst coated membrane (CCM) supplied by W.L. Gore & Associates (PRIMEA MEA Series 5710), which had a cathode loading of $0.4\text{mg}_{\text{Pt}}/\text{cm}^2$ and an anode loading of $0.1\text{mg}_{\text{Pt}}/\text{cm}^2$. Electrochemical degradation experiments were carried out in a 30cm^2 PEFC, operating at 80°C , 1bar, H_2/O_2 mode, stoichiometry 1.5/1.5, fully humidified. The cell potential was 24000 times held at open circuit (30s) and 0.6V (30s). X-Ray tomography was carried out at the TOMCAT beamline of the Swiss Light Source. Cylindrical samples of the MEA ($\varnothing 0.7\text{mm}$) were punched out and measured in transmission (10keV). Tomograms were obtained with a voxel size of $0.35 \times 0.35 \times 0.35\mu\text{m}$. For FIB/SEM serial sectioning and TEM lamella preparation a Zeiss NVision 40 microscope was employed. A Phillips CM30 microscope (300kV) at ETH Zürich (EMEZ) was in use for TEM measurements.

Results

X-ray tomography

The 2D image (Figure 1a) shows the bright catalyst layers, which enclose the darker polymer electrolyte. The catalyst layer for the oxygen reduction reaction is thicker than the layer for the hydrogen oxidation reaction. The cathode shows bubble like structures. According to the contrast, the surface of these bubbles contains more platinum than the inner part. Around these sites, the membrane is much thinner, which may lead to higher local current densities in operating PEFCs. The presence of large bubbles may increase the risk of a short circuit between the catalyst layers or pinhole formation. The 3D image shown in Figure 1b indicates that bubbles are a frequent structural feature of the cathode layer. A quantification of this bubble effect is possible by calculation of the layer thickness distribution.

¹ EPFL, Lausanne

This is shown for the cathode and membrane thickness in Figure 1c. The determined average membrane thickness is similar to the manufacturer's data ($18\mu\text{m}$), but the thickness distribution of the membrane shows that about 4% of the membrane is thinner than $10\mu\text{m}$. In fact, all our degradation experiments ended with pinhole formation of the membrane. A connection with the presence of thin membrane sites is supposable.

The morphology and thickness of the catalyst layer and membrane does not change much after electrochemical degradation (see experimental). Applying X-ray tomography, the porous structure of the catalyst layer could not be detected, because of the limited resolution ($\sim 1\mu\text{m}$), however, the determination of the thickness distribution by X-ray tomography is much faster than SEM (3-4 orders of magnitude) and non-destructive.

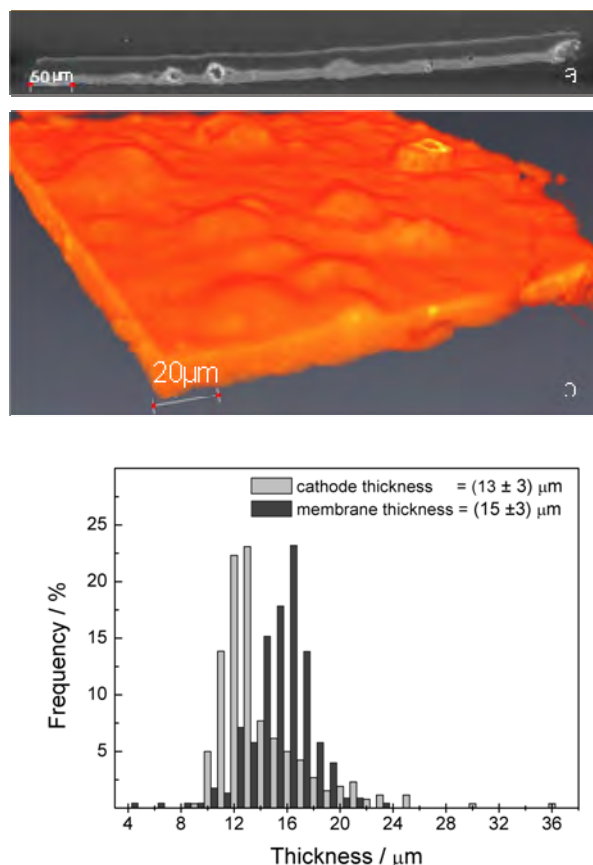


Figure 1. X-ray tomography analysis of a Gore PRIMEA CCM; a) crosssection 2D view of the CCM with anode on top, membrane and cathode below; b) 3D image of the cathode, membrane side on top; c) thickness distribution of cathode layer and membrane.

FIB/SEM serial sectioning

For the determination of porosity changes, the pristine and aged cathode layers were analyzed by FIB/SEM serial sectioning. A cube of the catalyst layer was exposed by ion milling. This cube was subject to serial sectioning with a slice thickness of 4nm. The resulting stack of SEM images was aligned, segmented and reconstructed. Figure 2a shows the first SEM image out of a stack of 455 images.

A 3D image of the pristine catalyst layer is shown in Figure 2b. The xy-plane is the milling plane. The pores of the catalyst layer are displayed in green and red. Green pores are connected to each other, red pores are separated from the pore network and obviously have no or limited contact to oxygen during PEFC operation. Differences in porosity of pristine and aged catalyst layers are small.

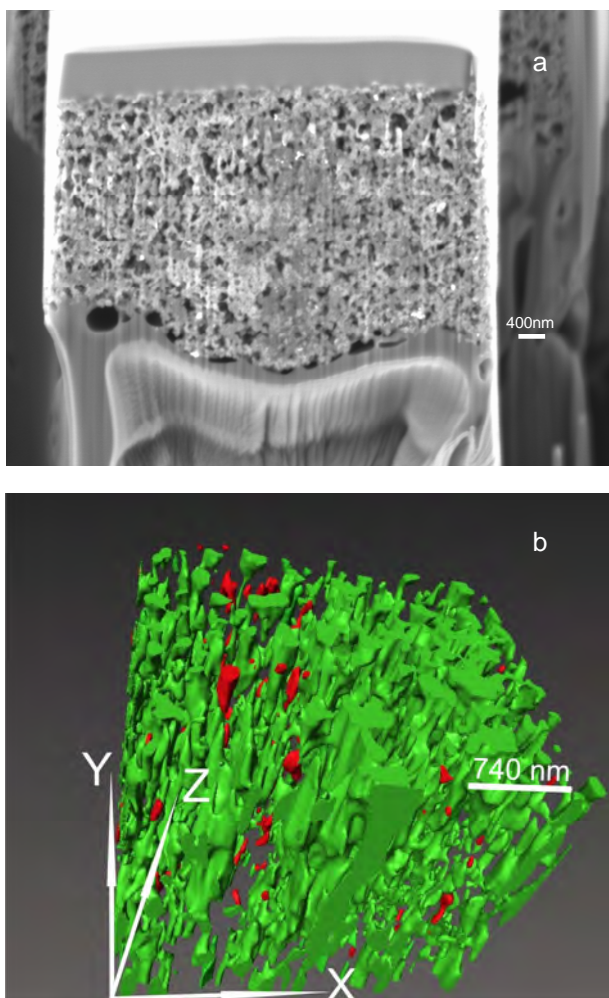


Figure 2. FIB/SEM serial sectioning, a) SEM image of an exposed cathode catalyst cube adjacent to the membrane (below) and covered with carbon (top) before sectioning, b) 3D image of catalyst cube reconstructed from 455 segmented SEM images. Connected pores in green, separated pores red.

TEM

TEM lamellas of pristine and aged catalyst layers were prepared using the FIB (Figure 3a and b). We measured particle sizes at several regions of the lamellas (Figure 3c and d). For the pristine catalyst layer the particle size distribution is narrow ($d=2.2\pm 0.9\text{nm}$) and becomes much broader after the electrochemical ageing experiment. The average particle size increases to $4.6\pm 2.8\text{nm}$.

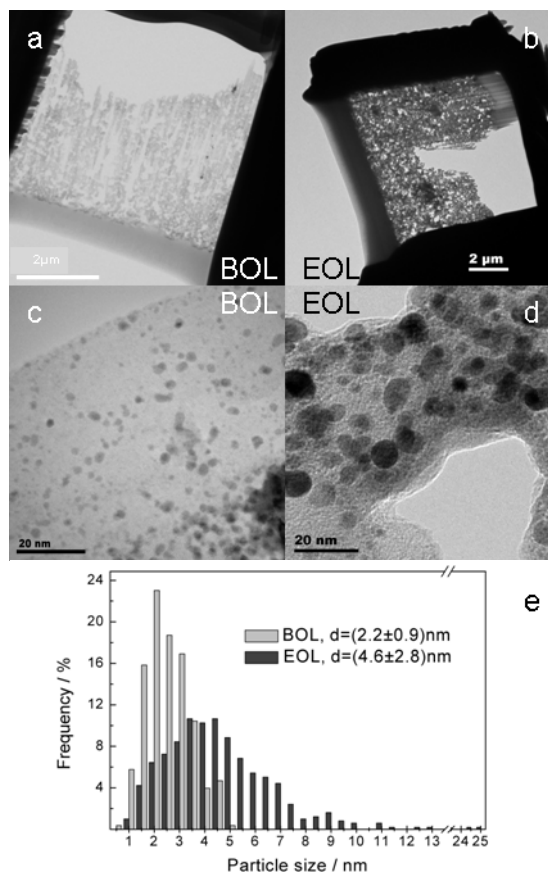


Figure 3. a) and b) TEM lamellas cut out of the pristine (BOL) and aged (EOL) cathode catalyst layer; c) and d) HRTEM images of the catalyst BOL and EOL; e) Pt particle size distribution before and after electrochemical degradation.

Conclusions

3D imaging of a pristine and electrochemically aged CCM allows to some extent the separation of degradation mechanism. X-ray tomography and FIB/SEM serial sectioning show minor morphological changes of the catalyst layer thickness and carbon support porosity. In contrast the Pt particles size increases clearly during electrochemical ageing. Performance loss during ageing seems therefore mainly connected to loss of active Pt surface area. For the employed ageing conditions carbon support corrosion is less distinct.

References

- [1] H.A. Gasteiger, S.S. Kocha, B. Sompalli, F.T. Wagner, Appl Catal. B-Environ. **56**, 9-35 (2005).
- [2] P.J. Ferreira, G.J. la O', Y. Shao-Horn, D. Morgan, R. Makharia, S. Kocha, H.A. Gasteiger, J. Electrochem. Soc. **152**, A2256-A2271 (2005).
- [3] S. Zhang, X.-Z. Yuan, J. Chen Hin, H. Wang, K.A. Friedrich, M. Schulze, J. Power Sources **194**, 588-600 (2009).
- [4] F.A. de Bruijn, V.A. T. Dam, G.J.M. Janssen, Fuel Cells **8**, 3-22 (2008).

Investigation of transport mechanisms on Pt surfaces during hydrogen under potential deposition on micro-patterned electrodes

B.C. Seyfang, T. Lippert, G.G. Scherer, A. Wokaun

phone: +41 56 310 2362, e-mail: guenther.scherer@psi.ch

Electrochemical reactions taking place in PEFCs need to be catalyzed at typical operation temperatures below 100°C to avoid damage to the polymer electrolyte membrane. Electrocatalysts employed in PEFCs, typically noble metals, have to exhibit high catalytic activity, while the catalyst loading should be kept to a minimum due to their high price. The catalyst activity in terms of electrocatalytic active area (ECA) of a PEFC electrode can be determined by cyclic voltammetry in the hydrogen underpotential region (H_{upd}) [1].

Already in 1985, McBreen [2] described the phenomenon that platinum surfaces, which are not in direct contact to the solid polymer electrolyte, demonstrate H_{upd} behavior. Two mechanisms were proposed being responsible [3], either migration of adsorbed hydrogen atoms or formation of a thin proton-conducting water film at the surface of platinum. By utilizing micro-patterned glassy carbon electrodes coated with a 50 nm thick Pt film, we were successful to carry out experiments and to identify the latter mechanism as being responsible.

Experimental

The experimental setup used is shown schematically in Figure 1. A Pt-coated micro-patterned glassy carbon electrode [4] serves as working electrode and is pressed onto a Nafion 212 membrane. A non-coated micro-patterned glassy carbon electrode is pressed onto the other, catalysed membrane side, representing the reference and counter electrode. The micro-channels of the electrodes can be flushed with humidified gases, argon on the working electrode and hydrogen on the reference/counter electrode side. Humidification is necessary to ensure sufficient proton conductivity of the membrane. Cyclic voltammograms were recorded using a Zahner IM6 electrochemical work station with a sweep rate of 50 mV/s. The H_{upd} desorption peak was integrated to obtain ECAs, with the current of the double layer capacity serving as baseline; 80 and 450 mV were the integration limits.

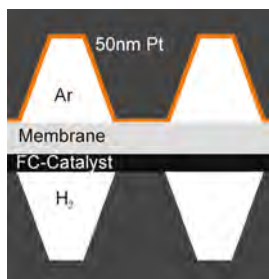


Figure 1. Fuel cell-type arrangement using micro-patterned glassy carbon structures.

Results

Three cyclic voltammograms were recorded while varying the humidification of the Argon flow. The resulting curves are displayed in Figure 2. The resulting curves are displayed in Figure 2. The continuous line represents the first CV, recorded under fully humidified conditions. Integration of the resulting

curve reveals an ECA value of 3.9 cm²/cm². The second CV, recorded after flushing with dry argon for 10 minutes reveals an ECA value of 1.6 cm²/cm² and a reduced double layer capacity. For the third CV, recorded after re-humidification, an ECA of 3.8 cm²/cm² and in addition the value of the original double layer capacity was obtained again.

Throughout the experiment the high frequency resistance was monitored. It did not increase while dry argon was fed into the cell. This is supported by the fact that the CVs recorded under dry conditions are not tilted, hence the assumption that the ionic phase of membrane and catalyst layer did not dry during the experiment is justified.

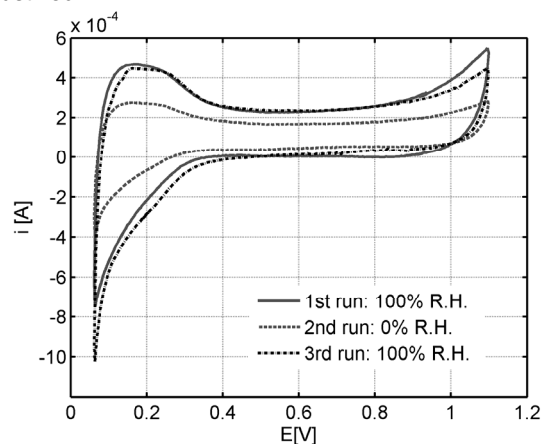


Figure 2. Cyclic voltammograms as function of the argon flow humidification obtained on a micro-patterned and Pt-coated glassy carbon electrode included in an arrangement as shown in Figure 1, using a Nafion 212 membrane. Sweep rate 50 mV/s, voltage range of 60-1100 mV, and temperature 40°C.

Therefore, we conclude that a water film is responsible for the observed H_{upd} features at this part of the platinum surface not being in direct contact to the solid polymer electrolyte.

References

- [1] S.S. Kocha in: Wolf Vielstich, Hubert A. Gasteiger, A. Lamm (Ed.) Handbook of Fuel Cells - Fundamentals, Technology and Application, Vol. 3, John Wiley & Sons, Hoboken, NJ, 2003.
- [2] J. McBreen, J. Electrochem. Soc. **132**, 1112-1116 (1985).
- [3] U.A. Paulus, Z. Veziridis, B. Schnyder, M. Kuhnke, G.G. Scherer, A. Wokaun, J. Electroanal. Chem. **541**, 77-91(2003).
- [4] B.C. Seyfang, R. Fardel, T. Lippert, G.G. Scherer, A. Wokaun, Appl. Surf. Sc **255**, 5471-5475 (2009).

Negative resistance values in locally resolved impedance spectra of polymer electrolyte fuel cells

I.A. Schneider, M.H. Bayer, A. Wokaun, G.G. Scherer

phone: +41 56 310 2795, e-mail: ingo.schneider@psi.ch

Negative resistance values in locally resolved impedance spectra of polymer electrolyte fuel cells (PEFCs) have been reported for cells, which were operated on fully humidified air and hydrogen [1]. Recently, we have shown that this feature, which appears in the local spectra of the outlet region, is linked to local ac concentration polarization losses $\eta_{up}(\omega)$, which are caused by a changing oxygen consumption with ac current in upstream parts of the flow field [1]. The low frequency real axis intercept of the local spectra $Z(\omega)$ yields negative values, as the ratio K of $\eta_{up}(\omega)$ and the ac modulation voltage $\eta_{mod}(\omega)$ exceeds unity at low modulation frequencies downstream the flow field ($\phi(K(\omega \rightarrow 0)) \rightarrow 0^\circ$). This effect forces the local ac current to become out of phase to $\eta_{mod}(\omega)$ [1]. Consequently, the negative resistance is not observed in the local impedance spectrum $Z_{loc}(\omega)$, i.e., when the ac current is applied locally [1].

In general, any PEFC, which exhibits gradually increasing concentration or ohmic losses along the flow field as a consequence of fuel, oxidant, and/or water depletion, is prone to exhibit negative resistance values at lower gas flow rates. Based on these findings, we have identified systems, which exhibit this unique behavior in locally resolved impedance spectra of PEFCs [2].

The first example presented here (Figure 1) shows the effect of hydrogen dilution and its depletion along the anode flow field on the overall and the locally resolved impedance response of a PEFC.

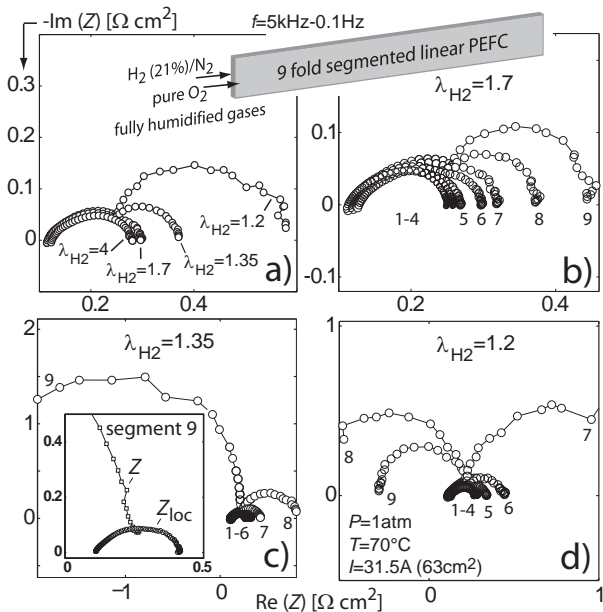


Figure 1. Effect of H_2 dilution on (a) the overall and (b-d) the locally resolved impedance response of a PEFC.

Negative resistance values are observed in the local spectra at a low anode flow rate (Figure 1b-d). The cathode is operated on fully humidified pure oxygen. The complete disappearance of the low frequency loop in $Z_{loc}(\omega)$ (inset in Figure 1c), therefore, underlines that the

formation of the loop must be linked to hydrogen depletion along the anode flow field. Note, that no low frequency loop is observed, when the cell is operated on fully humidified pure gases under the same conditions (thin membrane and moderate current density [2,3]). Under fully humidified conditions, liquid water is at least present at the cathode and, therefore, the water and oxygen partial pressure are kept at a constant level along the cathode flow field. This also holds, in principle, for the anode, where an even insufficient water back transport from the cathode will result in an increasing, yet not in a decreasing hydrogen concentration toward the anode outlet (as water depletes in the same direction). Consequently, no low frequency capacitive loop is observed as a result of fuel or oxidant depletion, if the cell is operated on fully humidified pure gases, as the depletion of hydrogen and oxygen along the flow field relies on the presence of diluting nitrogen.

The results are also relevant for PEFCs, which are operated on diluted liquid fuels like methanol. The appearance of a low frequency capacitive loop in integral DMFC anode spectra (DHE mode) has been reported ($f < 1\text{Hz}$) for cell operation at low methanol stoichiometry [4]. In particular at low anode stoichiometry $\lambda \leq 2$ (1M MeOH) the diameter of this low frequency loop increased strongly. The discussion given in that work [4] implies that the increasing loop diameter is associated with a hindered removal of CO_2 bubbles at lower anode flow rate. However, if we take into account the complete disappearance of the low frequency loop at high methanol flow rates ($\lambda \geq 10$), also an increasing mass transport limitation due to the finite fuel flow rate could play an important role. This effect is clearly seen in the locally resolved EIS and i/E data in Figure 2 ($\lambda = 1.3$).

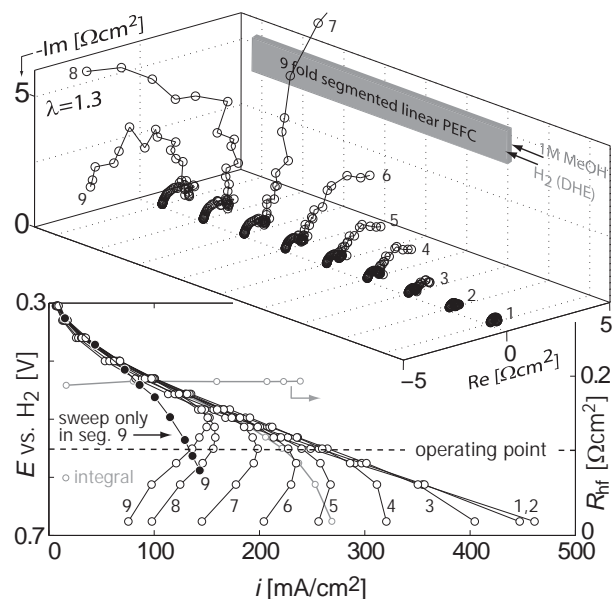


Figure 2. Locally resolved DMFC anode impedance spectra and respective polarization curves at low MeOH stoichiometry.

The local i/E curves clearly demonstrate that the ever increasing fuel consumption toward higher cell polarization at the anode inlet enforces concentration polarization losses in downstream regions of the cell. Thereby, the slope of the local i/E curve becomes infinite or even negative at that point where these losses compensate or even overcompensate the increase in total cell polarization [1,2]. Consequently, the local polarization resistance approaches infinity (segment 7) or becomes even negative (segment 8,9) in the local spectra (Figure 2). Note that the low frequency loop virtually disappears in the local spectrum at the fuel inlet. Another interesting example is the effect of water depletion along the anode flow field (Figure 3). In case of thick membranes, a second low frequency capacitive loop becomes apparent in the spectrum, even if the cell is operated on fully humidified pure gases and at moderate current density [3], as shown in Figure 3a for a H_2/O_2 -PEFC, which employs a MEA with a ($250\mu m$) N120 membrane. Evidently, considering fully humidified pure feed gases, the low frequency capacitive loop can not be related to fuel or oxidant depletion, although the loop diameter shows a strong dependence on the anode flow rate. However, this effect is accompanied by an increase of the total high frequency resistance (Figure 3a), which already indicates that the low frequency capacitive loop might be associated with water depletion/drying effects at the anode side.

As a matter of fact, the employment of a thick ($250\mu m$) N120 membrane in this experiment hampers the back transport of water and, thereby, enhances anode drying due to electroosmotic drag. The net flux of water is positive along the flow field. This manifests itself in a gradually increasing HFR value towards the gas outlets (Figure 3b,c). At a lower anode gas flow rate, water depletes stronger along the flow field and losses due to anode drying become strongly limiting. The increasing size of the low frequency loop in the integral spectrum (Figure 3a) and the appearance of negative resistance values in the locally resolved spectrum (Figure 3d,e) must be attributed to this effect. This is illustrated in Figure 3f. At a lower anode flow rate the ratio $K(\omega)=\eta_{up}(\omega)/\eta_{mod}(\omega)$ exceeds unity in the outlet segment 9 at low frequencies (inset in Figure 3f). The results show that the ac voltage $\eta_{up}(\omega)$ is predominantly caused by a sinusoidal changing HFR $\Delta R_{hf}(\omega)$, due to a changing (positive) net water flux with ac current in upstream parts of the anode flow field. The negative resistance behavior is not observed for $Z_{oc}(\omega)$, i.e., when the ac current is applied locally to the outlet segment (Figure 3f). The local spectrum $Z(\omega)$ can be obtained by the calculation of $Z(\omega)=Z_{oc}(\omega)/(1-K(\omega))$ [1,2] as demonstrated in Figure 3f.

The results presented here clearly give proof that the appearance of negative resistance values in locally resolved impedance spectra of PEFCs are a direct consequence of *down the channel* inhomogeneities, due to mass transport limitations along the flow channels. As the cell polarization is changed, the respective concentration profiles along the flow fields approach new steady state values. If local processes are fast, the time to reach steady state is governed by the time constant of channel mass transport, yet it can exceed this value, if slower processes, e.g. membrane hydration/dehydration, become limiting. The local polarization resistance exhibits negative values, if local losses due to the changing reactant composition along the flow channels exceed the total perturbation voltage amplitude. This forces the local cell current to decrease, despite a higher total cell polarization.

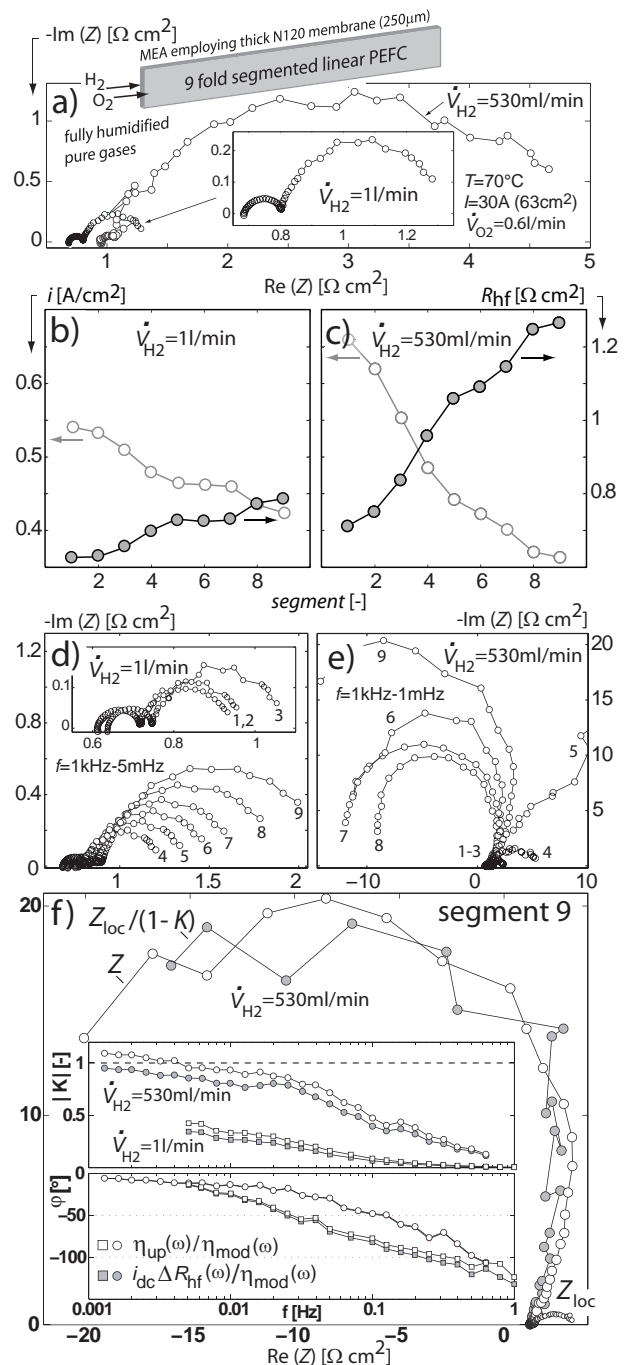


Figure 3. Effect of water depletion on (a) the overall impedance response, (b,c) the local current density and local HFR, and (d-f) the locally resolved impedance response of a PEFC.

References

- [1] I.A. Schneider, G.G. Scherer in Handbook of Fuel Cells, Vol. 6, W. Vielstich, H.A. Gasteiger and H. Yokokawa, Editors, John Wiley & Sons, New York (2009).
- [2] I.A. Schneider, M.H. Bayer, A. Wokaun, G.G. Scherer, ECS Trans., **25**, 937 (2009).
- [3] V.A. Paganin, C.L.F. Oliveira, E.A. Ticianelli, T.E. Springer, E.R. Gonzalez, Electrochim. Acta, **43**, 3761 (1998).
- [4] J.T. Mueller, P.M. Urban, J. Power Sources, **75**, 139 (1998).

Modeling the effect of the air flow rate on locally resolved impedance spectra of polymer electrolyte fuel cells

I.A. Schneider, M.H. Bayer, A. Wokaun, G.G. Scherer

phone: +41 56 310 2795, e-mail: ingo.schneider@psi.ch

A pseudo 2D (1+1D) transient model for a PEFC air cathode is presented. The model reflects experimentally obtained key phenomena [1-3] of the air flow rate on locally resolved impedance spectra. The model accounts for (i) convective mass transport along the cathode gas channels, and (ii) oxygen concentration dependent cathode cell reaction. The fuel cell cathode is treated as a number of $k=1..90$ 1D sandwiches, each sandwich consists of $i=1..10$ elements. These sandwiches communicate with one another exclusively via the convective down the channel flow. Thereby, we assume a laminar flow profile in the cathode gas channel (Figure 1). In the flow channel, oxygen is transported in flow direction via convection, and perpendicular to the flow channel and within the GDL via diffusion (Fick's 1st law). The electrode is treated to be part of the GDL ($i = 10$). The faradaic current $j_{Fk}(t)$ is assumed to obey Tafel's law (Tafel slope $b=0.03V$). Thereby, we take into account both the dependence of exchange current density $j_0(t)$ and Nernst potential $E(t)=E^*+\eta_{Nk}(t)$ on the local oxygen concentration at the electrode $c_{k,10}(t)$. In addition, we account for the double layer charging current $j_{Ck}(t)$ and the ohmic resistance R_Ω . The resulting set of equations (Figure 1) was solved numerically. Locally resolved impedance spectra $Z_k(\omega)$ were obtained via discrete Fourier transform, i.e. $Z_k(\omega)=F\{\Delta\eta(t)\}/F\{\Delta j_k(t)\}$.

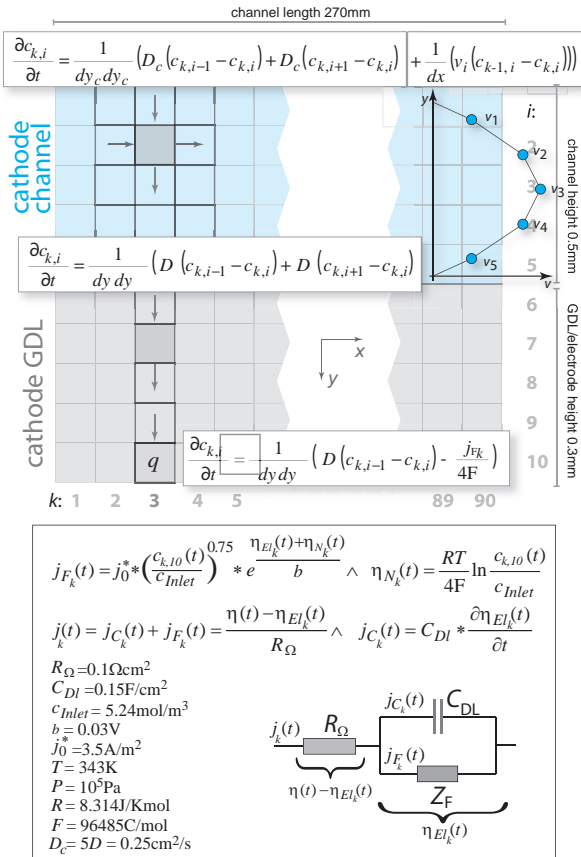


Figure 1. Pseudo 2D transient model for a PEFC air cathode [4].

The effect of mass transport limitations along the cathode flow channels is illustrated in Figure 2 for the local transient response to a voltage step. For differential flow conditions ($\lambda_{air}=10000$), mass transport limitations along the cathode flow channel are negligible. Consequently, the oxygen concentration in the cathode gas channel is virtually unaffected by the voltage step (Figure 2a(i)). However, the oxygen concentration gradient across the GDL approaches a new steady state value within a time frame of around 40ms (Figure 2a(ii)). Interestingly, the characteristic time constant for mass transport across the GDL $\tau_D = d^2/D = 11.5\text{ms}$ and the time constant for double layer charging $\tau_C = C_{DL}b/j = 9\text{ms}$ are of the same order. Consequently, only one time constant is observed here in the local current transients $\Delta j_k(t)$ (Figure 2a(iii)).

The effect of mass transport limitations along the cathode flow channel becomes important at technical air flow rates (Figure 2b, 2c). At an overall higher oxygen consumption after the step, the finite mass flow rate limits the formation of the new oxygen concentration profile along the gas channel (Figure 2b(i), 2c(i)). Already at an air stoichiometry of $\lambda_{air}=2.0$, it takes a total of around 280ms before a new steady state is reached (Figure 2b(ii)). At an even lower air stoichiometry of $\lambda_{air}=1.17$, this time frame virtually doubles to a value of around 500ms (Figure 2c(ii)). The higher oxygen consumption along the cathode flow channel after the step and the increasing time that is needed to reach steady state in the *down the channel* direction (Figure 2b(i), 2c(i)) manifest in the local concentration polarization transients $\Delta \eta_{ck}(t)$ (Figure 2b(ii), 2c(ii)). A direct consequence of the locally changing concentration polarization $\Delta \eta_{ck}(t)$ is the appearance of a second time constant in the local current transients $\Delta j_k(t)$ (Figure 2b(iii), 2c(iii)). The second time constant is therefore linked to the effect of oxygen depletion along the cathode gas channel [2,3].

An interesting phenomenon becomes apparent in the local concentration polarization transients $\Delta \eta_{ck}(t)$ at low air stoichiometry ($\lambda_{air}=1.1$). As demonstrated in Figure 2c(ii), $\Delta \eta_{ck}(t)$ approaches values in the outlet region, which become virtually equal ($k=70$) or even higher ($k>70$) than the applied perturbation voltage of $\Delta \eta = 1\text{mV}$. As a direct consequence, the respective local cell current transients $\Delta j_k(t)$ approach a value (Figure 2c(iii)), which is virtually unchanged ($k=70$) or even lower ($k>70$) than the respective local steady state current density, despite the higher total cell polarization after the step [2,3]. The appearance of negative polarization resistance values in the respective locally resolved impedance spectra $Z_k(\omega)$ are a direct consequence of this phenomenon. Locally resolved spectra, as obtained after Fourier transform of the time domain data (Figure 2), are presented for air stoichiometries of $\lambda_{air}=10000$, 2, and 1.17 in Figure 3. The results are consistent with the experimental observations [2,3]. At very high air flow rates ($\lambda_{air}=10000$) mass transport along the cathode flow channel is not limiting. The time constant for mass transport through the GDL and for double layer charging

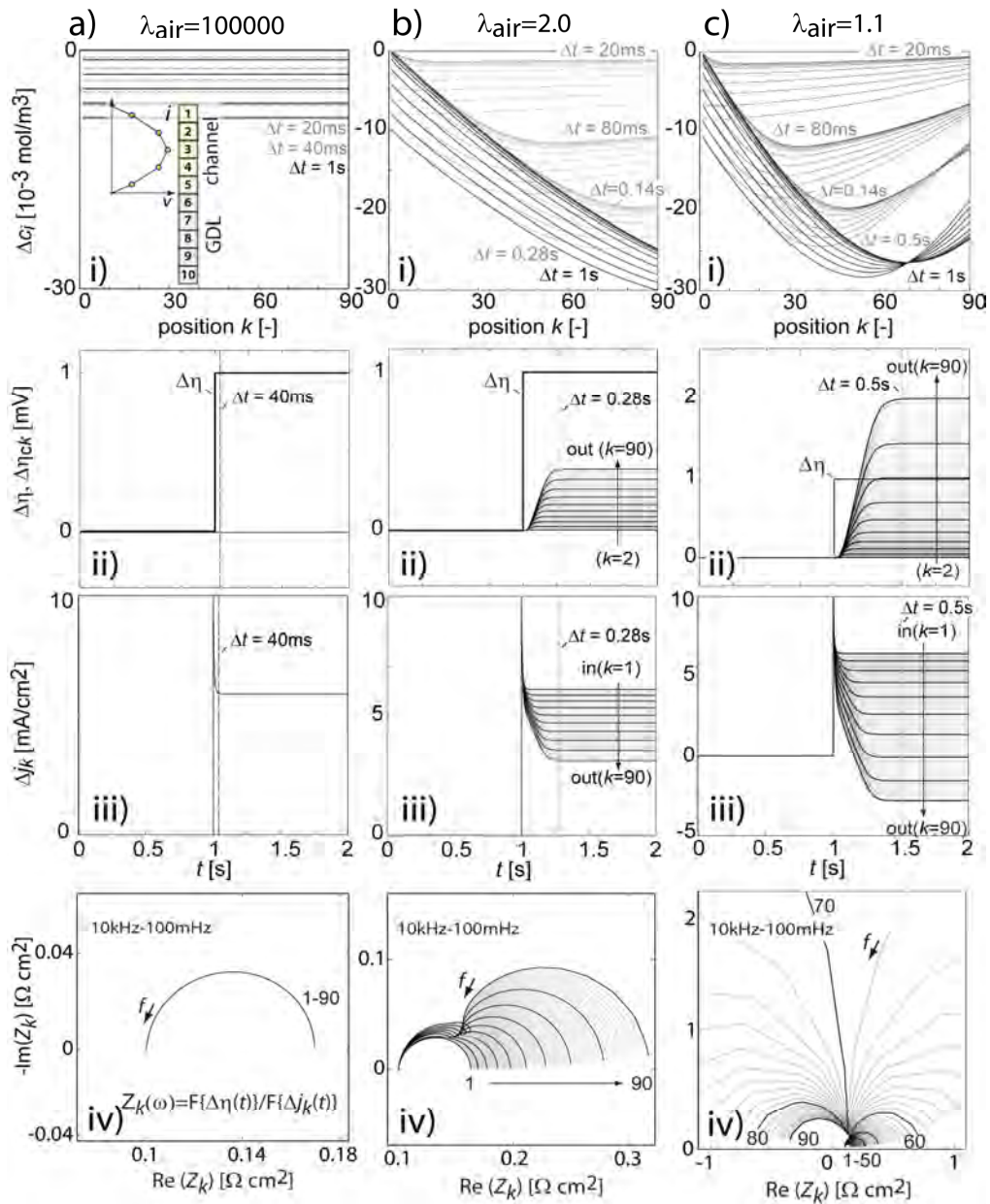


Figure 2. Modeled local transient response of an air fed PEFC to a voltage step of $\Delta\eta=1\text{mV}$ for a) differential ($\lambda_{\text{air}}=100000$), and b, c) finite air flow rates ($\lambda_{\text{air}}=2.0$, $\lambda_{\text{air}}=1.1$): (i) change of the oxygen concentration profile (local concentration gradient across the flow channel and the GDL as a function of channel position) for distinct time intervals Δt after the step, (ii) total perturbation voltage $\Delta\eta(t)$ and, local concentration polarization transients $\Delta\eta_{\text{ck}}(t)$ due to changing consumption of oxygen in upstream parts of the gas channels at higher cell polarization after the step (iii) local transients of cell current $\Delta j_k(t)$, and (iv) locally resolved impedance spectra. $j=0.5\text{A/cm}^2$ [4].

are of the same order and, therefore, only one time constant is observed in $\Delta j_k(t)$ (Figure 2a(iii)). Consequently, the respective locally resolved impedance spectrum (Figure 2a(iv)) exhibits a single capacitive loop along the flow field. However, the second time constant, which appears in the local current transients $\Delta j_k(t)$ as a result of finite gas flow rate (Figure 2b(iii), 2c(iii)) manifests in the local spectra $Z_k(\omega)$ in a second low frequency capacitive loop (Figure 2b(iv), 2c(iv)). For $\lambda_{\text{air}}=1.17$ (Figure 2c(iv)) the polarization resistance approaches infinity ($k=70$) or becomes even negative ($k>70$), as $\Delta\eta_{\text{ck}}(t)$ approaches or even exceeds $\Delta\eta=1\text{mV}$ in the outlet region (Figure 2c(iii)).

References

- [1] D.J.L. Brett, S. Atkins, N.P. Brandon, V. Vesovic, N. Vasileiadis, A.R. Kucernak, *Electrochem. Solid-State Lett.* **6**, A63 (2003).
- [2] I.A. Schneider, D. Kramer, A. Wokaun, G.G. Scherer, *J. Electrochem. Soc.* **154**, B770 (2007).
- [3] I.A. Schneider, G.G. Scherer, 'Local transient techniques in polymer electrolyte fuel cell (PEFC) diagnostics' in *Handbook of Fuel Cells*, Vol. **6**, W. Vielstich, H.A. Gasteiger H. Yokokawa, Editors, John Wiley & Sons, New York (2009).
- [4] I.A. Schneider, M.H. Bayer, A. Wokaun, G.G. Scherer, *ECS Trans.*, **25**, 937 (2009).

A segmented microstructured flow field approach for sub-millimeter resolved local current measurement in channel and land areas of PEFCs

I.A. Schneider, S. von Dahlen, A. Wokaun, G.G. Scherer

phone: +41 56 310 2795, e-mail: ingo.schneider@psi.ch

Flow field plates are used in practical PEFCs to distribute the reactant gases over the active area and to remove reaction products. The flow fields exhibit a channel and land structure. The reactant gases are forced through the gas channels, whereas the current is collected from the gas diffusion layer (GDL) under the land area. Evidently, the use of flow fields in PEFCs entails inhomogeneities in current generation over the active electrode area.

Our recent work has focused on the effect of *down the channel* inhomogeneities on PEFC transient response in electrochemical impedance spectroscopy (EIS), cyclic voltammetry (CV) or current step experiments [1]. In this context, the results of locally resolved EIS experiments in practical PEFCs have clearly demonstrated that a 1-dimensional treatment of data, as obtained in practical PEFCs, is not only inadequate for the interpretation of results, due to the finite reactant flow rate and a changing gas composition in the *down the channel* direction, but can also lead to wrong conclusions [1]. As a consequence, the use of differential cells, which are operated at very high gas stoichiometry, has been cited to justify the use of 1-dimensional mathematical models [2]. This is an important step forward. However, by providing virtually homogenous reaction conditions along the gas channel, a differential cell can solely be regarded as a quasi 2-dimensional cell. Even in a differential cell inhomogeneities are expected to occur as a consequence of mass transport limitations and a changing gas composition in the direction *perpendicular to the flow channel*. Different compression of the porous GDL in channel and land areas and anisotropic charge and mass transport properties must also be taken into account in this context.

The assessment of the significance of these inhomogeneities on PEFC transient response requires, beyond current density distribution measurements, the application of locally resolved transient techniques on the millimeter scale of PEFC flow field structures. To the best of our knowledge, no reports on the application of locally resolved transient techniques in the area of channels and lands of a polymer electrolyte fuel cell have been published to date. Even reports, which scrutinize the effect of the flow field structure on the local current density in the channel and land area of PEFCs experimentally, are sparse, due to the difficulty to collect the local cell current on the small scale of technical PEFC flow field structures.

In order to make headway in the assessment of the significance of inhomogeneities on the channel and land scale on PEFC transient response and on cell performance, one must simplify the experimental system, which in turn yields unequivocal and quantitative applicable results for the local cell current.

The cathode is responsible for the significant majority of PEFC voltage loss and degradation. Cathode losses comprise kinetic, proton transport, and oxygen transport contributions, whereas anode contributions are usually excluded from the discussion [2], considering fast hydrogen oxidation reaction (HOR) kinetics, surplus

platinum catalyst loading, and rapid transport of molecular hydrogen. If we restrict thereby our attention to phenomena, which are related to the cathode flow field structure, a cell design must be chosen, where the anode acts as a quasi homogenous counter electrode across the cell area. Therefore, precautions must be taken. On the one hand, the anode must be operated at a high gas flow rate to ensure low residence time and to exclude a notable change in anode gas composition between the hydrogen inlet and outlet. On the other hand, inhomogeneities, which are induced by the anode flow field structure must be insignificant on the length scale of the technical cathode flow field. To meet this requirement, a microstructured flow field may be used at the anode. Recently, Seyfang et al. [3] reported on a simplified micro-PEFC concept with high power density. This approach employs no GDL, the cell current is directly collected from the cathode and anode catalyst layer of a catalyst coated membrane (CCM). If a segmented microstructured flow field is operated in that way at the anode of a differential cell, the direct measurement of the local cell current with sub-millimeter resolution becomes possible in a fully catalyzed MEA, as a result of the finite in-plane conductivity of the CCM. This novel segmented micro flow field approach is presented in Figure 1 [4].

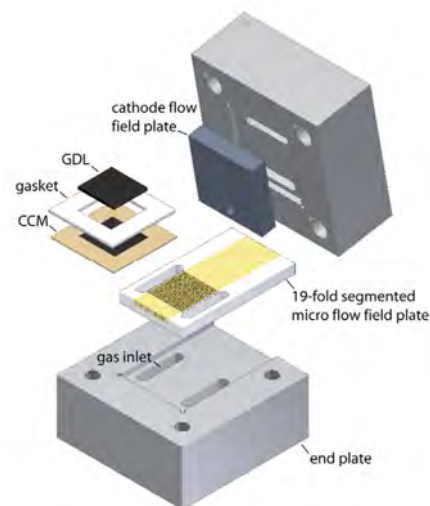


Figure 1. Novel segmented microstructured flow field approach for the direct measurement of the local current with sub-mm resolution.

At the anode, a segmented pin type microstructured flow field is directly attached to the catalyst coated membrane (CCM). The membrane also acts as the anode seal [3]. The microstructured flow field is 19-fold segmented in the direction *perpendicular to the cathode gas channel*. Thereby, the current density distribution in channel and land areas of the cathode flow field can directly be accessed by the measurement of the respective branch currents. In this configuration, the anode is operated in cross flow mode (Figure 1). A high anode gas stoichiometry ensures a quasi homogenous anode gas composition in the direction *perpendicular to*

the cathode gas channel. The resulting 19-fold segmented pin-type flow field ($A=0.6\text{cm}^2$) exhibits a number of 760 gold pins per cm^2 . With this prototype design, the current density distribution in a PEFC can directly be measured with a high spatial resolution of $400\mu\text{m}$ [4].

Figure 2 shows the integral i/E characteristics and the corresponding high frequency resistance (HFR) R_{hf} ($f=5\text{kHz}$) of a conventional differential cell and of a cell, which is identical, except for the anode, and which employs the microstructured flow field (Figure 1). High performance is achieved at ambient pressure in both, H_2/O_2 and H_2/air operation mode. Under the same operating conditions, both cells show virtually equal performance. Evidently, the integral i/E curve is governed by several factors. However, if we take into account the similar HFR values of around $R_{\text{hf}}=0.07\Omega\text{cm}^2$ (Figure 2) in all measurements, the result clearly demonstrates that the employment of the segmented microstructured flow field at the anode has no noteworthy effect on the cell characteristics.

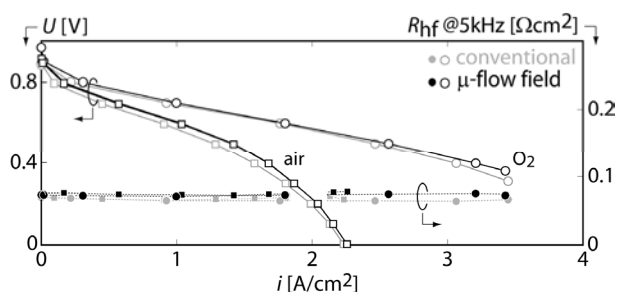


Figure 2. Characteristics of a conventional differential cell and a cell which employs a microstructured anode flow field (Figure 1).

The result of sub-millimeter resolved current density distribution measurements in channel and land areas of the cathode flow field (Figure 1) is shown in Figure 3 for fully humidified operating conditions (Figure 3a) and for dry operation (Figure 3b) of the cell. The results for cathode operation on fully humidified pure oxygen and fully humidified air are compared in Figure 3a. The current density distribution is quasi homogenous for operation on pure oxygen ($i_{\text{cell}}=1\text{A}/\text{cm}^2$). Under fully humidified conditions, no significant difference in the water vapor pressure in channel and land areas of the cell can be expected, and consequently, the oxygen partial pressure is kept at a constant level in the binary gas mixture. This provides virtually homogenous reaction conditions throughout the oxygen electrode area, unless liquid water starts to block pores and thereby, inhibits the access of reactants to the active sites at higher cell currents. Note that the slightly decreasing performance in the channel region (Figure 3a, segment 8-12) is probably related to a higher contact resistance [4].

This is different for air operation, where mass transport related inhomogeneities exist even at a rather low cell polarization (Figure 3a). As most of the total cell current is generated in the channel area, the local current density approaches maximum values of more than 2.5 times the average value ($i_{\text{cell}}=1\text{A}/\text{cm}^2$). This results in a high cell polarization and a low cell voltage of $U_{\text{cell}}=0.1\text{V}$ vs. $U_{\text{cell}}=0.6\text{V}$ for operation on pure oxygen (Figure 3a). Within the channel area, the oxygen concentration is kept high by the convective gas flow and, consequently, all parts of the channel (Figure 3a, segment 8-12) show virtually the same performance. A limiting current density is still not reached at high local current density values

beyond $2.5\text{A}/\text{cm}^2$. However, already within a distance of 1mm from the channel, the cell performance drops below one tenth of this maximum value, as a consequence of the increasing diffusion path length for oxygen and its depletion in diluting nitrogen in the land area. The inverse characteristics is observed for operation of the cell on dry oxygen (50% r.h. H_2), as a result of water formation (Figure 3b). The rising water partial pressure under the rib manifests in a performance gain in the land area, due to the increasing hydration of the ionomer.

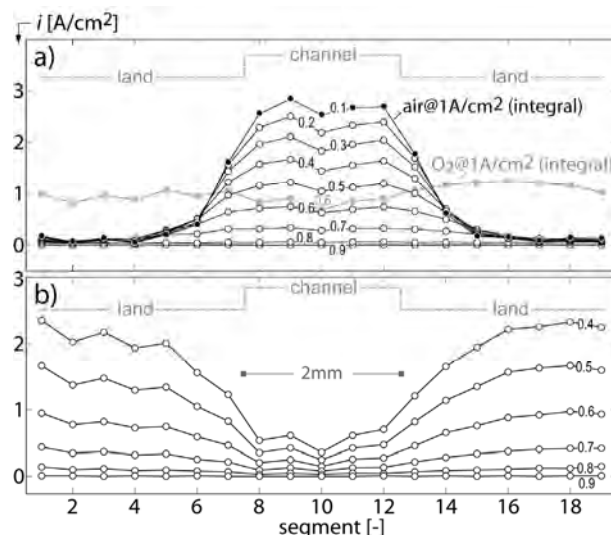


Figure 3. Current density distribution in channel and land areas of a $1\times 2\text{mm}$ channel cathode flow field (number denotes voltage). The gases were fed to the cell either a) fully humidified ($T_{\text{dew, H}_2, \text{O}_2, \text{air}}=70^\circ\text{C}$) or b) dry ($T_{\text{dew, H}_2}=55^\circ\text{C}$, dry oxygen). $T_{\text{cell}}=70^\circ\text{C}$, $T_{\text{abs}}=1\text{atm}$, $V_{\text{H}_2}=100\text{ml}/\text{min}$ ($\lambda_{\text{H}_2}=24@i_{\text{cell}}=1\text{A}/\text{cm}^2$), $V_{\text{O}_2}=V_{\text{air}}=200\text{ml}/\text{min}$ ($\lambda_{\text{O}_2}=96@i_{\text{cell}}=1\text{A}/\text{cm}^2$, $\lambda_{\text{air}}=20@i_{\text{cell}}=1\text{A}/\text{cm}^2$), Gore Primea 5710 CCM ($0.1\text{mg}/0.4\text{mg Pt}/\text{cm}^2$ at anode/cathode).

The segmented microstructured flow field approach, as presented in this work, allows for the first time the direct measurement of the local current in the area of channel and lands of PEFC flow fields with sub-millimeter resolution. The novel method allows the precise measurement of both high and low level current signals with high signal to noise ratio (SNR) and, thereby, leverages the application of locally resolved transient techniques like CV and EIS in the area of channels and lands [4]. The results clearly show that effects, which occur due to inhomogeneous operation of PEFCs in the *down the channel* direction on the length scale of tenth of centimeters have their counterparts in the *perpendicular to the flow channel* direction on the millimeter scale of channel and lands and, hence, must be considered with equal attention.

References

- [1] I.A. Schneider, G.G. Scherer in Handbook of Fuel Cells, 6, W. Vielstich, H.A. Gasteiger and H. Yokokawa, Editors, John Wiley & Sons, New York (2009).
- [2] M.F. Mathias, D. Baker, J. Zhang, Y. Liu, W. Gu, ECS Trans. **13**, 129 (2008).
- [3] B.C. Seyfang, M. Kuhnke, T. Lippert, G.G. Scherer, A. Wokaun, Electrochem. Commun. **9**, 1958 (2007).
- [4] I.A. Schneider, S. von Dahlen, A. Wokaun, G.G. Scherer, J. Electrochem. Soc. **3**, B338 (2010).

Simultaneous measurement of local flooding and current transients in channel and land areas of a polymer electrolyte fuel cell

I.A. Schneider, S. von Dahlen, M.H. Bayer, P. Boillat, M. Hildebrand, E. Lehmann, P. Oberholzer, G.G. Scherer, A. Wokaun

phone: +41 56 310 2795, e-mail: ingo.schneider@psi.ch

Polymer electrolyte fuel cells (PEFCs) operate at temperatures of $T < 100^\circ\text{C}$. Water coexists in both the liquid and the vapor phase. The porous gas diffusion layer (GDL) and the catalyst layer (CL) allow simultaneous gas and liquid flows. The local build up of liquid water in the cell may, however, lead to flooding of reactant gas transport pathways and as a consequence, the cell is prone to suffer from phenomena such as performance loss, reactant starvation and cell degradation.

Despite improved physical models [1] and emerging diagnostic tools e.g., advanced imaging techniques [2], the picture of liquid water transport and its accumulation in the porous cell components is still nebulous. The same holds for flooding related phenomena. In particular, the demonstration of a correlation of the local water content and performance loss remains challenging, if we consider that local mass transport limitations are not necessarily governed by the effect of flooding by liquid water.

In this context, the use of transient techniques provides an avenue to separate flooding related losses from the immanent limitation due to mass transport in the porous layers by means of the time constant. We present a potential step technique for the simultaneous examination of local flooding and local performance on the cathode side of a PEFC. We focus on the significance of liquid water accumulation in the porous layers within cathode channel and land areas on the local cell performance. For this purpose, submillimeter-resolved current density distribution measurements [3] and in plane neutron radiography [2] have been used simultaneously for the first time.

The experimental setup is shown in Figure 1a. The neutron beam passes through the cell in the direction parallel to the cathode flow field channels. Anisotropic resolution enhancement techniques [2] provide a high spatial resolution of $20\ \mu\text{m}$ in horizontal direction at an unrivaled low exposure time of only 10 s. The temporal resolution is notwithstanding insufficient to resolve flooding transients after a potential step. A temporal resolution better than the total exposure time becomes possible, if total exposure time is accumulated by the averaging of multiple series of neutron images as received onto synchronized repetitive cell perturbation from steady state (OCV \rightarrow 0.1V). With this approach (Fig. 1a) a temporal resolution of 2 s was achieved at a spatial resolution of $20\ \mu\text{m}$.

The differential cell used in the measurement employs a parallel 3-channel graphite flow field at the cathode (channel/land width: 1.2 mm) along with an untreated $280\ \mu\text{m}$ thick Toray TGPB-090 carbon paper GDL and a $200\ \mu\text{m}$ PTFE gasket ($V_{\text{air}} = 200\ \text{ml} / \text{min}$). At the anode a segmented microstructured pin-type flow field is directly attached to the CCM (Nafion 112, $0.5\ \text{mg Pt} / \text{cm}^2$, 70 % Pt/C) [3]. The segmented anode operates as a quasi-homogeneous counter electrode ($V_{\text{H}_2} = 200\ \text{ml} / \text{min}$) and allows the direct measurement of the local current density within four characteristic areas of the cathode flow field (Figure 1b).

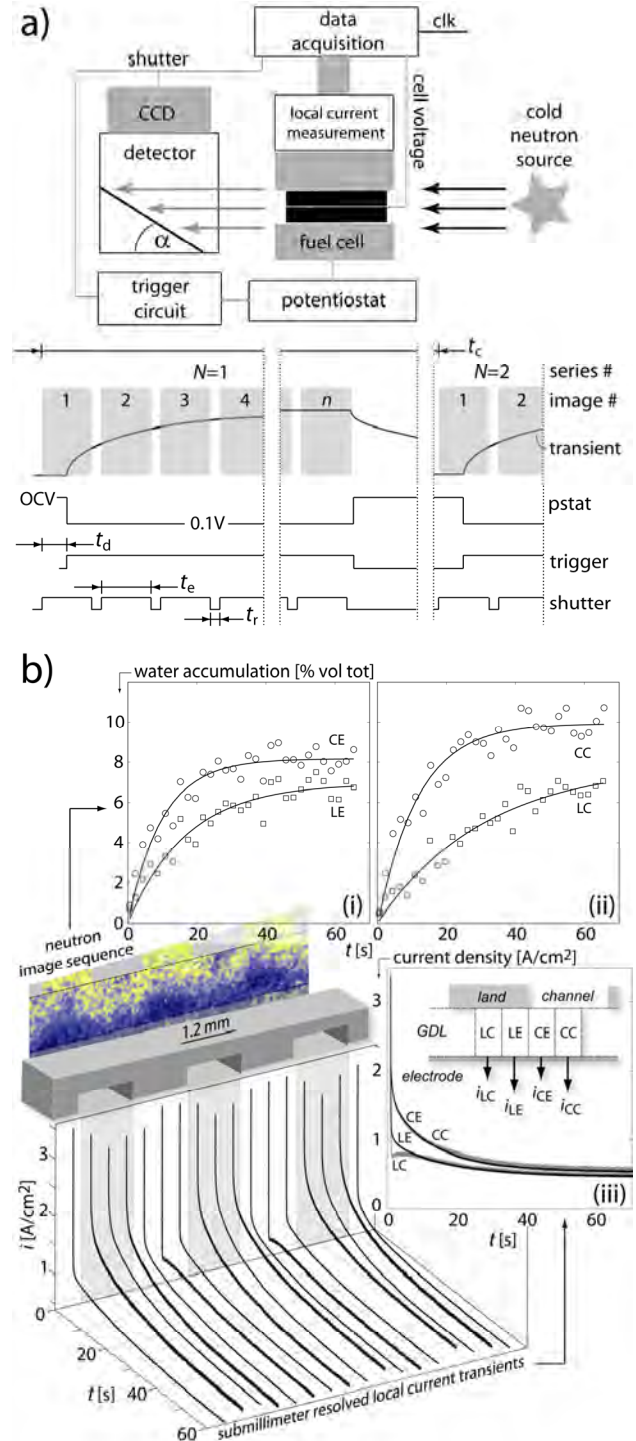


Figure 1. a) Experimental setup and timing chart, b) local transients of current and liquid water content in different areas of the cathode flow field ($T_{\text{cell}} = T_{\text{hum,H}_2} = T_{\text{hum,air}} = 40^\circ\text{C}$). Note, that the observed liquid water distribution may depend on the anode diffuser, which cannot be chosen arbitrary in our design. We focus primarily on a correlation of the liquid water distribution at the cathode and the local cell performance.

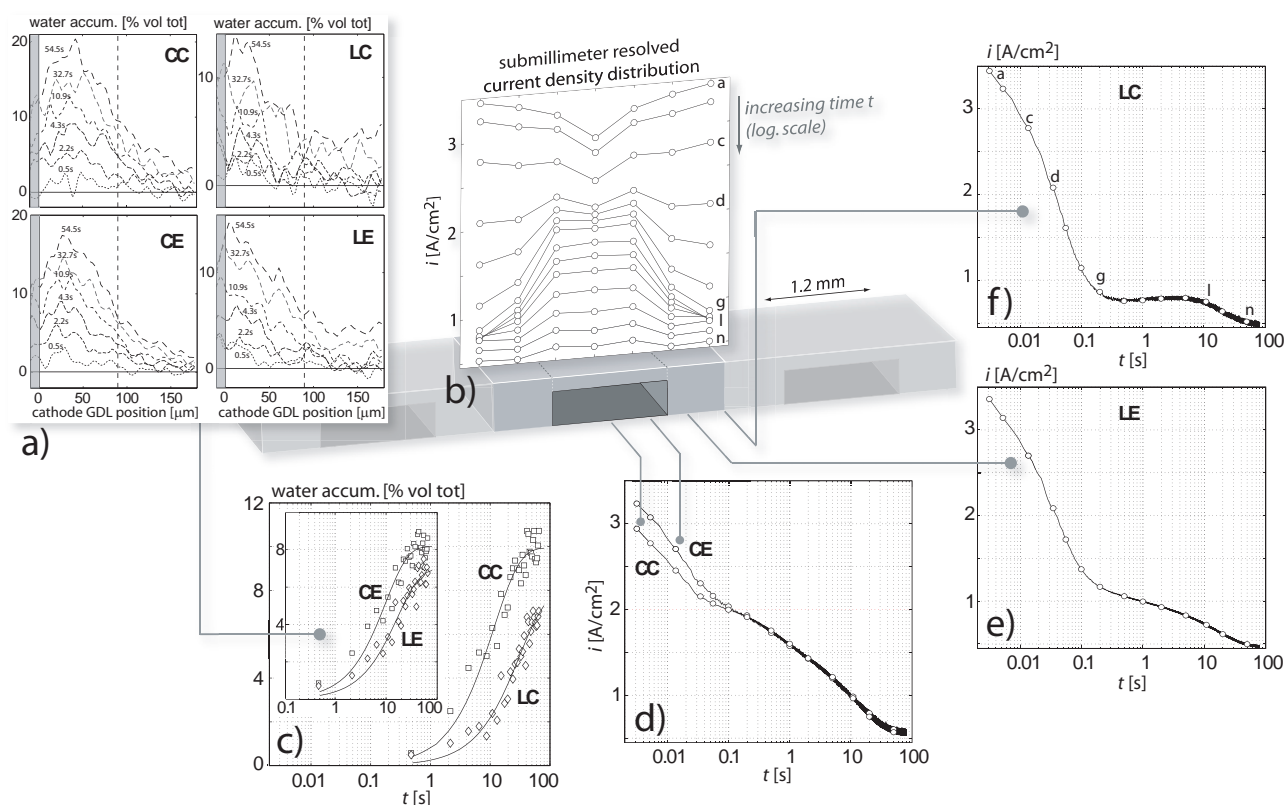


Figure 2. Liquid water accumulation (a, c) and current density distribution (b, d-f) in channel and land areas after a potential step.

Local transients of the liquid water accumulation and current density are shown in Figure 1b (i - iii). Liquid water accumulates within the cathode GDL within some 10's of seconds, after cell perturbation. The weaker increase of the total water content in the land center cannot solely be explained by the lower current density. A higher compression and a lower permeability of the GDL under the ribs might favor water permeation through the membrane. However, the average saturation change approaches comparable values of around 13% in channel (CC) and land (LC, LE) areas after a time frame of 60s. The same time constant is observed in the local current transients. The associated performance loss is most strongly pronounced in the channel area. In the land area, the local current already drops to low values, before a notable liquid water accumulation. This phenomenon is illustrated in more detail in Figure 2.

The characteristics of the current transients (Figure 2b, 2d-f) are governed by the ohmic resistance, double-layer charging, oxygen diffusion and liquid water accumulation. Upon cell perturbation the local cell current is limited initially by the local ohmic resistance. Under the conditions used here, the resistance distribution will depend mainly on electronic GDL properties. Therefore, the current density distribution passes a maximum under the ribs for the first 5-10ms after the step (Figure 2b (a-c)). The current decay within this time frame must be attributed to double layer charging and to a decreasing oxygen concentration at the electrode. The oxygen concentration profiles develop initially within both channel and land areas primarily in *through plane* direction. However, with the onset of the development of the oxygen concentration profile in *in plane* direction, the current density starts to drop severely under the ribs, as a result of oxygen depletion. This effect is most pronounced in the rib center (Figure 2b (c-g), 2f (c-g)).

It occurs within the first 100-200ms after the step, already before notable liquid water accumulation in the GDL (Figure 2a, 2c) and leads temporary to a pronounced maximum in current density in the channel area (Figure 2b (g)). The hypothesis of an ongoing performance loss of the air electrode provides a basis to explain the characteristics of the local current transients during the flooding period ($t > 200$ ms): Any effect of water accumulation on electrode performance becomes most strongly pronounced in the channel area, whereas it is irrelevant in the land area as long as the already low limiting current density (Figure 2f (g-l)) can be sustained by the electrode. The strong performance loss of the cell on liquid water accumulation is primarily related to the specific experimental conditions used here ($T_{\text{cell}} = 40$ °C, non PTFE treated GDL). Under practical conditions ($T_{\text{cell}} = 70$ °C) a strong maximum in the channel region was still observed at steady state.

A missing clear correlation between the integral cell performance and the liquid water content under the ribs is not an unexpected finding. At an already small contribution of the ribs to the total current at higher cell polarization, the effect of liquid water accumulation in the GDL on total mass transport related losses is expected to be small. The performance of the ribs is therefore governed more likely primarily by the cell design e.g. by the flow field structure or the clamping pressure rather than just by the amount of liquid water.

References

- [1] A. Weber, J. Newmann, LBNL Paper 316E (2008).
- [2] P. Boillat, G. Frei, E.H. Lehmann, G.G. Scherer, A. Wokaun, *Electrochem. Solid State Lett.* **13**, B25 (2010).
- [3] I.A. Schneider, S. von Dahlen, A. Wokaun, G.G. Scherer, *J. Electrochem. Soc.* **157**, B338 (2010).

In-plane current transients in channel and lands areas of a polymer electrolyte fuel cell during start-up

I.A. Schneider, S. von Dahlen, A. Wokaun, G.G. Scherer

phone: +41 56 310 2795, e-mail: ingo.schneider@psi.ch

Durability is one of the most important issues, which must be considered in the design and during the operation of polymer electrolyte fuel cells (PEFCs). Mechanically and chemically induced membrane degradation, dissolution and migration of platinum catalyst particles and corrosion of the carbon support in the catalyst layer have been identified as major critical issues. Corrosion due to inhomogeneous anode gas composition is a well known source of degradation in phosphoric acid fuel cells [1]. More recently, similar corrosion processes have been identified in PEFCs, as a consequence of localized fuel starvation and during start-up or shut-down processes [2].

During start-up of a fuel cell, the air, which is present in the fuel gas compartment during shut-off, must be replaced by hydrogen. Thereby, the cell voltage E approaches OCV as the potential of the respective fuel electrode changes from air to the H_2 potential (Figure 1).

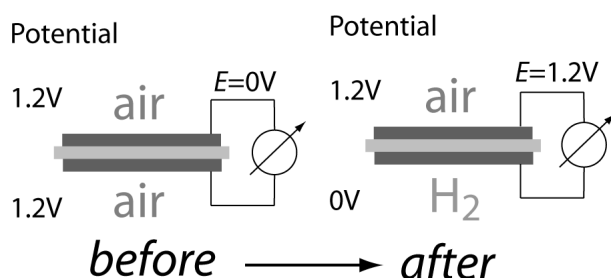


Figure 1. Schematic of the fuel and oxygen electrode potential and the cell voltage E during shut-off and after start-up.

In practical fuel cells the use of flow fields induces mass transport limitations in the *down the channel* direction and in the *perpendicular to the channel* direction. Temporary, these limitations result in an inhomogeneous anode gas distribution over the fuel electrode during start-up of the cell. As a consequence of high in plane ionic resistivity, significant potential gradients can exist over the electrode area. The inhomogeneous anode gas distribution in a PEFC therefore leads to electronic in-plane current transients as hydrogen rich parts of the cell (source) drive a reverse-current through hydrogen starved regions (sink). It has been proposed that the reverse-current phenomenon can occur even within small regions of local hydrogen starvation of a size of fractions of a millimeter [2].

In this work, the reverse-current phenomenon could be monitored for the first time with sub-millimeter resolution on the scale of channel and land areas of PEFC flow field structures. The results are shown in Figure 2 for the start-up procedure. During start-up the transition from air to H_2 potential is delayed under the land. Since the cell voltage E is always equal in channel and land regions, hydrogen rich parts of the cell (channel) drive a reverse current through hydrogen starved regions (land) during the transient. Thereby, the oxygen electrode is exposed temporary to high potentials and prone to carbon corrosion and Pt dissolution. High local current densities

up to values of 200 mA/cm^2 were obtained, although no external cell current was drawn from the cell. Note, however, that a part of the in-plane currents are capacitive charging currents [4]. A similar phenomenon is also observed during shut-down of the cell.

The experimental setup [5] will be used to evaluate the effect of the flow field design on the reverse-current phenomenon. Local cyclic voltammetry allows the *in situ* investigation on the impact on catalyst degradation in channel and land areas [5].

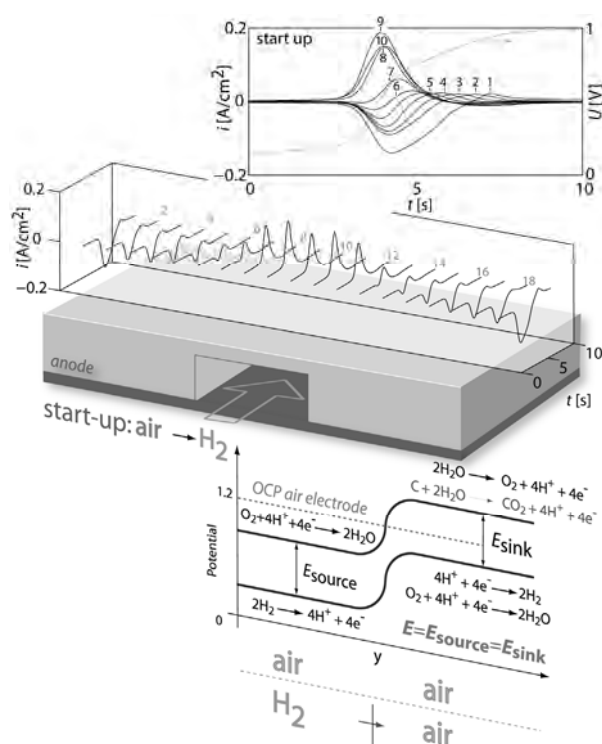


Figure 2. Experimentally measured in-plane current transients during start-up and sketch of electrochemical potentials [3].

References

- [1] M. Farooque, A. Kush, L. Christner, J. Electrochem. Soc., **137**, 2025 (1990).
- [2] C.A. Reiser, L. Bregoli, T.W. Patterson, J.S. Yi, J.D. Yang, M.L. Perry, T.D. Jarvi, Electrochem. Solid State Lett. **8**, A273 (2005).
- [3] M.V. Lauritzen, P. He, A.P. Young, S. Knights, V. Colbow, P. Beattie J. New. Mat Electrochem. Sys. **10**, 143 (2007).
- [4] B. Wetton, R. Bradean, K. Eggen, Proc. 20th International Symposium on Transport Phenomena, Victoria BC, July 7-10 (2009).
- [5] I.A. Schneider, S. von Dahlen, A. Wokaun, G.G. Scherer, J. Electrochem. Soc., **3**, B338 (2010).

Dynamic measurement and modeling of the water vapor concentration during ac impedance measurements in PEFCs

M.H. Bayer, A. Wokaun, G.G. Scherer, I.A. Schneider

phone: +41 56 310 5304, e-mail: michael.bayer@psi.ch

Electrochemical impedance spectroscopy (EIS) is a widely used method for the characterization of polymer electrolyte fuel cells (PEFCs). Our recent work has focused on the effect of *down the channel* inhomogeneities on PEFC impedance response [1]. In this context, we have shown that the process of water formation and its accumulation along the flow fields governs the impedance response of PEFCs under sub-saturated conditions. As a consequence of ac current, water partial pressure oscillations build up along the flow fields [2]. The slow hydration and dehydration of the membrane with ac current, as a consequence of changing water production rate, results in the appearance of low frequency inductive loops [1-3].

Based on these key experimental results, we have developed a 1+1 dimensional impedance model for sub-saturated PEFCs [4]. A detailed validation of the model requires the dynamic measurement of the water partial pressure in the flow channels. Tunable diode laser absorption spectroscopy (TDLAS) has been used to study the water partial pressure in PEFCs under steady state and dynamic conditions [5]. This method is used here for the *in situ* measurement of the frequency response of the water vapor concentration $Z_c(\omega) = \delta c(\omega) / \delta \eta(\omega)$ along the anode and cathode flow field during ac impedance measurements.

Experimental

The implementation of the TDLAS measurement into our linear cell ($A_{\text{cell}} = 63 \text{ cm}^2$) [1] requires a special flow field design, as shown in Figure 1.

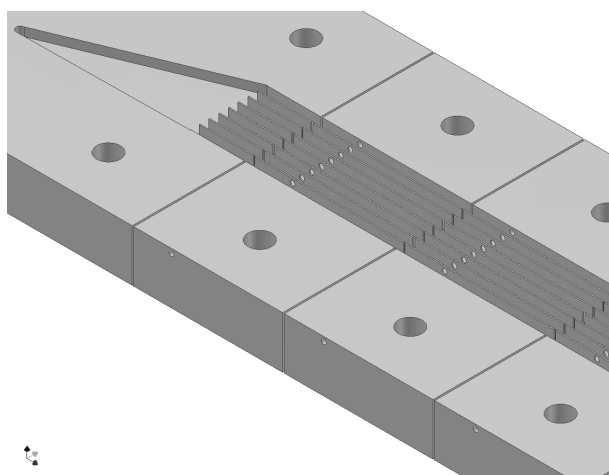


Figure 1. Segmented flow field plate for TDLAS measurements.

The ninefold segmented flow fields consist of eight 2mm deep and 2mm wide channels. The channels are separated by 0.25mm wide lands. In each of the nine segments holes were drilled through the flow field perpendicular to the flow channels (Figure 1). Micro collimators emit the laser beam right at the outer channel wall of one side of the flow field. The laser light then passes through eight 2mm wide channels and seven 0.25mm deep holes. This results in a total absorption path length of 17.75mm before the light

enters into small class rods on the opposite side of the flow field. The rods seal the outer channel wall and pass the light toward an InGaAs detector.

Please note that in the holes the gas equilibrates by diffusion. Therefore, it is important to have narrow lands. By implementing only 0.25mm wide lands, the characteristic frequency for water diffusion into the holes under the lands is in the order of 350Hz and does not introduce a noteworthy attenuation at relevant modulation frequencies below 1Hz.

A distributed feedback (DFB) laser diode (32mW) was used in the measurement. The laser diode (central wavelength of 1392.5nm (7181.3 cm^{-1})) is connected to a laser diode control unit. During ac impedance measurements in the linear PEFC, the transmitted light intensity at $\nu = 7181.2 \text{ cm}^{-1}$ was measured as a function of time. The photo current of the detector is converted into voltage by a resistor ($R_{\text{det}} = 100 \Omega$).

For the determination of the frequency response $Z_c(\omega) = \delta c(\omega) / \delta \eta(\omega)$, the detector voltage and the cell voltage were digitized simultaneously via 16Bit A/D converters (100 samples per second). The digital signals are passed through a digital 4Hz low pass filter and are corrected for their dc value. After multiplication of the ac data with a Van Hann window function and zero padding, the time domain data is transformed into frequency domain via a fast Fourier transform algorithm. The modulus and the phase of $Z_c(\omega)$ is then determined from the spectra for a given modulation frequency. Calibration was done by measuring the detector signal at different humidity levels.

The linear cell was operated on dry oxygen (330ml/min) and humidified hydrogen (990ml/min, r.h. 23%). The gases were supplied in co-flow mode to the linear cell through heated hoses ($T_{\text{H}_2/\text{O}_2} = 80^\circ \text{C}$). The MEA consisted of a catalyst coated membrane (CCM) (Nafion 112, 0.5 mg Pt/cm^2 , 70wt% Pt/C, PAXITECH) and ETEK W140 gas diffusion layers.

Results & Discussion

Calculated results, as obtained from the pseudo 2D model as described in [4], are shown in Figure 2. The modeled data is consistent with the experimental results obtained earlier [2]. The membrane resistance decreases from the gas inlets towards the gas outlets (Figure 2b), as a direct consequence of water formation and accumulation along the flow field and, hence, an improved hydration of the ionomer by product water. The local current density increases in the same direction (Figure 2a). The low frequency inductive loop, which becomes apparent in the calculated spectra (Figure 2c,d) is basically the result of changing membrane hydration with ac current at lower frequencies, as water concentration oscillations build up along the gas channels [1].

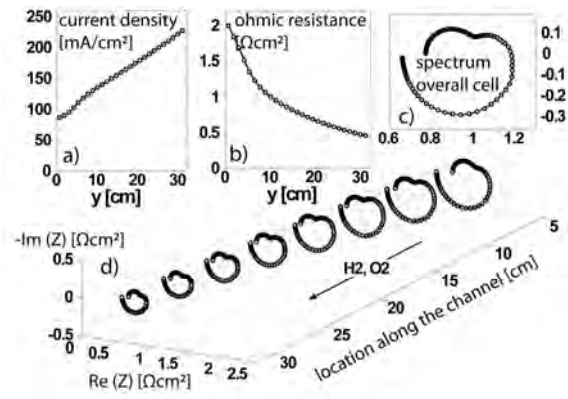


Figure 2. Calculated current density distribution (a), local membrane resistance (b), integral spectra (c), and locally resolved impedance spectra (d) ($i_{cell}=10A$, $1kHz \geq f_{mod} \geq 1mHz$, 20pts/dec).

A sinusoidal perturbation signal is applied during ac impedance measurements. The ac current affects the local water concentration at lower frequencies, due to a changing water formation rate and changing electro osmotic drag (EOD) of water [1,4]. The water concentration oscillations only slowly penetrate into the bulk of the membrane, as a result of poor water diffusion and high water uptake capacity of the polymer electrolyte. Consequently, the characteristic response of the water vapor concentration on ac voltage $Z_c(\omega)$ appears at low frequency. A detailed analysis of the calculated ac water profiles, which cause the low frequency characteristic, as shown in Figure 2c,2d, has been published earlier [4]. In this work, a comparison between experimental and calculated data is given. Figure 3 shows the modulus of the ac signal, as measured at the cathode outlet, for four different modulation frequencies [4]. A distinct peak is observed at the respective modulation frequency, with only minor side peaks. The observation of this signal is a direct proof that the ac current causes an oscillation of the water partial pressure at the respective modulation frequency in the gas channels.

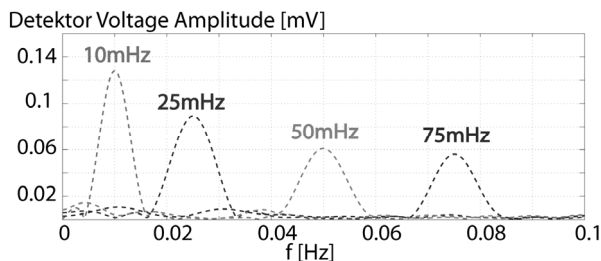


Figure 3. Modulus of the signal at the photodiode after the laser passed the cell through cathode outlet, for four distinct modulation frequencies (ac current amplitude $\sim 15mA/cm^2$).

The detector signal is utilized for the calculation of the concentration oscillation $\delta c(\omega)$ by using calibration data. $Z_c(\omega)$ is obtained by division of $\delta c(\omega)$ with the ac voltage $\delta \eta(\omega)$ at a given frequency. Thereby, the characteristic response of the water partial pressure $Z_c(\omega)$ on ac voltage was obtained for frequencies below 1Hz. Modulus and phase of experimental and modeling results are compared in Figure 4. The phase (upper graph in Figure 4) shows excellent agreement for the three positions near the anode outlet and the cathode inlet and outlet. The water concentration oscillation in the cathode channel is in principle in phase to the ac voltage, since the water production rate is in phase to the ac current. In the anode outlet the oscillation changes from 'out of phase' toward 'in phase' between

100mHz and 10mHz as back diffusion starts to compensate drying, due to electro osmotic drag. The calculated frequency response of the modulus (lower graph in Figure 4) is similar to the experimental result, at first sight. However, note that the measured modulus of the water concentration oscillation is about half as high as the modeled data. This phenomenon is currently subject to investigation. It is observed that the modulus of the oscillation is higher at the cathode outlet as compared to the cathode inlet, as a result of water accumulation along the flow field.

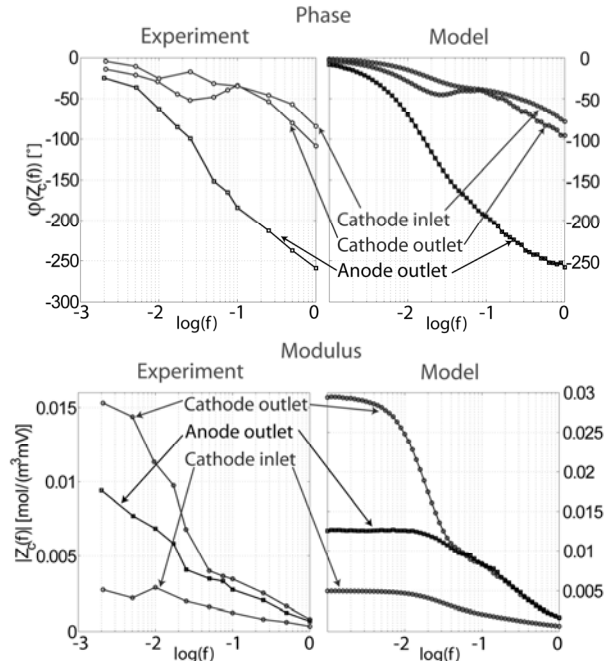


Figure 4. Calculated (left) and measured (right) phase (upper) and modulus (lower) of $Z_c(\omega)$ for 3 distinct positions along the channel.

Conclusions and Outlook

By using TDLAS, the characteristic frequency response of the water partial pressure has successfully been measured in the gas channels of a low humidity PEFC during EIS. The experimental results are in good agreement with modeled data [4]. As a next step, the water partial pressure will be measured at more positions along the channel. In combination with locally resolved impedance spectroscopy and neutron radiography, the dynamic water partial pressure measurement offers an excellent validation tool for PEFC transient and ac impedance models [4].

References

- [1] I.A. Schneider, G.G. Scherer, 'Local Transient Techniques' in PEFC Diagnostics', Handbook of Fuel Cells, Vol. 6, W. Vielstich, H.A. Gasteiger, H. Yokokawa, Editors, John Wiley & Sons, Chichester, UK, 673 (2009).
- [2] I.A. Schneider, M.H. Bayer, P. Boillat, G.G. Scherer, ECS Transactions, **11**, 461 (2007).
- [3] I.A. Schneider, M.H. Bayer, A. Wokaun, G.G. Scherer, J. Electrochem. Soc., **155**, B783 (2008).
- [4] M.H. Bayer, A. Wokaun, G.G. Scherer, I.A. Schneider, ECS Transactions, **25**, 949 (2009).
- [5] S. Basu, M.W. Renfro, B.M. Cetegen, J. Power Sources, **162**, 286 (2006).

Application of the Kramers Kronig relations on locally resolved impedance spectra of PEFCs

M.H. Bayer, A. Wokaun, G.G. Scherer, I.A. Schneider

phone: +41 56 310 5304, e-mail: michael.bayer@psi.ch

Localized electrochemical impedance spectroscopy (LEIS) is widely used in electrochemistry. Here, the applied perturbation signal results in a modulation of the cell voltage $\Delta\eta(\omega)$ over the entire electrode area, due to the highly conductive end-plates. The local ac current density response $\Delta j(x,\omega)$ is measured directly. Per definition, the local cell impedance is the ratio $Z_{loc}(x,\omega)=\Delta\eta(\omega)/\Delta j(x,\omega)$.

Our earlier work has shown, however, that the local ac current density is the response to both the ac cell voltage and the ac concentration oscillations due to the ac current in upstream parts of the cell, when this technique is applied to a PEFC in flow configuration [1,2]. Consequently, $Z_{loc}(x,\omega)$ is not a strictly local quantity, but depends on the overall cell perturbation.

The Kramers Kronig (KK) relations are a widely used tool to check if experimentally obtained frequency responses are causal and stable linear response functions. These functions have a correlation between the imaginary and real parts of their Fourier transform, known as the KK relations. In this work, the application of the KK relations on local spectra is investigated.

Based on key experimental results [1,2], we introduce a one-dimensional, analytic, 'down the channel' model for the calculation of the local cell impedance spectra. The oxygen concentration profile and the current distribution are calculated through the equation system (1).

$$j(x) = j_0 \cdot \frac{c(x)}{c_{atm}} \cdot \exp\left(\frac{\eta}{b}\right) \quad (1)$$

$$\frac{dc}{dx} = -\frac{j(x)}{4 \cdot F \cdot t_c} - v \frac{dc}{dx}$$

In the model, the flow velocity v is assumed constant along the flow field, even though it changes in a real cell, due to the electrochemical reactions. In the steady state calculation, the time derivatives are set to zero. Inlet conditions are defined through the given inlet concentration $c(x=0)=c_0$. Using these constraints the steady state solution for the current is given by (2).

$$j(\xi) = j_{mean} \cdot \lambda \cdot \exp(-k \cdot \xi) \cdot k \quad (2)$$

$$k = -\ln\left(1 - \frac{1}{\lambda}\right), \quad \xi = \frac{x}{l}$$

In equation (2) l represents the channel length, λ the stoichiometry, and j_{mean} the mean current density. They are connected to the velocity by equations (3,4).

$$v = \frac{\lambda \cdot j_{mean} \cdot l}{4 \cdot F \cdot t_c \cdot c_0} \quad (3)$$

$$j_{mean} = \int_0^1 j(\xi) d\xi \quad (4)$$

Consequently, the slope of the local i/e curves yields

$$\frac{dj(\xi)}{d\eta} = \frac{j_{mean}}{b} \cdot \lambda \cdot \exp(-k \cdot \xi) \cdot k \cdot (1 - \xi \cdot k) \quad (5)$$

In (5), the slope of the local i/e curve changes sign, as seen in the experiments [1,2], at $\xi_t = 1/k$. Downstream from this point, the current density decreases with increasing overpotential, due to the oxygen consumption along the channel [1,2]. Obviously, the steady state distribution is a function of λ only. For the impedance response, this changes as the set of equations can no longer be formulated as a function of λ only. The local immittance is given by equation (6), with $\omega_c = 2v/l$.

$$Z_{loc}(\xi, \omega) = \frac{1}{Y_{loc}(\xi, \omega)} = \left(\frac{j(\xi)}{b} \cdot \left(1 - \frac{k \cdot \omega_c}{\omega} \cdot \sin\left(\frac{\omega \cdot \xi}{\omega_c}\right) \cdot \exp\left(-i \frac{\omega \cdot \xi}{\omega_c}\right) \right) \right)^{-1} \quad (6)$$

In (6) we make use of the fact that a time derivative in (1) is expressed as a multiplication of the Fourier transformed function with $i\omega$. The function $Z_{loc}(\xi, \omega)$ is plotted in Figure 1 for distinct positions along the channel.

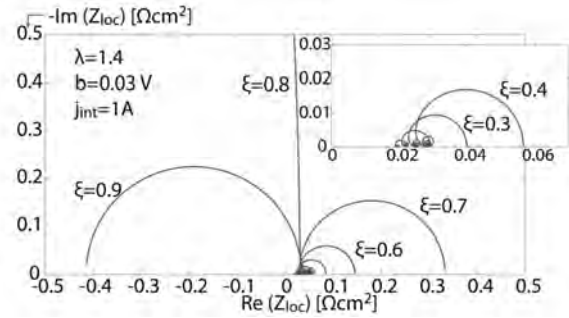


Figure 1. Local cell impedance $Z_{loc}(\xi, \omega)$ for $\lambda=1.4$ ($\omega_c=10.4s^{-1}$)

As shown in the experimental results [1,2], in the inlet region a small capacitive loop is seen, which increases in size along the channel. Finally, in the outlet region, the impedance response shows a negative low frequency intersection, as expected from the local polarization curves for $\xi > \xi_t \approx 0.8$. The local cell impedance spectra are checked for KK consistency. For the calculation of the imaginary part out of the real part, equation (7) is used.

$$\text{Im}[Z_{loc}(\xi, \omega_0)] = \frac{2\omega_0}{\pi} \int_0^{\infty} \frac{\text{Re}[Z_{loc}(\xi, \omega)]}{\omega^2 - \omega_0^2} d\omega \quad (7)$$

The data investigated is linear, stable and stationary, as the set of equations (1) is linearized in order to get the local cell immittance (6), and the model does not assume explicit time dependence of the system. Only causality is not *a priori* given, due to the oxygen concentration oscillations, which build up in the gas channel [1,2]. To illustrate this, the directly calculated imaginary part of $Z_{loc}(\xi, \omega)$ is plotted in Figure 2 and compared to the numerically calculated one using equation (7) for three distinct positions along the channel. For the two spectra, where the real part is

positive, the curves agree perfectly, however, for the one with negative real parts (at $\xi=0.9$), they do not match.

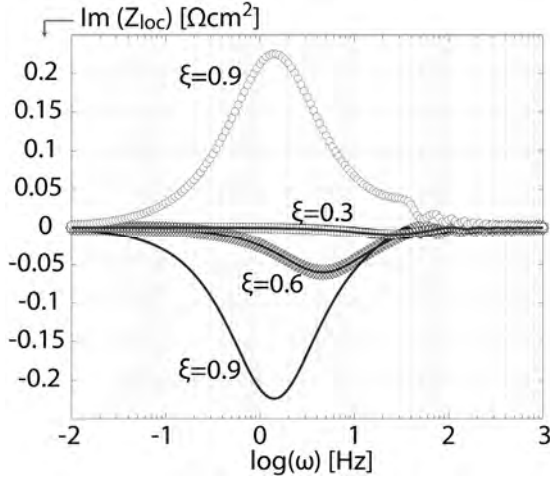


Figure 2. Modeled imaginary part using equation (6) (lines) and imaginary part calculated with the KK relations (symbols) for three distinct positions along the flow field.

The use of an analytical model allows an exact investigation of the causality of the complex response functions. In the frequency domain, a response function is non-causal, if it exhibits poles at complex frequencies with negative imaginary parts. It can be shown that $Z_{loc}(\xi, \omega)$ has poles with negative imaginary parts, if $\xi > \xi_i$. However, $Y_{loc}(\xi, \omega)$ is a holomorphic function, i.e. it has no poles. This results in KK consistency of the local cell admittance for all positions along the channel. Obviously, $Z_{loc}(\xi, \omega)$ fails the KK check, as soon as negative low frequency intersections are present. It has been demonstrated before that in electrochemical systems, which exhibit passivation, the admittance is KK consistent, while the impedance fails the KK check in the presence of negative low frequency intersections [3]. A similar behavior is seen here, but in the present case negative low frequency intersections in the local spectra are not caused by electrode passivation, but by oxygen depletion along the gas channel.

The local cell admittance is defined as the ratio of the local current density and the ac voltage. As stated before, the local ac current is, however, not only caused by the ac cell polarization but also by the ac oxygen concentration oscillation in the gas channel, due to the ac current in upstream parts of the cell. Therefore, it is interesting to investigate, why $Y_{loc}(\xi, \omega)$ is, nevertheless, a causal response function for all positions ξ .

A *gedankenexperiment* is used to analyze the local cell admittance. The cell is divided into two segments, similar to the experiments, which have been performed, using an electrically disconnected outlet segment [2]. The segment currents are linked to the voltages by four admittance functions Y_{nm} , which are all causal response functions to the corresponding perturbation, only. The ac current response can be calculated, using equation (8).

$$\begin{pmatrix} j_1 \\ j_2 \end{pmatrix} = \begin{pmatrix} Y_{11} & Y_{12} \\ Y_{21} & Y_{22} \end{pmatrix} \cdot \begin{pmatrix} \eta_1 \\ \eta_2 \end{pmatrix} \quad (8)$$

In (8) it becomes obvious that in general the causality criterion is not necessarily fulfilled for local cell spectra, as through the coupling term Y_{21} one can get finite j_2 even though η_2 is zero. Thereby Y_{21} represents the current in segment 2 caused by the concentration oscillation, due to the ac voltage in segment 1. Since a

'down the channel' model is used, Y_{12} is zero. The local cell admittances are per definition given by (9).

$$Y_1 = \frac{j_1}{\eta_1}, \quad Y_2 = \frac{j_2}{\eta_2} \quad (9)$$

The combination of (8) and (9) yields a result for the local cell admittances expressed through the causal response functions Y_{nm} , shown in equation (10).

$$Y_1 = Y_{11}, \quad Y_2 = Y_{21} \frac{\eta_1}{\eta_2} + Y_{22} \quad (10)$$

The result (10) shows that Y_1 is causal, since it is identical to Y_{11} . Y_2 , however, is a linear combination of two functions. The second term Y_{22} is a causal response function, while the first term fulfills the causality condition only if η_1/η_2 is causal. This condition is trivially fulfilled for a single real PEFC, as $\eta_1 = \eta_2$, due to the equipotential condition at the end-plates. Consequently, Y_2 consists of a linear combination of causal, linear response functions and, hence, is a causal, linear response function itself.

A similar result can be formulated for the local cell impedance, with causal response functions Z_{nm} shown in equation (11).

$$Z_1 = Z_{11}, \quad Z_2 = Z_{21} \frac{j_1}{j_2} + Z_{22} \quad (11)$$

In contrast to the admittance, in (11) the ratio j_1/j_2 is, however, not a constant but a frequency dependent function, as the current distribution changes with frequency, due to the oxygen concentration oscillation along the gas channel, which approaches zero at high frequencies and tends towards the steady state gradient of the concentration with respect to cell polarization for low frequencies. Consequently, even for calculated data, KK consistency of Z_2 cannot be assumed a priori.

Conclusion

In this work, the application of the Kramers Kronig relations on localized impedance spectra of air fed PEFCs is investigated. The local cell impedances and local admittances, as calculated using a simple, one-dimensional, analytic, 'down the channel' model, are checked for KK consistency. It is shown that due to the build-up of oxygen concentration oscillations along the gas channel, a KK check can fail for the local cell impedance. In admittance representation, however, the KK check is always successful for the modelled data. It is demonstrated that this phenomenon can be attributed to the equipotential condition. Consequently, the presence of oxygen concentration oscillation in the gas channel, caused by the applied perturbation, still leaves a causal, local system, as long as the voltage is homogeneously distributed, as given for single PEFCs. Therefore, the KK relations are an adequate tool to check the local cell response for errors, if they are applied on the local cell admittance.

References

- [1] I.A. Schneider, S.A. Freunberger, D. Kramer, A. Wokaun, G.G. Scherer, J. Electrochem. Soc., **154**, B383 (2007).
- [2] I.A. Schneider, D. Kramer, A. Wokaun, G.G. Scherer, J. Electrochem. Soc., **154**, B770 (2007).
- [3] A. Sadkowsky, J.-P. Diard, C. Montella, J. Electrochem. Soc., **156**, F7 (2009).

Investigations of local hysteresis effects in a PEFC

S. von Dahlen, F. Barchetti, P. Boillat, A. Kästner, P. Oberholzer, G.G. Scherer, A. Wokaun, I.A. Schneider

phone: +41 56 310 2541, e-mail: steffen.vondahlen@psi.ch

Water management is a major topic in the development of polymer electrolyte fuel cells (PEFCs). On the one hand, high water content entails high conductivity of the employed polymer electrolyte membrane; on the other hand, flooding of the gas diffusion layer (GDL) hampers the reactant mass transport.

The application of flow fields for the distribution of the reactant gases generates strong inhomogeneities over the active area in both, the *along the channel* and the *perpendicular to the channel* direction [1]. By applying a novel fuel cell approach with a 19-fold segmented microstructured flow field at the anode, local current density measurements on channel and rib scale can be correlated with the water content obtained from neutron imaging. The novel approach with a high spatial resolution of 400 μm is described in detail elsewhere [2]. The cell was operated on H_2/air (both fully humidified) in a voltage range between OCV and 0.05 V, with a sweep rate of 10 mV/s. Neutron images were taken with a spatial resolution of 20 μm and a time resolution of 10 s. The investigated cathode flow field consisted of three gas channels, with 1.2 mm channel and 1.2 mm rib width (Figure 1). For interpretation, the 19 segments of the microstructured flow field on the anode side were averaged to three characteristic areas in the flow field structure: channel, rib edge and rib center.

The current densities in these three characteristic areas are virtually equal down to a voltage of 0.6 V (Figure 1). In the rib center areas, a limiting current density is reached in the lower voltage range. No noticeable hysteresis can be observed in this polarization curve. In the channel areas, at lower voltages current density is significantly higher than in the rib areas. Despite a rising polarization, current density declines after a maximum is passed. Moreover, the lower current densities during the return sweep generate a hysteresis loop and indicate changes in cell performance, possibly due to changes in water content.

The three curves in Figure 2 represent the water content in the GDL. The interplay of water accumulation and removal during the sweep generates strong hysteresis loops. Comparing the characteristic areas, in the rib

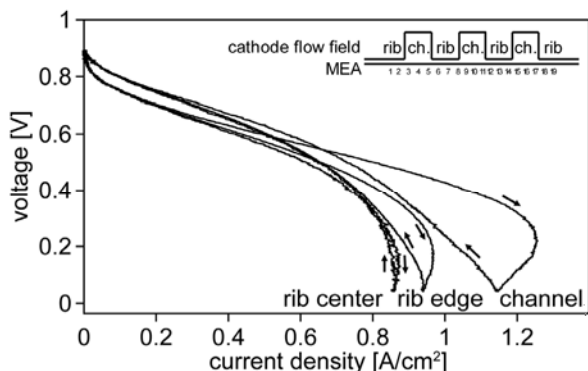


Figure 1. Local polarization curves measured in a differential fuel cell with a segmented microstructured flow field.

areas the hysteresis is most pronounced, but maximum water content is lowest, ascribed to the reduced water generation based on lower current densities. However, a surprising observation is the considerable change in water content from 8% to 15% in the lower voltage region, although the current density remains virtually constant. During a portion of the return sweep, water content is invariant in the rib areas, probably due to hampered water removal. In the rib areas, current density is limited by oxygen mass transport, whereas the reactant depletion induced by increasing diffusion path length is supposed to outweigh flooding effects.

In the channel areas, smaller diffusion path length and higher porosity as a result of lower GDL compression enable improved reactant mass transport. However, the higher current densities entail an enhanced generation of product water. Liquid water accumulates in the pores of the GDL, which can cause reactant mass transport limitations, due to flooding. The sluggish accumulation of water is a possible explanation for the existence of the current density hysteresis loop in the channel areas. Recently, Gerteisen et al. published results of an investigation showing a similar behavior in a non-segmented cell [3].

Various local hysteresis effects in current density and water content have been presented. The current density hysteresis in the channel areas is ascribed to flooding of the GDL pores. In the rib areas, the strong water content hysteresis is caused by the hampered water removal. Local differences existing in water content and current density emphasize the need of taking into account channel and rib scale to unravel local performance losses based on water management in PEFCs.

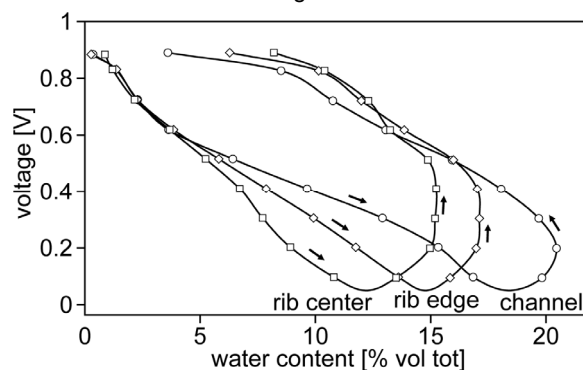


Figure 2. Local water content curves measured in a differential fuel cell with a segmented microstructured flow field. Markers denote midpoints of the images.

References

- [1] I.A. Schneider, G.G. Scherer in Handbook of Fuel Cells, Vol. 6, W. Vielstich, H.A. Gasteiger, H. Yokokawa, Editors, John Wiley & Sons, Chichester (2009).
- [2] I. A. Schneider, S. von Dahlen, A. Wokaun, G.G. Scherer, J. Electrochem. Soc. **157**, 338-341 (2010).
- [3] D. Gerteisen, T. Heilmann, C. Ziegler, J. Power Sources **187**, 165-181 (2009).

Locally resolved cyclic voltammetry in channel and land areas of a PEFC

S. von Dahlen, A. Wokaun, G.G. Scherer, I.A. Schneider

phone: +41 56 310 2541, e-mail: steffen.vondahlen@psi.ch

Polymer electrolyte fuel cells (PEFCs) are efficient electrochemical power sources. The catalyst coated membrane (CCM) is the most important part of a PEFC. The CCM consists of a thin proton conducting polymer electrolyte membrane. Carbon supported Platinum particles (Pt/C) are used to catalyze the electrochemical reactions. In practical fuel cells, the reactant gases are distributed over the active area by using flow field plates. PEFC flow fields exhibit a channel land structure. It is well known that the use of flow fields leads to local inhomogeneities over the active area [1].

The ECA (electrochemically active surface area) of the platinum catalyst is an important parameter for the characterization of PEFCs. The ECA can be determined *in situ* by using cyclic voltammetry (CV) in H_2/N_2 mode [2,3]. Therefore, an inert gas flow is employed at the working electrode to avoid traces of oxygen. The CVs exhibit hydrogen underpotential deposition (H_{upd}) peaks. These peaks appear in a potential range between 0.3 and 0.05 V vs. the hydrogen counter/reference electrode. The area under the peaks is directly proportional to the ECA [2]. Unfortunately, at low potentials cathodic currents due to the formation of molecular hydrogen overlap with the H_{upd} region and hamper an accurate determination of the ECA.

In this context, in particular, the convective inert gas flow at the working electrode has a detrimental effect as shown for integral CVs in the inset of Figure 1. Our earlier work has clearly demonstrated that the inert gas flow induces strong hydrogen evolution currents in both the cathodic and the anodic sweep as molecular hydrogen is removed by the inert gas flow and must be compensated by the formation of additional hydrogen [5]. In the *along the channel* direction this effect is most pronounced at the nitrogen inlet. The hydrogen evolution currents level off down the channel as a result of formation and accumulation of molecular hydrogen [1,5]. A similar effect could be demonstrated recently in the *perpendicular to the channel* direction [4]. A novel cell design allows for the first time locally resolved CV measurements in channel and land areas of PEFCs with sub-millimeter resolution [4]. Figure 1 displays local CVs as obtained in channel and land areas of a single 2mm channel flow field. Under the channel (segments 8-12) the hydrogen evolution currents show highest values and exhibit a nearly congruent shape. The strong cathodic currents of more than 100 mA/cm² lead to a severe error in the estimation of the local ECA in the channel region. In the land areas, however, the cathodic currents decrease strongly in the *perpendicular to the channel* direction. This is a result of the increasing diffusion path length for molecular hydrogen. Note that this effect occurs within a distance of some hundred micrometers from the channel.

Possible mitigation strategies should focus on the porosity of the GDL. High liquid water content or compression would be beneficial in this context [4]. However, the most effective solution to alleviate this detrimental effect is simply to stop the convective inert gas flow during the CV measurement.

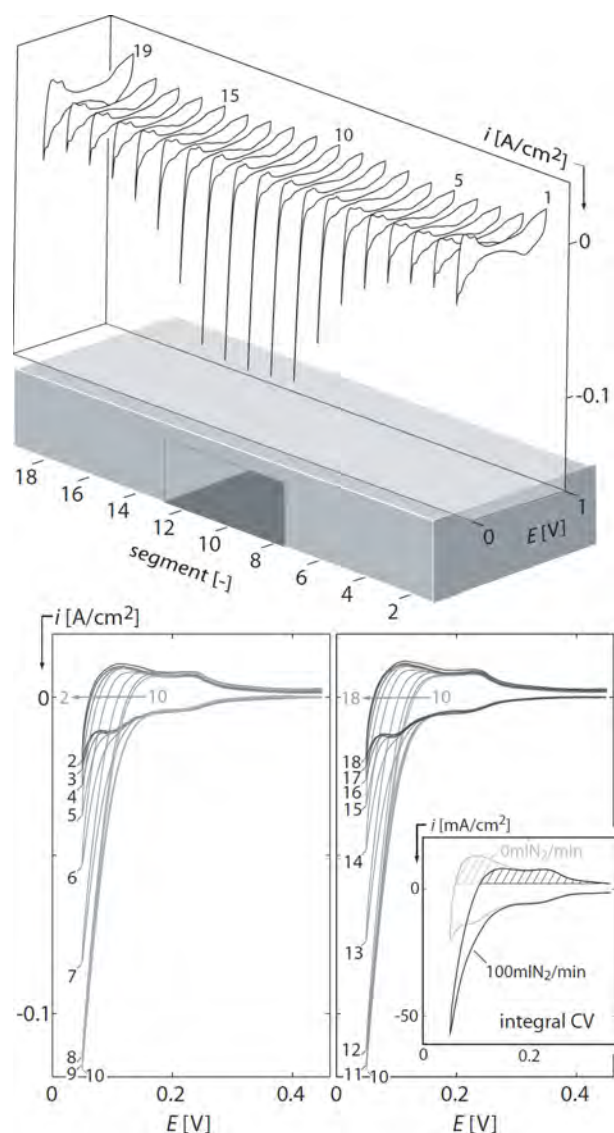


Figure 1. Effect of the convective inert gas flow: Integral CVs (inset) and local CVs as obtained in channel and land areas of a single 2mm channel flow field [4] (number indicates the segment). The local CVs were obtained at a N_2 flow rate of $V_{N_2}=100\text{ml/min}$ ($V_{H_2}=100\text{ ml/min}$, $v=10\text{mV/sec}$, fully humidified gases, $T=70^\circ\text{C}$).

References

- [1] I.A. Schneider, G.G. Scherer in Handbook of Fuel Cells, Vol. 6, W. Vielstich, H.A. Gasteiger, H. Yokokawa, Editors, John Wiley & Sons, Chichester (2009).
- [2] J. Bett, K. Kinoshita, K. Routsis, P. Stonehart, J. Catal. **29**, 160-168 (1973).
- [3] S.S. Kocha in Handbook of Fuel Cells, Vol. 3, W. Vielstich, H.A. Gasteiger, A. Lamm, Editors, John Wiley & Sons, Hoboken, NJ (2003).
- [4] I.A. Schneider, S. von Dahlen, A. Wokaun, G.G. Scherer, J. Electrochem. Soc. **157**, 338-341 (2010).
- [5] I.A. Schneider, D. Kramer, A. Wokaun, G.G. Scherer, Electrochem. Comm. **9**, 1607-1612 (2007).

Detectability of membrane defects by local online gas analysis

G. Schuler, A. Wokaun, F.N. Büchi

phone: +41 56 310 2411, e-mail: felix.buechi@psi.ch

Degradation of polymer electrolyte fuel cell membranes under real world operating conditions is still an issue. Up to now, investigation of the membrane degradation is mainly monitored by electrochemically measured integral hydrogen permeation [1]. In comparison to this standard method, online permeation measurement by local gas analysis has the advantage of locally resolved permeation measurement without the switch to pure nitrogen operating conditions on the cathode side. Local permeation investigations support general membrane degradation characterization by more detailed interpretation of changes in local membrane structure. As local permeation measurement by gas analysis is restricted to discrete positions along the representative sample channel [2], detectability of local defects within the active area is unclear. In order to evaluate detectability and permeation rate of local pores, membranes with defined pore positions and pore size were analyzed and characterized under various conditions.

Experimental

Local membrane permeation was measured with the hardware described in [2]. This includes a linear fuel cell of technical size with an active area of 200cm^2 , anode and cathode side flow fields with 28 parallel channels with cross section dimensions of $0.5 \times 0.8\text{mm}$. Eleven gas extraction ports are positioned in the representative mid channel area of the flow field on anode and cathode side. Two additional integral gas ports sample gas at the integral in- and outlet of the cell (Fig.2A). Gas ports allow for local gas extraction and subsequent species analysis by mass spectrometry. 10% helium is added to the anode side gas supply and acts as membrane permeation tracer gas, which is afterwards locally detected on the cathode side. Different methods and membranes were evaluated for defined pore insertion. This included perforation tests by electron beam lithography and laser processing of nafion N211 membranes ($d=25\mu\text{m}$, DuPont) and Kapton HN100 foils ($d=25\mu\text{m}$, DuPont). Operating conditions of the electron beam lithography were $I=40\text{mA}$, $U=100\text{kV}$, dose= $20\text{mC}/\text{cm}^2$, electron beam diameter $d=50\text{nm}$, pattern frequency $f=9.7\text{MHz}$ and focused pore size of $3\mu\text{m}$. For laser perforation, a 308nm XeCl-excimer laser in conjunction with round pinhole masks for beam shaping and focal lenses for demagnification was used. A sequence of 20 laser pulses with an energy density of $7\text{J}/\text{cm}^2$ was used for membrane perforation with pore size of $40\mu\text{m}$. Two model membranes were perforated. Membrane 1 was perforated with pores in the area of the gas analysis channel and membrane 2 with pores in the neighbouring channel. Both model membranes were perforated with three pores of identical size at the positions indicated in figure 2A. Two pores were chosen 3mm after (pore 1, 2) and one pore 3mm before of a gas extraction port (pore 3) in order to evaluate the influence of pore position in relation to discrete gas analysis locations. Permeation characteristics of these perforated membranes were investigated in two configurations: 1) membrane directly assembled between the flow field plates (membrane only); 2) entire membrane electrode

assembly (MEA configuration). Woven carbon cloth electrodes with micro porous layer (Etek Elat A6STDSIV2.1) were used in the MEA configuration. All measurements were conducted at 80°C cell temperature, open circuit conditions with the virtual load point of $0.2\text{A}/\text{cm}^2$ with anode and cathode stoichiometries of 2, dry gases, 90% hydrogen and 10% helium tracer addition at the anode and inert nitrogen atmosphere at the cathode in order to suppress thermal degradation during the measurements.

Results

Comparison of electron beam lithography and laser perforation showed the difficulty of continuous pore perforation in nafion. Electron beam lithography tests showed, that higher doses are required for continuous pores, which raise the risk of vacuum chamber contamination and deflection of the electron beam due to charging effects. In addition, maximum membrane size in electron beam lithography was limited to approximately 25cm^2 . Due to low absorption characteristics at the given wavelength of the laser light in nafion, Kapton foils with sufficient absorption behaviour [3] were chosen as model material. The switch to Kapton foils was possible without any disadvantage, as the measurement focused pore permeation behaviour under dry conditions with inert gas supply on the cathode side. Figure 1 shows the conical pore shape and size of the laser perforated Kapton foils. The averaged minimum reproducible diameters of continuous pores were $41\mu\text{m}$ on anode- and $68\mu\text{m}$ on cathode side and therefore represent comparably highly degraded membrane conditions.

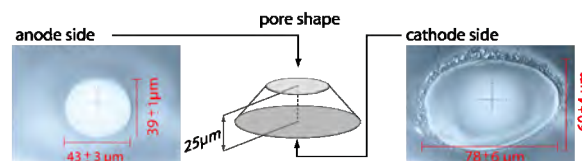


Figure 1. Size and shape of laser perforated model membrane (HN100, $25\mu\text{m}$, DuPont). Perforation: 308nm XeCl-excimer laser, 20 pulses, energy density $7\text{J}/\text{cm}^2$. Anode and cathode side refer to assembly positioning in the fuel cell. Perforation direction from cathode side.

Figure 2B shows the cumulative local permeation in membrane only configuration at different overpressure conditions. Due to the missing flow resistance of the gas diffusion layers, a pore flow with turbulent orifice characteristics [4] and maximum permeate rate of $23\text{ml}/\text{min}$ per pore at anode overpressure of 0.1bar was measured. Under 0.1bar anode side overpressure, the permeation per pore accounted for 47% of the entire flow rate of a single channel, what therefore influences the uniformity of the gas distribution to the parallel channels. This lead to lower nitrogen flow in the sample channel and subsequent overestimated helium concentration due to lower permeate dilution (Fig.2B, grey). Comparison of the mean integral outlet port with the port at 90% of the channel length allowed for calculation of the effective permeation by flow correction (Fig. 2B, black). Figure 2C shows the permeation

measurement with the same membrane including electrodes on both sides. Comparison of Fig.2B and 2C illustrates the influence of the electrode. This includes deceleration to laminar flow conditions to a maximum permeation rate of 1.2ml/min, which accounts for 5% of the permeation rate without electrode and differences in detected permeation per pore. These differences (Fig.2C pore 1-3) stem from the distances between pore and the subsequent gas port due to horizontal permeation through the electrodes (Fig.3, II,III) in the neighbouring channels and local inhomogeneities of the electrodes. In the case of pores in the sample channel the permeation to the neighbouring channel is the reason for the exponential decay of cumulative permeation along the channel. The permeation detection of pores in the neighbour channel is shown in figure 2D. Comparison with Figure 2C shows the same range of permeation at the average integral outlet.

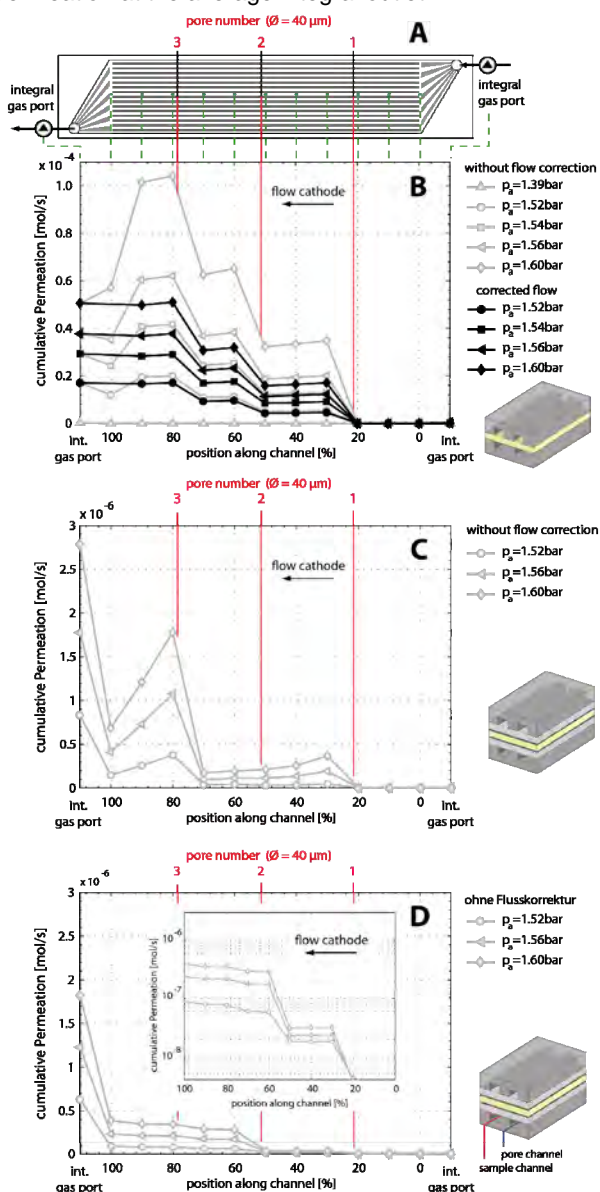


Figure 2. Convective pore permeation experiments. Model membrane: Kapton HN100, $d=25\mu\text{m}$. Pore shape and size see fig.1. A) Flow field with local gas analysis positions; B) Membrane 1 without electrodes; C) Membrane 1 with electrodes; D) Membrane 2 with electrodes. Operating conditions: Anode 90% H_2 , 10% He, $p_a=1.4\text{--}1.6\text{bar}$; Cathode: 100% N_2 , $p_c=1.5\text{bar}$. Membrane 1: 3 pores in sample channel; Membrane 2: 3 pores in neighbour channel. $T_{\text{cell}}=80^\circ\text{C}$, virtual load point: $0.2\text{A}/\text{cm}^2$, $\lambda_a=\lambda_c=2$, $rH=0\%$. Electrodes: Etek Elat A6STDSI V2.1.

Again, differences in permeation of the three pores of identical size stem from relative pore position to the subsequent gas port and electrode inhomogeneities. In addition, the pore permeation rate can be influenced by the position of the pores on the channel-rib scale, due to higher compression of the electrode under the rib and the resulting lower porosity and higher tortuosity of the electrode. Inhomogeneities of the electrode and the pore position on channel-rib scale are assumed to be the reason for almost non detectable permeation of pore 3 in Figure 2D. The cumulative permeation along the channel with pores in the neighbouring channel shows stagnant or steady increase of permeate concentration after a pore position, which stems from the preferential permeation into the pore channel and subsequent permeation in the neighbouring channel due to the short vertical permeate transport path (Fig.3, I, PTP_v). Therefore the shape of the cumulative permeation along the channel and the condition at the integral outlet port enables to distinguish between pores in the sample or neighbouring channel.

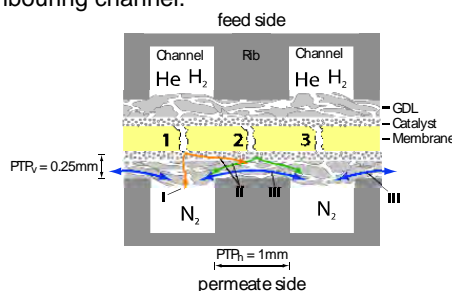


Figure 3. Permeate detectability influences: Influence of the pore position relative to the channel rib structure (1-3), influences of material inherent and cell assembly initiated electrode inhomogeneities and different permeation paths (I-III).

Conclusion

The influence of convective permeation of local membrane defects was investigated by characterization of model pores with local gas analysis. Permeation measurements under membrane only and with electrodes set-up showed the dominant permeation resistance of the electrodes in the pore diameter range of $40\mu\text{m}$. For identical pore size and pore shape, the effective measured local convective permeation varies due to different permeation behaviour and different detection conditions. Detectability of single pores by local gas analysis depends on pore position in the sample or neighbouring channel, relative position on the channel-rib scale, pore to gas port distance, electrode inhomogeneities and effective local driving force. Differences in pore detectability enable to distinguish between defects in the sample or neighbouring channels. These results of pore detectability and absolute pore permeation rates in combination with the electrode influences enable interpretation of local convective permeation results of degrading fuel cell membranes under real world operating conditions.

References

- [1] S. S. Kocha, J. D. Yang, J.S. Yi, *AICHE Journal*, **5**, 1916-1925 (2006).
- [2] G.A. Schuler, A. Wokaun, F.N. Büchi, *J. Power Sources*, **6**, 1647-1656 (2010).
- [3] E.E. Ortelli et al., *Macromolecules*, **14**, 5090-5097 (2000).
- [4] C.J.M. van Rijn, *Membrane Science and Technology*, **10**, 87-109 (2004).

1+1-D dynamic full physics polymer electrolyte fuel cell model

M. Zaglio, A. Wokaun, J. Mantzaras, F.N. Büchi

phone: +41 56 310 5165, e-mail: maurizio.zaglio@psi.ch

The investigation of the dynamic behavior of polymer electrolyte fuel cells (PEFC) is of high importance for the automotive application, where rapid variation of the load requirement must be satisfied. Understanding of fuel cells, whose electrochemical processes are strictly interlinked with species and energy transport, is facilitated by model based approaches. One core leveling of modeling is the description at the cell level, The 1+1-D model under development is used for studying the behavior of the PEFC under transient conditions.

Model

The model is applied for the study of cells of technical size with active areas of few hundreds cm^2 and long channels. The domains of the model are shown in Figure 1, with the schematic 1+1-D discretization grid:

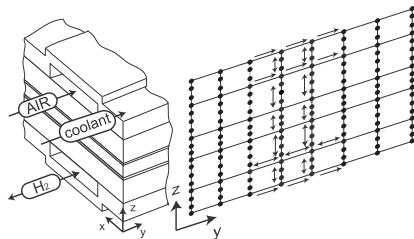


Figure 1. PEFC model domains and discretization.

Due to the high aspect ratio, transport in along-the-channel direction is by far dominated by convection in the channels, and transport in the MEA components can accordingly be neglected in this direction. In a multi-channel configuration, the approximation to neglect gradients in x-direction seems reasonable. It is also strongly motivated by the considerably lower computational cost of a quasi-two dimensional model as compared to a three dimensional model [1].

The model incorporates all important processes in the direction normal to the MEA: multispecies, multiphase diffusion of species, transport of water through the membrane by diffusion and electro-osmotic drag, heat generation and transport, electrochemical reaction in the catalyst layer. Mass transport along the channels is simulated with plug-flow assumption.

Parameters for the mass transport in the membrane and in the GDLs have been fitted to experimental data with a multiparameter optimization procedure based on an evolutionary algorithm [2].

The partial differential equations (PDE) describing the mass, momentum and energy transport in each domain, as well as the electrochemical phenomena, are approximated using the central difference discretization method. The resulting differential-algebraic system is solved in Matlab.

In its present configuration, the model is able to predict the transient response of a linear PEFC of technical size to current variations and is used to determine the parameter distributions in the cell in space and time.

Results

In Figure 2 responses of the cell voltage and different domains to a load step change of the integral current density from 0.5 to 1.0 Acm^{-2} for a cell operated at 70 °C with fully humidified feeds is shown. After an initial drop, the potential moves smoothly to the new steady-state in about 20s. The current density has an overshoot at the cell inlet, where more oxygen is available and the cell reacts faster to the load change, while at the cell outlet it gradually approaches the new steady state (see Figure 2b). The transient time is mainly related to the water transport in the membrane and saturation change in the GDL. The membrane ohmic overpotential, dependent on the water content, reaches the new steady-state in about 20s (Figure 2c). In Figure 2d-f the liquid water saturation in the cathode GDL, in three sections along the channel is shown. It increases due to the higher water generation at the interface after the current change. The transient time is shorter at the inlet, Figure 2d, because the channel inlet responds more rapidly than the outlet of the cell.

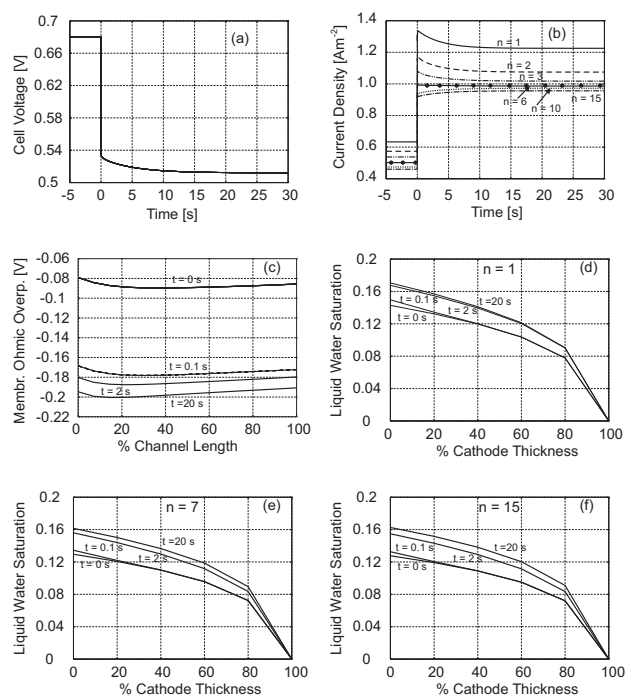


Figure 2. Cell potential, a, current density distribution in time ($n=1$ channel inlet, $n=15$ channel outlet), b, membrane ohmic overpotential along the channel, c, and liquid water saturation in the cell (0 membrane interface, 100 channel interface), d-e, after a load step change at $t=0$.

References

- [1] S. Freunberger et al., J. Electrochem. Soc., **153**, A396-A405 (2006).
- [2] M. Zaglio et al., submitted to J. Power Sources (2010).

Sub-millimeter current density distribution in PEFC at sub-zero temperatures

T. Colinart¹, F.N. Büchi

phone: +41 56 310 2411, e-mail: felix.buechi@psi.ch

In the development of polymer electrolyte fuel cell (PEFC) technology water management and freeze-start capabilities, including sub-zero operation and freeze and thaw cycles, pose significant technical challenges, especially for the automotive application [1].

The liquid water can undergo a phase transition to form ice at the interface between the gas diffusion layer (GDL) and the MEA when the stack temperature drops below the freezing point. The ice formed in the cathode catalyst layer pores impedes oxygen transport to the active sites [2], leads to an increase in the electrical contact resistance at the interface membrane/catalyst layer [3].

Up to now, most knowledge on the low temperature behavior is restricted to the *cell* scale. Here we report on the current distribution in PEFC on the rib and channel scale of the flow field during cold starts, a recently introduced technique [4] is used for measuring.

Experimental

A specialized test cell with an active area of 1.2 cm² was developed. The cell components were consistently commercial. Flow field plates were made of sintered graphite and had channel and rib widths of 2.0 and 1.0 mm, respectively and a channel length of 10.0 mm. The electrochemical components consisted of catalyst-coated membranes (Nafion 50 μm) combined with Toray TPGH-060 gas diffusion layers. Reactant feeds were provided at a high constant flow rate resulting in a differential operation of the cell. The cell temperature was controlled by circulation of a cooling fluid (water-glycol mixture) in the metallic end plates. The cooling fluid temperature was set by a thermostat.

Sub-zero operation was performed according to the following procedure:

1. FC conditioning at rated conditions (65 °C) until stabilization of the cell voltage.
2. FC cooling from 65°C to the testing temperature.
3. FC start-up in potentiostatic mode (U=300mV).

Results

The steady state current density distribution on the channel and rib scale of a PEFC is a function of cell temperature. This is also true for the temperature range close to the freezing point of water. Figure 1 shows the steady state current density distribution between 23 and 1 °C. At *normal* operating temperatures (70 – 80 °C) operation with dry gases (as for the data in Figure 1) leads to a current density minimum over the channel area due to local membrane drying [5]. However at low temperatures also water vapour pressure is low and current density distributions with a peak in the channel, similar to those observed at normal operating temperatures with humidified reactants are observed. In fact the lower the temperature, and thus the lower the water vapour pressure, the more distinct becomes the current peak over the channel. It seems a reasonable

interpretation that this is due to higher liquid saturations of the GDL at lower temperatures.

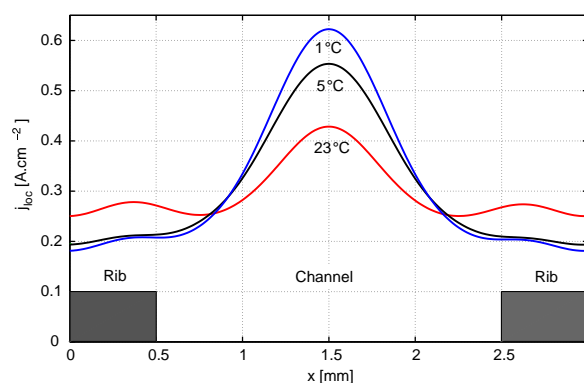


Figure 1. Current density distribution over a single repeating unit at an average current density of 0.3A/cm² for different temperatures in the range 1 < T < 23°C. Dry gases.

At temperatures below freezing, steady state experiments as in Figure 1 cannot be performed anymore. Therefore the development of the performance and local current density was investigated in isothermal start-up experiments as outlined above. Integral results at different temperatures are shown in Figure 2. At temperatures below -1 °C, after the load is connected, the integral current decreases immediately, the faster, the lower the temperature. Water starts to freeze in the catalyst and/or the gas diffusion layer, locally inhibiting the oxygen transport, and consequently the electrochemical reaction.

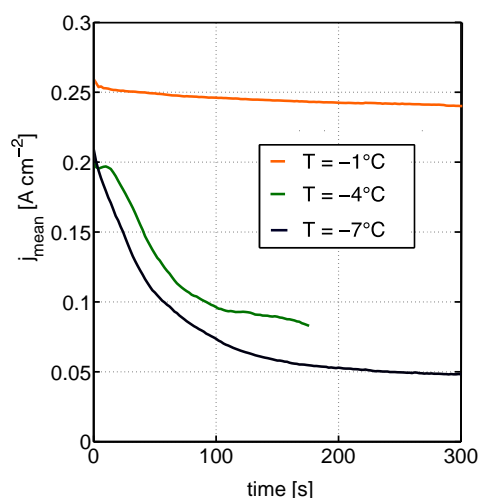


Figure 2. Mean current density production as function of time and temperature @ 300mV, for different sub-zero temperatures.

¹ Université de Bretagne-Sud (LIMATB), Lorient, France

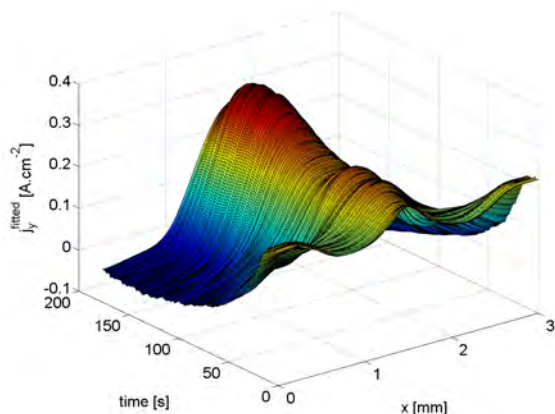


Figure 3. Current density distribution over a single repeating unit of channel and rib as function of time at -7 °C.

When focusing on the channel-rib scale, Figure 3 shows (exemplarily for -7 °C) the temporal development of the current density distribution. Initially the distribution shows little difference between the channel and land areas. However, under the rib the current starts to drop quickly while under the channel the peak current density seems to even increase slightly.

When the current is averaged over the rib and channel areas the same trend is observed. Figure 4 shows that when the current is averaged, also over the channel a monotonous decrease is observed. But still the current drops much quicker under the rib, here the current density decreases to zero in less than 60s. The difference between channel and rib can be explained by two trends (i) the lowest temperature in the cell after drawing current is under the rib (because of the heat capacity of the rib) and (ii) under the channel, the current density decreases slower, since more heat is produced and the heat capacity of the GDL only is low. Moreover, the short diffusion pathway under the channel may allow for super cooled water to be transported into the channel. Consequently, the channel domain is dominating the sub-zero performance. Temperature seems to influence the kinetic of ice formation, predominantly under the rib.

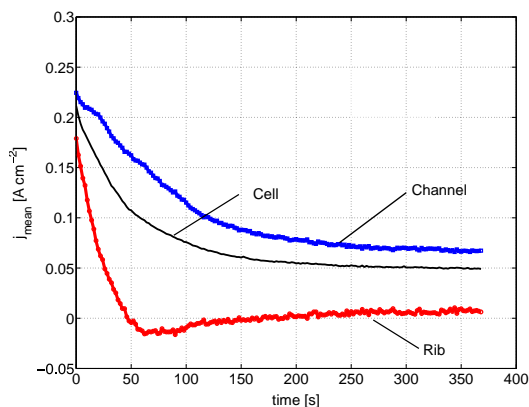


Figure 4. Integral current density and locally averaged current densities over the rib and over the channel as function of time at -7 °C.

References

- [1] J.P. Meyers, in Polymer electrolyte fuel cell durability, Eds. F.N. Büchi, M. Inaba and T.J. Schmidt, Springer, 369-382 (2009).
- [2] Y. Ishikawa, H. Hamad, M. Uehara, M. Shiozawa, J. Power Sources, **179**, 547-552, (2008).
- [3] E. Pinton, Y. Fourneron, S. Rosini, L. Antoni, J. Power Sources, **186**, 80-88, (2009).
- [4] S.A. Freunberger, M. Reum, J. Evertz, A. Wokaun, F.N. Büchi, J. Electrochem. Soc., **153**, A2158-A2165, (2006).
- [5] M. Reum, S.A. Freunberger, A. Wokaun, F.N. Büchi, J. Electrochem. Soc., **156**, B301-B310 (2009).

In-situ X-ray tomography and radiography of PEFCs

J. Eller, R. Flückiger, M. Stampanoni, A. Wokaun, F.N. Büchi

phone: +41 56 310 4580, e-mail: jens.eller@psi.ch

The experimental methodology for x-ray tomographic microscopy (XTM) of polymer electrolyte fuel cells at the TOMCAT beam line of the Swiss Light Source SLS has been further developed. The measurement technology for in-situ measurements has been advanced by newly designed active cells to be operated directly in the x-ray beam. For the first time ever, a running PEFC has been imaged with μm -resolution and the liquid water visible in the porous structures of the cell. From these measurements, the behavior of the liquid water in and on the porous gas diffusion layer, fingering through defined pore pathways to the surface, and building up droplets could be identified.

Placed between the flow field plate and the catalyst layer of PEFCs, gas diffusion layer (GDL) structures have to fulfill -- beyond chemical and mechanical stability -- two antagonistic tasks: high permeability for access of the gases to the catalyst layers and removal of product water and high conductivity for electric charge and heat conduction [1]. As the electrochemically produced water occupies part of the porous structure it thus strongly affects and limits the mass transport in gas phase and considerably influences the current distribution and fuel cell performance. Only synchrotron based XTM is capable to reveal the micro-scale liquid water distribution and the solid structure simultaneously with a pixel size smaller than 1 μm .

Experimental

A newly designed active cell sample holder was used at the TOMCAT beam line for the first time, as shown in Figure 1. The main focus of the new design was to enable electric contact and convective gas feed during the tomography scans, allowing in-situ tomography scans of operating cells. The two main transport modes of liquid water in the polymer membrane of PEFCs are drag of water due to proton flux through the membrane and water diffusion because of concentration gradients. If tomography measurements are performed after shutdown only water diffusion through the membrane remains active and changes the water distribution in the GDL materials until an equilibrium state is reached. Therefore in-situ tomography of operating cells is required for studying the water distributions under operating conditions.

Small carbon fiber reinforced plastic (CFRP) tubes were used for mechanical fixation and compression as well as for electrical contact of the GDL-membrane-electrode-assembly (MEA) and to establish a rotational symmetric flow field. The structure of the active cell is shown in a tomographic reconstruction of GDLs and MEA domain in Figure 2. The active area of the cell is 7 mm^2 such that the samples with a diameter of 3 mm fit into the field of view of the used 4x objective. Currents of up to 160 mA (2.29 A/cm^2) have been reached in pre-examinations. The active fuel cell was operated at room temperature. So far the gases were not humidified

to be absolutely sure, that the observed water was produced electrochemically in the small fuel cell.

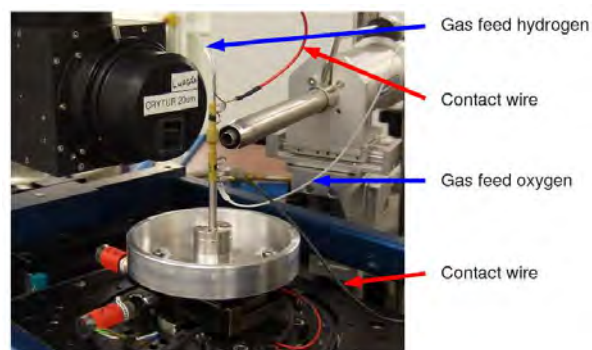


Figure 1. The new designed active cell sample holder at TOMCAT beam line sample stage. The two gas feed tubes and the two electric contact cables stay connected to the sample holder during the 180 degree rotation of the tomography scans .

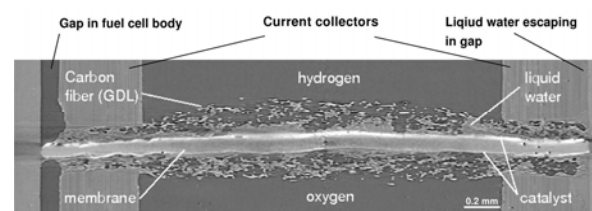


Figure 2. Vertical slice of a tomographic reconstruction of the active cell sample holder center. The two GDLs are fixed and contacted electric by the CFRP tubes. Liquid water escaped into the remaining gap between CFRP tubes and the sample holder wall.

For these experiments global tomography measurements with absorption contrast at 10 keV beam energy were made. Scan times could be reduced to 4 minutes with 2x binned camera sensor using 721 projections only with still acceptable reconstruction quality. For the unbinned sensor mode with 1501 projections a scan time of 12.5 minutes was needed. The 4x fold objective with a field of view of 3.7 mm gives a pixel size of 1.85 μm using unbinned sensor and a pixel size of 3.7 μm using 2x binned sensor.

Results

In-situ scans (see Figure 3) with a spatial resolution down to 1.85 μm of an operating fuel cell at different load states have been performed for the first time. The GDL material of this cell was Toray T060 with 20 % PTFE content. The cell could be operated stable at the TOMCAT beam line with currents of 1 mA, 5 mA, 10 mA and 20 mA, which correspond to current densities of 14.3 mA/cm^2 , 71.5 mA/cm^2 , 143 mA/cm^2 and 285 mA/cm^2 .

At scan times of 4 minutes the water pore network is stable enough to obtain tomography reconstructions of operating fuel cells without artifacts of moving water menisci. Unfortunately, the electrochemically produced water was removed from the MEA through the GDL into a gap between sample holder and CFRP tubes, as

shown in Figure 2. This unexpected and undesired pathway of water prevented the build-up of the necessary capillary pressure to flood the flow field of this test cell. Nevertheless we could observe water droplets on the GDL surface and study the water pore network feeding the droplets, as shown in Figure 3.

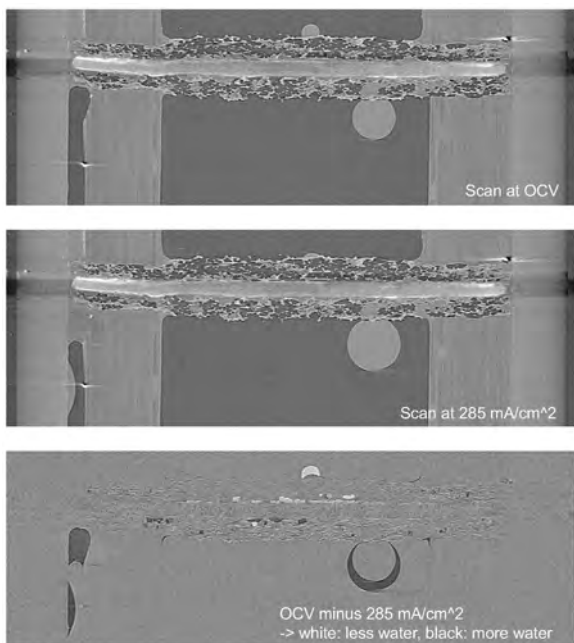


Figure 3. Vertical-slices of two sequential tomography scans (top and middle) at different load conditions. Subtracting the two data sets can reveal the change in water saturation with high contrast (bottom).

Further, Figure 4 demonstrates the strength of synchrotron based XTM of operating fuel cells: Even the growth of liquid water droplets on top of the catalyst layer can be studied, which is impossible to study by means of light microscopy or electron microscopy since they provide only surface views [2].

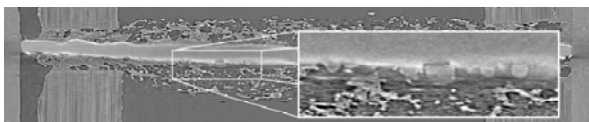


Figure 4. Water droplets on the cathode catalyst layer observed during OCV conditions..

Using x-ray radiography projections taken during load steps water back-diffusion from cathode to anode side after stopping the fuel cell (see Figure 5) and membrane swelling at startup of a dry membrane could be visualized.

Conclusions

The in-situ active fuel cell experiments show that transport of water in liquid phase to the gas channels takes place before a complete water saturation of GDL is reached. This coincides with former water column experiments [3].

Water transport in PEFC gas diffusion layers is a complex combination of water condensation, evaporation and intrusion. Therefore an improved sealed active fuel cell setup with adjustable temperature and humidification remains necessary to comprehensively study liquid water transport and its pathways with a unique 3D micrometer resolution at

conditions comparable to those of technical operated fuel cells.

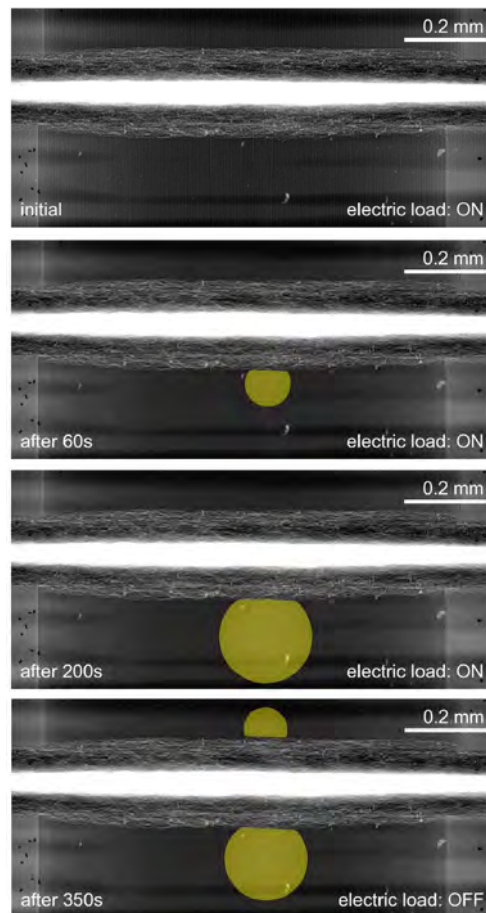


Figure 5. Radiography projections of an operating fuel cell with anode on top and cathode on bottom taken with a frame time of 450 ms. To increase weak radiography contrast the water droplets on the GDL surface have been highlighted in yellow. During fuel cell operation droplet growth can be observed at the cathode GDL surface. When the electric load is turned off, back diffusion of water to the anode sets in, which results droplet shrinking on cathode and droplet growing on anode GDL surface.

References

- [1] J. Becker, R. Flückiger, M. Reum, F.N. Büchi, F. Marone, M. Stampanoni, J. Electrochem. Soc. **156**, B1175 (2009).
- [2] F.Y. Zhang et al. J. Electrochem. Soc. **153**, A225 (2006).
- [3] F.N. Büchi, R. Flückiger, D. Tehlar, F. Marone, M. Stampanoni, ECS Trans. **16**, 587 (2008).

BATTERIES & SUPERCAPACITORS

MATERIALS

Preparation of an artificial SEI by surface modification of carbon electrodes

P. Verma, P. Maire, P. Novák

phone: +41 56 310 2161, e-mail: pallavi.verma@psi.ch

Irreversible charge loss (ICL) during the first charge of Li-ion battery is a vital issue. ICL is the charge consumed for reduction of the electrolyte on the surface of the negative active material (graphite). The degradation products of the electrolyte form an inhomogeneous passive layer called the Solid Electrolyte Interphase (SEI) [1]. Ideally SEI hinders electron transfer and allows Li^+ transport across the electrolyte/ electrode interphase. Thus SEI is a prerequisite for good cycling, rate capability and safe operation of the battery. Prime components of SEI are lithium alkyl carbonates, which are the reduction products of carbonate solvents. Here, carbon electrodes with a preformed carbonate passive layer are synthesized, to decrease the ICL. Glassy carbon (GC) is used as a model for graphite surface to simplify the modification and characterization. The modification is achieved in two steps: The first step is electrochemical grafting of an organic linker onto GC surface. The second step is chemical transformation of the end group of the linker into a suitable functional group. A surface modified carbon is schematically shown in Figure 1:

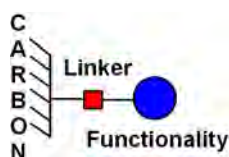


Figure 1. Schematic of a surface modified carbon.

Experimental

Step 1: Electrochemical grafting: All cyclic voltammetry (CV) experiments were carried out in a specially designed electrochemical cell. GC is the working electrode, Pt wire is the counter electrode and Ag wire is the reference electrode. Techniques of electrochemical grafting of alcohols, diazonium salts and iodonium salts were developed by grafting model compounds containing distinct marker atom. The experimental conditions used and main results are listed in table 1.

Model compound	Electrolyte	Scanned potential (vs. Ag/Ag ⁺)	XPS (at%)
<chem>HO-CH2-CH2-CH2-Cl</chem>	0.1M LiClO ₄ in parent alcohol	0.0V - 2.5V	8.8(Cl)
<chem>O2N-C6H4-N2+BF4-</chem>	5mM diazonium salt in CH ₃ CN (0.1M TEAB)	-1.8V - 0.3V	4.7(N)
<chem>Ph-I+(C≡C)3-CH2-CH2-CH2-Cl BF4-</chem>	5mM iodonium salt in CH ₃ CN (0.1M TEAB)	-1.5V - 0.3V	3.9(Cl)

Table 1. Operating conditions and XPS results of electrochemical grafting of model compounds on GC. Scan rate = 5mV/s. (TEAB = tetraethylammonium tetrafluoroborate)

Step 2: Chemical treatment: By combining alcohol grafting [2] and synthesis of carbonates [3,4], scheme shown in Figure 2 was developed to prepare GC surface modified with lithium alkyl carbonate. After grafting the GC was rinsed and reduced by LiH. It was converted to

carbonate by bubbling CO₂ through the reaction mixture. The samples were analyzed by CV and XPS.

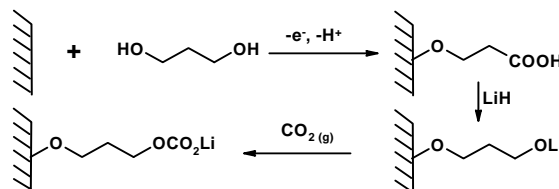


Figure 2. Scheme for modification of GC by ROCO₂Li.

Results

CV of pristine GC and GC after alcohol grafting at 10mV/s in 5mM K₃Fe(CN)₆ + 5mM K₄Fe(CN)₆ in 1M KCl aqueous solution illustrates that the grafted GC hinders electron transfer (Figure 3a). XPS C1s spectra of the treated GC samples prove the existence of the carbonate on the surface (Figure 3b). Treatment of graphite powders by similar methods and its effect on ICL is under progress.

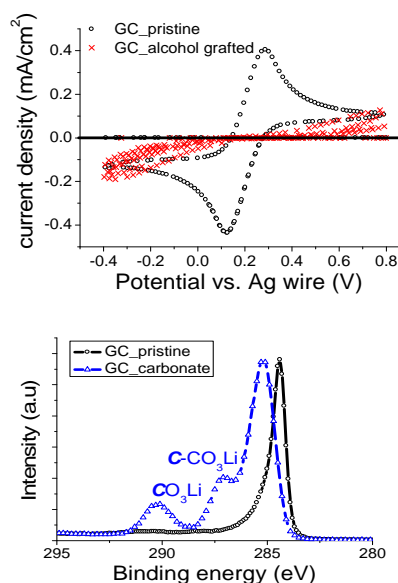


Figure 3. CV of pristine GC and GC after alcohol grafting (top). C1s spectra of pristine GC and GC containing carbonate (below).

References

- [1] E. Peled, D. Golodnitsky, G. Ardel, J. Electrochem. Soc. **144**, L208-L210 (1997).
- [2] H. Maeda, Y. Yamauchi, M. Hosoe, T. X. Li, E. Yamaguchi, M. Kasamatsu, H. Ohmori, Chem. Pharm. Bull. **42**, 1870-1873 (1994).
- [3] D. Aurbach, M. L. Daroux, P. W. Faguy, E. Yeager, J. Electrochem. Soc. **134**, 1611-1620 (1987).
- [4] L. Gireaud, S. Grugeon, S. Laruelle, S. Pilard, J.M. Tarascon, J. Electrochem. Soc. **152**, A850-A857 (2005).

Influence of concentration of ions on the exfoliation of graphite at very positive potentials

A. Hintennach, P. Novák

phone: +41 56 310 4542, e-mail: andreas.hintennach@psi.ch

A method correlating spatial and morphological information obtained by *in situ* Raman microscopy and SEM, respectively, was developed. This technique correlates Raman and SEM results with a lateral resolution of ca. 5 μm . Exfoliation of graphite used in positive electrodes of lithium-ion cells was then investigated with *in situ* Raman microscopy during electrochemical cycling up to very positive potentials ($>5\text{ V vs. Li/Li}^+$).

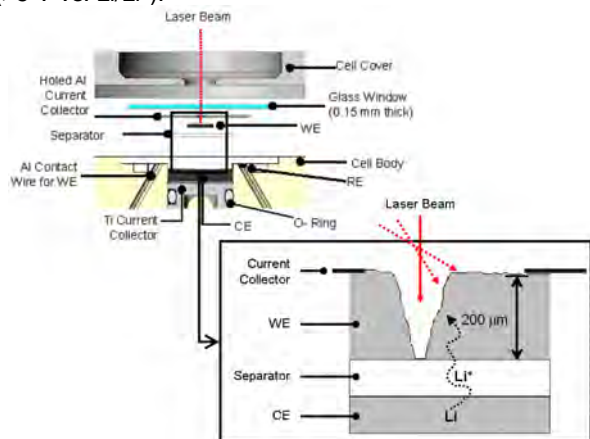


Figure 1. Experimental setup of the *in situ* Raman test cell. WE: Working electrode (graphite), CE: Counter electrode (lithium), RE: Reference electrode (lithium).

Correlation of Raman and SEM measurements

Graphite SFG44 was used as a model material. For the measurements artificial pores were first burned into the surface of the electrode with the focused laser beam of the Raman microscope. Figure 1 shows the used experimental setup and figure 2 the such created pore. The correlation of Raman and SEM information was enabled by the localizing of visible pores in the SEM pictures of the surface of the electrode, whereby the spatial resolution of the Raman spectra was about $x, y = 4\ \mu\text{m}$, $z = 6\ \mu\text{m}$. For the Raman microscopy varied angles of incidence ($\alpha_c = 0\text{--}70^\circ$, with respect to the z -axis) of the laser beam were used. For the determination of the concentration of ions the influence of the angle of incidence of the laser beam proved to be negligible.

After filling the *in situ* Raman cell with the electrolyte (1 M LiClO_4 in EC:DMC 1:1) an automated mapping technique utilizing the capabilities of the Raman microscope allowed the determination of the local concentration levels of ions on large areas on the surface of the electrode at different electrochemical states.

In situ Raman measurements

Some parts of the graphite electrode exfoliated when exposed to very positive potentials. Using Raman microscopy local concentrations of ions were estimated during the electrochemical experiment. Changes in the local concentrations of ions on later exfoliated (mapping point 1 in figure 3) and non exfoliated (mapping points 2–4) areas on the surface of the electrode during

electrochemical cycling are shown in figure 3. The measurement points a1–a4 suggest a significant gradient in the normalized concentration levels of ions on the surface of the electrode during electrochemical cycling. Where such gradients were detected, exfoliation effects were confirmed later using Raman spectroscopy and SEM. The measurement points b2–b16 and c2–c16 showed neither strong gradients in the concentration levels of ions nor exfoliation was observed on the respective spots of the electrode.

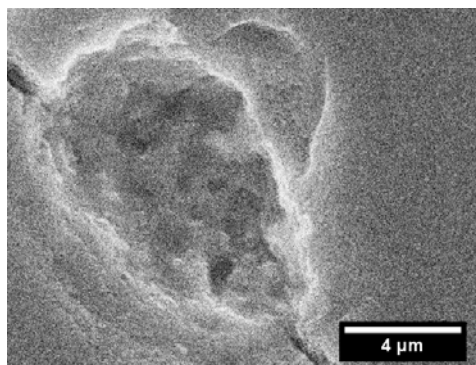


Figure 2. SEM image of a laser burned artificial pore on the surface of a model SFG44 graphite electrode.

As exfoliation of graphite was localized within the same areas where strong gradients in the concentration levels of ions were detected – well before the exfoliation of graphite was detectable – we hypothesize that the concentration gradients on the surface of the electrode favor exfoliation of graphite during electrochemical cycling up to very positive potentials ($>5\text{ V vs. Li/Li}^+$).

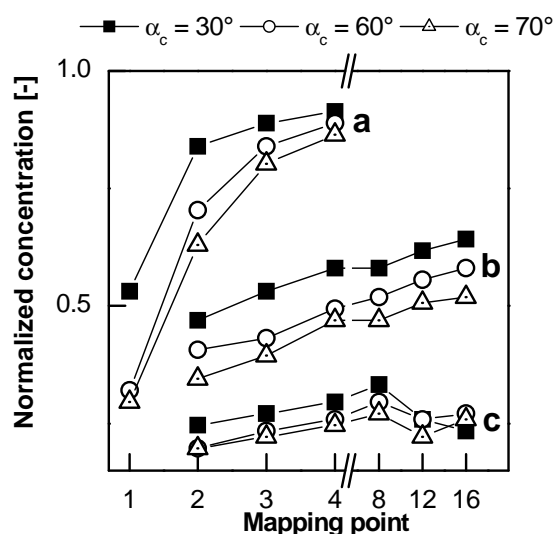


Figure 3. Local concentration of ions on the surface of the electrode and within the artificial pore as calculated from *in situ* Raman measurements. Different angles of incidence α_c with respect to the z -axis were used.

***In situ* Raman monitoring of a microwave-assisted synthesis of LiFePO₄ nanoparticles for lithium-ion batteries**

A. Hintennach, I. Bilecka¹, M. Niederberger¹, P. Novák

phone: +41 56 310 4542, e-mail: andreas.hintennach@psi.ch

There are traditional heating based synthesis routes to nano-particles for electrodes of lithium-ion batteries. However, microwave-assisted (MW) synthesis proved to be a more efficient, faster, and thus more convenient method.[1–2] Most of the growing numbers of publications in the field treat the microwave synthesis as a “black box” with no or eventually quasi *in situ* monitoring of the course of the reaction.

In the field of batteries the crystal size and shape of electroactive materials have a significant influence on a number of parameters including practical specific charge, long-term cycling stability, and safety.[2,4] A new method based on *in situ* Raman spectroscopy, therefore, was developed by us to acquire information about the growth of the resulting crystals from the microwave synthesis process. The combination of a microwave reactor with a Raman spectrometer allowed investigations in the given fast reaction environment with the ability to control the reaction parameters.

While traditional heating based synthesis technology allows the *in situ* appliance of almost every spectroscopic method the access to microwave ovens is very limited due to the need of a shield to protect the environment against leaking microwave radiation. Moreover, the possible influence of the microwave radiation on, e. g., sensors, cables, and/or liquids has to be considered. Raman spectroscopy utilizes laser light with a frequency within the visible spectrum. As visible light can be easily transduced by glass fibers it is widely used in telecommunication networks. As glass fibers can be introduced into a microwave oven – glass does not interfere with the radiation – they are an ideal “window” for monitoring spectroscopically the microwave-assisted synthesis of nano-particles for the electrodes for lithium-ion batteries. The absorbance in the fiber is negligible, thus, the Raman spectroscopy is an ideal tool, opposite to, e. g., FTIR spectroscopy.

In the present work we focus on an *in situ* Raman controlled microwave-assisted synthesis of nano-sized LiFePO₄ particles for the use in electrodes for lithium-ion batteries. Moreover the dependence of the reaction course on temperature and concentration of the educts was investigated using a model reaction of ZnO formation, to be used for the calibration of the method on the basis of data previously described in the literature.[2] Finally, an automated synthesis approach was developed which allows a feedback of the spectroscopic information to the microwave reactor resulting in a self-regulating system.

Optical setup

The microwave synthesis was performed in a setup as described in [3,4]. For the *in situ* Raman measurements a bunch of commercial glass fibers was installed through the microwave’s expansion port. The bunch of fibers was led by a small glass tube and it physically almost touched the reaction glass vessel (figure 1). The fiber bunch was moved during synthesis and measurements when necessary to adjust the distance between the

fibers and the glass vessel. As the excitation source a laser (HeNe, 632.8 nm) of a Raman microscope was used. Focusing the laser beam on the end of the glass fiber vertically mounted under the Raman microscope allowed the excitation laser light to be led by the glass fiber into the microwave reactor. The backscattering light intensity is quite weak. This light was transduced through the bunch of the glass fibers to the Raman microscope. The backscattered light was detected by the CCD after focusing the Raman microscope on the end of the fibers. As the material of the glass fibers does not interact with the microwave radiation there are no thermal effects that had to be considered. Note that two Raman microscopes were used from practical reasons for the excitation and the detection, respectively. A simple laser would be sufficient for the excitation, of course.

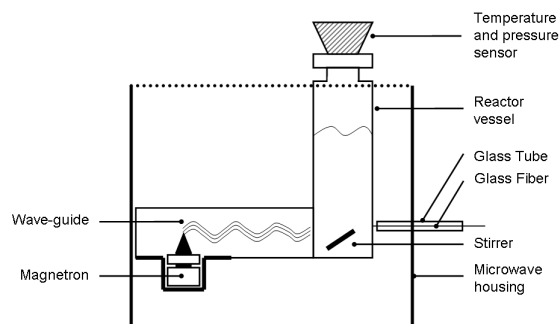


Figure 1. Experimental setup of the microwave reactor with the attached bunch of glass fibers that lead the laser excitation beam to the sample vessel and returned the radiation of the Raman effect.

Spectroscopic analysis of the MW synthesis

Program scripts were written which controlled the Raman measurements and the microwave reactor, respectively. The computer control device of the microwave reactor was controlled by a HP-Basic script allowing a port based communication with the control script of the Raman microscope.

To avoid possible thermal effects of the laser on the sample the shutter of the exciting laser was automatically closed when no Raman spectroscopic data were acquired. In addition, the power of the exciting laser source was limited by external filters between laser source and the optical setup of the exciting microscope.

After a calibration of the *in situ* Raman measurements within the microwave with known concentrations of known materials (ZnO and LiFePO₄, respectively), the computer script controlling the Raman microscope was adapted to provide automatically the intensities of the main relevant peaks and their integrals.

The ZnO synthesis was chosen to verify the *in situ* Raman monitoring, as excellent literature data is available for the microwave-assisted synthesis protocol of ZnO.[3] While the reaction progressed the *in situ* Raman spectra changed (figure 2). Roughly speaking, the intensity of the peaks in figure 2 reflected the

¹ Laboratory for Multifunctional Materials, ETH Zürich.

concentration of ZnO in the reaction solution. After defined parameters from the *in situ* Raman spectral information were reached or exceeded (magnitude and integrals of relevant Raman peaks at specific stirring speed of the solution in the microwave reactor), the program script of the Raman microscope delivered this information to the microwave controller which then adjusted the microwave synthesis parameters (power, waiting time, stirring speed, and quenching). Concomitantly, the acquired reaction parameters (pressure, temperature, quenching time, and microwave heating power) were recorded. This setup allowed a control loop which ensured a fast adaptation of the process parameters on the progress of the reaction. Due to the fact that the *in situ* Raman measurements were not fast enough to detect very fast changes (<10 s) of the microwave-assisted reaction, every experiment with a set of given reaction parameters was repeated six times but with a small offset for the Raman measurements on the time scale. Moreover, this approach proved the reproducibility and allowed the preset of the parameters of the Raman spectra before the synthesis was started.

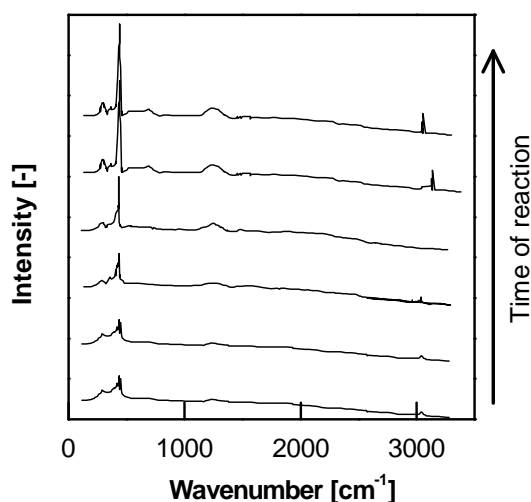


Figure 2. Evolution of the *in situ* Raman spectrum of a model material, ZnO during the *in situ* Raman monitored microwave synthesis.

Results

Figure 3 shows a typical *in situ* Raman spectrum of the reaction environment after completed microwave-assisted synthesis of LiFePO₄. Considering the known Raman peaks for the solvent benzyl alcohol, the LiFePO₄ peaks could be separated with high resolution from the busy Raman spectrum. The acquired spectra correspond to a published one of LiFePO₄ [5] and proved to be reproducible with different measurement times (10–35 s). The intensities of the peaks of the LiFePO₄ precipitate proved to be depended on the stirring speed and, therefore, on the homogeneity of the reaction mixture. With time the intensities of the peaks for the LiFePO₄ precipitate increased, while the intensities of the peaks of the solvent remained constant. The latter decreased with increasing stirring speed. Therefore, the stirring speed was adjusted to achieve the maximum intensity of the LiFePO₄ peaks.

With the described approach the microwave synthesis of nano-sized LiFePO₄ particles was optimized in respect to the yield of the particles, using the *in situ* Raman feedback controlled loop. In figure 4 the electrochemical data of optimized particles are compared with the data

from our previous work [4]. A significant improvement of the specific charge (discharge capacity) was achieved even at very high C-rates (>4 C).

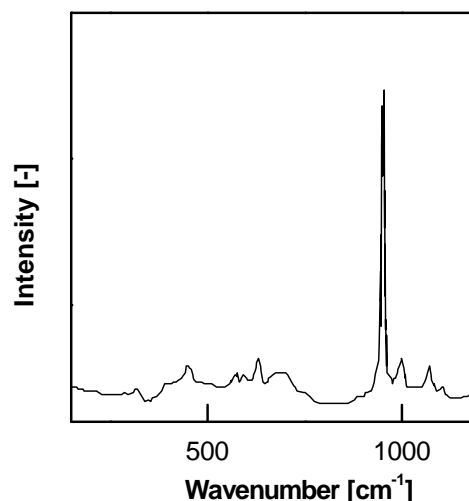


Figure 3. *In situ* Raman spectrum of LiFePO₄ in the reaction environment.

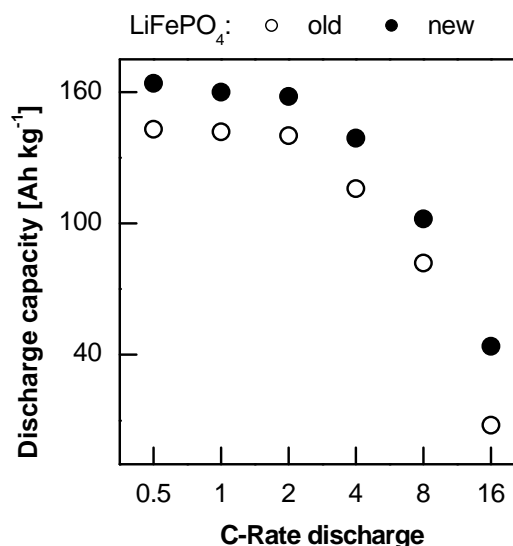


Figure 4. Influence of optimized microwave reaction parameters (temperature and, therefore, rate of the reaction) on the electrochemical characteristics of the synthesized nano-sized LiFePO₄. Electrochemical cycling between 2.0 V and 4.5 V (vs. Li/Li⁺).

References

- [1] N.E. Leadbeater, J.R. Schmink, *Nat. Protoc.* **3**, 1-7 (2008).
- [2] I. Bilecka, I. Djerdj, M. Niederberger, *Chem. Commun.*, 886-888 (2008).
- [3] I. Bilecka, P. Elser, M. Niederberger, *Acs Nano* **3**, 467-477 (2009).
- [4] I. Bilecka, A. Hintennach, I. Djerdj, P. Novák, M. Niederberger, *J. Mater. Chem.* **19**, 5125-5128 (2009).
- [5] D.A. Prystupa, A. Anderson, B.H. Torrie, *J. Raman Spectrosc.* **25**, 175-182 (1994).

Layer formation on $\text{Li}_{1+x}\text{Mn}_2\text{O}_{4-\delta}$ films after electrochemical characterisation

F. Simmen, A. Foelske, M. Horisberger, Th. Lippert, P. Novák, A. Wokaun

phone: +41 56 310 4194, e-mail: franziska.simmen@psi.ch

The spinel $\text{Li}_{1+x}\text{Mn}_2\text{O}_{4-\delta}$ is a potential candidate to be used as electrode material for lithium-ion batteries. It is an easy and cheap to prepare material with the advantage of a higher usable electrode voltage and being non-toxic as compared to LiCoO_2 . A significant irreversible charge consumption during charging is however considered to be not favourable for technical applications. The irreversibility in the charging properties occurs due to manganese dissolution and the formation of an additional layer, the so-called solid electrolyte interphase (SEI). An SEI can be formed by the electrolyte decomposition products within a defined potential range. The existence and formation of an SEI has been reported for anode materials [1, 2] as well as on positive, cycled electrodes [3-5]. The thickness of SEI layers on anode materials is reported to be up to several tens of nm, the thickness of SEI layers on positive electrodes, however, is only a few nm [3]. Therefore the choice of appropriate characterization techniques is limited.

For our studies, well defined thin $\text{Li}_{1+x}\text{Mn}_2\text{O}_{4-\delta}$ films deposited on Pt coated silicon are used to study the SEI formation without the influence of additional components present in composite electrodes like carbon black and binder. The preparation and properties of $\text{Li}_{1+x}\text{Mn}_2\text{O}_{4-\delta}$ thin films on other substrates like glassy carbon and stainless steel is reported elsewhere [6].

Experimental

$\text{Li}_{1+x}\text{Mn}_2\text{O}_{4-\delta}$ films were prepared by pulsed laser deposition (PLD, KrF, $\lambda=248$ nm, 10 Hz, 2.6 J cm^{-2} , 18000 pulses, $d_{t-s} = 4$ cm, $p_{\text{O}_2} = 0.2$ mbar) on Pt coated *p*-doped Si ($T \sim 500$ °C) with a typical thickness of ≈ 300 nm. The rod-like target was prepared by mixing $\text{Li}_{1.03}\text{Mn}_2\text{O}_4$ (99.7 % purity, Honeywell) with an excess of 2.5 Mol-% Li_2O , pressing (4000 bar), and sintering in oxygen (10 h, 750 °C).

The thin films were cycled in the potential range of 3.5-4.4 V versus Li/Li^+ using a Li foil (Aldrich) as anode. The used electrolyte was 1 M LiClO_4 in propylene carbonate (PC) (Ferro, USA, $\text{H}_2\text{O} < 15$ ppm). The electrode material was tested with cyclic voltammetry with a sweep rate of 0.05 mV s^{-1} (see Fig. 1) at 40 °C. After 6 complete cycles the cells were stopped at different potentials (3.5 V, 4.0 V, 4.125 V, 4.4 V). Afterwards the cycled thin films were washed in pure PC and dried under argon atmosphere in the glove box.

The cycled electrodes were characterised with scanning electron microscopy (SEM, Supra Zeiss, Inlens detector, 3kV) and X-ray photoelectron spectroscopy (XPS, $\text{Al}_{K\alpha}$, VG ESCALAB 220iXL). The samples were exposed to air for a very short time before entering the XPS chamber.

Results

The as-deposited $\text{Li}_{1+x}\text{Mn}_2\text{O}_{4-\delta}$ thin films are polycrystalline with a preferred (111) orientation and no impurities phases were detected using x-ray diffraction. The films showed a regular surface morphology consisting of octahedral and tetrahedral crystallites (see Fig. 2a, b).

During charging (oxidation) of the $\text{Li}_{1+x}\text{Mn}_2\text{O}_{4-\delta}$ thin film in an electrochemical cell, lithium is removed in a two step-process thus formally forming MnO_2 . During the discharging (reduction) step, lithium is inserted into the electrode thereby recovering the original spinel structure. In general, satisfactory cycle stability for $\text{Li}_{1+x}\text{Mn}_2\text{O}_{4-\delta}$ model electrodes on *p*-Si is obtained for up to ≈ 12 cycles.

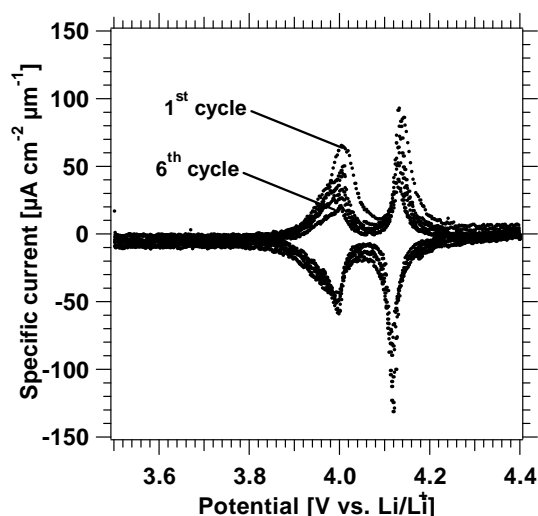


Figure 1. Typical cyclic voltammogram in 1M LiClO_4/PC electrolyte of $\text{Li}_{1+x}\text{Mn}_2\text{O}_{4-\delta}$ thin films deposited on Pt coated *p*-Si.

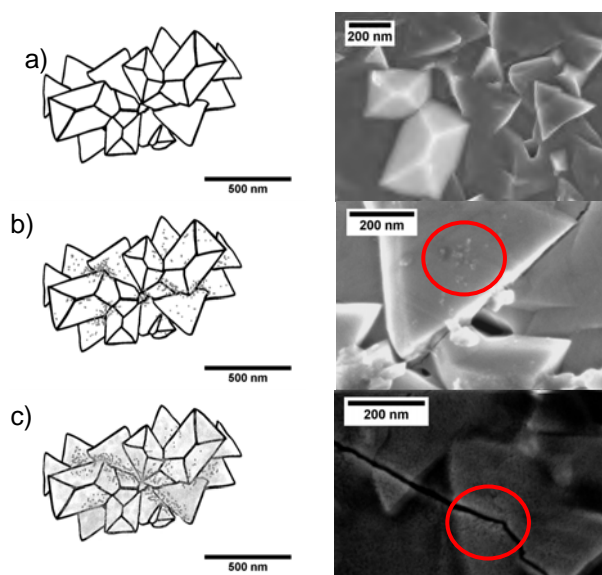


Figure 2. Right: SEM micrographs of a) an uncycled thin spinel electrode b) cycled spinel film at 4.125V, c) cycled spinel film at 4.4V; left: sketches of the possible additional layers.

To study the formation of an additional layer during electrochemical cycling, the cycling procedures were stopped after 6 completed cycles at different charging voltages. After washing and drying of the electrodes, different appearances of an additional layer on top of the virgin $\text{Li}_{1+x}\text{Mn}_2\text{O}_{4-\delta}$ surface (see Fig. 2a) were observed using scanning electron microscopy.

With increasing charging potential the additional layer becomes continuous in contrast to a globular or single network layer observed at low voltages. For layers formed at 4.4V these additional layers seem to consist of a combination of both types of layer formations. It was further observed that, these additional layers can be partly removed by washing the electrode after cycling with the pure organic solvent.

Characterising the $\text{Li}_{1+x}\text{Mn}_2\text{O}_{4-\delta}$ surface before and after cycling with XPS verified the presence of the additionally formed layer and gave chemical information about its composition (figure 3). Compared to surface species of an uncycled electrode the C1s spectra reveal that the amount of carbon bound to oxygen increases with increasing potential (figure 3a). In addition, oxygen species at a binding energy (BE) of 533.0 eV appear in the O1s spectra which can be attributed to C-O-X species (X = H, C) (figure 3b) [1, 7].

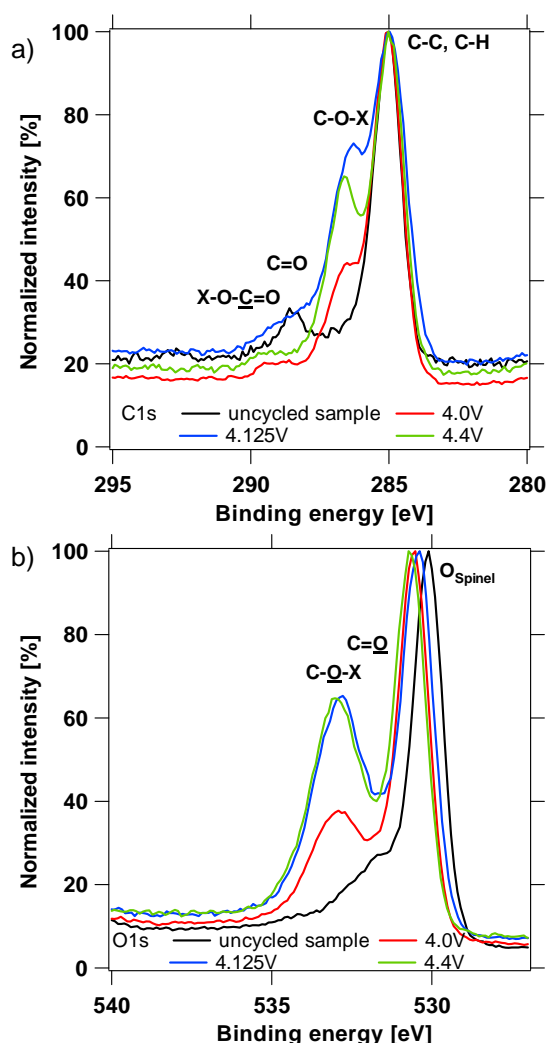


Figure 3. Comparison of a) C1s and b) O1s XPS spectra (X= H, C) as obtained from uncycled and cycled LiMn_2O_4 thin films stopped after 6 cycles at different charging potentials.

The C 1s signal is dominated by amorphous carbon (BE = 285.0 eV) and a small fraction of C=O (BE = 288.4 eV). The O1s is dominated by the spinel signal located at BE = 530.1 eV [8]. It is noted, untreated sample surfaces are already contaminated with carbon due to an ex-situ transfer. After cycling the fraction of C-O-X (X = H, C) increases for O1s and the C1s. In general, with increasing potential an increase of the C-O-X

fraction is observed. This seems to be correlated to the increase of polyether as a result of the charging process.

A quantitative analysis of the XPS spectra shows that with increasing charging potential from 4.0 V to 4.4 V the fraction of Mn decreases from 12.9 at% to 9.4 at% and the fraction of C increases from 40.6 to 44.5 at% (relative percentage). Although Mn^{2+} dissolution is a possible explanation for this observation (Hunter equation, see equation below), it also shows that the spinel electrodes are covered by a C-rich layer suppressing the Mn2p signal from the bulk material of the electrode.



Conclusions

Thin film Li-Mn-O spinel electrodes deposited on Pt coated *p*-Si can be used as possible model electrodes due to their defined composition, the absence of additives, and a homogenous surface morphology. Using scanning electron microscopy and X-ray photoelectron spectroscopy the presence of an additional layer on cycled electrodes was identified as a function of the charging potential. It was further determined that the surface coverage of the additionally formed layer increases with increasing cell potential, likewise the fraction of the C-O-X and the formed polyether.

References

- [1] M. Lu, H. Cheng, Y. Yang, *Electrochim. Acta* **53**, 3539 (2008).
- [2] S. Leroy, H. Martinez, R. Dedryvère, D. Lemordant, D. Gonbeau, *Appl. Surf. Sci.* **253**, 4895-4905 (2007).
- [3] M. Jo, Y.-S. Hong, J. Choo, J. Cho, *J. Electrochem. Soc.* **156**, A430-A434 (2009).
- [4] A.M. Andersson, D.P. Abraham, R. Haasch, S. MacLaren, J. Liu, K. Amine, *J. Electrochem. Soc.* **149**, A1358-A1369 (2002).
- [5] J. Lei, L. Li, R. Kosteccki, R. Muller, F. McLarnon, *J. Electrochem. Soc.* **152**, A774-A777 (2005).
- [6] F. Simmen, T. Lippert, P. Novák, B. Neuenschwander, M. Döbeli, M. Mallepell, A. Wokaun, *Appl. Surf. Sci.* **255**, 5303-5306 (2008).
- [7] A.M. Andersson, M. Herstedt, A.G. Bishop, K. Edström, *Electrochim. Acta* **47**, 1885-1898 (2002).
- [8] C.V. Ramana, M. Massot, C.M. Julien, *Surf. Interface Anal.* **37**, 412-416 (2005).

Dialkoxyaryl-polymers as cathode materials for lithium batteries

P. Maire, P. Nesvadba¹, L. Bugnon¹, P. Novák

phone: +41 56 310 5810, e-mail: pascal.maire@psi.ch

There is a growing demand for alternative materials to replace the transition metal oxides currently used as cathode materials in lithium-ion batteries. Lithium cobalt oxide is still the most frequently used material today, but the high price, limited resources, and the toxicity of cobalt hamper a mass production of large lithium-ion cells, e.g. for the use in electric vehicles. Organic polymers as cathode materials in lithium-ion batteries have therefore been a topic of intense research in the past years.¹

In this contribution we describe the electrochemical characterization of the novel polymer **1** bearing redox-active aromatic groups (Figure 1). The synthesis of the polymer was inspired by the recent use of 2,5-di-*tert*-butyl-1,4-dimethoxy benzene (DTBDMB) **2** as a redox shuttle in lithium-ion batteries.² A redox shuttle is an electrolyte additive that can be reversibly oxidized and reduced to provide an overcharge protection for lithium-ion batteries. The redox shuttle is oxidized at the positive electrode to form a radical cation, which then travels to the negative electrode, where it is reduced back to its initial form. Compound **2** was used as a very effective electrolyte additive in LiFePO₄/graphite cells, and it prevented damage of the cells even after hundreds of cycles of overcharging by 200 %. The high stability of **2** prompted us to synthesize polymer **1** and to evaluate its properties as a cathode material in lithium batteries.

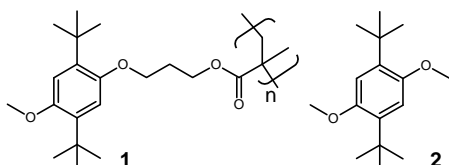


Figure 1. Structure of the novel polymeric cathode material **1** and the redox shuttle DTBDMB **2**.

Experimental

Electrodes for the use in coin-like test cells were prepared by coating aluminum current collectors with a slurry consisting of polymer **1** (28 wt %), graphite (48 wt %), soot (8 wt %), and PVDF binder (16 wt %) dissolved in *N*-methyl-2-pyrrolidone. After casting of the slurry by a doctor-blade method, the electrodes were dried under vacuum, and test cells were assembled in an argon filled glove box. A solution of LiPF₆ (1M) in a 1:1 mixture of ethylene carbonate/dimethyl carbonate (EC/DMC) was used as electrolyte, and the counter electrode was made from lithium foil.

Results

Cyclic voltammetry of electrodes made from **1** in half cells vs. lithium showed a pair of reversible redox peaks centered at a potential of 4.00 V vs. Li/Li⁺ (Figure 2), which is slightly positive to the potential of 3.85 V measured for the free 2,5-di-*tert*-butyl-1,4-dimethoxybenzene **2** in solution. The voltage of the cell is thus comparable with the voltage of classical lithium-ion batteries.

¹ BASF Schweiz AG, Basel

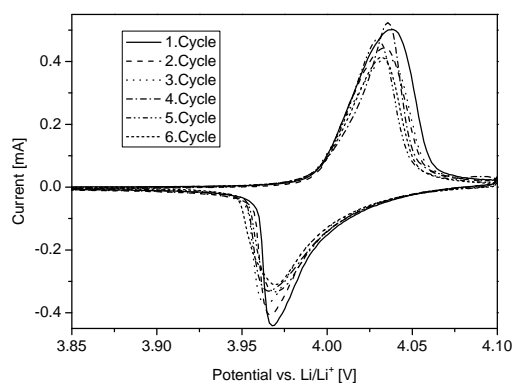


Figure 2. Cyclic voltammogram of poly-DTBDMB **1** in EC/DMC 1/1, 1M LiPF₆. Scan rate 50 μ V/s.

Assuming a one-electron oxidation of each monomer unit, the theoretical specific charge capacity of **1** accounts to 73 mAh/g. Under galvanostatic conditions at a rate of 1 C and within the voltage limits of 3.0 V and 4.1 V a specific discharge capacity of 53 mAh/g was obtained in the first cycle (Figure 3). In the subsequent cycles the cell was very stable, with less than 1.5 % capacity fading per cycle and high coulomb efficiency. The high stability of the molecule **2** is thus preserved in the polymeric material. The specific charge capacity of **1** is still too small for practical applications, but it could possibly be improved by reducing the weight of the polymeric backbone.

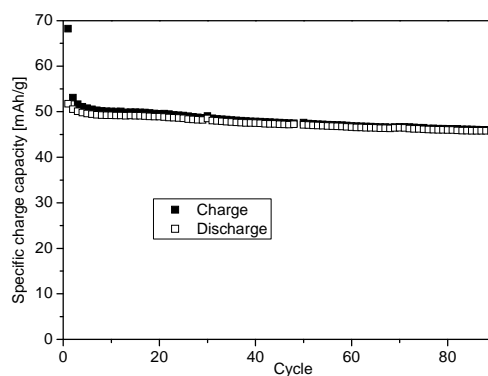


Figure 3. Galvanostatic cycling of composite electrodes made from **1** at a rate of 1 C in half cells vs. Li/Li⁺.

References

- [1] P. Novák, K. Müller, K.S.V. Santhanam, O. Haas, Chem. Rev. **97** (1), 207-281 (1997).
- [2] J. Chen, C. Buhrmester, J.R. Dahn, Electrochem. Solid State Lett. **8**, A59 (2005).

X-ray photoelectron spectroscopy study of imidazolium based ionic liquids

A. Foelske-Schmitz, R. Kötz

phone: +41 56 310 4193, e-mail: annette.foelske@psi.ch

Ionic liquids (ILs) are compounds consisting entirely of ions and exist in their liquid state at room temperature. They consist of a large, non-symmetric organic cation and a low coordinating anion, are electrochemically stable over a wide potential range, and do not show any vapour pressure. Therefore, structure and composition of these liquids can be studied using ultra high vacuum techniques such as X-ray photoelectron spectroscopy (XPS). The few XPS studies of ILs show that this method is perfectly suitable for quantitative chemical analysis and very sensitive to impurities [1-3]. Herein, we report on XPS analysis of four different 1-Ethyl-3-methylimidazolium [EMIM] based ionic liquids with varying anions (table 1).

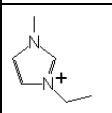
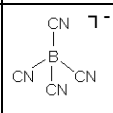
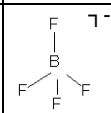
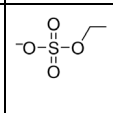
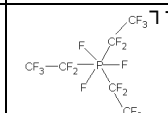
[EMIM]	[B(CN) ₄] ⁻	[BF ₄] ⁻	[ES] ⁻	[FAP] ⁻
				

Table 1. Chemical structure of the investigated ionic liquids

For analysis a droplet of each liquid was deposited on a sample holder made from stainless steel (SS) and for comparison on Teflon bound activated carbon (AC). XPS measurements were performed with an ESCALAB 220iXL spectrometer using monochromatic Al K α radiation for excitation.

Results

Comparison of the surface composition of the ILs prepared on SS with those prepared on AC revealed that impurities are significantly reduced or no longer detected when preparation was performed on the AC. For instance, [EMIM][B(CN)₄] on SS showed 4.9 at% of O, 1.6 at% of Si and 0.7 at% of Mg. These elements were absent on the IL prepared on AC, which might be ascribed to the strong adsorption ability of AC. Chemical composition of the investigated ILs prepared on AC is summarised in table 2. Overall, the data are in good agreement with the values calculated from the corresponding chemical structures of the investigated compounds.

[EMIM] ⁺	C / at%	N / at%	B / at%	F / at%	S / at%	O / at%	P / at%
[B(CN) ₄] ⁻	60.5	33.0	6.5	-	-	-	-
calculated	58.8	35.3	5.9	-	-	-	-
[BF ₄] ⁻	44.9	13.9	8.7	32.5	-	-	-
calculated	46.1	15.4	7.7	30.8	-	-	-
[ES] ⁻	53.1	12.7	-	-	8.2	26.0	-
calculated	53.4	13.3	-	-	6.7	26.6	-
[FAP] ⁻	35.4	5.5	-	55.6	-	-	3.5
calculated	36.4	6.1	-	54.5	-	-	3.0

Table 2. Chemical composition of the ionic liquids prepared on AC substrate; calculated values are given for comparison.

The C 1s spectra properly reflect the chemical bonds of carbon in the different ILs (figure 1). The C-N bond appears at a binding energy (BE) of 286.2 eV and the species at 287.25 eV corresponds to C neighbored by two N atoms of the [EMIM] cation. For [EMIM][FAP] additional signals appear which are attributed to C-F₂ (289.5 eV) and C-F₃ (292.5 eV).

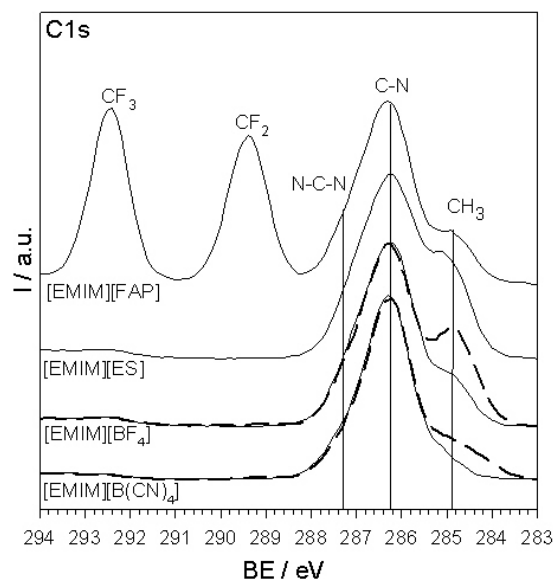


Figure 1. C1s XP spectra of the investigated ionic liquids; solid lines: prepared on AC; dashed lines: prepared on SS.

The species occurring at 284.8 eV correspond to CH₃ groups within the structure of the ILs and/or aliphatic hydrocarbons originating from surface contamination. Indeed, Gottfried et al. [3] have shown that the C 1s signal of properly prepared [EMIM][ES] shows half of the intensity measured by Smith et al. [1] in this energy range. Our data confirm this observation as the comparison of the C 1s spectra taken from ILs prepared on SS (figure 1; dashed lines) with those prepared on AC (figure 1; solid lines) show a significant decrease of intensity at 284.8 eV, which again might be ascribed to the strong adsorption ability of AC.

Acknowledgement

We thank Prof. A. Taubert (University of Potsdam) for supplying us with [EMIM][ES] and Merck KGaA for contributing the liquids [EMIM][B(CN)₄] and [EMIM][FAP].

References

- [1] E.F. Smith, I.J. Villar Garcia, D. Briggs, P. Licence, Chem. Commun., 5633 (2005).
- [2] V. Lockett, R. Sedev, C. Bassell, J. Ralston, Phys. Chem. Chem. Phys. **10**, 1330 (2008).
- [3] J.M. Gottfried, F. Maier, J. Rossa, D. Gerhard, P.S. Schulz, P. Wasserscheid, H.P. Steinrück, Z. Phys. Chem. **220**, 1439 (2006).

Supercapacitor aging in laboratory cells at constant voltage

R. Kötzt, P. Ruch, D. Cericola, A. Foelske-Schmitz

phone: +41 56 310 2057, e-mail: ruediger.koetz@psi.ch

Electrochemical double layer capacitors (EDLCs) are electrochemical devices in which the charge storage is primarily electrostatic and occurs within the electrochemical double layer [1, 2]. In order to maximize the specific interfacial area, activated carbon is the current electrode material of choice for these systems [3]. EDLCs feature higher specific power upon both charge and discharge but also intrinsically lower specific energy than galvanic cells due to the lack of a bulk contribution to charge storage [4, 5].

As both the specific energy and power of EDLCs are directly proportional to the square of the cell voltage [1, 2], a promising approach towards improvement of these two key properties is to increase the operating voltage. For instance, a cell voltage increase to 3.5 V roughly corresponds to a doubling of the specific energy of current EDLC technology based on a nominal voltage of 2.5 V. However, the device lifetime has been shown to decrease drastically with increasing voltage via a power law [6-9].

It is expected that the aging rate of an EDLC depends on the electrode material as well as on the type of electrolyte. Recently, ionic liquids (IL) and single walled carbon nanotubes (SWCNTs) were discussed as new electrolytes and electrode material for EDLC, respectively. IL are expected to exhibit a larger stability window, which should result in improved life times for a certain cell voltage.

Experimental

The activated carbon investigated in the present work was YP17 (Kuraray Chemical, Japan). Free-standing sheets bound with 10 wt% poly(tetrafluoroethylene) (PTFE, DuPont) were produced according to a procedure described previously [10]. SWCNT electrodes were prepared without binder as a self supporting mat according to the procedure described in [11].

The aging was performed at room temperature using a battery cycler (CCCC from Astrol Electronics, Switzerland) to impose a floating cell voltage of 3.5V for up to 500 h. Every 10 h, three galvanostatic full cell charge/discharge cycles were performed between 0V and 2.5V using a specific current of 0.28 A/g in order to determine the cell capacitance. Similarly, the specific capacitances of the positive and negative electrode were estimated.

The aged cells were disassembled in air and the electrodes washed in a Soxhlet reactor for at least 6 h using AN as the extraction solvent in order to remove residual electrolyte. Post mortem XPS and gas adsorption analysis was performed on these electrodes.

Chemical analysis of the aged electrode surfaces was performed using XPS (ESCALAB 220iXL from Thermo Scientific, USA, formerly V.G. Scientific) by means of monochromatized Al K (1486.6 eV) radiation. The binding energies were calibrated with respect to the Ag 3d5/2 level at 368.2 eV and the base pressure in the analysis chamber was always smaller than 10⁻⁶ Pa.

The porosity of each aged electrode was characterized by nitrogen adsorption at 77 K with an Autosorb-1 (Quantachrome Instruments, USA) after drying of the samples at 150 °C for at least 24 hours at pressures below 1 Pa. The specific surface area and pore size distribution was determined using the nonlocal density functional theory (NLDFT) kernel implemented in the AS1WIN software package from Quantachrome Instruments, USA. The isotherms were found to be best fitted by assuming a mixed slit/cylindrical pore shape.

Results

We performed aging tests at a constant cell voltage of 3.5 V with different electrolytes and different electrode materials. The electrolytes were Et4NBF4 in AN, Et4NBF4 in PC and a ionic liquid EMIBF4. For the electrode material we tested a standard activated carbon (YP17) and single walled carbon nanotubes, which could be prepared as a self standing mat [].

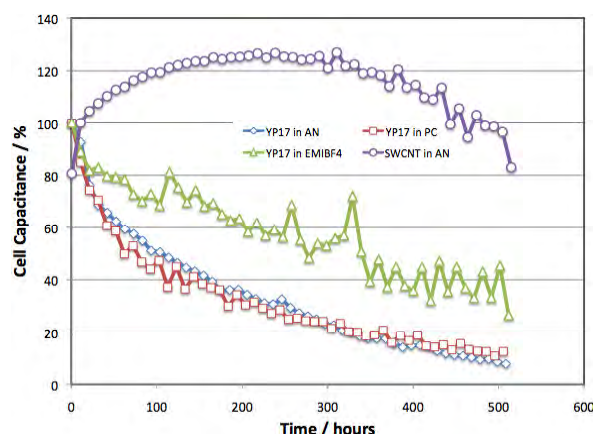


Figure 1. Cell capacitance as function of time for four differently configured capacitor cells. Activated carbon in AN (rombus) and in PC (squares), activated carbon in IL (triangles) and SWCNTs in AN (circles).

The fading of the cell capacitance during constant voltage tests at 3.5 V is shown in figure 1 for activated carbon (AC, YP17) in acetonitrile (AN), in propylene carbonate (PC) and in EMIBF4 together with SWCNTs in AN-based electrolyte.

It becomes evident from figure 1 that the aging of capacitor cells utilizing a ionic liquid or SWCNTs is reduced compared to the cells using activated carbon in AN- or PC-based electrolyte.

Although the aging of the cells (see figure 1) appears to be similar for activated carbon in PC- or in AN-based electrolytes, the underlying processes are completely different as is shown in figure 2. In both cases the aging is determined by the preferential degradation of one electrode, the positive in AN and the negative in PC. Due to the fact that the cell capacitance is mainly

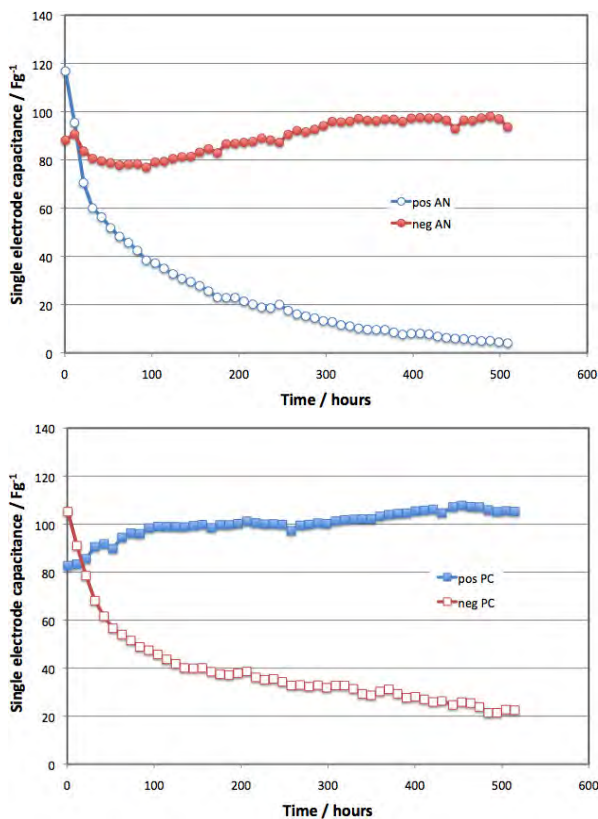


Figure 2. Single electrode capacitance as function of time for two capacitor cells utilizing activated carbon electrodes (top) in AN and (bottom) in PC

determined by the electrode with the lower capacitance the cell ages according to the worth electrode. The increase in capacitance of the better electrode in both cases can be explained by a shift of the electrode to more positive (PC) or negative (AN) potentials.

This finding has considerable impact on strategies to improve the respective EDLC lifetime. There is no general strategy to improve EDLC performance. Depending on the components chosen an individual strategy has to be developed for each type of capacitor.

Post mortem XPS and gas adsorption analysis (BET) of the aged electrodes clearly revealed that the surface area of the respective worth electrode was reduced by formation of a surface film. The XPS spectrum of such a film is reproduced in figure 3 for the aged positive electrode in AN and the aged negative electrode in PC after an aging test of 100 h together with the fresh activated carbon electrode.

The XPS C1s signal for the two electrodes is clearly shifted to higher binding energies indicating that most of the c atoms are oxidized and have formed c moieties with O, N, H or F as could be verified by elemental analysis of the XP results. Therefore, one can conclude that the accelerated aging of one electrode is a result of electrolyte decomposition leading to film formation on the respective electrode. Concomitantly, the BET analysis for these electrodes shows significantly reduced surface area.

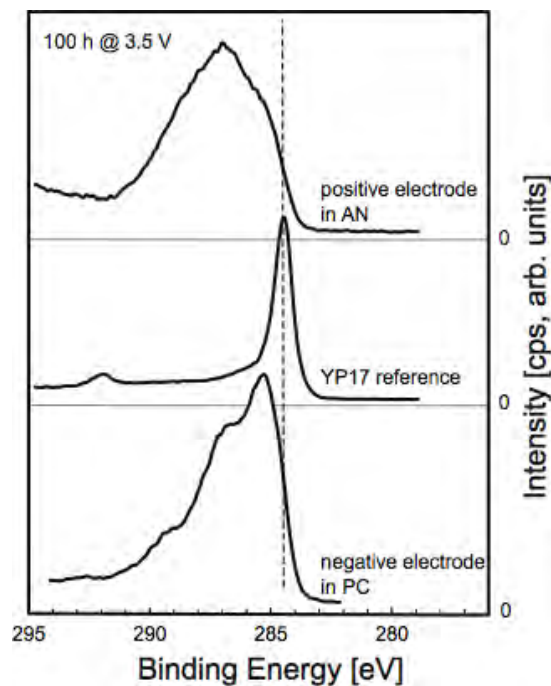


Figure 3. XPS spectra of the C1s level of the positive electrode aged in Et4NBF4 in AN and the negative electrode aged in Et4NBF4 in PC for 100 h.

Film formation on the electrodes aged in an ionic liquid or made of SWCNTs has yet to be analyzed. The fact that the degradation is smallest on SWCNTs may be explained by the low reactivity of the nanotube surfaces which are essentially basal planes of graphite.

Acknowledgement

The financial support of the Swiss National Science Fond (SNSF, project number 200021-117607) is gratefully acknowledged.

References

- [1] B.E. Conway, *Electrochemical supercapacitors: scientific fundamentals and technological applications*, Kluwer Academic, New York (1999).
- [2] R. Kötz, M. Carlen, *Electrochimica Acta* **45**, 2483 (2000).
- [3] A.G. Pandolfo, A.F. Hollenkamp, *J. Power Sources* **157**, 11, (2006).
- [4] A. Burke, *Electrochim. Acta* **53**, 1083 (2007).
- [5] P. Simon, Y. Gogotsi, *Nat. Mater.* **7**, 845 (2008)
- [6] T. Umemura, Y. Mizutani, T. Okamoto, T. Taguchi, K. Nakajima, K. Tanaka, *Proc. 7th Int. Conf. Prop. Appl. Dielectric Mater.* **3**, 944 (2003).
- [7] R. Kötz, M. Hahn, R. Gallay, *J. Power Sources* **154**, 550 (2006).
- [8] D. Linzen, S. Buller, E. Karden, R.W.D. Doncker, *IEEE Trans. Ind. Appl.* **41**, 4435 (2005).
- [9] O. Bohlen, J. Kowal, D.U. Sauer, *J. Power Sources* **172**, 468 (2007).
- [10] O. Barbieri, M. Hahn, A. Herzog, R. Kötz, *Carbon* **43**, 1303 (2005).
- [11] P.W. Ruch, D. Cericola, M. Hahn, R. Kötz, A. Wokaun, *J. Electroanal. Chem.* **636**, 128 (2009).

BATTERIES & SUPERCAPACITORS

DIAGNOSTICS

In situ synchrotron diffraction studies of NMC

V. Godbole, J.-F. Colin, P. Novák

phone: +41 56 310 5426, e-mail: vikram.godbole@psi.ch

LiCoO₂ is a widely used cathode material in today's commercial Li-ion batteries. However the toxicity and price of Co was the drive behind developing a better cathode material. Li_{1+x}(Ni_{1/3}Mn_{1/3}Co_{1/3})_{1-x}O₂ (0 ≤ x ≤ 0.13), commonly known as NMC, delivers higher power and safety [1], and is seen as a potential cathode material for use in high voltage range. Recent studies on overlithiated NMC (x=0.1) and stoichiometric NMC (x=0) cycled till 5.0V vs. Li/Li⁺ showed that the charge retention for the overlithiated NMC (x=0.1) is better after few cycles as compared to the stoichiometric NMC (x=0). Differential Electrochemical Mass Spectrometry (DEMS) measurements showed that there occurs oxygen evolution above 4.7V for the overlithiated sample (x=0.1) during its first charge. This phenomenon is not observed for the stoichiometric sample (x=0) [2].

These new results are quite interesting and understanding the reason behind the oxygen release is a key factor to understand the better stability of the overlithiated NMC. This in turn could also help us in designing a new high voltage cathode material. Thus an *in situ* X-ray diffraction study was conducted at the Swiss Light Source (SLS) with an aim of understanding the structural changes occurring in the overlithiated sample, which lead to its superior charge retention.

Experimental

A range of overlithiated NMC (0.01 ≤ x ≤ 0.1, varying x by 0.01) was synthesized along with the stoichiometric sample (x=0) using a citric acid route. For this purpose LiNO₃ (Fluka, ≥ 99%), Ni(NO₃)₂·6H₂O (Sigma-Aldrich), Mn(NO₃)₂·4H₂O (Fluka, ≥ 97%) and Co(NO₃)₂·6H₂O (Fluka, ≥ 98%) were taken in the required molar ratio and mixed in a solution of citric acid (Sigma-Aldrich, ≥ 98%) in water. The solution was stirred overnight and then dried at 250°C. The dry sample was subjected to heat treatment at 450°C (12h) and 850°C (12h) in air with intermediate grinding.

The *in situ* measurements were performed in a coffee bag cell [3]. Self standing films prepared using the phase-inversion process [4] were used for the preparation of the electrodes. In order to avoid peaks from the current collector during the diffraction measurements, an Al current collector (2cm*2cm) with a hole (r=0.6cm) in the centre was used. The self standing films were pressed from both sides onto the current collector to produce an electrode for the coffee bag cell. The coffee bag cells were assembled in a glovebox and measured *in situ* at the MS-powder beamline at SLS, PSI Villigen using the automatic sample changer [3]. The cells were cycled against Li (Aldrich, 99.9%) as the counter electrode in PC/DMC (1:1 wt) 1M LiPF₆ (all from Ferro) as electrolyte at C/20 rate between 2.5-5.0V vs. Li/Li⁺. The *in situ* diffraction patterns were recorded at a wavelength of 0.7085Å and a spot size of 0.5mm*0.5mm.

Results

Elemental analysis of the samples used at the SLS was performed using ICP-OES. The observed composition for the same is reported in Table 1 along with the composition expected from the stoichiometry during the synthesis.

Sample	Expected composition	Observed composition
SLS0	Li _{1.00} (NMC) _{1.00} O ₂	Li _{0.92} (NMC) _{1.00} O ₂
SLS1	Li _{1.01} (NMC) _{0.99} O ₂	Li _{0.93} (NMC) _{1.00} O ₂
SLS3	Li _{1.03} (NMC) _{0.97} O ₂	Li _{0.96} (NMC) _{1.00} O ₂
SLS4	Li _{1.04} (NMC) _{0.96} O ₂	Li _{0.98} (NMC) _{1.00} O ₂
SLS5	Li _{1.05} (NMC) _{0.95} O ₂	Li _{0.98} (NMC) _{1.00} O ₂
SLS7	Li _{1.07} (NMC) _{0.93} O ₂	Li _{1.02} (NMC) _{0.98} O ₂
SLS8	Li _{1.08} (NMC) _{0.92} O ₂	Li _{1.04} (NMC) _{0.96} O ₂
SLS9	Li _{1.09} (NMC) _{0.91} O ₂	Li _{1.03} (NMC) _{0.97} O ₂
SLS10	Li _{1.10} (NMC) _{0.90} O ₂	Li _{1.05} (NMC) _{0.95} O ₂

Table 1. Expected and observed composition from ICP-OES analysis for different samples (Here NMC=Ni_{1/3}Mn_{1/3}Co_{1/3}).

Although the observed composition is ~0.05 Li deficient as compared to the expected values, the NMC is seen to crystallize in the expected R-3m space group with cell parameters a=2.864Å, c=14.234Å and γ=120°, which are in accordance with the literature [5,6].

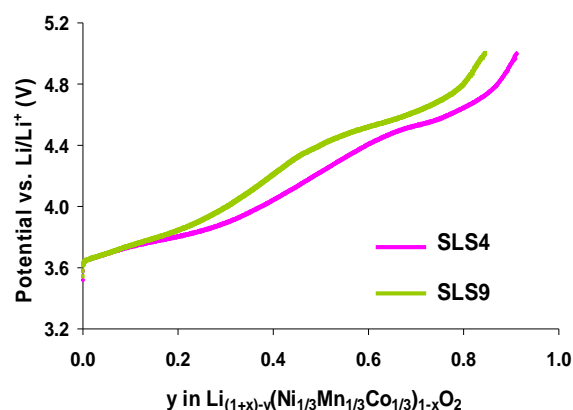


Figure 1. Charging curves for SLS4 [Li_{0.98}(Ni_{1/3}Mn_{1/3}Co_{1/3})_{1.00}O₂] and SLS9 [Li_{1.03}(Ni_{1/3}Mn_{1/3}Co_{1/3})_{0.97}O₂], in PC/DMC 1M LiPF₆ against Li counter electrode.

Electrochemical characterization studies for two of the samples viz. SLS4 and SLS9 are detailed in Figure 1. Clearly evident is the fact that both the materials reached 5.0V without any noticeable disturbance from the electrolyte degradation. Also to be noticed is the fact that despite using a current collector with a hole in the centre, almost whole of the theoretical specific charge has been obtained for both the samples, indicating that the charging was homogeneous.

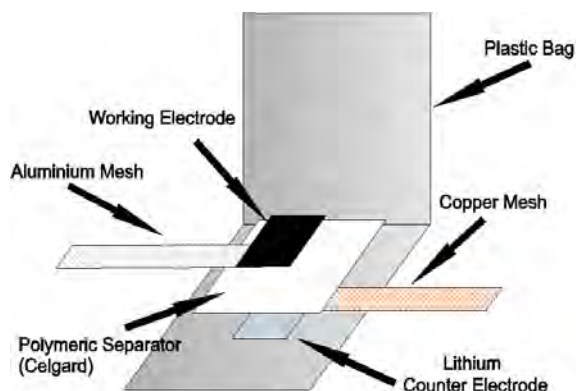


Figure 2. Sketch of a "coffee bag" cell used for the in situ measurements.

In order to ensure that the NMC used for the measurement at the SLS shows similar behaviour to that reported in literature, pattern matching was performed on the patterns recorded at various potentials for SLS4 [$\text{Li}_{0.98}(\text{Ni}_{1/3}\text{Mn}_{1/3}\text{Co}_{1/3})_{1.00}\text{O}_2$] and the variation in the cell parameters as a function of potential is shown in Figure 3. It can be seen that SLS4, which has observed composition close to the stoichiometric NMC, shows similar trend for changes in cell parameters as have been reported earlier [7].

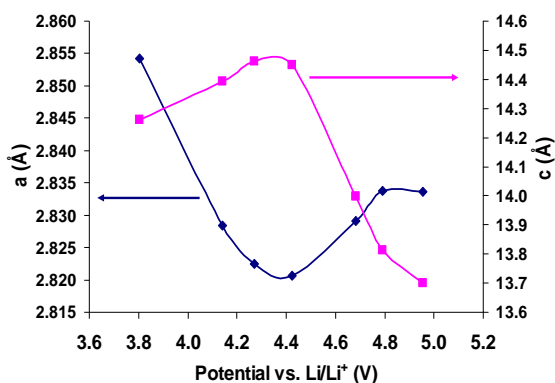


Figure 3. Evolution of cell parameters for SLS4 [$\text{Li}_{0.98}(\text{Ni}_{1/3}\text{Mn}_{1/3}\text{Co}_{1/3})_{1.00}\text{O}_2$] on charging.

In the next step the XRD patterns for the overlithiated NMC [SLS9- $\text{Li}_{1.03}(\text{Ni}_{1/3}\text{Mn}_{1/3}\text{Co}_{1/3})_{0.97}\text{O}_2$] were analyzed. From the patterns in Figure 4 one can observe the formation of two completely new peaks above 4.7V vs. Li/Li^+ , whose intensities increase until end of the first charge i.e. till 5.0V vs. Li/Li^+ . These peaks do not disappear during the following discharge. On the other hand no such new peaks were detected for the stoichiometric compound. The structural changes behind the formation of these new peaks are expected to help us understand the different charge retention behaviour for the stoichiometric and overlithiated NMC and are currently under detailed investigation. Using profile matching, the classical $3a^*3a$ and $\sqrt{3}a^*\sqrt{3}a$

superstructures have been excluded as one of the reasons for the same. Further analysis is expected to shed more light on this matter.

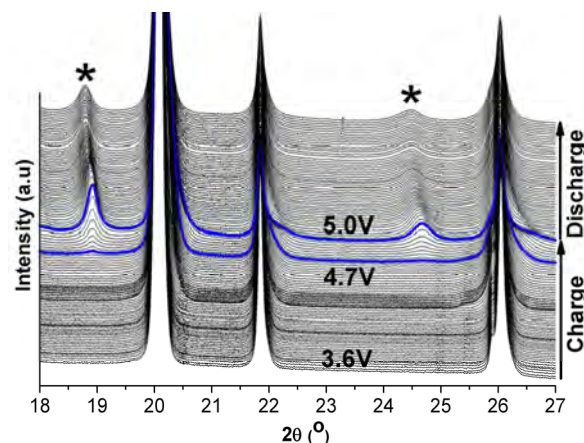


Figure 4. XRD patterns recorded in situ during the first cycle of SLS9 [$\text{Li}_{1.03}(\text{Ni}_{1/3}\text{Mn}_{1/3}\text{Co}_{1/3})_{0.97}\text{O}_2$] (* marks the new peaks).

Conclusion

It was seen that the NMC tested at the SLS campaign could be indexed with the expected R-3m space group and had lattice parameters comparable to those reported earlier. Although the samples were $\sim 0.05\text{Li}$ deficient than expected from the synthesis, their cycling behavior was as expected. The evolution of lattice parameters during 1st charge of the stoichiometric sample also shows a similar trend to that reported in the literature. As for the overlithiated samples two new peaks are seen to appear at higher potentials for all the cases. These two new peaks do not disappear on further discharge suggesting a permanent structural change induced during cycling to high potentials. The structural changes leading to the formation of these peaks are yet unknown; however our analysis could exclude the formation of classical superstructures as a reason for this behavior. Further refinement is on-going, to understand in more detail the changes occurring in the stoichiometric and overlithiated NMC on cycling.

References

- [1] I. Belharouak, Y.-K. Sun, J. Liu, K. Amine, J. Power Sources **123**, 249 (2003).
- [2] F. La Mantia, F. Rosciano, N. Tran, P. Novák, J. Appl. Electrochem. **38**, 895 (2008).
- [3] F. Rosciano, M. Holzapfel, H. Kaiser, W. Scheifele, P. Ruch, M. Hahn, R. Koetz, P. Novák, J. Synch. Rad., **14**, 488. (2007).
- [4] A. Du Pasquier, P.C. Warren, D. Culver, A.S. Gozdz, G.G. Amatucci, J.-M. Tarascon, Solid State Ionics **135**, 251 (2000).
- [5] T. Ohzuku, Y. Makimura, Chem. Lett. **7**, 642 (2001).
- [6] K.M. Shaju, G.V. Subba Rao, B.V.R. Chowdari, Electrochim. Acta **48**, 147 (2002).
- [7] K.-W. Nam, W.-S. Yoon, H. Shin, K. Yoon Chung, S. Choi, X.-Q Yang, J. Power Sources **192**, 656 (2009).

In situ neutron diffraction study of Li insertion in $\text{Li}_4\text{Ti}_5\text{O}_{12}$

J.-F. Colin, V. Godbole, H. Kaiser, P. Novák

phone: +41 56 310 2410, e-mail: jean-francois.colin@psi.ch

The comprehension of lithium insertion mechanisms is a major step in the improvement of electrode materials for lithium-ion batteries. So potential electrode materials have been extensively studied through *ex situ* X-ray and neutron diffraction. To obtain more dynamical information on the insertion during cycling, different groups developed *in situ* X-ray diffraction [1,2]. Unfortunately, although this method gives important information about the global structure changes, it doesn't allow a simple localization of lithium.

Despite some past tries [3], a reliable *in situ* electrochemical neutron cell has never been described. This is due to the contradictory needs of both electrochemical cycling and neutron diffraction. As the interaction of neutrons with matter is weak, a high amount of powder should be used to acquire a good diffractogram, but this big quantity of compounds is detrimental to the electrochemical cycling as it increases the overpotentials in the cell.

We present here the development of a novel *in situ* electrochemical cell for neutron diffraction. After a preliminary study which showed the feasibility of the method [4] we choose to follow the lithium insertion in the $\text{Li}_4\text{Ti}_5\text{O}_{12}$ which occurs through a transition from spinel $\text{Li}^{3a}_4[\text{Ti}_{5/3}\text{Li}_{1/3}]^{16d}\text{O}_4$ to rock-salt type structure $\text{Li}_2^{16c}[\text{Ti}_{5/3}\text{Li}_{1/3}]^{16d}\text{O}_4$ [5]. The reason for the material choice was that (i) $\text{Li}_4\text{Ti}_5\text{O}_{12}$ is suggested for negative electrodes of Li-ion batteries and (ii) it is an excellent model material for structural studies.

Experimental

The hardware of the used *in situ* cell is described elsewhere [4]. The preparation of the working electrode is a two step process. First a composite powder is prepared by mixing of 2.2g $\text{Li}_4\text{Ti}_5\text{O}_{12}$ (Süd-Chemie AG, Moosburg, Germany), 375mg of Carbon Super P, 100mg of graphite KS6 (both from TIMCAL SA, Bodio, Switzerland), and 675mg of NH_4HCO_3 . In a second step, the powder is placed in an oven under vacuum at 150°C to decompose NH_4HCO_3 . This leads to a porous electrode which is then transferred in an argon filled glovebox for the cell assembly. The electrolyte used was a 1M LiPF_6 in a 1:1 (%wt) mixture of ethylene carbonate (EC) and dimethyl carbonate (DMC; Ferro, Ohio, USA). The separator was a Celgard 2400 membrane (Celgard LLC, North Carolina, USA) and the counter electrode was lithium metal (Aldrich, 99.9%).

The *in situ* neutron diffraction was performed at the PSI at the HRPT beamline of the SINQ at the wavelength of 1.494\AA .

Results

The diffractograms obtained for $\text{Li}_4\text{Ti}_5\text{O}_{12}$ during the first electrochemical cycle are shown in the figure 1. We can observe that the major peaks of the phase are clearly visible. Especially interesting is the peak doublet (773)/(666) at $135\text{--}136^\circ$, the ratio of the intensity of these two peaks indeed reflects the $\text{Li}_4\text{Ti}_5\text{O}_{12} / \text{Li}_7\text{Ti}_5\text{O}_{12}$ ratio.

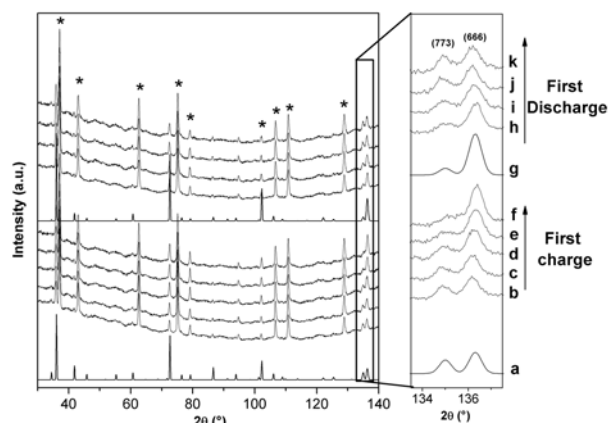


Figure 1. Evolution of the neutron diffraction pattern during Li insertion-deinsertion process and comparison with simulated patterns: a) simulated pattern of $\text{Li}_4\text{Ti}_5\text{O}_{12}$, b) $\text{Li}_4\text{Ti}_5\text{O}_{12}$, c) $\text{Li}_{4.7}\text{Ti}_5\text{O}_{12}$, d) $\text{Li}_{5.4}\text{Ti}_5\text{O}_{12}$, e) $\text{Li}_{6.1}\text{Ti}_5\text{O}_{12}$, f) $\text{Li}_{6.8}\text{Ti}_5\text{O}_{12}$, g) simulated pattern of $\text{Li}_7\text{Ti}_5\text{O}_{12}$, h) $\text{Li}_{5.9}\text{Ti}_5\text{O}_{12}$, i) $\text{Li}_{5.2}\text{Ti}_5\text{O}_{12}$, j) $\text{Li}_{4.6}\text{Ti}_5\text{O}_{12}$, k) $\text{Li}_{4.1}\text{Ti}_5\text{O}_{12}$. Asterisks indicate aluminium peaks coming from the container.

As we can observe on the enlargement given in the figure 1, when lithium is inserted into the structure the intensity of the (773) peak decreases as the intensity of (666) increases. This was expected from the simulation of the patterns obtained with the structural models proposed by Ozhuku [5]. The reversibility of this process is clearly visible on the patterns obtained during the following discharge.

The refinement of the data shows a small decrease of the cell parameter a from 8.3636\AA for $\text{Li}_4\text{Ti}_5\text{O}_{12}$ to 8.3580\AA for $\text{Li}_7\text{Ti}_5\text{O}_{12}$. This evolution is accompanied with an increase of the Ti-O bond length from 1.99\AA to 2.03\AA which is consistent with the bigger radius of Ti^{3+} compare to Ti^{4+} .

The (773)/(666) doublets of all the patterns were used in a 2 phases Rietveld refinement to determine the proportion of each phase in the mixture. The structural models obtained previously were fixed and only scale factors were allowed to be refined.

The results are given in the table 1. We can observe that, as expected, the amount of $\text{Li}_7\text{Ti}_5\text{O}_{12}$ increases during charge and decreases during the discharge. But an important deviation to the theoretical value, calculated from the consumed charge, is observed, especially when the two phases are present in significant quantities. This is due to the strong overlapping of the peaks that hinders the good retrieval of integrated intensity, when one phase is strongly dominant this problem is not significant anymore.

These results show the efficiency of our cell which allows to acquire neutron diffractograms during the course of electrochemical cycling. Thanks to this cell, we were able to follow the phase transition occurring during lithium insertion in $\text{Li}_4\text{Ti}_5\text{O}_{12}$.

Composition	Li ₄ Ti ₅ O ₁₂ (%wt) calculated	Li ₄ Ti ₅ O ₁₂ (%wt) theoretical
Li ₄ Ti ₅ O ₁₂	92.0 (±3.8)	100
Li _{4.7} Ti ₅ O ₁₂	87.7 (±4.3)	77.7
Li _{5.4} Ti ₅ O ₁₂	68.8 (±3.8)	53.3
Li _{6.1} Ti ₅ O ₁₂	42.4 (±3.4)	30.3
Li _{6.8} Ti ₅ O ₁₂	2.9 (±3.2)	0
Li _{5.9} Ti ₅ O ₁₂	37.8 (±2.9)	36.7
Li _{5.2} Ti ₅ O ₁₂	64.6 (±3.6)	58.7
Li _{4.6} Ti ₅ O ₁₂	92.8 (±4.0)	80
Li _{4.1} Ti ₅ O ₁₂	91.2 (±4.5)	99.7

Table 1. Results of the quantitative analysis carried through Rietveld refinement.

Nevertheless, we identified opportunities of further improvement of the method. A new cell for *in situ* neutron diffraction was designed to be used on a more powerful beamline, namely the D20 at the ILL (Grenoble, France). The goals were to improve the time resolution by reducing the counting time for each diffractogram, and also to reduce the quantity of powder in order to get a better electrochemical performance. Another important issue is the geometry change from a rectangular flat shape to a radial configuration, to overcome the difficult analysis of diffraction data due to the absorption effect. The figure 2 shows the scheme of this new cell.

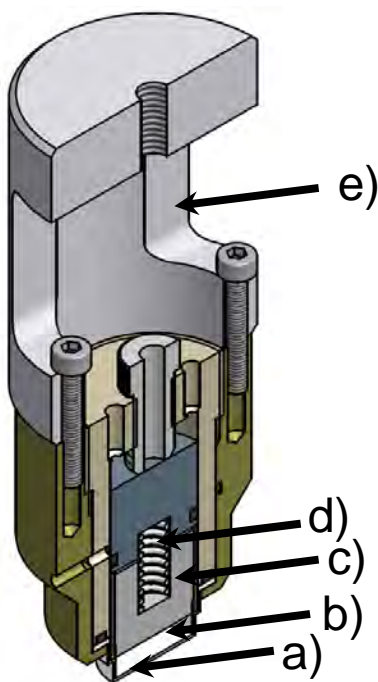


Fig. 2. Sketch of the newly developed *in situ* electrochemical cell for neutron diffraction: a) vanadium container for the active material, b) space to be filled by the stacking of electrodes and separator, c) titanium current collector for the lithium counter-electrode, d) spring, e) adaptor to the D20.

The diameter of the sample container is 15mm and its height is 3mm, reducing the amount of sample from 3g to 300mg, which makes the electrochemistry much more efficient. To check if this was not detrimental to the quality of the diffractograms, tests were carried out at the D20 beamline. The figure 3 gives a comparison between two diffractograms from Li₄Ti₅O₁₂ taken with the new and the old cell respectively. We can observe that the pattern acquired with the new cell clearly profit from the higher intensity of the D20 beamline, since much more peaks coming from the titanate are visible despite

that the acquisition time was reduced by a factor 50. We can also notice the very flat background which makes the analysis of the data much easier.

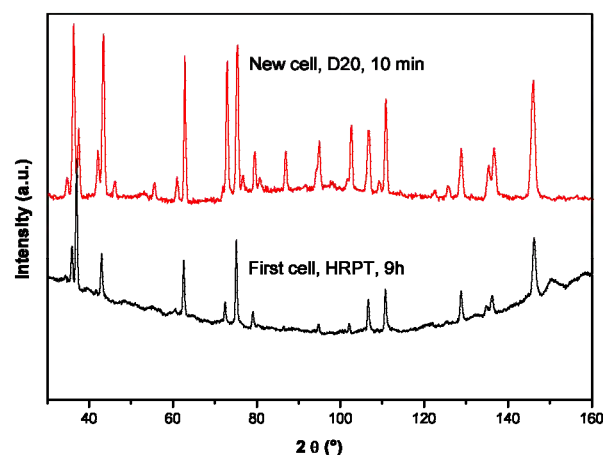


Fig. 3. Comparison of the Li₄Ti₅O₁₂ diffractograms obtained with the new and old *in situ* neutron cell.

Conclusion

A first study of the electrochemical lithium insertion in Li₄Ti₅O₁₂ by *in situ* neutron diffraction was carried out. We were able to follow important structural parameters such as the oxygen position along the electrochemical cycling. Further improvements were conducted by design of a new cell which allows us to get a much better time resolution and higher quality patterns. We now possess a very efficient tool for structural characterization of the lithium insertion in electrode materials.

References

- [1] E. Levi, M.D. Levi, G. Salitra, D. Aurbach, R. Oesten, U. Heider and L. Heider, *Solid State Ionics* **126**, 109-119 (1999).
- [2] M. Morcrette, Y. Chabre, G. Vaughan, G. Amatucci, J.B. Leriche, S. Patoux, C. Masquelier, J.M. Tarascon, *Electrochim. Acta* **47**, 3137-3149 (2002).
- [3] O. Bergstrom, A.M. Andersson, K. Edstrom, T. Gustafsson, *J. Appl. Cryst.* **31**(5), 823-825 (1998).
- [4] F. Rosciano, M. Holzappel, W. Scheifele, P. Novák, *J. Appl. Cryst.* **41**, 690-694 (2008).
- [5] T. Ozhuku, Ueda A., Yamamoto N., *J. Electrochem. Soc.* **142**, 1431 (1995).

Investigation of the lithium-sulfur battery system

H. Schneider, P. Maire, P. Novák

phone: +41 56 310 2115, e-mail: holger.schneider@psi.ch

Current state of the art lithium-ion batteries have reached a high level of performance and reliability. However, the specific charge of the transition metal oxides currently employed as cathode materials (usually less than 200 mAh/g) restricts their application e.g. in vehicles. Therefore, there is a need for alternative approaches. Sulfur offers several advantages, given that it is relatively cheap and environmentally benign. With respect to the reaction $16 \text{Li} + \text{S}_8 \leftrightarrow 8 \text{Li}_2\text{S}$, theoretically a very high specific charge of 1675 mAh/g (based on the weight of sulfur) and consequently high specific and volumetric energy densities (2500 Wh/kg and 2800 Wh/l, respectively) can be reached for lithium-sulfur cells [1]. Even if complete reaction is usually not achievable and in spite of the relatively low voltage (~ 2.2 V), these values demonstrate the high potential of this system. However, the successful application has been hampered by several challenges. Both sulfur and the end product of the reaction, lithium disulfide, are electrical insulators which makes complete utilization of the active material difficult. Moreover, the reaction does not proceed in one step but several polysulfide intermediates are formed, such as Li_2S_8 , Li_2S_6 and Li_2S_4 . These species are well soluble in most of the organic solvents employed, which means they can directly diffuse to the lithium anode where they are reduced. This polysulfide shuttle leads to quick capacity fading due to the loss of active material and coverage of the lithium anode with an insulating layer. Therefore, more research is needed in order to design reliable sulfur batteries with high energy density.

Experimental

The work conducted so far has been aimed at finding optimal combinations with respect to electrode compositions and electrolytes. Sulfur has been used as received from Sigma Aldrich and for the carbon conductive additive carbon Super P from TIMCAL has been used. All solvents employed have been distilled from sodium to obtain them free of water. Moreover, preliminary experiments have been performed in order to explore the possibility to establish the spectroscopic characterization of the intermediate species which form upon cycling the batteries. The results obtained so far are shown and described in more detail below.

Results

First of all, the most suitable electrolyte had to be identified. Standard carbonate-based electrolytes had to be excluded, as they lead to complete failure of the lithium-sulfur batteries tested, which we tentatively blame on possible reactions with the polysulfide species formed intermediately. Instead, we used ether based solvents with different lithium salts. Figure 1 shows a typical potential curve during the first galvanostatic cycle of a lithium-sulfur cell.

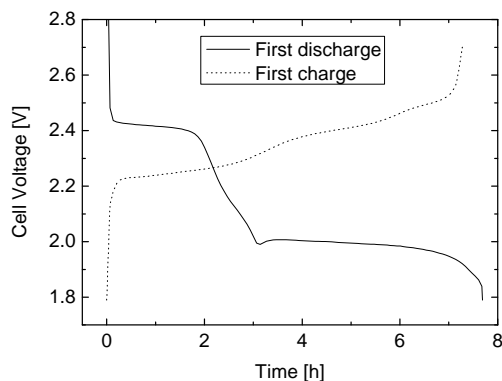


Figure 1. Cell voltage during the first galvanostatic cycle of a lithium-sulfur cell (1M LiTFSI in triethyleneglycoldimethylether).

One can clearly observe two potential plateaus during the first discharge, where the first one stems from the reaction of the longer chain polysulfides while the second plateau, which accounts roughly for 75% of the whole charge capacity of the cell, is due to the reduction of the short-chain polysulfides to the final products of the reaction, Li_2S_2 and Li_2S .

Figure 2 shows the performance of a standard lithium-sulfur cell made up from 60% sulfur, 30% carbon Super P and 10% Kynar binder using different lithium salts in triethyleneglycoldimethylether (triglyme).

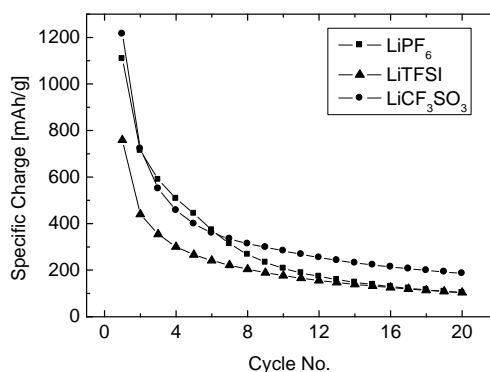


Figure 2. Specific charge of the sulfur electrode in cells with different lithium salts in triglyme.

It can be seen that variation of the lithium salt employed has a noticeable influence on the cell performance. Moreover, the influence of additives which form a more efficient protective SEI on the lithium anode and therefore slow down the polysulfide shuttle has been investigated. One compound described in the literature before is LiNO_3 [2]. As can be seen in Figure 3, it improves the capacity retention of the lithium-sulfur cell.

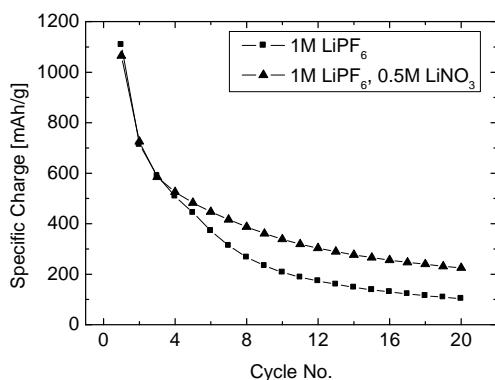


Figure 3. Specific charge of the sulfur electrode with and without adding lithium nitrate to the electrolyte (LiPF_6 in triglyme).

In order to improve the performance of the lithium-sulfur battery system, a detailed understanding of the processes occurring during cycling such as SEI and polysulfide formation is essential. Spectroscopic methods are particularly suitable for the characterization of the species involved and the intermediates which are formed during charging and discharging the cell. For instance, it should be easily possible to follow the evolution of the sulfur content in an electrode while cycling employing Raman spectroscopy. Figure 4 is displaying the Raman spectrum of pure sulfur, as recorded using a Raman microscope (Horiba Jobin Yvon).

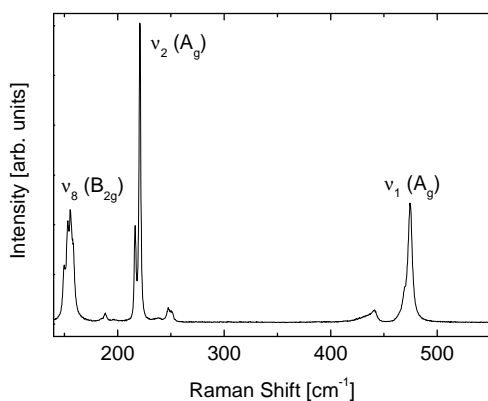


Figure 4. Raman spectrum of pure sulfur as recorded with a Raman microscope (Horiba Jobin Yvon).

In this manner, the sulfur content in the top-most layers of an electrode can be probed, although extreme care has to be taken to avoid overheating of the electrode surface by the laser beam.

In addition, the polysulfides which are formed during the electrochemical reactions strongly absorb in the visible and ultraviolet region. In the solvents employed the longer chain polysulfides (e.g. Li_2S_6) show an intense red color, while the shorter chain polysulfides (e.g. Li_2S_4) display a green color. In order to illustrate this, a carbon-sulfur electrode was shortcut with a lithium anode (in an LiPF_6 / TriEGDME electrolyte) in a recently developed cell, designed to monitor visible changes in both the electrode and the electrolyte, as is shown in Figure 5.



Figure 5. Sulfur-carbon electrode in an LiPF_6 / triglyme electrolyte after shortcircuiting with a lithium anode.

This opens the possibility to characterize the species and follow the reactions occurring via UV/VIS spectroscopy. Moreover, their concentration and spatial distribution within a cell can be followed via Raman spectroscopy in a time- and space-resolved manner. Figure 6 shows an exploratory spectrum recorded with a Raman microscope (Horiba Jobin Yvon) from a polysulfide solution of the average stoichiometrical constitution Li_2S_6 , being in good comparison to data from the literature [3].

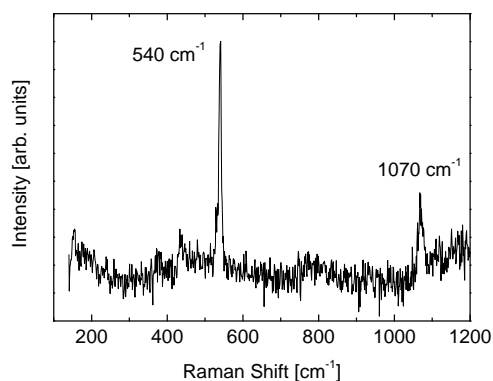


Figure 6. Spectrum of a polysulfide solution recorded with a Raman microscope.

The intermediates involved upon charging and discharging such a cell will be studied in more detail in order to find possible solutions for some of the challenges involved with the polysulfide shuttle. In summary, the experiments conducted so far showed possible approaches towards an improvement of lithium-sulfur batteries. Methods have been developed which enable the characterization and registration of reaction intermediates both with respect to time and space. This is an important step towards a better understanding of this system, which is necessary to spot appropriate solutions for the challenges currently involved.

Acknowledgements

The authors are very grateful for the financial support from BASF SE.

References

- [1] X. Ji, K. T. Lee, L. F. Nazar, *Nat. Mat.* **8**, 500-506 (2009).
- [2] D. Aurbach, E. Pollak, R. Elazari, G. Salitra, C. S. Kelly, J. Affinito, *J. Electrochem. Soc.* **156**, A694-A702 (2009).
- [3] P. Dubois, J. P. Lelieur, G. Lepoutre, *Inorg. Chem.* **27**, 73-80 (1988).

Investigations on the SEI formation kinetics on graphite surfaces with *post mortem* SEM and *in situ* DEMS

W. Märkle, C.Y. Lu, D. Goers¹, M.E. Spahr¹, P. Novák

phone: +41 56 310 2474, e-mail: wolfgang.maerke@psi.ch

Despite a lot of ongoing research on new materials for lithium-ion battery anodes, graphite is generally not surpassed due to its favorable combination of good cyclability, specific charge, and low cost. However, for a proper performance of the graphite electrodes it is inevitable that a film, called solid electrolyte interphase (SEI), covers the particle surface. This film is formed out of electrolyte decomposition products mainly during the first lithium intercalation cycle. The ideal SEI is an electronic insulator and solely permeable for Li^+ ions. An improper film formed during the first cycle can lead to exfoliation of graphene sheets due to solvated Li^+ cointercalation [1] and gas formation. As consequence, the interparticle contact deteriorates which may lead to the failure of the electrode. A crucial point for a good performance of the anode – and thus for the whole cell – is therefore to make sure that the conditions in terms of graphite and electrolyte choice are ideal for the formation of a good SEI. Besides a proper choice of the electrolyte, many properties of the graphite itself can influence the SEI formation reaction, e.g., the particle size distribution [2] and/or the graphite surface properties [3]. The reason for this behavior can be attributed to an overpotential effect on the SEI formation in the electrode [4], which can be so large that the formation of a protecting film is no longer assured and the other mentioned effects come into play which exfoliate the graphite particle. Here, a closer look on the SEI formation kinetics depending on the graphite surface properties as well as on the electrolyte mixture is performed by *post mortem* investigations of the film morphology on the particles and by *in situ* differential electrochemical mass spectrometry (DEMS).

Experimental

Electrodes were prepared by casting a mixture of 90% (w/w) TIMREX[®] SFG44 graphite (TIMCAL), pristine or heat-treated for 2 days at 3000 °C in an inert atmosphere, and 10% binder (SOLEF PVDF 1015, Solvay), both suspended in N-methylpyrrolidone (Fluka), on a copper foil. After drying, electrode disks (1.3 cm²) with an active mass loading of 3.6 – 4.2 mg/cm² were punched out. Standard laboratory cells described elsewhere [5] were used for the experiments. Lithium foil (Alfa Aesar) was used as both counter and reference electrode. The two electrodes were separated by a glass fiber separator soaked with electrolyte and pressed against each other with a spring (pressure about 2 kg/cm²). As electrolyte mixtures, ethylene carbonate (EC)/dimethyl carbonate (DMC) 1:1 (w/w), 1 M LiPF₆ and EC/propylene carbonate (PC) 2:1 (w/w), 1 M LiPF₆ (all from Ferro) were used. *Post mortem* scanning electron micrographs (SEM) were recorded after disassembling the cells in an argon-filled glove box and washing the electrodes thoroughly with DMC. For the DEMS experiments, lithiated graphite was used as counter electrode. The setup is described elsewhere [6].

Results

Electrodes containing TIMREX[®] SFG44 graphite (pristine as well as heat-treated, denoted as SFG44HT, the latter with an increased crystallinity and a lower amount of oxygen containing surface groups), were cycled in EC/DMC and EC/PC electrolyte. The first charge/discharge cycle at a specific current of 10 mA/g shows a more or less pronounced additional potential plateau between 0.5 and 0.9 V vs. Li/Li^+ (Figure 1), depending on the electrolyte and the surface properties of the graphite. The length of this plateau is generally attributed to the extent of exfoliation. A lower amount of active surface groups as well as the presence of PC in the electrolyte promotes exfoliation. For these conditions, the electrolyte has obviously a higher influence on the stability than the surface properties as the exfoliation plateau length is comparatively small for the heat-treated SFG44HT in the EC/DMC mixture.

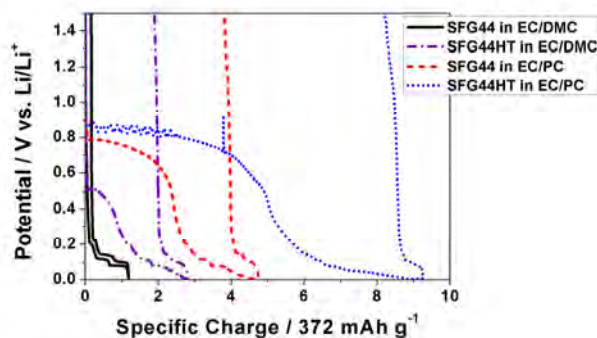


Figure 1: First charge/discharge cycle at 10 mA/g of TIMREX[®] SFG44 and SFG44HT in EC/DMC 1:1, 1 M LiPF₆ and EC/PC 2:1, 1 M LiPF₆.

Post mortem SEM of electrodes, cycled at 160 mA/g in the first charge/discharge cycle and at 50 mA/g for the following 10 cycles, clearly revealed differences in the film morphology on the graphite particles. For the pristine SFG44 graphite cycled in EC/PC, the particles are smoothly covered with a film (Figure 2a). The film on SFG44HT when cycled in EC/DMC shows a rough texture with some small ball-like shaped film structures (Figure 2b). If the latter graphite is cycled in EC/PC electrolyte, a very poor SEI layer is formed and the blank surface of the particle is still undoubtedly recognizable (Figure 2c). The bad protecting properties of the film in the third example are clearly evident by the exfoliated graphite structure. The different film morphologies are attributed to different kinetic inhibition of the electrolyte decomposition reaction on the graphite surface. The ball-like structures on the heat-treated graphite in Figure 2b indicate that the decomposition reaction takes place at distinct nucleation points on the surface.

¹ TIMCAL SA, Bodio

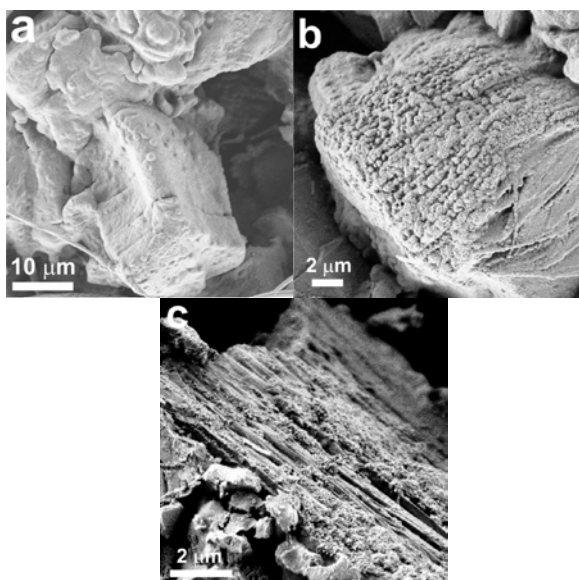


Figure 2: Post mortem SEM of graphite particles cycled at 160 mAh/g. a) TIMREX® SFG44 in EC/PC 2:1, 1 M LiPF₆; b) SFG44HT in EC/DMC 1:1, 1 M LiPF₆; c) SFG44HT in EC/PC 2:1, 1 M LiPF₆.

These nucleation points are related to the active surface groups – a low amount of them cannot provide a film which covers the particle entirely as it is the case for the pristine SFG44 with a high amount of oxygen surface groups. Therefore, the strong kinetic hindrance for the electrolyte decomposition on the non-active surface groups, which are proposed to be, e.g., hydrogen terminated carbons, leads to an insufficient SEI coverage of the surface. This effect increases if the electrolyte itself shows an inhibition for the decomposition as it is the case for EC/PC compared to EC/DMC. The “film” properties are even worse, the surface is not protected at all, and the particle exfoliates strongly, cf. Figure 1. However it has to be admitted that, even the SFG44 graphite exfoliates to some extent in PC containing electrolyte despite the apparently smooth film which covers the entire particle as can be seen in Figure 2a. Thus, under these conditions, the reaction leading to exfoliation, i.e., the solvated Li⁺ cointercalation is obviously not fully suppressed.

The SEI formation reaction is accompanied with the release of gaseous reaction products from the electrolyte decomposition reaction. The evolved gas was monitored with DEMS and correlated with the respective electrochemical curves. Regarding the pristine and the heat-treated graphite in the EC/PC electrolyte, it revealed that a significant current is already flowing at more positive potentials than for the onset of the film forming reaction (Figure 3). This current is attributed to the solvated cointercalation reaction of Li⁺ which finally leads to the exfoliation of graphene sheets. The specific charge consumed between the current onset and the start of the gas evolution was about 5 mAh/g for the pristine graphite while for the heat-treated sample about 13 mAh/g were flown. The unwanted solvated cointercalation reaction is therefore more pronounced for the SFG44HT graphite. In addition, the intensity of the mass spectrometry signals for the evolved gases is significantly higher for the pristine graphite. This stresses the improved electrolyte decomposition reaction when more nucleation points on the surface are present.

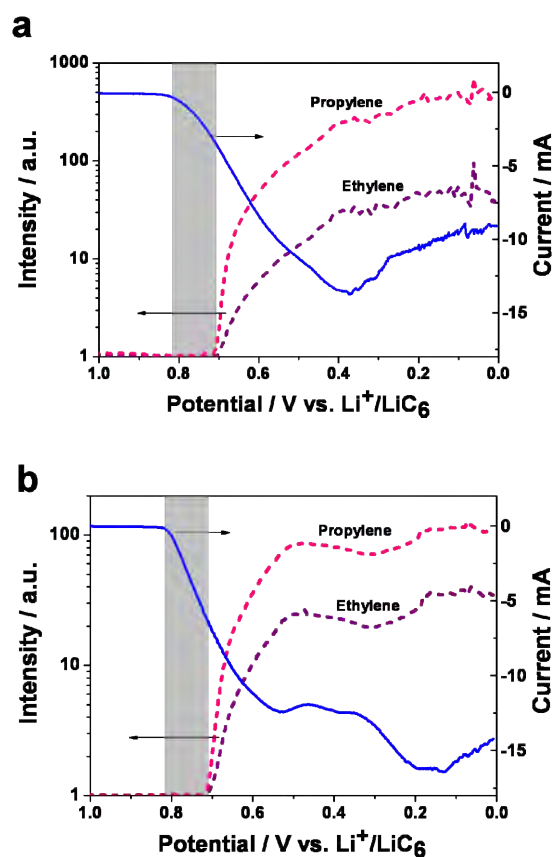


Figure 3: DEMS in cyclic voltammetric mode ($v = 0.2$ mV/s) of a) TIMREX® SFG44 graphite, and b) SFG44HT graphite in EC/PC 2:1, 1 M LiPF₆. The shadowed area highlights the potential difference between current onset and start of gas evolution.

Nevertheless in both cases, solvated cointercalation of Li⁺ was not suppressed as if it is evident from the additional potential plateaus in Figure 1 as well as the delayed gas evolution onset compared to the start of the current in the DEMS experiments. These experiments gave some interesting insights into the competition between SEI formation and exfoliation reaction and confirm the important choice of the right conditions in terms of graphite type and electrolyte.

References

- [1] J. O. Besenhard, M. Winter, J. Yang, W. Biberacher, *J. Power Sources* **54**, 228-231 (1995).
- [2] H. Buqa, A. Würsig, D. Goers, L. J. Hardwick, M. Holzapfel, P. Novák, F. Krumeich, M. E. Spahr, *J. Power Sources* **146**, 134-141 (2005).
- [3] S. H. Ng, C. Vix-Guterl, P. Bernardo, N. Tran, J. Ufheil, H. Buqa, J. Dentzer, R. Gadiou, M. E. Spahr, D. Goers, P. Novák, *Carbon* **47**, 705-712 (2009).
- [4] M. E. Spahr, D. Goers, J. Dentzer, C. Vix, A. Würsig, H. Buqa, W. Märkle, P. Novák, in preparation.
- [5] P. Novák, W. Scheifele, F. Joho, O. Haas, *J. Electrochem. Soc.* **142**, 2544-2540 (1995).
- [6] A. Würsig, W. Scheifele, P. Novák, *J. Electrochem. Soc.* **154**, A449-A454 (2007).

Characterization of bi - material electrode for electrochemical double layer capacitor / lithium ion battery hybrids

D. Cericola, P. Novák, R. Kötz, A. Wokaun

phone: +41 56 310 5172, e-mail: dario.cericola@psi.ch

Among electrochemical energy storage devices electrochemical double layer capacitors (EDLC) and rechargeable lithium ion batteries (LiB) represent the two extremes in terms of specific power and specific energy, respectively. The charging process of an EDLC, which is purely electrostatic and involves only the surface, allows a high power [1, 2]. On the other hand LiBs allow high energy [2] since the faradaic charging process involves the bulk of the electrode material. The idea of combining their power and energy has been realized by hybridization of the two devices. Hybridization on the "internal" level, where a single device is built combining EDLC and LiB electrode materials, can be carried out in a "parallel" or "serial" arrangement of the two materials.

Simulations of external parallel hybrid devices demonstrate that the parallel arrangement is more promising than the serial one [3]. The parallel arrangement allows a current sharing between the two devices which permits the EDLC to deliver the high current which are not accessible by the battery alone.

The internal parallel hybrid can be achieved by the combination of an EDLC material and a LiB material in a bi - material electrode on both electrodes of a device. Such a kind of device has not been presented yet. Bi-material electrodes characterized in a Li containing electrolyte were introduced by few authors [4 - 6] observing an increased energy density compared to a conventional EDLC.

The understanding of the behavior and the interaction of the two materials within the bi - material electrode is of fundamental relevance for the development of an internal parallel hybrid. The current sharing between the two materials during an electrochemical experiment is the key parameter in this context.

Experimental

The current - sharing experiments were performed in the experimental setup schematically reported in Figure 1. A segmented bi-material electrode is used as working electrode in a three electrode cell. The current collector of the working electrode is segmented and the different segments are connected externally of the cell. Two current sensors are used in the external circuit to measure the two branches of the total current. The cell is then connected to a galvanostat / potentiostat as shown in Figure 1, in particular a battery cycler Computer Controlled Cell Capture, (CCCC Astrol Electronics, Switzerland). The current sensors used are two precision shunts (100m Ω , Isabellenhütten, Germany), which ohmic drop was measured by a Data Acquisition Switch Unit 34970A geared with a 34901A multiplexer (Agilent Technologies).

The active materials considered were the activated carbon YP17 (Kuraray Chemical, Japan), a lithium manganese oxide LMO (Honeywell, Germany). Free-standing bound electrodes based on the two different active materials were prepared with the composition 80% active material, 10% additives (Super-P carbon and graphite) and 10% PTFE as binder.

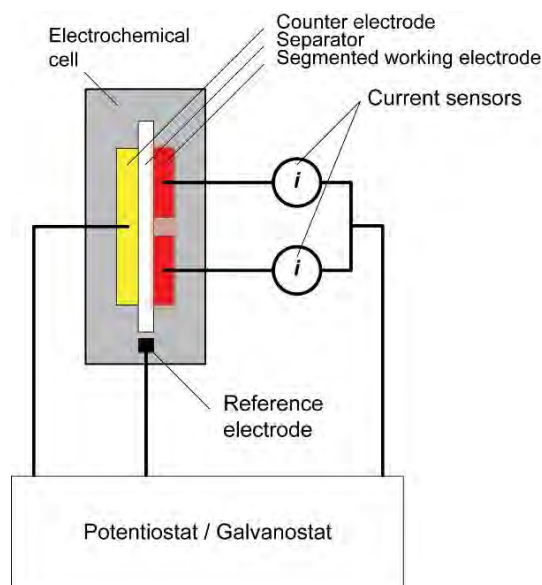


Figure 1. Schematic of the experimental setup for single electrode current sharing experiments..

The electrochemical cells were assembled and sealed in an Ar filled glovebox (with H₂O and O₂ content of < 1ppm). All cell parts were dried at reduced pressure (< 20mbar) at 120 C for at least 12 h before assembling as well as the glass fiber separator (type EUJ116 from Hollingsworth & Vose, UK) and the electrodes. Counter electrode and reference electrode were metallic lithium (Sigma-Aldrich). The electrolyte used was 1 M LiClO₄ dissolved in a mixture of ethylene carbonate / dimethyl carbonate in the ratio 1 to 1 with a water content of less than 20 ppm (Ferro, United States).

The electrochemical characterization consisted in galvanostatic / potentiostatic charge discharge cycles between 3.3 V and 4.3 V vs. reference electrode. A protocol constant current constant potential (CCCV) was applied in order to ensure the complete charge or discharge of the electrode after the constant current step. The charging was performed at constant currents of 17.5 mA/g followed by a potential holding step at 4.3 V for overall time of 8 h. The discharging was performed at constant currents of 17.5, 70, 350, 1400 mA/g followed by a constant potential holding at 3.3 V for an overall duration of 8 h. The corresponding C rates are evaluated according to the hybrid electrode specific charge.

Results

A complete charge / discharge cycle at the specific current of 17.5 mA g⁻¹ and the corresponding current sharing are reported in Figure 2A and B. The charge portion of the cycle can be ideally divided in three parts. In part (i) the potential profile shows a typical capacitor behavior as a straight line and the current sharing in Figure 2B confirms that the main part of the current goes through the capacitor material YP17. The potential profile has a plateau like shape in part (ii) which is a

typical battery feature and correspondingly the current passes mainly through the battery material LMO. At the end of the charging step when LMO is fully charged part (iii) can be identified, where the current passing through YP17 became again dominant. The discharge profile is precisely symmetric.

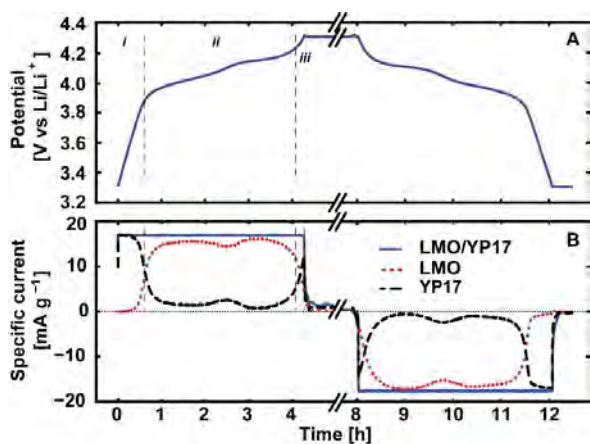


Figure 2. Galvanostatic charge/discharge cycle of a segmented hybrid electrode at the specific current of 17.5 mA/g. The potential profile is shown in A, the total current (blue) and the currents flowing in LMO (red) and YP17 (black) are shown in B.

The results of the characterization at different discharge rates are shown in Figure 3. The currents were normalized with respect to the total current in order to simplify the comparison. The contribution of the two active materials is clearly dependent by the discharge rate. The main part of the current is provided by LMO at slow discharge of 17.5 mA g⁻¹ (0.3C) and 70 mA g⁻¹ (1C). The potential plateau of the battery material LMO can be easily distinguished at these discharge rates.

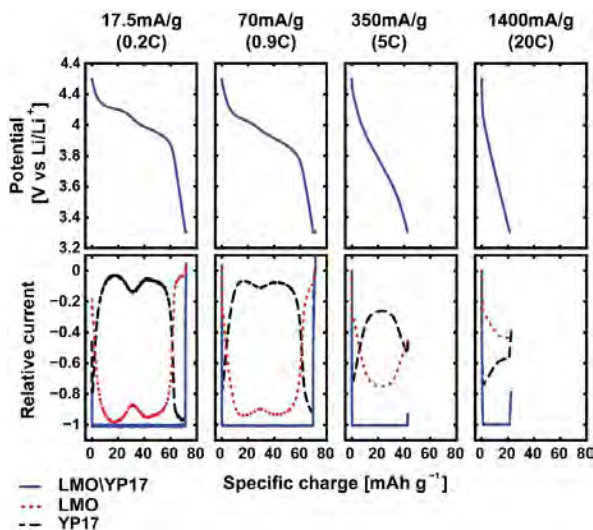


Figure 3. Galvanostatic discharges of a segmented hybrid electrode at different specific currents. The upper part shows the potential profiles, the bottom part shows the corresponding current sharing: total current (blue) current flowing in LMO (red) and in YP17 (black).

At the higher discharge rate of 350 mA g⁻¹ (5C) and 1.4 Ag⁻¹ (20C) the contribution of the current provided by YP17 became significantly more important and it is dominant at the highest discharge rate. The potential plateau, indicating a significant contribution of the battery material, can be hardly recognized in at 5C and it is completely absent at 20C.

Conclusion

A Bi-material electrode based on activated carbon and lithium manganese oxide for an electrochemical double layer capacitor / lithium ion battery hybrid energy storage device has been investigated. The current sharing in single electrode galvanostatic charge / discharge cycles has been presented for the first time. This characterization has clearly shown that the contribution of the two materials to the overall current changes with different discharge regimes. The bi-material electrode has a battery – like behavior at slow discharge rate where the charge is mainly provided by the battery material LMO. At high discharge rate the activated carbon provides the dominant contribution to the total current and the behavior of the bi – material electrode is close to an EDLC electrode.

This peculiarity makes bi-material electrodes very attractive and promising components in the wide scenario of hybrid electrochemical energy storage devices.

Acknowledgement

Financial support of SNSF project number 200021–117607 is gratefully acknowledged.

References

- [1] R. Kötz, M. Carlen, *Electrochim. Acta* **45**, 2483-2498 (2000).
- [2] M. Winter, R.J. Brodd, *Chem. Rev.* **104**, 4245-4269 (2004).
- [3] D. Cericola, P.W. Ruch, R. Kötz, P. Novák, A. Wokaun, *J. Power Sources* **195**, 2731-2736 (2010).
- [4] I. Plitz, A. DuPasquier, F. Badway, J. Gural, N. Pereira, A. Gmitter, G.G. Amatucci, *Appl. Phys. A: Materials Science & Processing* **82**, 615-626 (2006).
- [5] X. Hu, Y. Huai, Z. Lin, J. Suo, Z. Deng, *J. Electrochem. Soc.* **154**, A1026-A1030 (2007).
- [6] X. Hu, Z.H. Deng, J.S. Suo, Z.L. Pan, *J. Power Sources* **187**, 635-639 (2009).

CATALYSIS & INTERFACES

Longevity studies of ultra low Pt anodes for PEFCs

B. Schwanitz, H. Schulenburg, M. Horisberger, A. Wokaun, G.G. Scherer

phone: +41 56 310 5629, e-mail: bernhard.schwanitz@psi.ch

High Pt catalyst loadings and limited PEFC stability are still strong impediments for the wider commercialization of polymer electrolyte fuel cells (PEFCs). The Pt loading for state of the art PEFCs anodes varies between 50 and 100 $\mu\text{g}/\text{cm}^2$ [1]. It is discussed if only a fraction of the catalyst particles participates in the hydrogen oxidation due to its fast kinetics [2]. As shown previously DC magnetron sputter deposition technique can lower Pt loading down to 25 $\mu\text{g}/\text{cm}^2$ without significant loss in performance [3]. Yet, long term stability is an issue to be considered simultaneously next to performance. A basic stability test is to measure the cell voltage over time at a certain current density. In addition accompanying electrochemical impedance spectroscopy (EIS) can give hints for possible sources of loss in fuel cell performance.

Experimental

PEFC anodes were obtained by DC magnetron sputtering of Pt onto a micro porous layer of Vulcan XC72 supported on Carbon Cloth (GDL: LT1410W E-TEK) [3]. The Pt loading was controlled by the sputtering time, and determined by Rutherford Back Scattering Spectroscopy. Commercial electrodes (E-TEK LT140EW; 0.5 $\text{mg}_{\text{Pt}}/\text{cm}^2$) were used as cathode and as anode for comparison. Membrane electrode assemblies (MEAs) were prepared by hot pressing without prior ionomer impregnation. Nafion 212 membranes were used in all experiments. Long term stability of the sputtered anodes in a 30 cm^2 single cell was investigated at 0.5 A/cm^2 , 80°C, 1 bar, $\text{H}_2/\text{O}_2 = 1.5/1.5$, and fully humidified gases. Anode loading for PEFC1, PEFC2 and PEFC3 were 3, 15 and 500 $\mu\text{g}_{\text{Pt}}/\text{cm}^2$. All impedance spectra were measured at $i = 0.3 \text{ A}/\text{cm}^2$. Cyclic voltammetry (CV) was carried out at 80°C, 1 bar, $\text{H}_2/\text{N}_2 = 200 \text{ ml}/\text{min}/200 \text{ ml}/\text{min}$, fully humidified, scan rate 100 mV/s, in the potential range between 0.08 V and 1V.

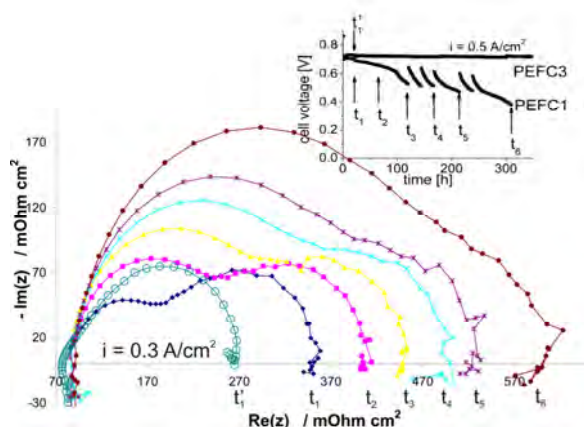


Figure 1. Nyquist plots of a PEFC with a 3 $\mu\text{g}_{\text{Pt}}/\text{cm}^2$ anode recorded at 0.3 A/cm^2 after different run times $t_1 - t_6$ of the cell at constant current density (0.5 A/cm^2). Plot of commercial PEFC3 with 500 $\mu\text{g}_{\text{Pt}}/\text{cm}^2$ is shown at t_1' for comparison. Inset: U-t-curve of the same PEFC running at 0.5 A/cm^2 .

Results and Discussion

PEFC1 shows a voltage loss of 1.12 mV/h compared to PEFC3 with 0.03 mV/h after 310 h run time at 0.5 A/cm^2 (inset, Figure 1). Impedance spectra for PEFC1 have been recorded at 0.3 A/cm^2 for run times $t_1 - t_6$. The Nyquist plots of PEFC1 show two half circles. Reference 4 suggests that the high frequency (hf) semi circle can be attributed to the anode, and the low frequency one to the cathode under our testing conditions. Yet, often the anode semi circle can be neglected due to the fast hydrogen oxidation kinetics. This was found for the commercial system PEFC3 containing a much higher Pt loading for the anode (Figure 1). This is different for PEFCs with sputtered low Pt loaded anodes. With increasing lifetime, the cell voltage of PEFC1 drops and the first semi circle increases, while the second one stays constant. Thus, it is suggested that degradation leading to performance loss is mainly due to the anode. Mass transport limitation and/or a change in kinetics may play a role, however this is not clear to this point.

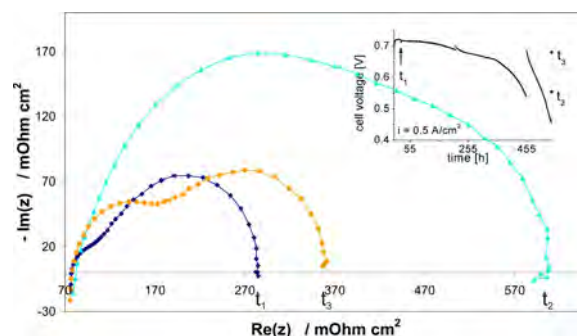


Figure 2. Nyquist plots of a PEFC with 15 $\mu\text{g}_{\text{Pt}}/\text{cm}^2$ anode recorded at 20h, after 524h and after subsequent cycling the anode 4 times between 0.08-1 V (t_3). Inset: U-t-curve of the same PEFC running at 0.5 A/cm^2 .

The results displayed in Figure 2 show that the cell voltage loss is to some extent reversible. After the performance loss and an increase of the hf-semicircle (524h), the anode of PEFC2 was cycled four times between 0.08 – 1V. As a consequence, the cell showed a decrease of the hf-semicircle and an increase in cell voltage at 0.5 A/cm^2 (t_3). This recovery of the cell voltage suggests a poisoning of the anode as cause for the voltage decrease with time.

References

- [1] H.A. Gasteiger, S.S. Kocha, B. Sompalli, F.T. Wagner, Appl. Catal. B : Environmental, **56**, 9-35 (2005).
- [2] A.T. Haug, R.E. White, J.W. Weidner, W. Huang, S. Shi, T. Stoner, N. Rana, J. Electrochem. Soc, **149**, A280-A287 (2002).
- [3] B. Schwanitz, H. Schulenburg, M. Horisberger, A. Wokaun, G.G. Scherer, PSI Electrochemistry Laboratory - Annual Report 2008, 72, ISSN No. 1661-5379 (2008).
- [4] R. O'Hayre, W. Colella, S.-W. Cha, F.B. Prinz, Fuel Cell Fundamentals, John Wiley & Sons, New York, 209-224, (2006) ISBN 978-0-470-25843-9.

Carbon corrosion in polymer electrolyte fuel cells

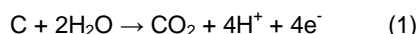
N. Linse, A. Wokaun, G.G. Scherer, L. Gubler

phone: +41 56 310 4668, e-mail: nicolas.linse@psi.ch

In automotive applications, fuel cell degradation caused by start/stop processes is expected to be a major source of performance loss [1]. During start-up and shut-down of the fuel cell by anode air purging, potentials up to 1.5V can occur at the cathode electrode. These elevated potentials lead to substantial structural changes in the cathode catalyst layer, caused by corrosion of the carbon support material. It has been shown that these carbon corrosion induced changes are the main reason for fuel cell performance loss upon start/stop cycling [2]. To be able to develop start/stop protocols which can mitigate degradation, it is necessary to understand the effect of important operating parameters on the carbon corrosion rate.

Experimental

To determine the influence of humidity, temperature and potential on the carbon corrosion rate, fuel cells operated in H₂/N₂ mode were exposed to single triangular potential pulses in order to simulate the detrimental conditions occurring during fuel cell start-up and shut-down. Carbon corrosion rates were calculated by integration of the resulting CO₂ concentration peaks in the cathode exhaust gas (cf. equation 1).



All experiments were performed using 16cm² cells with parallel flow fields and MEAs fabricated by hot pressing of a Nafion 212 membrane and commercially available electrodes (0.4 mgPt/cm²). For the experiments with different upper potential limits, the cell was operated with fully humidified gases at 80°C. Pulse duration was kept constant by changing the scan rate, starting at 30mV/s for an upper limit of 1.0V. The lower potential limit was 0.6V in all cases. For humidity and temperature variation experiments, potential pulses between 0.6V and 1.3V were applied. Experiments with varied temperatures were performed using fully humidified gases. In order to determine the effect of reactant gas humidity, temperature was kept constant at 70°C and 80°C, respectively.

Results

Increasing the upper potential limit of the applied voltage pulse leads to a strong increase in carbon corrosion rate (Figure 1a). This exponential-like behaviour explains the severe fuel cell degradation observed in start/stop cycling experiments under open circuit potential conditions and the strong mitigating effect of an external load [2]. A similar trend was found for varied temperatures (Figure 1b). In this case, however, the strong increase of corrosion rate with increasing temperature is based on two effects. First, temperature itself influences the reaction rate. Second, water vapour partial pressure, which increases exponentially with temperature in case of fully humidified gases, has a significant promoting effect on the carbon corrosion rate. Measurements with varied reactant gas humidifications at constant temperatures exhibit a linear correlation between water vapour partial pressure and carbon corrosion rate (Figure 2). Increasing the temperature leads to a parallel shift towards higher corrosion rates.

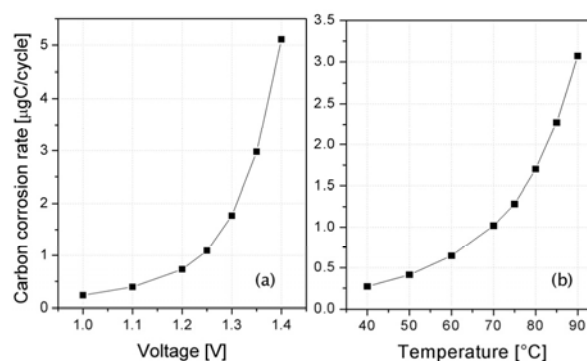


Figure 1. Influence of (a) upper potential limit (100%RH, 80°C) and (b) temperature (100%RH) on carbon corrosion rate.

Additionally, Figure 2 shows the corrosion rates displayed in Figure 1b, now plotted against the respective water vapour partial pressure values instead of temperature. If only the effect of temperature is considered (i.e. at a constant water vapour partial pressure), the increase of corrosion rate with temperature is significantly smaller compared to the exponential-like behaviour shown in Figure 1b, where both, temperature and water vapour partial pressure influence corrosion rate.

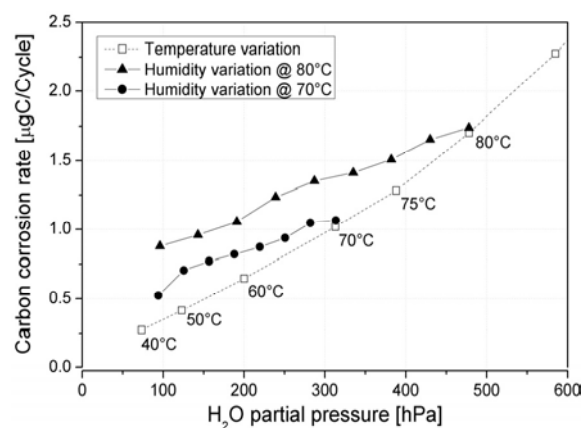


Figure 2. Influence of water vapour partial pressure on carbon corrosion rate for temperatures of 70°C and 80°C. Additionally, carbon corrosion rates from Figure 1b are plotted against the respective water vapour partial pressures (dashed line).

The results show that a reduction of humidity and temperature are suitable to mitigate start/stop induced degradation. Since changes in temperature are usually too time-consuming in practical applications, dry gas purging prior to start-up or shut-down with an applied resistance is a viable method to increase fuel cell lifetime.

References

- [1] R. Shimoi, T. Aoyama, A. Iiyama, SAE World Congress, Fuel Cell Vehicle Applications Session, SP-2236, 105-115, April 20-23, Detroit, USA, (2009).
- [2] N. Linse, C. Aellig, A. Wokaun, G.G. Scherer, L. Gubler, ECS Transactions **25**, 1849-1859 (2009).

Influence of modified glassy carbon substrate on electrochemical platinum deposition

A. Savouchkina, A. Foelske-Schmitz, R. Kötzt, G.G. Scherer, A. Wokaun

phone: +41 56 310 5532, e-mail: anastasia.savouchkina@psi.ch

The lifetime of polymer electrolyte fuel cells (PEFC) is greatly limited by the degradation of the cathode catalyst and its support. One goal of our studies is to identify the correlation between corrosion behavior of the catalyst and the properties of the carbon support. Highly oriented pyrolytic graphite (HOPG) or glassy carbon (GC) K-type are used as supports for the investigated model electrodes. GC K-type is a non-graphitizing carbon produced by pyrolysis of phenolic resins. It is known from literature [1, 2], that heating GC K-type at 450°C in air results in opening of the micropores (1-5 nm in diameter) already present in the material and formation of a porous layer with a thickness of up to 40 µm, depending on the temperature and the length of the thermal treatment. On the one hand, this opening of the pores and the presence of the porous surface layer are supposed to improve the adhesion of the platinum catalyst to the support and, thus, render it more stable under corrosive conditions. On the other hand, the layer should not be too thick, as the increased double layer capacity (from µF/cm² up to mF/cm²) complicates the electrochemical characterization of the catalysts by obscuring the platinum features in the respective cyclic voltammograms (CV). Electrochemical platinum deposition was done upon un-treated and thermally treated GC samples and the results were compared.

Experimental

The electrochemical deposition of platinum upon glassy carbon was performed in a glass cell, in which a polyether ether ketone (PEEK) sample holder exposed a 1 cm² circular area of glassy carbon to the plating solution containing aqueous 5 mM hexachloroplatinic acid and 0.5 M sulfuric acid. The solution was prepared using UHQ (ultra high quality) water (> 18 mΩ cm⁻¹). Glassy carbon was employed as counter electrode (CE) and mercury/mercury sulfate (MSE; +680 mV vs. hydrogen standard electrode) in a separate electrolyte compartment as reference electrode (RE) connected to the main cell by a salt bridge. The working electrode was immersed into the platinum plating solution at a potential of +200 mV vs. MSE (to avoid electroless platinum deposition). For Pt deposition the potential was stepped from this value to the deposition potential of -700 mV vs. MSE. After the application of the deposition potential, the electrode potential was stepped back to +200 mV vs. MSE and the working electrode removed from the solution. The pulse train was applied using a computer controlled (PARcontrol 0.86) potentiostat/galvanostat (EG&G Princeton Applied Research A 370).

Scanning electron microscopic (SEM) images of the sample surfaces were obtained with ZEISS SUPRA 55 VP SEM. Images were evaluated using the image software Image J (W. Rasband, NIH, USA).

Results

The electrochemical deposition of Pt is well known from literature [3, 4]. It is common to control the size and the size distribution of the deposited platinum nanoparticles

by changing the length of the applied pulse. Herein, the size and the size distribution of Pt nanodots were investigated as a function of the modified carbon support. The current transients recorded during platinum deposition show similar current values for untreated glassy carbon and HOPG and increased values for thermally treated GC (Figure 1). These high current values, however, are largely due to the double layer charging, the reduction of oxygen-containing functional groups on the carbon substrate surface, created in the process of thermal treatment, and/or the evolution of hydrogen in the active layer.

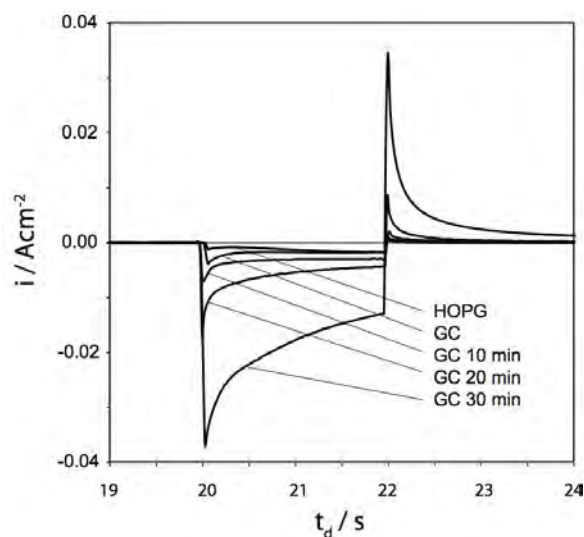


Figure 1. Current transients recorded during platinum deposition on various substrates.

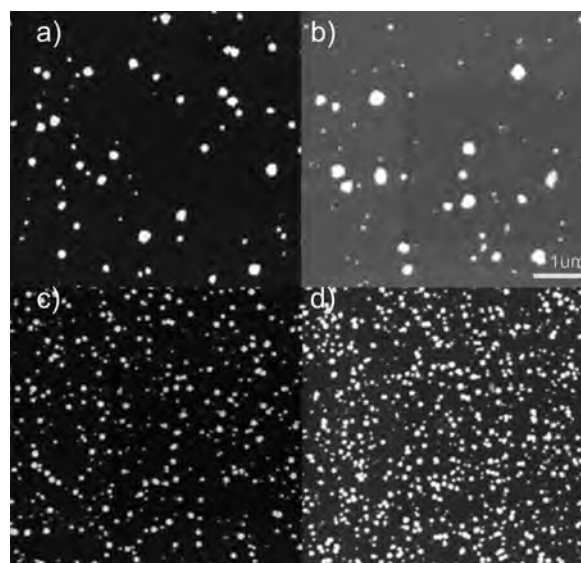


Figure 2. Electrochemical platinum deposition (pulse length 2s) upon a) untreated GC; b) GC heated for 10min@450°C; c) GC heated for 20min@450°C and d) GC heated for 30min@450°C.

These considerations were confirmed by recording current transients for pulsing GC in 0.5M sulfuric acid which did not contain any platinum and observing the same results as for Figure 1.

The resulting SEM images (Figure 2) show differences for the treated and untreated GC substrates. A decrease in Pt particle diameter and an increased Pt coverage was observed after thermal treatment for various deposition pulse lengths. For the pulse length of 2 s, for instance, the average Pt dot diameter on untreated GC is 120 nm and on GC thermally treated for 30 minutes it is 65 nm (Figure 3). Also, for thermally treated GC, pulses longer than 2 s do not lead to any further growth of the dots' mean diameter (contrary to the growth observed for untreated GC, Figure 3), however, the surface coverage (area of the glassy carbon electrode covered with platinum nanodots) significantly increases (by 50 %) for longer thermal treatment. For the pulse length of 2 s, for example, the surface coverage for untreated glassy carbon is 4 % as opposed to 10 % for GC thermally treated for 30 minutes (Figure 3 bottom). Moreover, on untreated GC samples the slightly increased surface coverage due to longer pulses seems to originate from a larger diameter. Meanwhile, on thermally pre-treated GC the increased surface coverage due to longer pulses is solely due to larger amount of deposited Pt, as the diameter of the dots is always smaller than for untreated GC and does not significantly change once a certain pulse length (in this case 2 s) is reached. These observations may be explained by the opening of the pores, a process leading to enhanced density of defects, which offer more nucleation sites for crystallization. The micropores at the surface also suppress surface diffusion of platinum atoms and, thus, further 2 D crystal growth which obviously occurs on the untreated GC samples.

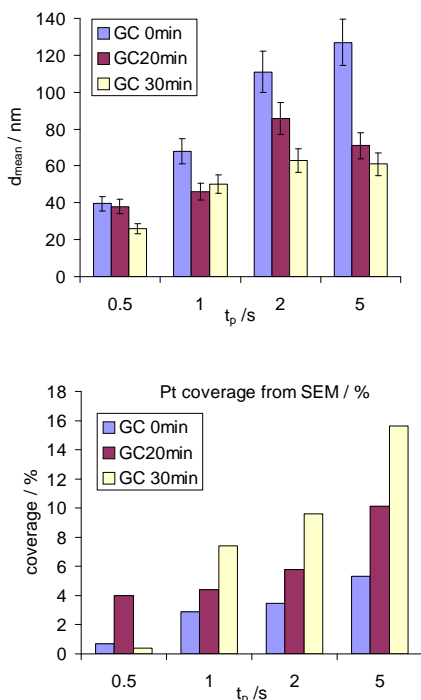


Figure 3. Top: mean Pt dot diameter for the pulse length of 0.5, 1, 2 and 5 s for GC thermally treated for 0, 20 and 30 minutes. Bottom: Pt coverage of the GC surface for the pulse length of 0.5, 1, 2 and 5 s for GC thermally treated for 0, 20 and 30 minutes

Further differences between untreated and heated GC substrates can be found for the particle diameter distribution. Untreated GC samples (as well as HOPG) display quite a wide range of particle diameters; for the pulse length of 2 s it is possible to find dots with 25 but also 300 nm (Figure 4 top left). On the contrary, the dots on thermally treated GC show a narrower size distribution with a sharp pronounced “mean diameter” value (Figure 4 bottom right). This behaviour becomes more pronounced with increasing heating time (compare GC 10min 2s, GC 20min 2s and GC 30min 2s in Figure 4). Therefore, it is possible to gain more control over the diameter of electrochemically deposited Pt dots without having to dramatically decrease the pulse length.

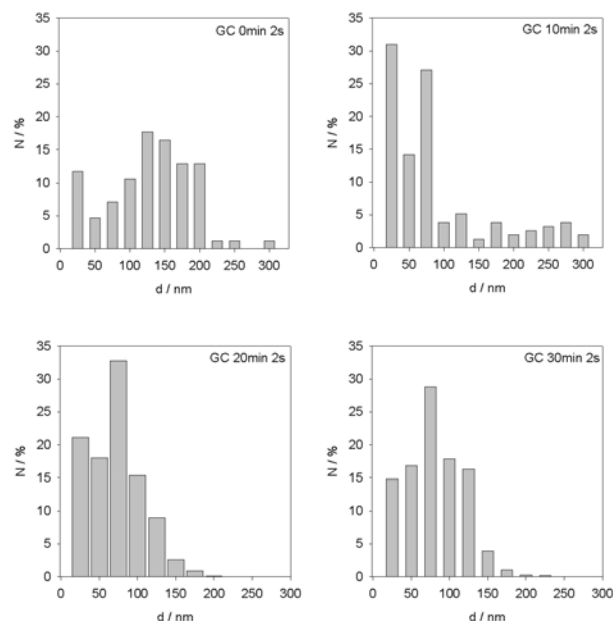


Figure 4. Pt dots diameter distribution for the pulse length of 2 s on untreated GC and GC thermally treated for 10, 20 and 30 minutes).

In general, several intriguing differences were stated for electrochemical platinum deposition on untreated and thermally treated GC. The diameter but also diameter distribution of the Pt dots as well as the surface coverage is clearly related to the length of the thermal pre-treatment of the GC substrate. Further investigations will be conducted to determine, whether the corrosion behaviour of the substrate is equally dependent on the thermal pre-treatment of GC.

Acknowledgement

The authors would like to thank Swiss National Foundation (SNSF) for financing the project 200021-121719/1.

References

- [1] A. Braun, M. Bärtsch, O. Merlo, B. Schnyder, R. Kötz, O. Haas, A. Wokaun, *Carbon* **41**, 759-765 (2003).
- [2] A. Braun, M. Bärtsch, B. Schneider, R. Kötz, O. Haas, H. G. Haubold, G. Goerigk, *J. Non-Cryst. Solids* **260**, 1-14 (1999).
- [3] J. V. Zoval, J. Lee, S. Gorer, R. M. Penner, *J. Phys. Chem. B* **102**, 1166-1175 (1998).
- [4] C. Paoletti, A. Cemmi, L. Giorgi, R. Giorgi, L. Pilloni, E. Serra, M. Pasquali, *J. Power Sources* **183**, 84-91 (2008).

THE ELECTROCHEMISTRY LABORATORY

IMPRESSIONS

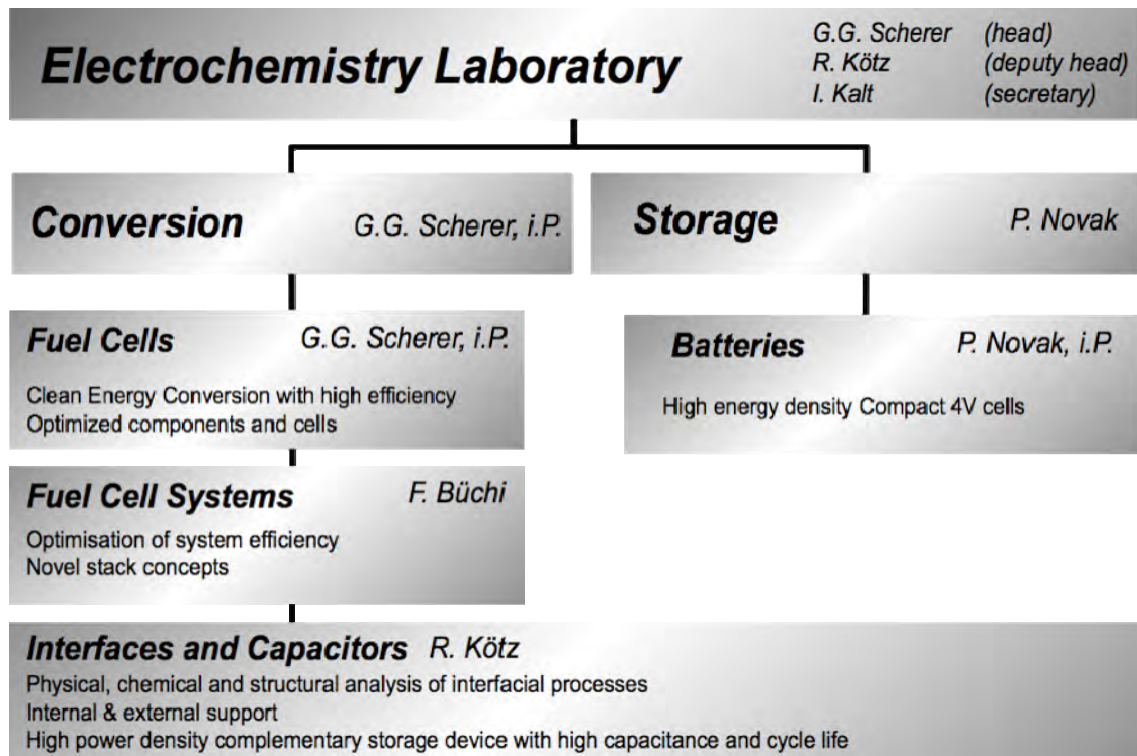


Impressions of the PSI
"Tochtertag" held on
November 9, 2009 (top)

and of the 25th One-Day-
Symposium on Topics in
Electrochemistry on May 6,
2009 (left and below).



STRUCTURE



ECL-PERSONNEL

Staff

Ben youcef Hicham, Dr. (since March) ♦ **Bernard Jérôme, Dr.** ♦
Boillat Pierre, Dr. (since June) ♦ **Büchi Felix, Dr.**

Colin Jean-François, Dr. ♦ **Colinart Thibaut** (until August)

Foelske Annette, Dr.

Gloor Thomas ♦ **Gubler Lorenz, Dr.**

Henkensmeier Dirk, Dr. (until April) ♦ **Hofer Marcel**

Kaiser Hermann ♦ **Kalt Isabella** ♦ **Kötz Rüdiger, Dr.**

Lüscher Sandro

Maire Pascal, Dr. ♦ **Märkle Wolfgang, Dr.** ♦ **Marmy Christian**

Novák Petr, Dr.

Perego Raffaella, Dr.

Sasaki Tsuyoshi (since May) ♦ **Scheifele Werner** (until July) ♦ **Scherer Günther G., Dr.** ♦
Schneider Holger, Dr. (since April) ♦ **Schneider Ingo, Dr.** ♦ **Schulenburg Hendrik, Dr.** ♦
Siegrist Raphael (since June) ♦ **Sommer Heino, Dr.** (since July)

Thut Jürg

Wambach Jörg, Dr. (until April)

PhD Students

Bayer Michael ♦ **Ben youcef Hicham** (until February) ♦ **Bernardo Philippe** ♦
Boillat Pierre (until May)

Cericola Dario

Dockheer Sindy

Eller Jens (since January)

Flückiger Reto (until June)

Godbole Vikram

Hess Michael (since October) ♦ **Hintennach Andreas**

Jetsrisuparb Kaewta (since June)

Kreitmeier Stefan (since October)

Linse Nicolas

Menampambath Mini Mol (until December)

Oberholzer Pierre

Patey Timothy (until September)

Ruch Patrick (until August)

Savouchkina Anastasia ♦ **Schuler Gabriel** ♦ **Schwanitz Bernhard** ♦
Seyfang Bernhard (until September) ♦ **Simmen Franziska**

Verma Pallavi ♦ **Von Dahlen Steffen**

Wallasch Frank

Zaglio Maurizio ♦ **Zellweger Hans** (until February)

THESE PHD STUDENTS FROM ECL GRADUATED IN 2009

**Dr. Hicham
Ben youcef**



*Radiation grafted ETFE based membranes for fuel cells:
improved mechanical and oxidative stability*

Ph.D. Thesis, No. 18215, ETH Zürich, February 2009

Examiners Prof. Dr. A. Wokaun, PSI/ETH Zürich
Prof. Dr. A.D. Schlüter, ETH Zürich
Dr. G.G. Scherer, PSI Villigen

Dr. Pierre Boillat



*Advanced characterization of polymer electrolyte fuel cells
using high resolution neutron imaging*

Ph.D. Thesis, No. 18397, ETH Zürich, May 2009

Examiners Prof. Dr. A. Wokaun, PSI/ETH Zürich
Prof. Dr. J. Mesot, PSI/ETH Zürich
Dr. G.G. Scherer, PSI Villigen

Dr. Patrick Ruch



*Charge storage and aging phenomena in electrochemical
double layer capacitors*

Ph.D. Thesis, No. 18400, ETH Zürich, Mai 2009

Examiners Prof. Dr. A. Wokaun, PSI/ETH Zürich
Prof. Dr. R. Nesper, ETH Zürich
Dr. R. Kötz, PSI Villigen

Dr. Reto Flückiger



*Transport phenomena on the channel rib scale of polymer
electrolyte fuel cells*

Ph.D. Thesis, No. 18509, ETH Zürich, July 2009

Examiners Prof. Dr. A. Wokaun, PSI/ETH Zürich
Prof. Dr. D. Poulidakos, ETH Zürich
Dr. G.G. Scherer, PSI Villigen
Dr. F. Büchi, PSI Villigen

**Dr. Bernhard
Seyfang**



Simplification and investigation of polymer electrolyte fuel cells using micro-patterned glassy carbon flow fields

Ph.D. Thesis, No. 18508, ETH Zürich, July 2009

Examiners Prof. Dr. A. Wokaun, PSI/ETH Zürich
Prof. Dr. P. Rudolf von Rohr, ETH Zürich
Dr. G.G. Scherer, PSI Villigen
PD Dr. T. Lippert, PSI Villigen

Dr. Timothy Patey



Oxide nanoparticles for electrodes in lithium-ion batteries

Ph.D. Thesis, No. 18648, ETH Zürich, November 2009.

Examiners Prof. Dr. A. Wokaun, PSI/ETH Zürich
Prof. Dr. P. Novák, PSI/ETH Zürich
Prof. Dr. W.J. Stark, ETH Zürich

EXCHANGE STUDENTS, DIPLOMA THESES, SUMMER STUDENTS

Régis Müller	<i>Membrane degradation in polymer electrolyte fuel cells</i> Universität Basel, August 2008 – February 2009.
Christof Aellig	<i>Investigation of start/stop induced degradation in polymer electrolyte fuel cells with the help of potential cycling</i> ETH Zürich, February – June 2009.
Stephan Bähler	<i>Bestimmung der mechanischen Eigenschaften von PEFC-Membranen unter definierten Temperatur- und Feuchtigkeitsbedingungen</i> ETH Zürich, February – June 2009.
Chia-Ying Lu	<i>Investigation of the mechanism of graphite exfoliation in propylene and ethylene carbonate based electrolytes</i> University of Amiens, FR, February – August 2009.
Raphael Gyr	<i>Diisopropenylbenzene as new crosslinker for radiation grafted ETFE based membranes for fuel cells</i> ETH Zürich, May – July 2009.
Baptiste Latouche	<i>Micro x-ray tomography of polymer electrolyte fuel cells</i> Institut National Polytechnique, PHELMA, Grenoble, France, May - July 2009.
Rosie Marriott	<i>Synthesis and characterization of organic model passivation layers on lithium-ion battery electrodes</i> Durham University, UK, June – September 2009.
Fabian Welte	<i>Introduction to radiation grafted membranes for fuel cells</i> Gymnasium Klettgau, DE, October 2009.

SEMINAR, INVITED SPEAKERS

Prof. Manfred Wilhelm Universität Karlsruhe, DE	<i>New developments in mechanical characterisation of materials</i> January 19, 2009.
Prof. Jürgen Janek Justus-Liebig-Universität Gießen, DE	<i>Interface kinetics of solid electrolytes</i> January 26, 2009.
Dr. Tsuyoshi Sasaki Toyota Central R&D Labs., Inc., Aichi, JP	<i>Research activity on Li-ion battery at Toyota Central R&D Laboratories</i> March 09, 2009.
Prof. Gerd Ganteför, Universität Konstanz, DE	<i>Chemical properties of clusters: Every atom counts</i> April 20, 2009.
Prof. Thomas Wandlowski Universität Bern	<i>In-situ ATR-SEIRAS: An approach to probe structure and reactivity at electrified solid/liquid interfaces</i> May 26, 2009.
Prof. Mohamad Al Sheikhly, University of Maryland, USA	<i>The fundamental radiation chemistry mechanisms and kinetics of the electron beam irradiation polymerization, and grafting</i> June 15, 2009.
Henrik Nordborg CADFEM (Suisse) AG, Aadorf	<i>Fuel cell simulations and customized code development with ANSYS-fluent and diffpack</i> June 22, 2009.
Prof. Klaus Müller University Trento, IT	<i>Solid-state NMR studies of polymeric fuel cell membranes</i> July 13, 2009.
Dr. Matthias Arenz TU München, DE	<i>Investigations on Pt based high surface area catalysts for PEM fuel cells</i> August 31, 2009.
Dr. Rittmar von Helmolt Opel, Mainz-Kastell, DE	<i>Fuel cell and range-extended battery vehicles - the future of electric propulsion</i> September 21, 2009.
Dr. Hans-Peter Brack SABIC Innovative Plastics AC Bergen op Zoom, NL	<i>An introduction to intellectual property for technologists</i> October 05, 2009.
Prof. Shunsuke Muto Nagoya University, JP	<i>Diagnostic analysis of Li ion secondary batteries by STEM-EELS/SI-MCR</i> October 12, 2009.
Prof. Siegfried Waldvogel Universität Bonn, DE	<i>Novel concepts for the electrochemical synthesis of organic compounds</i> December 07, 2009.

AWARDS

Günther G. Scherer

Christian Friedrich Schönbein Medal of Honour.

In recognition of his distinguished contributions to the science and technology of fuel cells

Scientific Advisory Committee of the European Fuel Cell Forum 2009, Lucerne, July 2, 2009.

CONFERENCES – SYMPOSIA

**25th One-Day-Symposium
May 6, 2009**

Electrochemistry: Learning from the past to master the future

Organizers: G.G. Scherer, R. Kötz and Petr Novák

Contributions from:

Dieter Kolb, University of Ulm, DE
Nenad Markovic, ANL Argonne, USA
Joachim Meier, MPI Stuttgart, DE
Jean-Marie Tarascon, CNRS Amiens, FR
Andreas Züttel, EMPA Dübendorf
Manfred Waidhas, Siemens Erlangen, DE

**IAEA 2nd Research Coordination Meeting
June 15-19, 2009**

*Development of novel absorbents and membranes by
radiation-induced grafting for selective purposes*

Organizer: G.G. Scherer

Contributions from 15 different countries



Lecturers and organization staff of the 25th One-Day-Symposium at PSI.

From left to right: Felix Büchi, Günther G. Scherer, Manfred Waidhas, Andreas Züttel, Elephant, Isabella Kalt, Dieter Kolb, Rüdiger Kötz, Nenad Markovic, Joachim Maier (not on the picture: Jean-Marie Tarascon)

REVIEW ACTIVITIES OF THE LABORATORY

Journals

Advanced Functional Materials

Carbon

Electrochimica Acta ♦ Electrochemistry Communications ♦ Electrochemical and Solid-State Letters♦
Energy ♦ Energy & Fuels

Fuel Cells

Journal of Alloys and Compounds ♦ Journal of Electroanalytical Chemistry ♦ Journal of the Electrochemical Society ♦ Journal of Membrane Science ♦ Journal of Micromechanical and Microengineering ♦ Journal of Physical Chemistry ♦ Journal of Power Sources ♦ Journal of Solid State Electrochemistry

Langmuir

Material Sciences and Engineering B

Nature Materials

Sensors

Organisations

Alexander von Humboldt-Stiftung, DE

Carl von Linde Junior Fellowship of IAS-TUM, DE

FWF Der Wissenschaftsfond, AT

Wissenschaftliche Kommission Niedersachsen, DE

Co-Referee's Report for Dissertations

H. Ben youcef, PSI/ETH Zürich, P. Boillat, PSI/ETH Zürich

R. Flückiger, PSI/ETH Zürich

T. Patey, PSI/ETH Zürich

P. Ruch, PSI/ETH Zürich

B. Seyfang, ETH/PSI Zürich

INDUSTRIAL PARTNERS

The Laboratory had the pleasure to collaborate with the following industrial partners during the year 2009:

BASF SE, Ludwigshafen, DE ♦ Belenos Clean Power, Biel

CEKA Elektrowerkzeuge AG, Wattwil

MES DEA, Stabio

Proton Motors, Puchheim, DE

TIMCAL SA, Bodio

PROJECT COLLABORATIONS WITH EXTERNAL PARTNERS

CCEM

F.N. Büchi, S. Ulli-Beer
Projektleiter

*hy.muve: Development of **hydrogen** powered **municipal vehicle***
with EMPA Dübendorf and Industrial Partners

BFE

F.N. Büchi
Projektleiter

Cal.PEF-CH: Modelbased investigation of PE fuel cell performance with focus on porous layer properties
with ZHAW, Winterthur

F.N. Büchi
Projektleiter

Röntgen Mikro-Tomographie an Polymerelektrolyt-Brennstoffzellen

F.N. Büchi
Projektleiter

Gasanalysis in polymer electrolyte fuel cells

L. Gubler
Projektleiter

Lebensdauer-Limitierungen von Brennstoffzellen-Membranen: Mechanismen, Methoden und Innovationen

L. Gubler, I.A. Schneider
Projektleiter

go.PEF-CH: Enhancing PEFC durability and reliability under application-relevant conditions
Partner: Berner Fachhochschule Technik und Informatik (BFH-TI, Biel BE), CEKA Elektrowerkzeuge AG & Co. KG (Wattwil SG), MES-DEA SA. (Stabio TI)

EU

P. Novák
Projektleiter

MAHEATT

Industry

P. Boillat, G.G. Scherer
Projektleiter

Diagnostics of polymer electrolyte fuel cells
Automotive industry

J.-F. Colin
Projektleiter

Oxide für Lithiumionen-Batterien
BASF SE, Ludwigshafen

T. Colinart, F.N. Büchi
Projektleiter

Diagnostics of polymer electrolyte fuel cells
Automotive Industry

W. Märkle
Projektleiter

Graphite für Lithiumionen-Batterien
TIMCAL SA, Bodio

P. Novák
Projektleiter

Projekt HE-Lion
BASF SE, Ludwigshafen

Nationalfonds

A. Foelske-Schmitz
Projektleiterin

Degradation mechanisms of electro-catalysts used in polymer electrolyte fuel cells

R. Kötz
Projektleiter

Graphite oxides and graphene for electrochemical energy storage

P. Maire
Projektleiter

Synthetic solid electrolyte interphase on carbon electrodes for lithium-ion batteries

P. Novák
Projektleiter

Advanced materials for efficient portable energy supplies

TEACHING ACTIVITIES

University Level Teaching

Prof. Dr. P. Novák,
Prof. Dr. A. Wokaun

Technische Elektrochemie
ETH Zürich, HS 2009

Prof. Dr. A. Wokaun,
Dr. G.G. Scherer,
Prof. Dr. K. Boulouchos

Renewable Energy Technologies II
ETH Zürich, FS 2009

PUBLICATIONS

Books and Reviewed Book Chapters

F.N. Büchi, M. Inaba¹,
T.J. Schmidt²

Polymer electrolyte fuel cell durability
Springer Science + Business Media, LLC 2009
ISBN 978-0-387-85534-9.

¹ Doshisha University, Kyoto, Japan

² BASF Fuel Cell GmbH, Frankfurt, Germany

F.N. Büchi

Mathematical modeling of fuel cells
Fuel Cells: Problems and Solutions, Edited by V.S. Bagotsky,
Chapter 15, 255-261 (2009)
John Wiley & Sons, Inc.
ISBN 978-0-470-23289-7.

F.N. Büchi

Heterogeneous cell ageing in polymer electrolyte fuel cell stacks
Polymer Electrolyte Fuel Cell Durability, Edited by F.N. Büchi,
M. Inaba, T.J. Schmidt, 431-439 (2009)
Springer Science+Business Media, LLC 2009 ISBN 978-0-387-85534-9, e-ISBN 978-0-387-85536-3.

S.A. Freunberger, M. Reum,
F.N. Büchi

Design approaches for determining local current and membrane resistance in polymer electrolyte fuel cells (PEFCs)
Handbook of Fuel Cells – Fundamentals, Technology and Applications, Edited by W. Vielstich,
H.A. Gasteiger, H. Yokokawa
John Wiley & Sons, Chichester, Vol. 6, Chapter 41, 603-615
(2009) ISBN 978-0-470-72311-1.

L. Gubler, G.G. Scherer

Durability of radiation grafted fuel cell membranes
Polymer Electrolyte Fuel Cell Durability, Edited by F.N. Büchi,
M. Inaba, T.J. Schmidt
Springer, New York, 133-155 (2009)
ISBN 978-0-387-85534-9. doi: 10.1007/978-0-387-85536-3.

L. Gubler, G.G. Scherer

Radiation grafted proton conducting membranes
Handbook of Fuel Cells – Fundamentals, Technology and Applications, Edited by W. Vielstich, H.A. Gasteiger,
H. Yokokawa,
John Wiley & Sons, Chichester, Vol. 5, Chapter 20, 313-321
(2009) ISBN 978-0-470-72311-1.

P. Novák, D. Goers¹,
M.E. Spahr¹

Carbon materials in lithium-ion batteries
Carbon materials for electrochemical energy storage systems
Edited by F. Béguin and E. Frackowiak
CRC Press - Taylor and Francis Group, Boca Raton-New York,
263-328 (2009) ISBN 10: 1420053078,
ISBN 13: 9781420053074.

¹ TIMCAL SA, Bodio

I.A. Schneider, G.G. Scherer

Local transient techniques in polymer electrolyte fuel cell (PEFC) diagnostics
Handbook of Fuel Cells – Fundamentals, Technology and Applications, Edited by W. Vielstich, H.A. Gasteiger, H. Yokokawa,
John Wiley & Sons, Chichester, Vol. 6, Part 4, Chapter 45,
673-686 (2009) ISBN 978-0-470-72311-1.

Peer Reviewed Papers

J. Becker¹, R. Flückiger,
M. Reum, F.N. Büchi,
F. Marone, M. Stampanoni

Determination of material properties of gas diffusion layers: Experiments and simulations using phase contrast tomographic microscopy

J. Electrochem. Soc. **156**, B1175-B1181 (2009).

doi: 10.1149/1.3176876

¹ Fraunhofer ITWM, Kaiserslautern, Germany

H. Ben youcef, L. Gubler,
S. Alkan Gürsel, T. Yamaki¹,
S. Sawada¹, A. Wokaun,
G.G. Scherer

Crosslinker effect in ETFE based radiation grafted proton conducting membranes: II. Extended fuel cell operation and degradation analysis

J. Electrochem. Soc. **156**, B532-539 (2009).

doi: 10.1149/1.3082109.

¹ Japan Atomic Energy Agency (JAEA), Japan

J. Bernard, S. Delprat¹,
F.N. Büchi, T.M. Guerra¹

Fuel cell hybrid powertrain: Towards minimization of hydrogen consumption

IEEE Transaction on Vehicular Technology **58**, 3168-3176 (2009).

doi: 10.1109/TVT.2009.2014684

¹ Université de Valenciennes et du Hainaut-Cambrésis, France

H. Ben youcef, L. Gubler,
S. Alkan-Gürsel,
D. Henkensmeier,
A. Wokaun, G.G. Scherer

Novel ETFE based radiation grafted poly(styrene sulfonic acid-co-methacrylonitrile) proton conducting membranes with increased stability

Electrochem. Commun. **11**, 941-944 (2009).

doi: 10.1016/j.elecom.2009.02.047

I. Bilecka¹, A. Hintennach,
I. Djerdj¹, P. Novák,
M. Niederberger¹

Efficient microwave-assisted synthesis of LiFePO₄ mesocrystals with high cycling stability

J. Mater. Chem. **19**, 5125-5128 (2009).

doi: 10.1039/b909545d

¹ ETH Zürich

I. Czekaj, F. Loviat,
J. Wambach, A. Wokaun

Nickel deposition on γ -Al₂O₃: Modelling metal particle behaviour at the support

Chimia **63**, 193-196 (2009).

doi: 10.2533/chimia.2009.193

S.Y. Chew, S.H. Ng,
J. Wang¹, P. Novák,
F. Krumeich², S.L. Chou¹,
J. Chen¹, H.K. Liu¹

Flexible free-standing carbon nanotube films for model lithium-ion batteries

Carbon **47**, 2976-2983 (2009).

doi: 10.1016/j.carbon.2009.06.045

¹ University of Wollongong, Australia

² ETH Zürich

- S.Y. Chew, T.J. Patey, O. Waser¹, S.H. Ng, R. Büchel¹, A. Tricoli¹, F. Krumeich¹, J. Wang², H.K. Liu², S.E. Pratsinis¹, P. Novák
- Thin nanostructured LiMn₂O₄ films by flame spray deposition and in situ annealing method*
 J. Power Sources **189**, 449-453 (2009).
 doi: 10.1016/j.powsour.2008.12.085
¹ ETH Zürich
² University of Wollongong, Australia
- G. Frei, E.H. Lehmann, D. Mannes, P. Boillat
- The neutron micro-tomography setup at PSI and its use for research purposes and engineering applications*
 Nucl. Instrum. Methods Phys. Res., Sect A **605**, 111-114 (2009)
 doi: 10.1016/j.nima.2009.01.135
- J.L. Gómez Cámer¹, J. Morales¹, L. Sánchez¹, P. Ruch, S.H. Ng, R. Kötz, P. Novák
- Nanosized Si/cellulose fiber/carbon composites as high capacity anodes for lithium-ion batteries: A galvanostatic and dilatometric study*
 Electrochim. Acta **54**, 6713-6717 (2009).
 doi: 10.1016/j.electacta.2009.06.085
¹ Universidad de Córdoba, Spain
- Ph. Graf¹, A. Manton^{1,4}, A. Foelske, A. Shkilnyy^{2,3}, A. Masic³, A.F. Thünemann⁴, A. Taubert^{1,2,3}
- Peptide-coated silver nanoparticles: Synthesis, surface chemistry, and pHtriggered, reversible assembly into particle assemblies*
 Chem. Eur. J. **15**, 5831-5844 (2009).
 doi: 10.1002/chem.200802329
¹ University of Basel, Basel
² University of Potsdam, Golm, Germany
³ Max-Planck-Institute of Colloids and Interfaces, Golm, Germany
⁴ BAM Federal Institute for Materials Research and Testing, Berlin, Germany
- L. Gubler, M. Slaski, F. Wallasch, A. Wokaun, G.G. Scherer
- Radiation grafted fuel cell membranes based on co-grafting of α -methylstyrene and methacrylonitrile into a fluoropolymer base film*
 J. Membr. Sci. **339**, 68-77 (2009).
 doi: 10.1016/j.memsci.2009.04.031
- A. Hintennach, P. Novák
- Influence of surfactants and viscosity in the preparation process of battery electrodes containing nanoparticles*
 Phys. Chem. Chem. Phys. **11**, 9484-9488 (2009).
 doi: 10.1039/b911674e
- F. La Mantia, F. Rosciano, N. Tran, P. Novák
- Quantification of oxygen loss from Li_{1+x}(Ni_{1/3}Mn_{1/3}Co_{1/3})_{1-x}O₂ at high potentials by differential electrochemical mass spectrometry*
 J. Electrochem. Soc. **156**, A823-A827 (2009).
 doi: 10.1149/1.3205495
- E.H. Lehmann, P. Boillat, G.G. Scherer, G. Frei
- Fuel cell studies with neutrons at the PSI's neutron facilities*
 Nucl. Instrum. Methods Phys. Res., Sect A **605**, 123-126 (2009)
 doi: 10.1016/j.nima.2009.01.143
- F. Loviat, I. Czekaj, J. Wambach, A. Wokaun
- Nickel deposition on c-Al₂O₃ model catalysts: An experimental and theoretical investigation*
 Surf. Sci. **603**, 2210-2217 (2009).
 doi: 10.1016/j.susc.2009.04.032
- W. Märkle, N. Tran, D. Goers¹, M.E. Spahr¹, P. Novák
- The influence of electrolyte and graphite type on the PF₆⁻ intercalation behavior at high potentials*
 Carbon **47**, 2727-2732 (2009).
 doi: 10.1016/j.carbon.2009.05.029
¹ TIMCAL SA, Bodio

- S.-H. Ng, T.J. Patey,
R. Büchel¹, F. Krumeich¹,
J.-Z. Wang², H.-K. Liu²,
S.E. Pratsinis¹, P. Novák
*Flame spray-pyrolyzed vanadium oxide nanoparticles for
lithium battery cathodes*
Phys. Chem. Chem. Phys. **11**, 3748-3755 (2009).
doi: 10.1039/b821389p
¹ ETH Zürich
² University of Wollongong, Australia
- S.H. Ng, C. Vix-Guterl¹,
Ph. Bernardo, N. Tran,
J. Ufheil, H. Buqa,
J. Dentzer¹, R. Gadiou¹,
M.E. Spahr², D. Goers²,
P. Novák
*Correlations between surface properties of graphite and the
first cycle specific charge loss in lithium-ion batteries*
Carbon **47**, 705-712 (2009).
doi: 10.1016/j.carbon.2008.11.008
¹ Institute for Material Science of Mulhouse, France
² TIMCAL SA, Bodio
- S.H. Ng, F. La Mantia,
P. Novák
*A multiple working electrode for electrochemical cells: A tool
for current density distribution studies*
Angew. Chem. Int. Ed. **48**, 528-532 (2009); Angew. Chem.
121, 536-540 (2009).
doi: 10.1002/annir.200803981
- T.J. Patey, R. Büchel,
M. Nakayama¹, P. Novák
*Electrochemistry of LiMn₂O₄ nanoparticles made by flame
spray pyrolysis*
Phys. Chem. Chem. Phys. **11**, 3756-3761 (2009).
doi: 10.1039/b821572n
¹ Tokyo Institute of Technology, Japan
- T.J. Patey, A. Hintennach,
F. La Mantia, P. Novák
*Electrode engineering of nanoparticles for lithium-ion batteries
- role of dispersion technique*
J. Power Sources **189**, 590-593 (2009).
doi: 10.1016/j.jpowsour.2008.09.091
- T.J. Patey, R. Büchel¹,
S.H. Ng, F. Krumeich¹,
S.E. Pratsinis¹, P. Novák
*Flame co-synthesis of LiMn₂O₄ and carbon nanocomposites for
high power batteries*
J. Power Sources **189**, 149-154 (2009).
doi: 10.1016/j.jpowsour.2008.10.002
¹ ETH Zürich
- M. Reum, S.A. Freunberger,
A. Wokaun, F.N. Büchi
*Measuring the current distribution with sub-millimeter
resolution in PEFCs
II. Impact of operating parameters*
J. Electrochem. Soc. **156**, B301-B310 (2009).
doi: 10.1149/1.3043422
- M. Reum, A. Wokaun,
F.N. Büchi
*Measuring the current distribution with submillimeter resolution
in PEFCs
III. Influence of the flow field geometry*
J. Electrochem. Soc. **156**, B1225-B1231 (2009).
doi: 10.1149/1.3187913
- F. Rosciano, J.F. Colin,
F. La Mantia, N. Tran,
P. Novák
*Electrochemical stress at high potential to investigate phase
transitions in Li_{1+x}(Ni_{1/3}Mn_{1/3}Co_{1/3})_{1-x}O₂*
Electrochem. Solid-State Lett. **12**, A140-A144 (2009).
doi: 10.1149/1.3130042
- P.W. Ruch, R. Kötz,
A. Wokaun
*Electrochemical characterization of single-walled carbon
nanotubes for electrochemical double layer capacitors using
non-aqueous electrolyte*
Electrochim. Acta **54**, 4451-4458 (2009).
doi: 10.1016/j.electacta.2009.03.022

- P.W. Ruch, D. Cericola,
M. Hahn, R. Kötz,
A. Wokaun
On the use of activated carbon as a quasi-reference electrode in non-aqueous electrolyte solutions
J. Electroanal. Chem. **636**, 128-131 (2009).
doi: 10.1016/j.jelechem.2009.09.007
- P.W. Ruch, L.J. Hardwick,
M. Hahn, A. Foelske,
R. Kötz, A. Wokaun
Electrochemical doping of single-walled carbon nanotubes in double layer capacitors studied by in situ Raman spectroscopy
Carbon **47**, 38-52 (2009).
doi: 10.1016/j.carbon.2008.08.023
- H. Schulenburg, E. Müller¹,
G. Khelashvili², T. Roser,
H. Bönemann², A. Wokaun,
G.G. Scherer
Heat-treated PtCo₃ nanoparticles as oxygen reduction catalysts
J. Phys. Chem. C **113**, 4069–4077 (2009).
doi: 10.1021/jp808134j
¹ ETH Zürich
² Forschungszentrum Karlsruhe, Germany
- B.C. Seyfang, R. Fardel¹,
T. Lippert, G.G. Scherer,
A. Wokaun
Micro-patterning for polymer electrolyte fuel cells: Single pulse laser ablation of aluminium films from glassy carbon
Appl. Surf. Sci. **255**, 5471-5475 (2009).
doi: 10.1016/j.apsusc.2008.07.189
¹ Empa Dübendorf
- F. Simmen, T. Lippert,
P. Novák, B. Neuen-
schwander¹, M. Döbeli,
M. Mallepell, A. Wokaun
Influence of the substrate material on the properties of pulsed laser deposited thin Li_{1+x}Mn₂O_{4-δ} films
Appl. Surf. Sci. **255**, 5303-5306 (2009).
doi: 10.1016/j.apsusc.2008.08.016
¹ Berner Fachhochschule, Burgdorf
- V. Trabadelo¹, A. Retolaza¹,
S. Merino¹, A. Cruz²,
P. Heredia², A. Foelske,
H. Schiff, C. Padeste
Protein patterning by thermal nanoimprint lithography and NH₃-plasma functionalization of polystyrene
J. Vac. Sci. Technol. B **27**, 1060-1062 (2009).
doi: 10.1116/1.3123304
¹ Fundación Tekniker, Eibar, Gipuzkoa, Spain
² Gaiker, Parque Tecnológico, Zamudio, Bizkaia, Spain
- S.R. Waldvogel¹,
I.M. Malkowsky²,
U. Griesbach², H. Pütter²,
A. Fischer², M. Hahn, R. Kötz
Novel fluorine-free electrolyte system for supercapacitors
Electrochem. Commun. **11**, 1237-1241 (2009).
doi: 10.1016/j.elecom.2009.04.009
¹ Universität Bonn, Germany
² BASF SE, Ludwigshafen, Germany

Conference Proceedings / Other Papers

- Ph. Bernardo, J. Dentzer¹,
R. Gadiou¹, W. Märkle,
J. Saint², D. Goers²,
M.E. Spahr², P. Novák,
C. Vix-Guterl¹
Influence of graphite surface properties on the first lithium insertion in Li-ion batteries
Extended Abstract, CARBON 2009, Biarritz, France,
June 14-19 (2009), Abstract No. T4-835.
¹ Institute for Material Science of Mulhouse, France
² TIMCAL SA, Bodio
- M.H. Bayer, A. Wokaun,
G.G. Scherer, I.A. Schneider
Dynamic measurement and modeling of the water vapor concentration during ac impedance measurements in polymer electrolyte fuel cells (PEFCs)
Electrochem. Soc. Trans. **25** (1) 949-960 (2009).
- R. Kötz, P.W. Ruch,
D. Cericola,
In-situ monitoring of EDLC operation by physico-chemical techniques.
Extended Abstract, Advanced Automotive Battery & EC
Capacitor Conference AABC, Session 1,
Long Beach, California, USA, June 8-10 (2009).

- N. Linse, C. Aellig,
A. Wokaun, G.G. Scherer,
L. Gubler *Influence of operating parameters on start/stop induced degradation in polymer electrolyte fuel cells*
Electrochem. Soc. Trans. **25** (1) 1849-1859 (2009).
- M.M. Menampambath,
A. Wokaun, G.G. Scherer,
L. Gubler *Locally resolved degradation analysis of chemically aged radiation grafted polymer electrolyte membranes*
Proc. 5th European Summer School on Electrochemical Engineering, Almagro, Spain, September 6-11, 2009, Electrochemical Engineering: Industrial, Energy and Environmental Applications, 398-401 (2009). ISBN 978-84-934398-6-6
- M.M. Menampambath,
A. Wokaun, G.G. Scherer,
L. Gubler *Insights into the local degradation of chemically aged radiation grafted membranes*
Proc. European Fuel Cell Forum 2009, Luzern, June 29–July 2, 2009.
- P. Oberholzer, P. Boillat,
R. Perego, E.H. Lehmann,
G.G. Scherer, A. Wokaun *High resolution neutron imaging of liquid water in polymer electrolyte fuel cells (PEFC)*
Proc. 5th European Summer School on Electrochemical Engineering, Almagro, Spain, September 6-11, 2009: Electrochemical Engineering: Industrial, Energy and Environmental Applications, 430-432 (2009). ISBN 978-84-934398-6-6
- A. Savouchkina, A. Foelske-Schmitz, R. Kötz,
G.G. Scherer, A. Wokaun,
J. Ziegler, C. Padeste,
V. Auzelyte, H.H. Solak *Extreme ultraviolet Interference lithography for production of Pt nanoparticles on glassy carbon*
ECS Transactions, **25** (24) 175-184 (2009).
- I.A. Schneider, M.H. Bayer,
A. Wokaun, G.G. Scherer *Negative resistance values in locally resolved impedance spectra of polymer electrolyte fuel cells*
Electrochem. Soc. Trans. **25** (1) 937-948 (2009).
- G.A. Schuler, A. Wokaun,
F.N. Büchi *Experimental investigation of the local membrane permeation characteristics in PEFC*
Proc. European Fuel Cell Forum, Luzern, June 29-July 2 (2009).
- B. Schwanitz,
H. Schulenburg, A. Wokaun,
G. G. Scherer *Ultra low Pt anodes for polymer electrolyte fuel cells*
Proc. European Fuel Cell Forum, Luzern, June 29-July 2 (2009).
- B. Seyfang, P. Boillat,
G.G. Scherer, T. Lippert,
A. Wokaun *Miniaturized polymer electrolyte fuel cell without gas diffusion layers*
Proc. European Fuel Cell Forum 2009, Luzern, June 30-July 2 (2009).
- S. von Dahlen, A. Wokaun,
G.G. Scherer, I.A. Schneider *Locally resolved cyclic voltammetry in channel and land areas of a polymer electrolyte fuel cell*
Proc. 5th European Summer School on Electrochemical Engineering, Almagro, Spain, September 6-11, 2009: Electrochemical Engineering: Industrial, Energy and Environmental Applications, 433-436 (2009). ISBN 978-84-934398-6-6

T. Yamaki¹, S. Sawada¹,
M. Asano¹, Y. Maekawa¹,
M. Yoshida¹, L. Gubler,
S. Alkan Gürsel,
G.G. Scherer

Fuel-cell performance of multiply-crosslinked polymer electrolyte membranes prepared by two-step radiation technique

Electrochem. Soc. Trans. **25** (1) 1439-1450 (2009).
doi: 10.1149/1.3210700

¹ Japan Atomic Energy Agency, Takasaki, Japan

M. Zaglio, A. Wokaun,
J. Mantzaras, F.N Büchi

1-D dynamic model development and validation for PEFCs
Ext. Abstract 6th Symposium on Fuel Cell Modelling and
Experimental Validation (MODVAL 6) 66,
Bad Herrenalb/Karlsruhe, Germany, March 25-26, 2009.

M. Zaglio, A. Wokaun,
J. Mantzaras, F.N. Büchi

Development and validation of a dynamic model for PEFCs
Proc. European Fuel Cell Forum 2009, Luzern,
June 29-July 2 (2009).

TALKS

Invited Talks

H. Ben youcef

Radiation grafted membranes for fuel cells: research highlights from Paul Scherrer Institut (PSI)

Japan Atomic Energy Agency, Takasaki, Japan, August 10-12, 2009.

L. Gubler

New trends in hydrocarbon membrane development

Gordon Research Conference – Fuel Cells, Bryant University,
Smithfield RI, USA, July 26-31, 2009.

R. Kötz

In-situ monitoring of EDLCs operation by physico-chemical techniques

Advanced Automotive Battery Conference AABC, Long Beach,
USA, June 8-12, 2009.

R. Kötz

Single-walled carbon nanotubes and activated carbon for supercapacitor electrodes - a comparison

Keynote Lecture, 1st International Symposium on Enhanced Electrochemical Capacitors, ISEECap'09, Nantes, France, June 29 –July 2, 2009.

R. Kötz

Aging of carbon based supercapacitors

5th IUPAC International Symposium on Novel Materials and their Synthesis, Shanghai, China, October 18-22, 2009.

P. Maire

In situ Methoden zur Untersuchung von Alterungsvorgängen in Lithiumionen-Batterien

Workshop System Analysis for Nano Enabled Electrochemical Storage Systems (SANEES), Karlsruher Institut für Technologie (KIT), Germany, December 14, 2009.

P. Novák

Fuel cell research & development at Paul Scherrer Institut

Investment Conference on Fuel Cell, Foreign Investment Forum 2009, Seoul, Korea, November 5, 2009.

P. Novák

Batterien und Mobilität: Von der Grundlagenforschung zum Industrieprodukt

Physikalisches Kolloquium, Physikalisches Institut der Universität Heidelberg, Heidelberg, Germany, October 23, 2009.

- P. Novák *Material development for lithium-ion batteries: Challenges and trends*
Workshop on Material Science, Institute for Material Science of Mulhouse, Mulhouse, France, October 8, 2009.
- P. Novák *In situ characterization of materials for lithium-ion batteries*
Seminar at Tsinghua University, Beijing, China, August 24, 2009.
- P. Novák *Scientific challenges in the field of lithium-ion battery materials*
Seminar at Institute of Physics, CAS, Beijing, China, August 21, 2009.
- P. Novák *Battery research: A wedding of solid state electrochemistry with surface electrochemistry?*
International Symposium on Frontiers of Electrochemical Science and Technology, Xi'an, China, August 13, 2009.
- P. Novák *Mobilität und Elektrochemie: Wo ist der rote Faden der Batterieforschung?*
Seminar der Studiengruppe Energieperspektiven, Baden, June 4, 2009.
- P. Novák *Was hat Analytik mit Batterien und Mobilität gemeinsam?*
Seminar NanoMat - 10. Szene „Moleküle unter Strom“, Karlsruhe, Germany, March 12, 2009.
- G.G. Scherer *Contributions of electrochemical energy devices to a sustainable mobility*
Transforming Energy Lecture, University of Maryland, A. James Clark School of Engineering, College Park, MA, USA, February 26, 2009.
- G.G. Scherer *Radiation grafted fuel cell membranes*
University of Maryland, Department of Materials Science and Engineering, College Park, MA, USA, February 27, 2009.
- G.G. Scherer *Aspects of electrochemical energy research*
Universität Bern, Seminar für Anorganische, Analytische und Physikalische Chemie, April 2, 2009.
- G.G. Scherer *Brennstoffzellen und Superkondensatoren*
Battery Technology Day, Technopark Zürich, May 28, 2009.
- G.G. Scherer *Aspects of materials development for polymer electrolyte fuel cells*
E-MRS, Symposium C, Strasbourg, France, June 15-19, 2009.
- G.G. Scherer *Insights into the water management problem of PEFCs provided by neutron imaging*
International Symposium on Diagnostic Tools for Fuel Cell Technologies, Technical University of Trondheim, Norway, June 23-24, 2009.
- G.G. Scherer *Brennstoffzellentechnologien - Gemeinsamkeiten und Unterschiede*
„Von Anfang bis Zukunft: Die Brennstoffzelle schreibt Geschichte“
Max-Planck-Institut für Polymerforschung, Mainz, Germany, July 9, 2009.

- G.G. Scherer *Brennstoffzellentechnologien im Spannungsfeld zwischen Wunsch und Wirklichkeit*
Physikalisches Kolloquium, Universität Konstanz, Germany, July 21, 2009.
- G.G. Scherer *Novel proton-conducting polymer membranes*
60th Annual Meeting of the International Society of Electrochemistry, Beijing, China, August 16–21, 2009.
- G.G. Scherer *Aktuelle Themen der Materialforschung für die elektrochemische Energiewandlung und –speicherung*
Werkstoffwissenschaftlichen Kolloquium, Universität Erlangen-Nürnberg, Germany, December 1, 2009.
- G.G. Scherer *Solid polymer electrolytes for electrochemical systems prepared by radiation grafting*
Polymer Science and Technology: Vision & Scenario, APA 2009, New Dehli, India, December 16-20, 2009.
- I.A. Schneider *Current distribution and impedance response in polymer electrolyte fuel cells*
215th Meeting of The Electrochemical Society, San Francisco CA, USA, May 25, 2009.

Other Talks

- S. Balog, U. Gasser, K. Mortensen¹, L. Gubler, H. Ben youcef, G.G. Scherer *Correlation between morphology, water uptake, and proton conductivity in radiation grafted proton exchange membranes*
437. We-Heraeus-Seminar, 'Photons and Neutrons as Probes of Matter', Physikzentrum Bad Honnef, Germany, December 13–16, 2009.
¹ University of Copenhagen, Frederiksberg, Denmark
- M.H. Bayer, A. Wokaun, G.G. Scherer, I.A. Schneider *Dynamic measurement and modeling of the water vapor concentration during ac impedance measurements in polymer electrolyte fuel cells (PEFCs)*
216th Meeting of the Electrochemical Society, Vienna, Austria, October 4-9, 2009.
- P. Boillat, P. Oberholzer, G.G. Scherer, A. Wokaun, E.H. Lehmann *A study of water distribution transients in PEFC using time resolved high resolution neutron imaging*
6th Symposium on Fuel Cell Modelling and Experimental Validation (MODVAL 6), Bad Herrenalb, Germany, March 25-26, 2009.
- P. Boillat, P. Oberholzer, G.G. Scherer, A. Wokaun, E.H. Lehmann *Study of water dynamics in PEFC porous media using time resolved high resolution neutron imaging*
ASME 7th International Fuel Cell Science, Engineering & Technology Conference, Newport Beach, USA, June 8-10, 2009.
- P. Boillat, R. Flückiger, J. Eller, P. Oberholzer, G. Frei, A. Kästner, M. Stampanoni, R. Perego, E.H. Lehmann, F.N. Büchi, G.G. Scherer, A. Wokaun *Tracking water in fuel cells using PSI large research facilities*
JUM@P'09 – Joint Users Meeting at PSI, Villigen, October 12-13, 2009.
- P. Boillat *Looking in a fuel cell: X-ray and neutron tomography and radiography*
8th PSI Summer School on Condensed Matter Research, Zuoz, August 2-7, 2009.

- J. Bernard, S. Delprat¹,
T.M. Guerra¹, P. Dietrich,
F.N. Büchi
Energy efficient power management strategy for fuel cell hybrid vehicles
International Advanced Mobility Forum, Geneva, March 10-12, 2009.
¹ Université de Valenciennes et du Hainaut-Cambrésis, France
- F.N. Büchi, J. Eller,
R. Flückiger, F. Marone,
M. Stambanoni
Investigation of solid-liquid interactions in porous transport layers using X-ray micro tomography
216th Meeting of the Electrochemical Society, Vienna, Austria, October 4-9, 2009.
- F.N. Büchi, T. Colinar
Sub-millimeter current density distribution in PEFC at sub-zero temperatures
216th Meeting of the Electrochemical Society, Vienna, Austria, October 4-9, 2009.
- F.N. Büchi, R. Flückiger,
M. Reum, F. Marone,
M. Stambanoni
Contribution to the understanding of the heterogeneities on the channel/rib scale in PEFC
6th Symposium on Fuel Cell Modelling and Experimental Validation (MODVAL 6), Bad Herrenalb, Germany, March 25-26, 2009.
- D. Cericola, P.W. Ruch,
P. Novák, R. Kötz,
A. Wokaun
Approach to bi-material electrodes for electrochemical double layer capacitor – Li-ion battery hybrids
216th Meeting of the Electrochemical Society, Vienna, Austria, October 4-9, 2009.
- J.-F. Colin, V. Godbole,
P. Novák
In situ neutron diffraction study of $Li_4Ti_5O_{12}$
42nd IUPAC Congress - Chemistry Solutions, Glasgow, United Kingdom, August 2-7, 2009.
- S.M. Dockheer¹,
W.H. Koppenol¹,
L. Gubler
Oxidation mechanism of oligomer model compounds for polymer electrolyte fuel cell membranes
26th "MILLER" Conference on Radiation Chemistry, Keszthely, Hungary, August 28-September 2, 2009.
¹ ETH Zürich
- A. Foelske-Schmitz,
A. Savouchkina, R. Kötz,
G.G. Scherer, A. Wokaun
Electrochemical platinum deposition on modified glassy carbon electrodes
216th Meeting of the Electrochemical Society, Vienna, Austria, October 4-9, 2009.
- J. Gomez-Cámer¹,
J. Morales¹, L. Sanchez¹,
P. Ruch, S.H. Ng,
R. Kötz, P. Novák
Nanosized Si/cellulose fiber/carbon composites as high capacity anodes for lithium-ion batteries: A galvanostatic and dilatometric study
216th Meeting of the Electrochemical Society, Vienna, Austria, October 4-9, 2009.
¹ Universidad de Córdoba, Spain
- L. Gubler, N. Linse,
A. Wokaun, G.G. Scherer
Start/stop induced degradation in polymer electrolyte fuel cells and mitigation strategies
60th Annual Meeting of the International Society of Electrochemistry, Beijing, China, August 16-21, 2009.
- F. La Mantia, S.H. Ng,
P. Novák
A cell with multiple working electrodes: measuring the perpendicular current density distribution.
215th Meeting of the Electrochemical Society, San Francisco, California, USA, May 24-29, 2009.
- N. Linse, C. Aellig,
A. Wokaun, G.G. Scherer,
L. Gubler
Influence of operating parameters on start/stop induced degradation in polymer electrolyte fuel cells
216th Meeting of the Electrochemical Society, Vienna, Austria, October 4-9, 2009.

- P. Maire, W. Scheifele,
H. Kaiser, P. Novák *Colorimetric determination of lithium ion diffusion in graphite electrodes*
Lithium Battery Discussion - Electrode Materials, Arcachon, France, September 20-25, 2009.
- M.M. Menampambath,
A. Wokaun, G.G. Scherer,
L. Gubler *Insights into the local degradation of chemically aged radiation grafted membranes*
European Fuel Cell Forum 2009, Luzern, June 29–July 2, 2009.
- P. Novák, P. Maire *Diffusion kinetics of lithium-ions in graphite composite electrodes for lithium-ion batteries*
60th Meeting of the International Society of Electrochemistry, Beijing, China, August 16-21, 2009.
- A. Savouchkina,
A. Foelske-Schmitz,
R. Kötz, G.G. Scherer,
A. Wokaun, J. Ziegler,
C. Padeste, V. Auzelyte,
H.H. Solak *Extreme ultraviolet interference lithography for production of Pt nanoparticles on glassy carbon*
216th Meeting of the Electrochemical Society, Vienna, Austria, October 4-9, 2009.
- G.G. Scherer *Brennstoffzellen - Energiequellen der Zukunft?*
Lions Club Brugg/AG und Lions Club Bad Herrenalb, Germany, Paul Scherrer Institut, June 13, 2009.
- I.A. Schneider,
M.H. Bayer, A. Wokaun,
G.G. Scherer *Negative resistance values in locally resolved impedance spectra of polymer electrolyte fuel cells*
216th Meeting of the Electrochemical Society, Vienna, Austria, October 16, 2009.
- I.A. Schneider,
M.H. Bayer, A. Wokaun,
G.G. Scherer *Negative resistance values in locally resolved impedance spectra of polymer electrolyte fuel cells*
International Workshop on Impedance Spectroscopy, Chemnitz, Germany, October 29, 2009.
- G.A. Schuler, A. Wokaun,
F.N. Büchi *Local online gas analysis in PEFC*
International Symposium on Diagnostic Tools for Fuel Cell Technologies, Trondheim, Norway, June 23-24, 2009.
- G.A. Schuler, A. Wokaun,
F.N. Büchi *Experimental investigation of the local membrane permeation characteristics in PEFC*
European Fuel Cell Forum, Luzern, June 29 - July 2, 2009.
- H. Schulenburg,
E. Müller¹, G. Khelashvili²,
T. Roser,
H. Bönemann²,
A. Wokaun, G.G. Scherer *Heat-treated PtCo₃ nanoparticles as oxygen reduction catalysts*
7th Spring Meeting of the International Society of Electrochemistry, Szczyrk, Poland, March 22-25, 2009.
- H. Schulenburg,
B. Schwanitz, A. Wokaun,
G.G. Scherer *Pt-based catalysts for polymer electrolyte fuel cells*
Electrochemical Nanoscience Seminar, Universität Bern, July 1, 2009.
- B. Schwanitz,
H. Schulenburg,
A. Wokaun, G.G. Scherer *Ultra low Pt anodes for polymer electrolyte fuel cells*
European Fuel Cell Forum 2009, Luzern, June 29-July 2, 2009.
- B. Seyfang, P. Boillat,
G.G. Scherer, T. Lippert,
A. Wokaun *Miniaturized polymer electrolyte fuel cell without gas diffusion layers*
European Fuel Cell Forum 2009, Luzern, June 29-July 2, 2009.

- B. Seyfang, P. Boillat,
G.G. Scherer, T. Lippert,
A. Wokaun
Foregoing the gas diffusion layers in miniaturized polymer electrolyte fuel cells: Losses and profits
6th Symposium on Fuel Cell Modelling and Experimental Validation (MODVAL 6), Bad Herrenalb, Germany, March 25-26, 2009.
- P. Verma
Chemically modified carbons as negative electrodes in Li-ion batteries
PhD Students' Symposium 2009, EMPA Dübendorf, November 19, 2009.
- C. Vix-Guterl¹, S.H. Ng,
Ph. Bernardo, N. Tran,
J. Ufheil, H. Buqa,
J. Dentzer¹, R. Gadiou¹,
M.E. Spahr², J. Saint²,
D. Goers², P. Novák
Correlations between surface properties of graphite and the first cycle irreversible capacity in lithium-ion batteries
CARBON 2009, Biarritz, France, June 14-19, 2009.
¹ Institute for Material Science of Mulhouse, France
² TIMCAL SA, Bodio
- F. Wallasch, G.G. Scherer
Radiation grafted polymer membranes for fuel cell applications
IAEA Workshop, Villigen PSI, June 15-20, 2009.
- F. Wallasch, L. Gubler,
G.G. Scherer, A. Wokaun
Pre-irradiation grafted films as precursor for fuel cell membranes: Preparation and characterization
238th ACS National Meeting & Exposition, Washington, DC, USA, August 16-18, 2009.
- M. Zaglio, A. Wokaun,
J. Mantzaras, F.N. Büchi
Development and validation of a dynamic model for PEFCs
European Fuel Cell Forum 2009, Luzern, June 29-July 2, 2009.
- M. Zaglio, A. Wokaun,
J. Mantzaras, F.N. Büchi
1-D dynamic model development and validation for PEFCs
6th Symposium on Fuel Cell Modelling and Experimental Validation (MODVAL 6), Bad Herrenalb/Karlsruhe, Germany, March 25-26, 2009.

POSTERS

- V. Auzelyte, H. Sigg,
B. Schmitt,
A. Savouchkina,
A. Foelske-Schmitz,
H.H. Solak
ZnO films and nanostructures formed from chemical solution by annealing and EUV exposures
Trends in Nanoscience 2009, Kloster Irsee, Germany, Februar 28-March 4, 2009.
- S. Balog, U. Gasser,
K. Mortensen¹, L. Gubler,
H. Ben youcef,
G.G. Scherer
Correlation between morphology, water uptake, and proton conductivity in radiation grafted proton exchange membranes
First Joint Users' Meeting @ PSI: JUM@P '09, October 12-13, 2009.
¹ University of Copenhagen, Frederiksberg, Denmark
- H. Ben youcef,
D. Henkensmeier,
L. Gubler, A. Wokaun,
G.G. Scherer
Second generation of radiation induced grafted membranes for fuel cells: improved mechanical and oxidative stability
4th International Conference on Polymer Batteries and Fuel Cells (PBFC-2009), Yokohama, Japan, August 2-6, 2009.
- Ph. Bernardo, S.-H. Ng,
J. Dentzer¹, R. Gadiou¹,
M.E. Spahr², D. Goers²,
W. Märkle, P. Novák,
C. Vix-Guterl¹
Influence of graphite surface properties on the first lithium insertion in Li-ion batteries
CARBON 2009, Biarritz, France, June 14-19, 2009.
¹ Institute for Material Science of Mulhouse, France
² TIMCAL SA, Bodio

- I. Czekaj, F. Loviat,
J. Wambach, A. Wokaun
Nickel particles at the gamma-Al₂O₃: DFT modelling and XPS studies of model catalyst
25th Annual Meeting SAOG-GSSI "25 Years of Surface Science and SAOG", Institut de Physique P erolles, University of Fribourg, January 23, 2009.
- I. Czekaj, F. Loviat,
J. Wambach, A. Wokaun
DFT modelling and XPS studies of model Ni/Al₂O₃ catalyst: Nickel particles behavior at the support
EUROPACAT IX, Salamanca, Spain, August 29-September 4, 2009.
- S.M. Dockheer¹,
L. Gubler,
W.H. Koppenol¹
Strategies to improve durability of a solid polymer membrane for fuel cells
Fall Meeting of the Swiss Chemical Society 2009, EPF Lausanne, September 4, 2009.
¹ ETH Z urich
- J. Eller, F.N. B uchi,
R. Fl uckiger,
M. Stampanoni,
S. McDonald, F. Marone,
D. Tehlar
X-ray tomography study of liquid water in polymer electrolyte fuel cell
Interdisciplinary Symposium on 3D Microscopy, Interlaken, July 12-16, 2009.
- J. Eller, F.N. B uchi,
R. Fl uckiger,
M. Stampanoni,
S. McDonald, F. Marone,
D. Tehlar
X-ray tomography study of liquid water in polymer electrolyte fuel cell
Gordon Research Conference on Fuel Cells, Smithfield RI, USA, July 26-31, 2009.
- J. Eller, F.N. B uchi,
R. Fl uckiger,
M. Stampanoni,
S. McDonald, F. Marone,
D. Tehlar, A. Wokaun
X-ray micro tomography study of liquid water in gas diffusion layers of polymer electrolyte fuel cells
CIMST Interdisciplinary Summer School on Bio-medical Imaging, Z urich, August 24-September 4, 2009.
- J. Eller, F.N. B uchi,
S. McDonald, F. Marone,
M. Stampanoni,
A. Wokaun
Visualization of in-situ liquid water distribution of polymer electrolyte fuel cells using x-ray micro tomography
JUM@P '09: Joint Users' Meeting @ PSI, Villigen, October 12-13, 2009.
- L. Gubler,
M.M. Menampambath,
A. Wokaun, G.G. Scherer
Rapid aging and locally resolved post test analysis of fuel cell membranes
60th Annual Meeting of the International Society of Electrochemistry, Beijing, China, August 16-21, 2009.
- W. M arkle, D. Goers¹,
M.E. Spahr¹, P. Nov ak
Wetting behavior of porous graphite electrodes with carbonate based electrolytes
CARBON 2009, Biarritz, France, June 14-19, 2009.
¹ TIMCAL SA, Bodio
- K. Mortensen¹, U. Gasser,
S. Balog, S. Alkan G ursel,
G.G. Scherer
Structural characterization of radiation-grafted block copolymer films, using SANS technique
JUM@P '09: Joint Users' Meeting @ PSI, Villigen, October 12-13, 2009.
¹ University of Copenhagen, Frederiksberg, Denmark
- H. Schulenburg,
B. Schwanitz,
J. Krbanjevic,
M. Stampanoni,
A. Wokaun, G.G. Scherer
3D imaging of polymer electrolyte fuel cell electrodes by high-resolution X-ray tomography and FIB/SEM serial sectioning
Interdisciplinary Symposium on 3D Microscopy, Interlaken, Juli 12-16, 2009.

- H. Schulenburg,
B. Schwanitz,
J. Krbanjevic,
M. Stampanoni,
A. Wokaun, G.G. Scherer
3D imaging of polymer electrolyte fuel cell electrodes by high-resolution X-ray tomography and FIB/SEM serial sectioning
8th PSI Summer School on Condensed Matter Research, Zuoz,
August 1-7, 2009.
- H. Schulenburg,
B. Schwanitz,
J. Krbanjevic,
M. Stampanoni,
A. Wokaun, G.G. Scherer
3D imaging of polymer electrolyte fuel cell electrodes by high-resolution X-ray tomography and FIB/SEM serial sectioning
CIMST Interdisciplinary Summer School on Bio-medical Imaging,
Zürich, August 24–September 4, 2009.
- F. Simmen, T. Lippert,
P. Novák, M. Horisberger,
M. Döbeli, M. Mallepell,
A. Wokaun
Influence of metal layer coated glassy carbon substrates on the properties of PLD deposited $Li_{1+x}Mn_2O_{4-\delta}$ films
European Materials Research Society Spring Meeting,
Strasbourg, France, June 8-12, 2009.
- F. Wallasch, L. Gubler,
G.G. Scherer, A. Wokaun
Advanced fuel cell membranes using graft copolymerization
Asian Polymer Association (APA) 2009, New Delhi, India,
December 17-20, 2009.

CONFERENCES, WORKSHOPS & EXHIBITIONS

- P. Novák
60th Annual Meeting of the International Society of Electrochemistry
Beijing, China, August 16-21, 2009.
Organizing Committee
- F.N. Büchi
Gordon Research Conference on Fuel Cells
Smithfield, RI, USA, July 26-31, 2009.
Chair
- R. Kötz
1st International Symposium on Enhanced Electrochemical Capacitors, ISEECap'09
Nantes France, June 29 -July 2, 2009.
International Scientific Committee
- R. Kötz
5th IUPAC International Symposium on Novel Materials and their Synthesis
Shanghai, China, October 18-22, 2009.
Session Chair
- G.G. Scherer, R. Kötz,
P. Novák
Electrochemistry: Learning from the past to master the future
25th One-Day-Symposium, PSI Villigen, May 06, 2009.
Organizers
- G.G. Scherer
Development of novel absorbents and membranes by radiation-induced grafting for selective purposes
IAEA 2nd Research Coordination Meeting, PSI Villigen,
June 15-19, 2009.
Organizer
- G.G. Scherer
Polymer Science and Technology: Vision & Scenario
APA 2009, New Delhi, India, December 16-20, 2009.
International Advisory Committee

MEMBERSHIPS IN EXTERNAL COMMITTEES

R. Kötz	<i>Advisory Board Electrochimica Acta</i> Member
R. Kötz	<i>Publications Committee of the International Society of Electrochemistry</i> Chair
P. Novák	<i>International Society of Electrochemistry</i> Vice President
P. Novák	<i>Editorial Board Materials</i> Member
G.G. Scherer	<i>Asian Polymer Association, New Delhi, India</i> Honorary Member
G.G. Scherer	<i>Advisory Board Electrocatalysis</i> Member
G.G. Scherer	<i>Kantonsschule Wohlen</i> Maturitätsprüfungsexperte Biologie/Chemie
G.G. Scherer	<i>Advisory Board European Fuel Cell Forum</i> Member

PAUL SCHERRER INSTITUT



Paul Scherrer Institut, 5232 Villigen PSI, Switzerland
Tel. +41 (0)56 310 21 11, Fax +41 (0)56 310 21 99
www.psi.ch